

**Converting the elusive G protein-coupled adenosine
A₃ receptor into a highly-stable, well-characterized
receptor model for structural studies**

Dissertation

zur

Erlangung des Doktorgrades (Dr. rer. nat.)

der

Mathematisch-naturwissenschaftlichen Fakultät

der

Rheinischen Friedrich-Wilhelms-Universität Bonn

vorgelegt von

Jonathan Gerhard Schlegel

aus Münster

Bonn 2022

Angefertigt mit Genehmigung der Mathematisch-Naturwissenschaftlichen Fakultät der Rheinischen Friedrich-Wilhelms-Universität Bonn.

1. Gutachterin/Betreuerin: Prof. Dr. Christa E. Müller

2. Gutachter: Prof. Dr. Gerd Bendas

Tag der Promotion: 20.01.2023

Erscheinungsjahr: 2023

Die vorliegende Arbeit wurde in der Zeit von Juli 2018 bis September 2022 am Pharmazeutischen Institut der Rheinischen Friedrich-Wilhelms-Universität Bonn unter der Leitung von Frau Prof. Dr. Christa E. Müller angefertigt.

Table of contents

List of abbreviations	I
List of figures	III
List of tables	VI
1. Introduction	1
1.1 G protein-coupled receptors	1
1.1.1 Mechanism of GPCR activation	3
1.1.2 The GPCR environment	5
1.2 The adenosine A₃ receptor (A₃AR)	7
1.2.1 Distribution and pharmacology	10
1.2.2 Signaling	13
1.2.3 Medicinal chemistry — A ₃ AR ligands	14
1.2.3.1 Agonists	14
1.2.3.2 Antagonists	16
1.3 Structural biology	19
1.3.1 Structural biology of GPCRs	20
1.3.2 Structural biology in the field of drug discovery	22
1.3.3 Cryogenic electron microscopy	23
1.3.4 X-ray crystallography	24
1.3.5 Structural biology of membrane proteins: general approach and workflow	25
1.3.5.1 Expression	26
1.3.5.2 Solubilization	28
1.3.5.3 Purification	28
1.3.6 Crystallization within the lipidic cubic phase	29
1.4 The A₃AR from a structural point of view	31
1.4.1 The ligand binding pocket	31
1.4.2 Conserved motifs	34
1.4.2.1 NPxxY motif	34
1.4.2.2 DRY motif	34
1.4.2.3 PIF motif	35

1.4.2.4	CWxP motif	36
1.4.2.5	Sodium binding pocket	36
2.	Aim of this thesis	38
3.	Results and Discussion	40
3.1	Construct design	40
3.2	Introduction of fusion partners	42
3.2.1	Fusion partner inserted into the ICL3	43
3.2.2	N-terminal fusion partner.....	44
3.3	Further construct modifications	45
3.3.1	Results of further construct modifications.....	46
3.4	Analysis of initial A₃AR protein constructs	48
3.4.1	Thermostability of initial A ₃ AR constructs	48
3.4.2	Protein analysis of initial A ₃ AR protein constructs	50
3.5	Introduction of the S97^{3.39}K mutation within the sodium binding pocket ..	52
3.6	Construct optimization by junction site modifications	53
3.7	Combination of the S97^{3.39}K mutation and junction site modifications ..	58
3.7.1	Insights into the effects of junction site modifications	60
3.8	The role of N-terminal N-glycosylation sites	63
3.8.1	Enzymatic deglycosylation of N-terminal N-glycans.....	65
3.8.2	Glycosylation of JS53	66
3.8.3	Glycosylation state of JS68.....	68
3.9	Optimization of the N-terminal construct sequence	69
3.9.1	Transfer and improvement of the NNST sequence	72
3.10	The helix VIII exchange	74
3.11	Investigation of point mutations	77
3.11.1	Introduction of point mutations	78
3.11.2	Combination of point mutations	81
3.12	Investigation of the conserved disulfide bond connecting ECL2 and TM3 ..	82
3.13	Optimization of expression and purification conditions	85
3.13.1	Purification in the presence of various A ₃ AR ligands	87

3.13.2	Solubilization and purification with LMNG and the irreversible A ₃ AR antagonist LUF7602.....	89
3.14	Assessment of ligand binding by the CPM-based thermostability assay ____	90
3.14.1	Ligand screening campaign I.....	91
3.14.2	Ligand screening campaign II.....	92
3.14.3	Ligand screening campaign III	93
3.14.4	Ligand screening campaign IV	95
3.14.5	Ligand screening campaign V	96
3.14.6	The antagonists LUF7602 and AT563.....	98
3.14.7	Thermostability — conclusion.....	100
3.15	Mouse A₃AR constructs _____	101
3.16	Crystallization experiments _____	104
3.16.1	First crystallization experiment of JS68	104
3.16.2	Second crystallization of JS68.....	108
3.16.3	Crystallization of JS68 — conclusion	109
3.16.4	Crystallization of JS97.....	110
3.16.5	Crystallization of JS104.....	111
3.16.6	Crystallization experiments — conclusion.....	113
3.17	Development of irreversible A₃AR antagonists _____	114
3.17.1	Wash-out experiments	119
3.18	Construct validation _____	121
3.18.1	Ligand binding at constructs expressed in <i>Sf9</i> insect cells	121
3.18.2	Ligand binding at constructs expressed in CHO-S cells.....	123
3.18.3	NECA binding	124
3.18.4	Cholesterol depletion	128
3.18.5	Cholesterol replenishment	132
3.18.6	Transferring potential interaction partners	134
3.18.7	Ligand binding at solubilized A ₃ AR receptor constructs	136
3.18.8	Purification of A ₃ AR constructs expressed in CHO-S cells.....	138
3.18.9	Ligand binding at purified A ₃ AR constructs expressed in CHO-S cells.....	140
3.18.10	The BODIPY-labeled ligand TK-OT-024	141

4.	Summary & conclusions	145
5.	Methods	153
5.1	Molecular biology	153
5.1.1	Construct generation	153
5.1.2	Cloning	153
5.1.3	Agarose gel electrophoresis	153
5.1.4	Site-directed mutagenesis	154
5.1.5	Overlap extension PCR	154
5.1.6	Transformation into competent DH5 α <i>E. coli</i>	156
5.2	Recombinant protein expression in insect cells	157
5.2.1	Transformation into DH10Bac <i>E. coli</i>	157
5.2.2	Bacmid DNA preparation	158
5.2.3	Verification of the recombinant bacmid DNA	158
5.2.4	Cell culture of <i>Sf9</i> insect cells	159
5.2.5	Transfection & infection	159
5.2.6	Transfection control	160
5.2.7	Expression control	161
5.2.8	Membrane preparation	161
5.3	Expression in CHO-S cells	162
5.3.1	CHO-S cells — membrane preparation	162
5.3.2	PEI stock solution	163
5.4	Preparation of the DDM/CHS stock solution	163
5.5	Solubilization & Purification	163
5.6	Crystallization	164
5.7	Protein analysis	165
5.7.1	SDS-PAGE and western blotting	165
5.7.2	Size exclusion chromatography	166
5.7.3	Thermostability assay	166
5.8	Radioligand displacement assays	166
5.9	Wash-out experiments	168
5.10	CLR-MβCD inclusion complex	169

5.11	Cholesterol depletion and restoration	169
5.12	Solubilization of A₃AR constructs for radioligand binding studies	169
5.13	Analysis of data from radioligand binding experiments	169
5.14	Protein determination	170
5.15	Synthesis of compounds	170
6.	Supplementary	171
6.1	Constructs	171
6.2	Amino acid sequences	181
6.2.1	Human A ₃ AR.....	181
6.2.2	Mouse A ₃ AR.....	182
6.2.3	Tags.....	182
6.2.4	Fusion partner	182
6.2.4.1	b ₅₆₂ RIL	182
6.2.4.2	T4L.....	182
6.2.4.3	dsT4L	182
6.2.4.4	Flavodoxin.....	182
6.2.4.5	Rubredoxin.....	183
6.2.4.6	Xylanase.....	183
6.2.4.7	Lyso Fragment	183
6.2.4.8	PTD	183
6.2.4.9	PGS	183
6.3	Buffers	184
7.	Danksagung	186
8.	References	187

List of abbreviations

AC	Adenylate cyclase
AcMNPV	<i>Autographa californica</i> multiple nucleopolyhedrovirus
AR	Adenosine receptor
ATP	Adenosine triphosphate
β_1 AR	β_1 Adrenergic receptor
β_2 AR	β_2 Adrenergic receptor
BSA	Bovine serum albumin
CAM	Constitutively active mutant
cAMP	3',5'-Cyclic adenosine monophosphate
CCM	CLR consensus motif
CHAPS	3-[3-(Cholamidopropyl)dimethylammonio]-1-propanesulfonate
CHS	Cholesteryl hemisuccinate
CLR	Cholesterol
CMA	Carboxymethylaspartate
CMC	Critical micelle concentration
CPM	<i>N</i> -[4-(7-Diethylamino-4-methyl-3-coumarinyl)phenyl]maleimide
CRAC	Cholesterol recognition amino acids consensus
cryo-EM	Cryogenic electron microscopy
DAG	Diacylglycerol
DDM	<i>n</i> -Dodecyl- β -D-maltoside
DMSO	Dimethylsulfoxide
DTT	Dithiothreitol
ECL	Extracellular loop
<i>E. coli</i>	<i>Escherichia coli</i>
EDTA	Ethylenediaminetetraacidic acid
Endo H	Mannosyl-glycoprotein endo- β - <i>N</i> -acetylglucosaminidase
GABA	γ -Amino butyric acid
GAP	GTPase-activating protein
GDP	Guanosine diphosphate
GEF	Guanine nucleotide exchange factor
GIRK	G protein-coupled inwardly-rectifying potassium channel
GPCR	G protein-coupled receptor
GP64	Glycoprotein 64
GRK	G protein-coupled receptor kinase
GSK-3 β	Glycogen synthase kinase-3 β
GTP	Guanosine triphosphate
HA	Hemagglutinin
HEPES	4-(2-Hydroxyethyl)-1-piperazineethanesulfonic acid
ICL	Intracellular loop
IMAC	Immobilized metal-affinity chromatography
IPTG	Isopropyl- β -D-thiogalactopyranosid
IP ₃	Inositol trisphosphate
LCP	Lipidic cubic phase
LMNG	Lauryl maltose neopentyl glycol, 2,2-didecylpropane-1,3-bis- β -D-maltopyranoside
MAG	Monoacylglycerol
MAPKs	Mitogen activated protein kinases
M β CD	Methyl- β -cyclodextrin

monoolein	1-Oleoyl- <i>rac</i> -glycerin
mRNA	Messenger ribonucleic acid
M ₄ mAChR	M ₄ Muscarinic acetylcholine receptor
GlcNAc	<i>N</i> -Acetylglucosamine
NECA	5'-N-Ethylcarboxamidoadenosine
MP	Membrane protein
NMR	Nuclear magnetic resonance
NTA	Nitriloacetic acid
OTR	Oxytocin receptor
PAGE	Polyacrylamide gel electrophoresis
PCR	Polymerase chain reaction
PDB	Protein Data Bank
PIP ₂	Phosphatidylinositol 4,5-bisphosphate
PI3K	Phosphatidylinositol-3-kinase
PKA	Protein kinase A
PLC	Phospholipase C
PLC-β	Phospholipase C-β
PNGase F	N-glycosidase F
PEI	Polyethylenimine
<i>P. pastoris</i>	<i>Pichia pastoris</i>
PTM	Post-translational modification
RGS	Regulator of G protein signaling
SBDD	Structure-based drug design
<i>S. cerevisiae</i>	<i>Saccharomyces cerevisiae</i>
SDM	Site-directed mutagenesis studies
SEC	Size-exclusion chromatography
SDS	Sodium dodecyl sulfate
StaR	Stabilized receptor
<i>Sf9, Sf21</i>	<i>Spodoptera frugiperda</i> 9/21
T _M	Melting temperature
TM	Transmembrane
Tris	Tris(hydroxymethyl)aminomethane
T4L	T4-lysozyme
wt	Wildtype
X-gal	5-Brom-4-chlor-3-indolyl-β-D-galactopyranosid
5-HT	5-Hydroxytryptamine
[¹²⁵ I]ABA	<i>N</i> ⁶ -(4-Amino-3-[¹²⁵ I]iodobenzyl)adenosine

List of figures

Figure 1.	GPCR activation cycle.	3
Figure 2.	Schematic illustration of the G α protein subunit.....	4
Figure 3.	Structures of cholesterol and membrane phospholipids.....	7
Figure 4.	Overview of selected A ₃ AR agonists.	15
Figure 5.	Overview of selected A ₃ AR antagonists.	18
Figure 6.	Comparison between binding modes of ZM241385 (4EIY) and compound 4g (3UZA).	23
Figure 7.	Schematic illustration of the mesophase crystallization processes.	30
Figure 8.	Sequence alignment of the residues forming the sodium binding pocket of AR subtypes.	37
Figure 9.	Overview of employed receptor modifications.	40
Figure 10.	Analysis of the A _{2A} AR-bRIL- Δ C protein. ³⁸	42
Figure 11.	Schematic illustration of the insertion of fusion partners.....	43
Figure 12.	Fusion partner inserted into the ICL3.....	44
Figure 13.	N-terminal fusion partner.	45
Figure 14.	The design of the TM1 exchange.	46
Figure 15.	Results of further construct modifications.	48
Figure 16.	CPM thermostability assay results of initial A ₃ AR constructs.....	49
Figure 17.	Coomassie-stained SDS-PAGE gels and western blots of initial A ₃ AR constructs.....	51
Figure 18.	Results obtained by introducing the S97 ^{3.39} K mutation.	53
Figure 19.	Junction site modifications.	54
Figure 20.	Junction site modifications I.....	57
Figure 21.	Combination of S97 ^{3.39} K and junction site modifications.....	60
Figure 22.	Insights into the effects of junction site modifications.....	63
Figure 23.	The role of N-terminal N-glycosylation sites.....	65

Figure 24. Enzymatic deglycosylation of JS53.	67
Figure 25. Glycosylation state of JS68.	69
Figure 26. Optimization of the N-terminal construct sequence.	72
Figure 27. Transfer and improvement of the NNST sequence.	74
Figure 28. The helix VIII exchange.	75
Figure 29. The helix VIII exchange — results.	76
Figure 30. Investigation of point mutations I.	79
Figure 31. Investigation of point mutations II.	80
Figure 32. Combination of point mutations.	82
Figure 33. Investigation of the conserved disulfide bond C83 ^{3.25} -C166 ^{45.50}	85
Figure 34. Optimization of expression and purification conditions.	87
Figure 35. Solubilization and purification of JS54 in the presence of various ligands.	88
Figure 36. Solubilization and purification with LMNG and the irreversible A ₃ AR antagonist LUF7602.	90
Figure 37. Structures of ligands tested in the CPM thermostability assay campaigns.	91
Figure 38. Ligand screening campaign I.	92
Figure 39. Ligand screening campaign II.	93
Figure 40. Ligand screening campaign III.	95
Figure 41. Ligand screening campaign IV.	96
Figure 42. Ligand screening campaign V.	98
Figure 43. Thermostability in the presence of A ₃ AR antagonists LUF7602 and AT563.	100
Figure 44. Mouse A ₃ AR constructs.	103
Figure 45. Protein analysis of JS68 (crystallization I).	106
Figure 46. Protein analysis of JS68 (crystallization II).	109
Figure 47. Protein analysis of JS97 for crystallization.	111
Figure 48. Protein analysis of JS104 for crystallization.	112
Figure 49. Comparison of A ₃ AR crystallization experiments.	114

Figure 50. Wash-out experiments.....	120
Figure 51. Competition binding studies at A ₃ AR constructs expressed in <i>Sf9</i> insect cells.....	122
Figure 52. Competition binding studies at A ₃ AR constructs expressed in CHO-S cells.....	124
Figure 53. Homologous competition binding of NECA vs [³ H]NECA.	125
Figure 54. Assessment of ligand binding after cholesterol depletion.....	131
Figure 55. Homologous competition binding after CLR supplementation during expression.....	132
Figure 56. CLR replenishment.....	134
Figure 57. Competition binding curves of <i>Sf9</i> -CHO-S membrane preparations.....	135
Figure 58. Ligand binding at solubilized A ₃ AR constructs.....	137
Figure 59. Purification of the A ₃ AR crystallization construct JS68 expressed in CHO-S cells.....	139
Figure 60. CHO-S expression of JS68 — ligand binding.....	141
Figure 61. Structures of TK-OT-024 and TK-OT-019.....	142
Figure 62. Incubation with the BODIPY-labeled ligand TK-OT-024.....	144
Figure 63. Schematic illustration of employed receptor modifications.	145
Figure 64. Model of the A ₃ AR crystallization construct.....	146
Figure 65. Conclusion — Thermal stability of crystallization constructs.....	148
Figure 66. Conclusion ligand binding.....	149
Figure 67. Conclusion — Monodispersity and yield.	151

List of tables

Table 1.	Sequence identity and similarity within the AR family.	9
Table 2.	Affinities of Cl-IB-MECA and IB-MECA at ARs.....	10
Table 3.	Affinity of selected A ₃ AR agonists	16
Table 4.	Affinity of selected A ₃ AR antagonists	19
Table 5.	Overview of constructs to investigate junction site modifications.....	61
Table 6.	Images of the first A ₃ AR crystallization experiment.	107
Table 7.	Affinity novel A ₃ AR antagonists, including related compounds from the literature.....	117
Table 8.	Affinity of PSB-11 at various A ₃ AR constructs expressed in <i>Sf9</i> cells.	122
Table 9.	Affinity of PSB-11 at various A ₃ AR constructs expressed in CHO-S cells.	124
Table 10.	Affinity of A ₃ AR constructs for the agonist NECA.....	126
Table 11.	Affinity of PSB-11 to A ₃ AR constructs expressed with CLR supplementation.....	133
Table 12.	Effect of the expression system, the receptor modifications and receptor preparation on ligand affinity.	150
Table 13.	Mutagenesis PCR	154
Table 14.	PCR to generate mega primers — insert preparation.....	155
Table 15.	Overlap extension PCR	156
Table 16.	Verification PCR	159
Table 17.	Radioligand displacement assays.	168
Table 18.	A ₃ AR constructs generated in this thesis.	171
Table 19.	Composition of used buffers.	184

1. Introduction

1.1 G protein-coupled receptors

G protein-coupled receptors (GPCRs) form the largest and most diverse group of membrane proteins in the human body, comprising more than 800 members. Membrane proteins allow extracellular stimuli to be translated into intracellular reactions, facilitating vital cellular communication and homeostasis. GPCRs share a common architecture incorporating seven transmembrane regions (TM) with an extracellular N-terminus and an intracellular C-terminus.^{1; 2} A vast and heterogeneous spectrum of extracellular ligands such as ions, photons, small molecules, or even proteins are able to bind specifically to their designated GPCR and trigger conformational changes which subsequently induce a plethora of cellular signaling pathways.³ Due to their integral role, GPCRs are involved in many (patho-)physiological processes, including those of the cardiovascular, central nervous, and immune systems. Therefore, they represent an excellent target for drug development whose relevance is proven by the large number (> 30 %) of approved drugs interacting with GPCRs.⁴

GPCRs can be classified into subgroups based on classification systems such as the widely used A–F or the "GRAFS" system. The A–F system identifies six classes, named A–F, mainly based on amino acid sequence similarity.^{5; 6} The "GRAFS" system is based on five main families named Glutamate (G), Rhodopsin (R), Adhesion (A), Frizzled/Taste2 (F), and Secretin (S) according to phylogenetic criteria.^{2; 7} The largest class, class A, also known as "Rhodopsin-like family", accounts for ~80 % of all GPCRs and is divided into further subfamilies in the A–F system and four so-called branches (α , β , γ , δ) in the GRAFS system. These receptors are targeted by neurotransmitters, hormones, and photons.⁸ In the GRAFS system, class B is further divided into the Secretin and the Adhesion family, displaying the main difference between both classification systems.⁸ The adenosine receptor (AR) family with its four members, A₁AR, A_{2A}AR, A_{2B}AR, and A₃AR, is part of the α branch of the rhodopsin-like family.²

Key mediators of GPCR signal transduction are heterotrimeric G proteins (guanine nucleotide-binding proteins). G proteins are composed of three subunits: The G α protein, which is responsible for guanosine diphosphate (GDP)/guanosine triphosphate (GTP) binding, as well as GTP hydrolysis, G β and G γ , which form the tightly bound G $\beta\gamma$ dimer.^{9;}

¹⁰ In general, each GPCR couples to one or more G proteins and coupling specificity is mainly dictated by the G α protein subunits.¹¹ Interestingly, the large number of GPCRs contrasts with the relatively small number of different G α protein subunits of which there are just 21 isotypes in humans encoded by 16 genes.^{11–13} This point of convergence can only be achieved by conserved structural motifs and intracellular signaling pathways. G proteins can be classified into four main classes derived from their G α protein subunits: G_s, G_i, G_{q/11}, and G_{12/13}.^{10; 14} Each can regulate specific intracellular cascades affecting the concentration of second messenger molecules. While the G_s proteins induce the formation of 3',5'-cyclic adenosine monophosphate (cAMP) by stimulating the enzyme adenylate cyclase (AC), the G_i protein decreases cAMP levels by inhibiting AC. The G_{q/11} protein is able to regulate phospholipase C activity (PLC) which cleaves the membrane-bound phospholipid phosphatidylinositol-4,5-bisphosphate (PIP₂) into diacylglycerol (DAG) and inositol trisphosphate (IP₃) affecting versatile cellular responses. Among others, DAG activates protein kinase C, whereas IP₃ triggers the release of Ca²⁺ from the endoplasmic reticulum into the cytoplasm.^{10; 15} Coupling to G_{12/13} proteins leads to the activation of small GTPase families, including RhoGEF such as the p115-RhoGEF.^{15–17} The $\beta\gamma$ dimer itself initiates various signaling processes on its own, resulting in the modulation of G protein-coupled inwardly-rectifying potassium channels (GIRKs), voltage-dependent Ca²⁺ channels, AC, PLC, phosphatidylinositol-3-kinase (PI3K), G protein-coupled receptor kinases (GRKs) and mitogen-activated protein kinases (MAPKs).^{18; 19} The recruited GRKs catalyze the specific phosphorylation of intracellular serine/threonine residues within intracellular loops (ICLs) and the C-terminal tail of activated GPCRs. Phosphorylated residues then enable arrestin binding, which results in the blockade of further coupling to the cognate G proteins and thus leads to receptor desensitization.^{20–22}

GPCR-G protein signaling is classically based on a universal cycle of conserved steps describing the processes underlying GPCR activation (Figure 1).²³ In its inactive state, the G α protein is bound to GDP, which causes the association of the heterotrimeric G $\alpha\beta\gamma$ complex. Ligand-induced receptor activation promotes GDP release from the G α protein subunit and subsequent GTP binding, which ultimately triggers conformational changes within the G α protein and promotes dissociation into the G α protein and the G $\beta\gamma$ dimer.^{9; 10; 12} Due to the intrinsic GTPase activity of the G α proteins, GTP is hydrolyzed to GDP, allowing the reassembly of the heterotrimeric G $\alpha\beta\gamma$ complex and the start of a new G protein activation cycle. The group of GTPase-activating proteins (GAPs), including RGS

(regulator of G protein signaling), can allosterically modulate G α proteins and enhance GTP hydrolysis by >2000-fold.^{12; 24} GRK-catalyzed phosphorylation of GPCRs leads to arrestin recruitment with subsequent GPCR internalization and endosomal degradation, which displays a vital feedback mechanism.^{12; 21; 22}

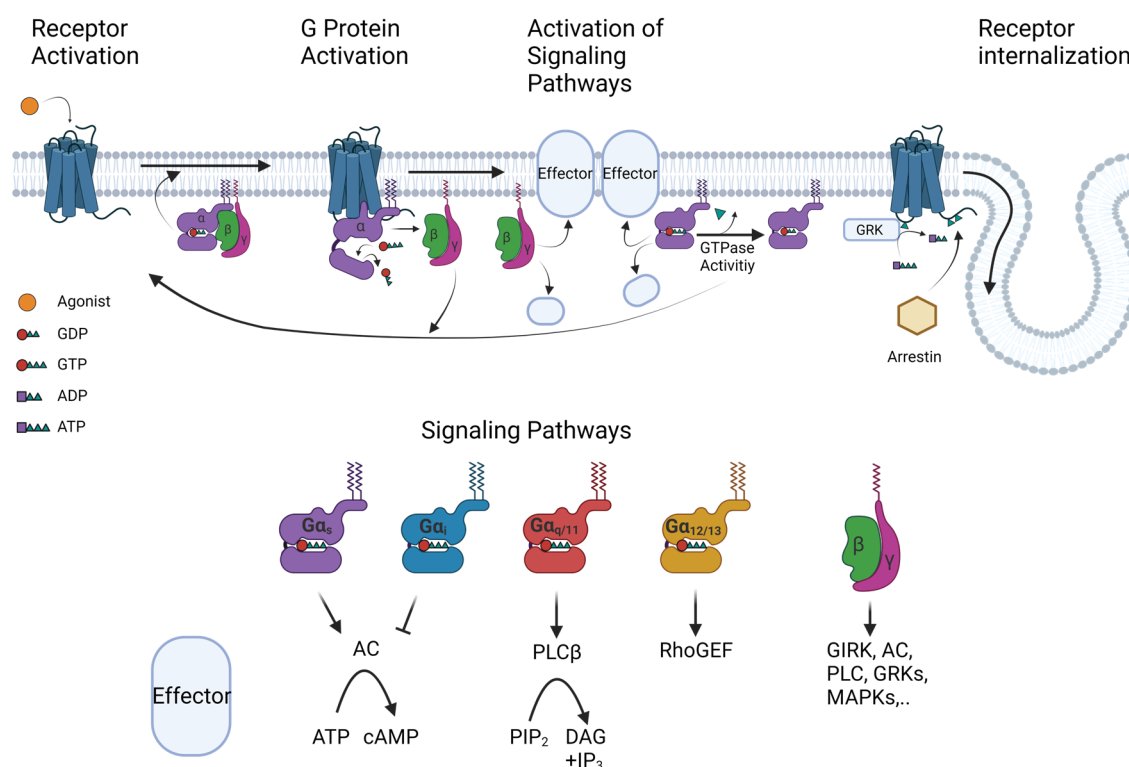


Figure 1. GPCR activation cycle.
Created with BioRender.com.

1.1.1 Mechanism of GPCR activation

Progress in the field of structural biology enabled the elucidation of GPCRs in different conformational states, which assisted in gradually uncovering the mechanics behind receptor activation. The comparison of inactive and active state structures revealed common structural activation features of class A GPCRs.^{9; 23; 25–27} Upon receptor activation, ligand binding induces conformational changes which are passed on through the transmembrane regions to the intracellular site of GPCRs with the aid of highly conserved motifs (see Section 1.4.2).^{23; 26} The most significant movement is conducted by the intracellular tip of the TM6, rotating outwards by over 10 Å in the β_2 -adrenergic receptor (β_2 AR). Additionally, the TM5 joins this outward movement, but less pronouncedly,

whereas TM7 slightly moves inwards, creating a cavity that can be engaged by signal transducers, such as G proteins.^{12; 23; 26} In the GDP-bound state, the G protein harbors the nucleotide between the Ras-like GTPase domain, which is composed of six-stranded β -sheets ($\beta 1$ – $\beta 6$) and five α -helices ($\alpha 1$ – $\alpha 5$), and the α -helical domain, which consists of six α -helices (αA – αF) (Figure 2).^{12; 28} The diphosphate moiety is coordinated by important interactions to the $\beta 1$ – $\alpha 1$ loop (P loop) and the $\alpha 1$ helix. The $\beta 5$ – $\alpha 4$ and $\beta 6$ – $\alpha 5$ loops provide essential interactions to bind the guanine ring.¹² When the C-terminal $\alpha 5$ helix enters the void formed by the TM movements, the nucleotide binding pocket is disrupted, and GDP is released.²⁸ The structural rearrangement caused by the embedding of $\alpha 5$ initiates perturbation of the adjacent $\beta 6$ – $\alpha 5$ -guanine interaction.^{9; 12; 29; 30} Involvement of the ICL2 and the hinge αN – $\beta 1$ may also contribute to the loosening of the link between the P loop and diphosphate moiety.^{30–32} In this way, the GPCR can act as a guanine nucleotide exchange factor (GEF) and transmit the signal originating from the orthosteric binding pocket to the $G\alpha$ protein, ultimately triggering GDP release.

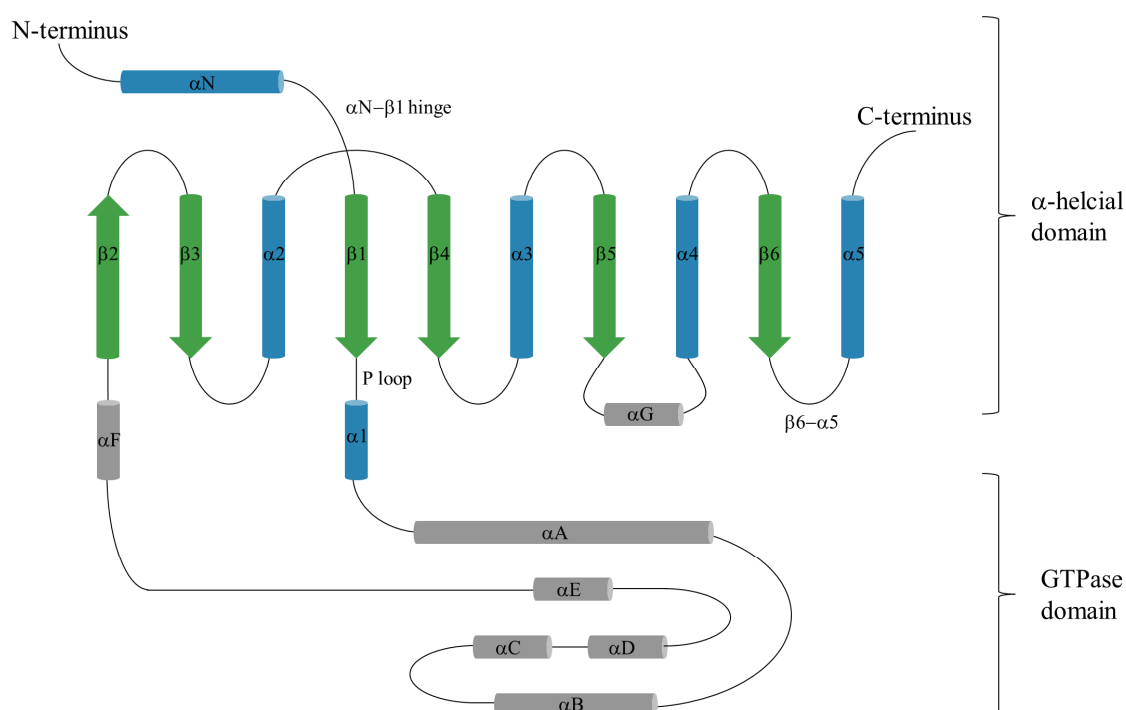


Figure 2. Schematic illustration of the $G\alpha$ protein subunit.

α -Helices and β -sheets are shown as cylinders and arrows, respectively. The α -helical domain is colored in blue and green, whereas the GTPase domain is colored in gray.^{9; 12}

1.1.2 The GPCR environment

GPCRs are an integral part of cellular membranes and thus are closely surrounded by the main membrane components glycerophospholipids and cholesterol (CLR), whose chemical structures are shown in Figure 3.³³ Consequently, it appears evident that the membrane environment is capable of influencing and modulating GPCRs. The sterol CLR, composed of a rigid fused four-ring scaffold, a 3 β -hydroxyl group at the one end, and a relatively flexible isooctyl side chain attached at position 17, is known to modify GPCR conformation, stability, and function.^{33; 34} In general, these effects can either be caused by direct binding of CLR to GPCRs resulting in allosteric modulation or indirectly through CLR's effects on membrane properties.³⁴ CLR is orientated perpendicularly to the phospholipids in lipid bilayers with its hydroxyl group close to the polar headgroups and its rigid core next to the acyl chains. Thus, CLR interacts with adjacent phospholipids and modulates their order and dynamics, impacting biophysical properties of membranes, such as the fluidity, thickness, compressibility, water penetration, and intrinsic curvature.³⁵ CLR molecules bound to a GPCR have already been observed in the first structures of the β_2 AR, revealing a CLR binding site between helices I–IV with a key interaction between ring D and the highly conserved W158^{4,50}.³⁶ This binding site was defined as CLR consensus motif (CCM) and was found to be present in 44 % of all human class A receptors.³⁶ Since then, CLR molecules have been found in many other GPCR structures, including the α_{2C} adrenergic receptor (6KUW, Chen et al., to be published), the serotonin 5-HT_{2B} receptor as well as the A_{2A}AR, among others.^{34; 37; 38} Besides the CCM, the so-called CLR recognition amino acids consensus (CRAC) and its reversed analog CARC were identified and proposed to bind CLR longitudinally with their L/V–(X)_{1–5}–Y/F–(X)_{1–5}–R/K and R/K–(X)_{1–5}–Y/F–(X)_{1–5}–L/V domains, respectively.^{33; 39} One limitation of the CRAC algorithm is its vast number of possible sequence strings considering X as any of one to five proteinogenic amino acids.⁴⁰ A comprehensive analysis based on 473 available GPCR structures revealed that most CLR molecules are located in network clusters (CNC), but these clusters do not comprise specific sequence motifs.³³

The other main components of membranes, phospholipids, have also been investigated, e.g., regarding their effects on the activity of the β_2 AR. The β_2 AR was reconstituted in High-Density-Lipoparticles of different lipid compositions and subsequently tested for ligand binding.⁴¹ The authors discovered that modulation of ligand binding was dependent on the lipid head group. Phosphatidylglycerol (PG) appeared to

favor agonist binding, whereas phosphatidylethanolamine (PE) appeared to favor antagonist binding, resulting in a 7.2-fold decreased IC_{50} of the agonist isoproterenol (0.6 nM vs. 4.3 nM). Conversely, binding of the antagonist alprenolol resulted in IC_{50} values of 2.8 nM and 9.3 nM in the presence of PE and PG, respectively. They stated that lipids differently stabilize and kinetically facilitate conformational changes at the intracellular receptor site, such as the outward movement of TM6, and PG most efficiently accelerated these changes.^{41; 42}

CLR's effects on ligand binding display an example of direct CLR-GPCR interactions. The human oxytocin receptor (OTR) revealed a reduced affinity for oxytocin (K_D 215 nM) when expressed in *Spodoptera frugiperda* 9 (*Sf9*) insect cells, which naturally have low CLR levels in their membranes. CLR replenishment led to a restoration of high-affinity binding of oxytocin (0.96 nM).^{43; 44} The OTR crystal structure showed that a CLR molecule binds to a membrane cavity at TM regions 4 and 5 in the vicinity of the orthosteric binding pocket, potentially explaining the observed CLR-dependent affinity alterations.^{34; 45} A similar study demonstrated that the loss of CLR during 3-[3-(cholamidopropyl)dimethylammonio]-1-propanesulfonate (CHAPS) solubilization of the serotonin 5-HT_{1A} receptor resulted in reduced agonist binding and G protein coupling but could partly be restored by CLR replenishment.⁴⁶ In contrast, CLR depletion did not alter [³H]ZM241385 binding to the A_{2A}AR but reduced downstream signaling.⁴⁷ The influence of CLR on GPCR functionality and signaling was the subject of further studies revealing highly individual receptor-dependent results ranging from no observable effects to significant consequences.⁴⁷⁻⁵⁰ Moreover, CLR effects on the oligomerization of GPCRs were postulated and thoroughly investigated.^{34; 51; 52} Altogether, the relation between CLR and GPCR remains extraordinarily complex and hardly predictable. However, CLR, as well as other membrane components, can undoubtedly have a substantial impact on the binding and function of GPCRs.

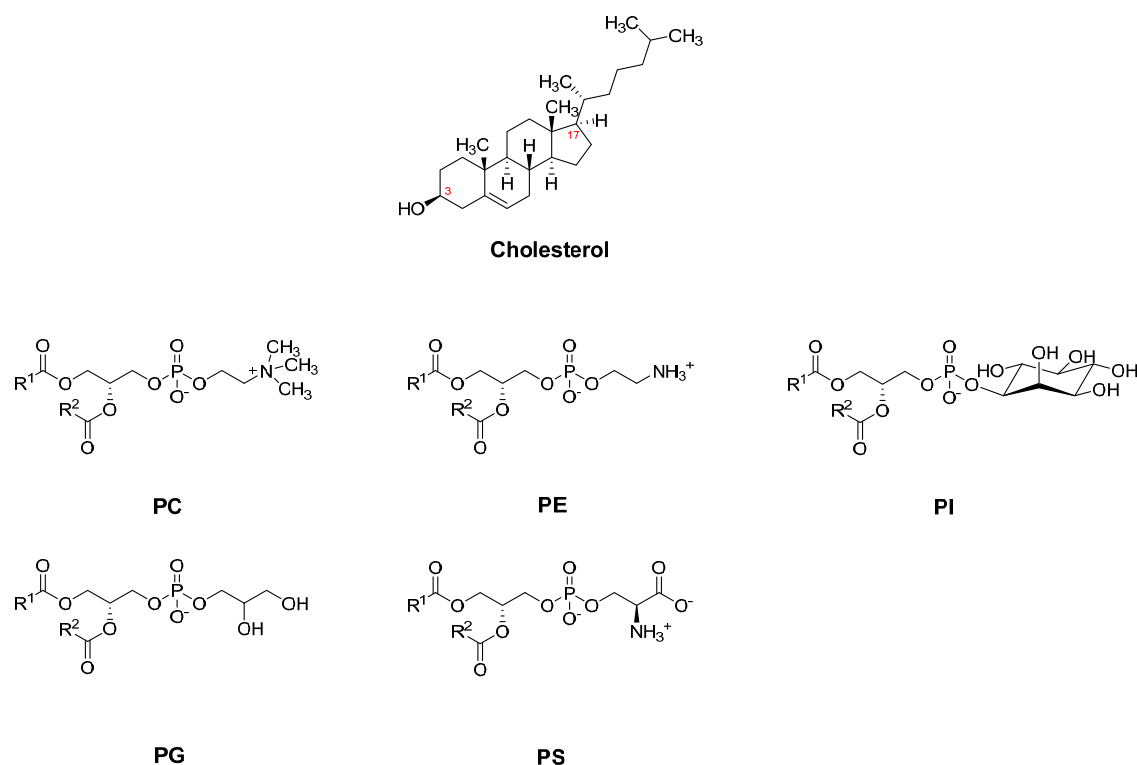


Figure 3. Structures of cholesterol and membrane phospholipids.

Alkyl chains of fatty acids are replaced by the labels R¹ and R². Phosphatidylcholine (PC), phosphatidylethanolamine (PE), phosphatidylinositol (PI), phosphatidylglycerol (PG) and phosphatidylserine (PS).

1.2 The adenosine A₃ receptor (A₃AR)

The first evidence of the A₃AR was found in the mid to late 1980s based on observations in pharmacological experiments investigating the activation of phospholipase C (PLC) via a novel AR subtype.⁵³ In 1991, Meyerhof et al. isolated a cDNA clone from a rat testis cDNA library, which encoded for a potentially novel GPCR.⁵⁴ They named this novel GPCR “tgpcr1” due to its location in testis but failed to determine the endogenous ligand.⁵⁴ Just one year later, in 1992, Zhou et al. were able to clone and characterize this GPCR, displaying the fragment “R226” from a rat striatal cDNA.⁵⁵ They assigned R226 to the family of ARs but differentiated this receptor from the already known A₁- and A₂ARs based on sequence identity, ligand affinity, and pharmacological profiling.⁵⁵ Consequently, they increased the index to three and termed it A₃AR.⁵⁵

The hA₃AR is encoded by the gene ADORA3, which was mapped on the human chromosome 1p21–p13 in 1997.⁵⁶ It consists of 318 amino acids and possesses the typical GPCR structure with seven helices spanning through the cell membrane, an extracellular N-terminus and an intracellular C-terminus.^{57; 58} It belongs to the family of ARs, which consists of four distinct members: The A₁AR, A_{2A}AR, A_{2B}AR, and A₃AR.⁵⁸ Within the

family of human ARs, the hA₁AR is the closest relative of the hA₃AR subtype, displaying a TM sequence identity and similarity of 52 % and 72 %, respectively (see Table 1). Interestingly, homology, expression levels, and especially antagonist binding differ significantly between rodent and human A₃ARs, which is an exception within the AR family.⁵⁹ In the human body, highest expression levels can be found in the lung and liver.⁶⁰ Contrary, testis and mast cells are tissues with the highest A₃AR levels in rats.^{54; 59; 61} The A₁-, A_{2A}-, and A_{2B}ARs possess >83 % sequence identity between their human and mouse orthologs, whereas identity between rodent (mouse, rat) and human A₃ARs is only ~74 %. The receptor starting sequence (N-terminus, TM1, ICL1) and the receptor terminal sequence (TM7, helix VIII, C-terminus) display regions that share the least identity between rat and human A₃AR, possessing identity values of 63 % and 66 %, respectively. TM2 and the extracellular loop 2 (ECL2), TM3 and ICL2, and TM6 and ECL3, on the other hand, define regions of high identity, even reaching up to 88 % identity.

Table 1. Sequence identity and similarity within the AR family.

Values in brackets refer to the comparison of TM1-7 of each receptor. TM regions were defined based on the corresponding UniProt entry. Alignments were carried out using the BLAST® sequence alignment (<https://blast.ncbi.nlm.nih.gov/Blast.cgi?PAGE=Proteins>).

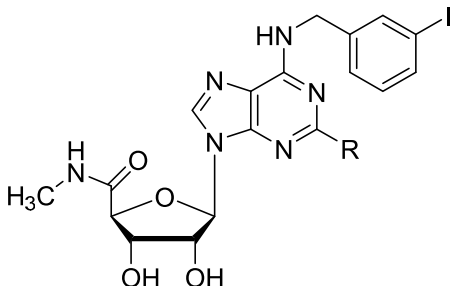
Human A ₃ AR vs. ARs ^a			Human A ₃ AR vs. rat A ₃ AR			
Receptor	Identity [%]	Similarity [%]	Identity [%]	Similarity [%]	Region	
hA ₁ AR	48 (52)	68 (72)	63	67	N-terminus, TM1, ICL1 (h 1–44, r 1–46)	
hA _{2A} AR	42 (46)	63 (64)	88	90	TM2, ECL2 (h 45–78, r 47–80)	
hA _{2B} AR	39 (42)	58 (61)	86	88	TM3, ICL2 (h 79–122, r 81–124)	
mA ₃ AR	73 (77)	84 (86)	72	76	TM4, ECL2 (h 123–172, r 125–174)	
rA ₃	74 (78)	86 (88)	77	81	TM5, ICL3 (h 173–216, r 175–218)	
sA ₃ AR	85 (87)	91 (92)	82	86	TM6, ECL3 (h 217–260, r 219–262)	
			66	72	TM7, helix VIII, C-terminus (h 261–318, r 263–320)	

^ah = human, m = mouse, r = rat, s = sheep

Not only expression levels and sequence identity but, more importantly, ligand binding differs crucially between human and rodent A₃ARs.^{59; 60; 62} In general, different binding profiles may hinder pharmacological evaluation since drug development needs preclinical testing. For example, adenosine-induced effects in rodents, which were

potentially A₃AR-mediated, appeared to be resistant to xanthine-based antagonists.⁶³ Antagonist binding, in particular, is affected much more than agonist binding.⁵⁸ Most of the potent and selective antagonists for the human A₃AR show weak or no binding to rodent A₃ARs. As an example, the two antagonists MRE 3008F20 and PSB-11 (for structures see Figure 5), which show high-affinity binding to the human A₃AR combined with high subtype-selectivity, fail to bind with high potency to the rat A₃AR.^{58; 62; 64; 65} The pyridine-based antagonist MRS1523 represents an exception (Figure 5). MRS1523 binds with high affinity and selectivity to the hA₃AR (K_i 18.9 nM) and also displays moderate binding to the rA₃AR (K_i 113 nM).⁶⁶ Agonists show a more consistent affinity profile between rodent and human receptors (Table 2). The two most employed agonists, IB-MECA (CF101) and Cl-IB-MECA (CF102), are also potent at rodent A₃ARs even with superior subtype-selectivity at rodent ARs.⁶⁷ Cl-IB-MECA possesses a ~100-fold A₁AR/A₃AR selectivity at human and a >1,000 fold selectivity towards all rodent AR subtypes.⁵⁹ Until now, it has not been possible to find an explanation for the observed interspecies differences.

Table 2. Affinities of Cl-IB-MECA and IB-MECA at ARs.

		A ₁ AR	A _{2A} AR	A _{2B} AR	A ₃ AR
		K _i (nM) or % activation at 10 μM			
Cl-IB-MECA (R = Cl)	human	220 ⁶⁸	5360 ⁶⁸	0 % ⁶⁸	1.4 ⁶⁸
	rat	820 ⁶⁹	470 ⁶⁹	n.d.	0.33 ⁶⁹
IB-MECA (R = H)	human	51 ⁶⁸	2900 ⁶⁸	0 % ⁶⁸	1.8 ⁶⁸
	rat	54 ⁶⁹	56 ⁶⁹	n.d.	1.1 ⁶⁹

n.d. not determined

1.2.1 Distribution and pharmacology

The A₃AR, which preferentially couples to Gα_{i/o} proteins, is widely expressed in the human body, whereby the lung and liver show the highest messenger ribonucleic acid (mRNA) levels.^{59; 60} Moreover, high A₃AR expression levels were found in various cancer cells and tissues, making the A₃AR a potential target in cancer research.⁵⁹ For example, high levels of the A₃AR were discovered in lung, liver, breast, prostate, melanoma,

pancreatic, and colorectal cancers, as well as cancer affecting the brain and the lymphatic system, like glioblastoma and lymphoma.^{57; 70–74} The role of the A₃AR cannot be uniquely characterized as pro-tumoral or anti-tumoral. Depending on the cancer type, activation can lead to both pro- and antiproliferative effects.^{57; 70} Cl-IB-MECA (CF102, Namodenoson, Table 2) is the most advanced compound in the clinical development of A₃AR agonists. It can induce apoptosis in hepatocellular carcinoma cells and has already completed clinical phase I/II trials for advanced hepatocellular carcinoma treatment (NCT00790218, NCT02128958).^{57; 70; 75} CF102 was overall found to be well-tolerated and safe.⁷⁵ Just recently, in December 2021, the first results of the clinical phase II study NCT02128958 were published, indicating a beneficial effect of CF102 on the overall mortality (CF102 68.00 % vs. Placebo 85.71 %). A detailed publication has not yet been published. Antagonists may also be investigated in future clinical trials due to the dual nature of the A₃AR in a cancer environment. In melanoma tumor models, activation led to an increase in proangiogenic factors, blood vessel density, cytokine production as well as infiltration of macrophages.^{57; 70; 76} Similarly, A₃-mediated elevation of the hypoxia-inducible factor-1 α and the vascular endothelial growth factor was shown in the human colon cancer cell line HT29 under hypoxic conditions.⁷⁷ Furthermore, researchers demonstrated that an increase in matrix metalloproteinase-9 levels in glioblastoma resulted from A₃AR activation by adenosine. They could mimic this effect by the A₃AR agonist Cl-IB-MECA and inhibit it by the A₃AR antagonist MRE 3008F20 or RNA interference.⁷⁸ In conclusion, the A₃AR plays a diverse role in various types of cancer, making it suitable as a cancer marker and as a target for anticancer therapy.⁷⁰

The expression on a large number of human immune cells like dendritic cells, mast cells, eosinophils, neutrophils, and monocytes suggests that the A₃AR is also involved in immune and inflammatory processes.^{59; 79} Therefore, targeting the A₃AR represents a promising approach in inflammatory and autoimmune diseases like asthma, rheumatoid arthritis, inflammatory bowel disease, and psoriasis.^{57; 58} The antagonists PFB-1650 and PFB-677 (structures are undisclosed) are currently under investigation in clinical trials for psoriasis (NCT03798236) and ulcerative colitis (NCT03773952), respectively. Until now, three phase II trials have been completed with the agonist CF101 (IB-MECA, Piclidenoson), which assessed its usage in the treatment of rheumatoid arthritis (NCT00280917, NCT01034306, NCT00556894). These studies proved the antirheumatic effect of CF101, which improved the patients' symptoms as measured with American

College of Rheumatology scores. The dose of CF101 was set to be 1 mg twice daily. The structurally related compound CF102 was investigated for the therapy of patients with liver carcinoma and cirrhosis at a dose of 25 mg twice daily (NCT00790218, NCT02128958).

The A₃AR is also expressed in microglia and astrocytes as well as in the thalamus, hypothalamus, and the cortex of the brain, among others.^{58; 59} Moreover, A₃ARs are present in the cardiovascular system, namely in the coronary and carotid arteries.^{80; 81} However, no direct presence of the A₃AR in cardiomyocytes could be observed until 2019.^{59; 82} In 2019, Wan et al. utilized a novel mouse animal model in which they selectively deleted the A₃AR gene (*Adora3*) in cardiomyocytes to prove the presence of A₃AR in ventricular cardiomyocytes of mice.^{83; 84} They showed that agonist-induced cardioprotection was lost in *Adora3*-deficient cardiomyocytes. Nevertheless, the determined mRNA level of A₃ARs in isolated cardiomyocytes from wildtype (wt) mice was significantly lower than that of the A₁AR (85 vs. 12,830 copies per 100 ng total RNA).^{83; 84} A₃AR activation protects ischemic cardiomyocytes from injury by involving myocardial adenosine triphosphate (ATP)-sensitive potassium channels (K_{ATP} channels).⁸³⁻⁸⁶

Various studies revealed that the A₃AR is involved in various kinds of pain.⁸⁷⁻⁸⁹ The three agonists IB-MECA, CI-IB-MECA, and MRS1898 (Table 2, Figure 4), possessing improved AR subtype-selectivity compared to adenosine, were able to block the development of allodynia caused by chronic constriction injury (CCI) or induced by the chemotherapeutic drugs paclitaxel, oxaliplatin, and bortezomib. Additionally, they boosted the effect of standard analgesic therapeutics. The investigation was carried out utilizing mouse (CCI) and rat (chemotherapeutics) based neuropathic pain models.^{90; 91} Moreover, pain resulting from inflammation, breast cancer, bone metastasis, and diabetes was also positively affected by A₃AR agonists.⁹²⁻⁹⁵ The mechanisms behind the antinociceptive effects are highly complex. In short, the effect is independent of the opioid and cannabinoid system. However, it is, among others, characterized by effects on the GABAergic system, the production of pro-/anti-inflammatory cytokines, and the activity of MAPKs and NF- κ B.^{91; 95-99} One potentially crucial advantage of targeting the A₃AR is the lack of desensitization and the reduced risk of addiction, which is, in contrast, well known, e.g., for morphine and other opioids.^{91; 95}

1.2.2 Signaling

Being a member of the GPCR receptor family, the A₃AR transduces extracellular stimuli into intracellular responses mediated by G protein coupling and activation. Agonist binding leads to conformational rearrangements and the exchange of GDP for GTP in the heterotrimeric G protein complex, which subsequently dissociates into the G α and G β /G γ protein subunits (see Section 1.1).¹¹ In the case of the G_i-coupled A₃AR, activation causes a decrease in cAMP by inhibition of the AC. Decreasing cAMP levels then result in inhibition of protein kinase A (PKA), which then affects several downstream signaling cascades: activation of glycogen synthase kinase-3 β (GSK-3 β); downregulation of beta-catenin, cyclin D1, c-Myc, and the reduction of NF- κ B's ability to bind to DNA.^{57; 59; 100} Moreover, A₃AR signaling interferes and regulates various pathways of MAPKs, PI3K/Akt and NF- κ B.^{57; 70} GSK-3 β plays a pivotal role in the Wnt signaling pathway, which is involved in carcinogenesis and embryonic development.⁵⁹ Phosphorylation by PKA/PKB/Akt inactivates GSK-3 β , which, in its active form, suppresses cell proliferation, and thus G_i-mediated PKA inhibition leads to decreased inactivation of GSK-3 β . A₃AR activation consequently dysregulates the Wnt signaling pathway explaining its involvement in tumorigenesis and anticancer therapy.^{57; 59; 70} Additionally to G_i protein coupling, the interaction with the G_q protein family is discussed in the literature but is significantly less validated and not proven by modern dynamic protein-protein interaction assays like NanoBiT.^{13; 57; 59; 101} In 1995, Palmer et al. tried to demonstrate coupling of the rat A₃AR to G_{q/11} proteins by immunoprecipitation, but results were not fully convincing, considering that experiments were carried out in a non-native environment based on receptor overexpression.¹⁰¹ Despite unclear G_q-coupling, experimental data indicate that A₃AR activation is able to stimulate phospholipase C- β (PLC- β), increase cellular Ca²⁺ levels and activate the monomeric G protein RhoA which then triggers phospholipase D activation.^{57; 59; 102–104} Desensitization and receptor internalization are crucial elements in the essential regulation of signaling. GPCR kinases phosphorylate serine and threonine residues in the C-terminus and can lead to internalization. In contrast to the A₁-, A_{2A}-, and A_{2B}ARs, this process occurs more rapidly within minutes at the A₃AR.^{58; 67; 105}

1.2.3 Medicinal chemistry — A₃AR ligands

The next sections will provide a brief overview of A₃AR ligands. Several detailed reviews have been published on this topic since the beginning of A₃AR ligand research in the early 1990s.^{58; 59; 62; 106}

1.2.3.1 Agonists

Since crystallization efforts will focus on the inactive receptor state, the main focus is on antagonists. Nevertheless, agonists will be briefly described to complete the overall picture of the A₃AR (Figure 4). Agonists are mainly derived from the endogenous ligand adenosine with modifications at the N⁶-, C2-, and 5'-positions as well as of the ribose moiety itself. The nonselective AR agonist NECA is an *N*-ethylcarboxamido-modified adenosine analog and possesses K_i values of 14, 20, and 6.2 nM at the A₁-, A_{2A}-, and the A₃ARs, respectively.^{62; 107} EC₅₀ and K_i values in the low micromolar range were determined for the A_{2B}AR depending on the test systems.^{108; 109} The methyl derivative MECA (*N*-methylcarboxamido) was used as a scaffold for the two closely related prototypical A₃AR agonists IB-MECA (CF101) and Cl-IB-MECA (CF102). Both compounds carry a 3-iodobenzyl moiety at position N⁶ of the adenine core. Cl-IB-MECA bears an additional chloro-substituent at position 2, which further enhances affinity and selectivity, reaching a K_i value of 1.4 nM while maintaining moderate selectivity (see Table 2). The corresponding 4'-thionucleoside analog LJ529 even binds with higher affinity (K_i 0.38 nM) but slightly lower selectivity vs. the A_{2A}AR (K_i (A₁AR) 193 nM, K_i (A_{2A}AR) 223 nM).¹¹⁰ Further modifications of the ribose moiety, such as its replacement by the fused cyclopentane-cyclopropane bicyclo[3.1.0]hexane ring system led to the discovery of the potent (*N*)-methanocarba derivatives such as compound CF502/MRS3558 (K_i 0.29 nM) with improved selectivity towards the other human AR subtypes (K_i (A₁AR) 260 nM, K_i (A_{2A}AR) 2300 nM); it interestingly carries an N⁶-3-chlorobenzyl substituent instead of a 3-iodobenzyl group.^{62; 68} Alkynyl substituents in position C2 of the adenine core were initially studied for the A_{2A}AR but were later utilized to develop A₃AR-selective agonists. Enlarging of the C2 substituent to phenylethynyl and combination with A₃AR-favorable modifications yielded a series of potent and selective agonists represented by 2-phenylethynyl-N⁶-methyladenosine (PEMADO) and its analog **9**.⁵⁸ Compound **9** is a full agonist with subnanomolar A₃AR affinity (K_i 0.44 nM) and excellent selectivity (K_i (A₁AR) 32,800 nM, K_i (A_{2A}AR) 41,700 nM).¹¹¹ Interestingly, PEMADO showed

similar affinity (K_i 3.4 nM) and selectivity but was determined to act as a partial agonist utilizing a non-radioactive fluorescence-based DELFIA Eu-GTP assay (K_i (A_1AR) 1,690 nM, K_i ($A_{2A}AR$) 8,530 nM).^{111; 112}

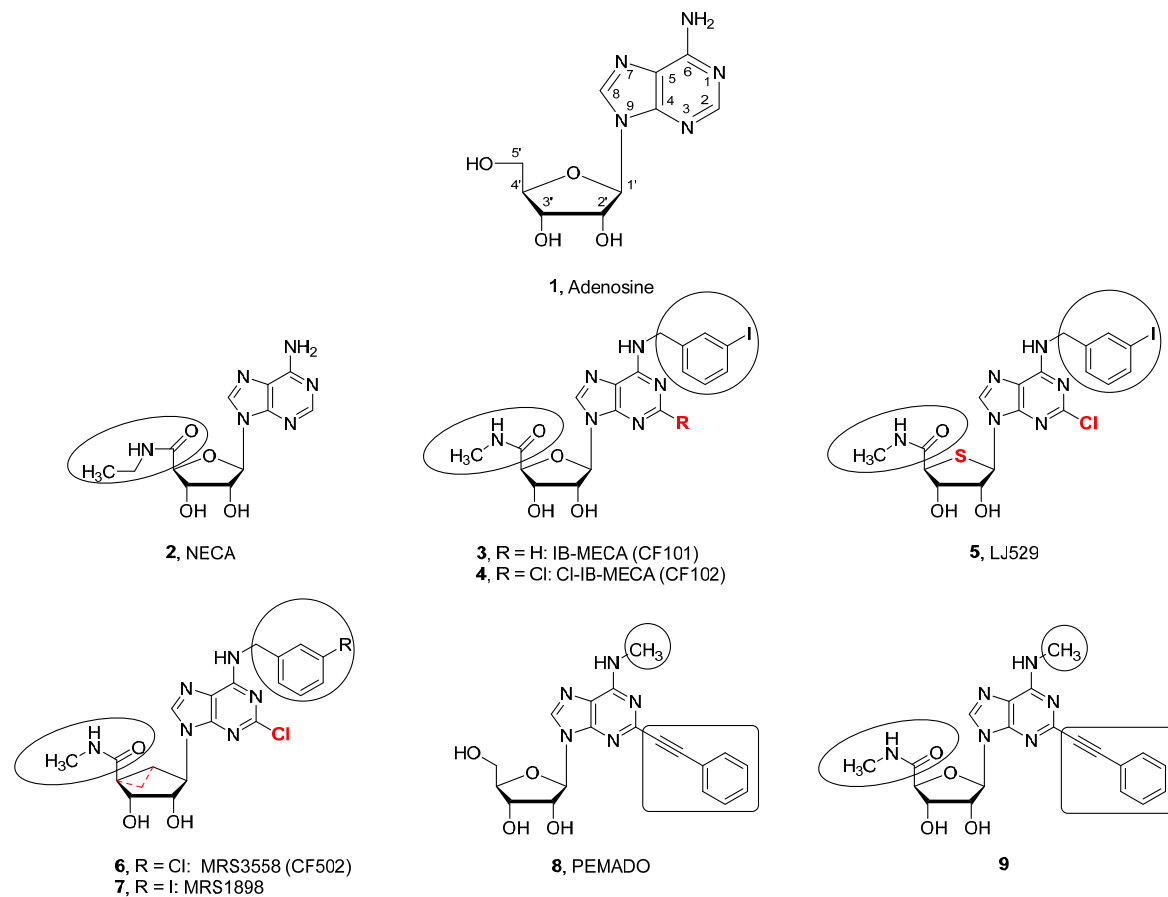


Figure 4. Overview of selected A_3AR agonists.
Differences compared to adenosine are circled or colored in red.

Table 3. Affinity of selected A₃AR agonists

Agonist	A ₁ AR	A _{2A} AR	A _{2B} AR	A ₃ AR
K _i (nM) or % activation at 10 μM				
1 ^{a,b}	ca. 100	310	15,000	290
2	14 ^c	20 ^c	3100 ^{a,d} , 109 ^{a,e} 83.5 ^{a,f} 1890 ^g , 5300 ^h , 5850 ^f	6.2 ^c
3 ⁱ	51	2900	0 %	1.8
4 ⁱ	220	5360	0 %	1.4, 11 ^j
5 ^k	193	223	n.d.	0.38
6 ⁱ	260	2300	38 %	0.29
7 ⁱ	136	784	n.d.	1.5
8 ^l	1690	8530	n.d.	3.4
9 ^m	32,800	41,700	n.d.	0.44

^a EC₅₀ values determined in cAMP accumulation assays, ^b ref. 113, ^c ref. 107, ^d ref. 108, ^e ref. 114, ^f ref. 115, ^g ref. 109, ^h ref. 116, ⁱ ref. 68, ^j ref. 117, ^k ref. 110, ^l ref. 112, ^m ref. 111, n.d. not determined

1.2.3.2 Antagonists

Over the past 30 years, extensive efforts have been put into the research of potent and selective A₃AR antagonists, resulting in a vast variety of different compounds. The most important scaffolds for A₃AR antagonists will be described briefly, focusing on compounds that are relevant to this thesis (Figure 5). Caffeine, a natural alkaloid that occurs in various plants and has been employed for centuries, displays one of the first AR antagonists described in literature, binding non-selectively to all ARs with micromolar affinities.^{113; 118} One of the first antagonists with moderate affinity at the A₃AR was CGS 15943, which was built upon a triazoloquinazoline scaffold (K_i 51 nM) initially designed for the A₁AR/A_{2A}AR.^{62; 119} Acylation of the amino group further enhanced its potency (MRS1220, K_i 0.65 nM).¹²⁰ Research on dihydropyridines led to the pyridine derivative MRS1523, which displayed good hA₃AR affinity (K_i 18.9 nM) while maintaining moderate rA₃AR affinity (K_i 113 nM).⁶⁶ Next, isoquinolone and quinazolines scaffolds were taken into consideration, leading to the development of the potent and selective compound VUF-5574 (K_i 4.03 nM, >2400-fold selectivity vs. A₁- and A_{2A}ARs).^{59; 121} The pyrazolo-triazolo-pyrimidine scaffold carrying a 2-furyl substituent at the 2-position and a phenylcarbamoyl moiety at the exocyclic amino group was explored

in the MRE compound series and was utilized to synthesize a radioligand as well as a water-soluble pyridine derivative and an irreversible ligand.^{64; 122–124} OT-7999 (TK-OT-008) displays the most prominent representative of the 1,2,4-triazolo[5,1-*i*]purine group with exceptionally high selectivity (K_i 0.95 nM), which was functionalized in TK-OT-018 and subsequently linked to BODIPY in TK-OT-024 (also see Section 3.18.10).^{106; 125} The two closely related compounds PSB-10 (K_i 0.43 nM) and PSB-11 (K_i 2.34 nM) harbor an imidazo[2,1-*i*]purin-5-one scaffold and were used to prepare the commonly used A_3 -radioligand [3H]PSB-11 (K_D 4.9 nM), which combined high affinity with low non-specific binding.^{62; 126; 127} In 2010, a series of N^2 -substituted pyrazolo[3,4-*d*]pyrimidines has been reported inspired by the adenine core achieving low nanomolar affinity (**21** K_i 0.18 nM).¹²⁸ Tricyclic xanthine-based antagonists are represented by **22** (K_i 4.0 nM) and **23** (0.8 nM) bearing a pyrido[2,1-*f*]purine-2,4-dione and a pyrrolo[2,1-*f*]purine-2,4-dione, respectively.^{129; 130} This scaffold was combined with knowledge on the irreversible A_1AR antagonist DU172 resulting in the synthesis of the irreversible A_3AR ligand LUF7602.¹³¹ Moreover, modifications near the 5'-position of nucleosides can convert agonists into potent antagonists by impeding the proper formation of an important H-bond caused by truncation of the 5'-uronamide moiety or by steric constraints. This can additionally result in partial agonists or antagonists without major inter-species differences.^{58; 132–134}

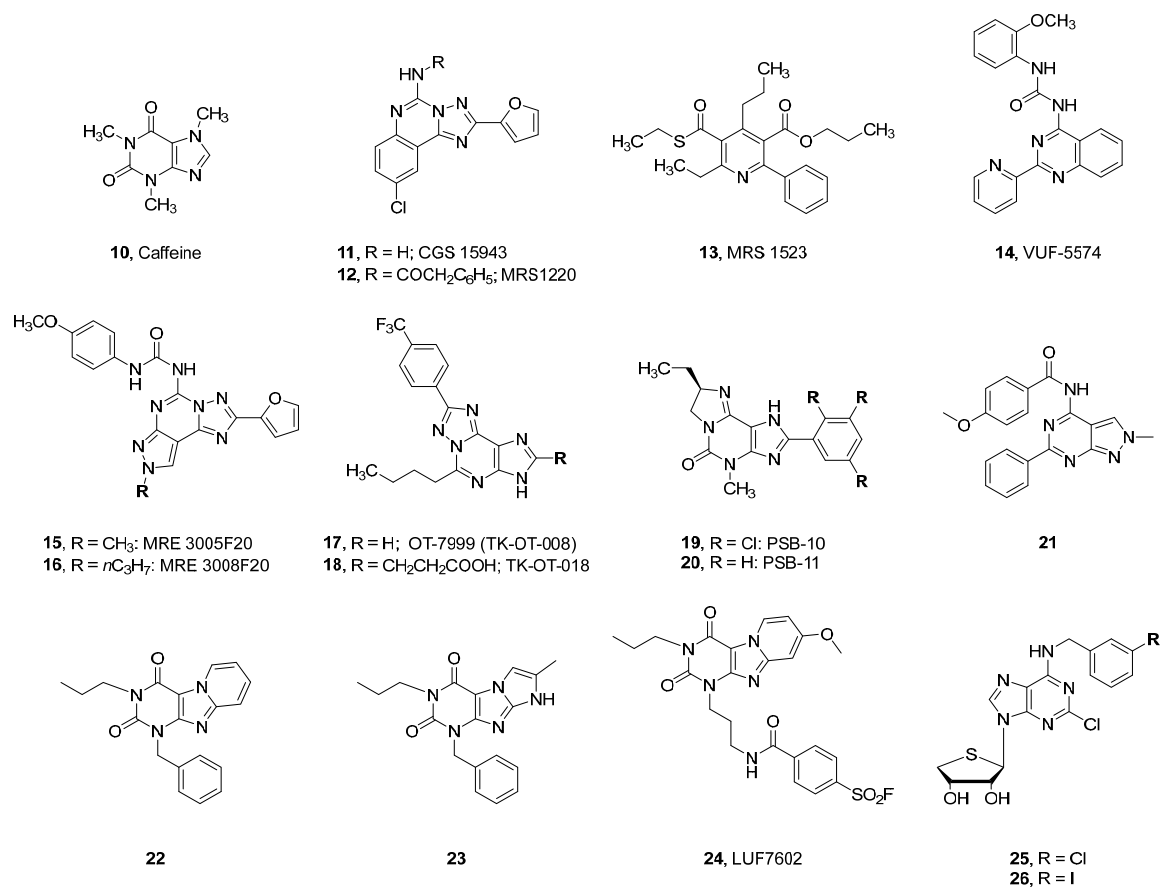
Figure 5. Overview of selected A₃AR antagonists.

Table 4. Affinity of selected A₃AR antagonists

Antagonist	A ₁ AR	A _{2A} AR	A _{2B} AR	A ₃ AR
	K _i (nM) or % inhibition			
10 ^a	44,900	23,400	33,800	13,300
11 ^b	3.5	4.2	66 ^c	51
12	305 ^d	52 ^d	n.d.	0.65 ^e
13	>10,000 ^f	3660 ^f	>10,000 ^f	18.9 ^g 113 ^{d,g}
14	>10,000 ^{d,h}	>10,000 ^{d,h}	n.d.	4.03 ^h
15 ⁱ	1097	1390	261	0.2
16 ⁱ	1197	140	2065	0.8
17 ^j	>10,000	>10,000	>10,000	0.95
18 ^k	>1000	>1000	>1000	2.81
19 ^l	1700	2700	30,000	0.43
20 ^l	1640	1280	2100 ^{c, m}	2.34
21 ⁿ	1037	3179	53.9 ^c	0.18
22 ^o	50	119	n.d.	4.0
23 ^p	>1000	>1000	>1000 ^b	0.8
24 ^q	794	1259	0 % (at 1 μM)	10
25 ^r	38 % (10 μM)	18 % (10 μM)	n.d.	1.66 6.2 ^d
26 ^r	2490	341	n.d.	4.16 3.89 ^d

^a ref ¹¹³, ^b ref ¹¹⁹, ^c IC₅₀ from cAMP accumulation assay, ^d rat ARs, ^e ref ¹²⁰, ^f ref. ¹³⁵, ^g ref. ⁶⁶, ^h ref ⁵⁹, ⁱ ref. ¹²⁴, ^j ref. ¹⁰⁶, ^k see ref ¹²⁵, ^l see refs. ⁶²; ¹²⁷, ^m mouse ARs, ⁿ ref. ¹²⁸, ^o ref. ¹²⁹, ^p ref. ¹³⁰, ^q apparent K_i at A₃AR, ref. ¹³¹, ^r ref. ¹³²; ¹³³, n.d. not determined

1.3 Structural biology

Structural biology seeks to elucidate the 3D architecture of complex molecules and proteins with the aim to gain insights into processes and interactions in a cellular environment. The function of proteins such as enzymes, transporters, receptors, or membrane proteins (MPs) in general is closely linked to their structure and structural changes on an atomic level.¹³⁶ Thus, information about atomic arrangements can be utilized to deduce their functionality and can subsequently be employed to modulate their function. On the one hand, this knowledge helps to find the cause of pathophysiological processes, and on the other hand, it assists in finding drugs that might cure diseases.^{136; 137} In 1958,

the first structure of a complex protein, namely myoglobin, was determined using X-ray crystallography and published by Kendrew et al.¹³⁸ Shortly thereafter, in 1960, Perutz et al. solved the structure of its “big brother” hemoglobin.¹³⁹ These structures displayed milestones in structural biology and helped to understand the mechanism underlying the O₂ transport in the human body. John Kendrew and Max Perutz were rewarded with the Nobel prize in chemistry for their outstanding research in 1962. The structure of the glycoside hydrolase lysozyme in complex with different inhibitors was a starting point of modern structural biology in drug discovery. It was the first study that aimed to understand the active binding site and its interactions with competitive inhibitors.¹⁴⁰ Since then, the research field of structural biology has grown through continuous improvement and the development of new methods, which have led to a large variety of available structures.^{136;}¹⁴¹ Today (10/04/2022), 169,166 entries are referring to structures solved by X-ray diffraction in the protein data bank (PDB), which was established in 1971 and is the most extensive database in structural biology (<https://www.rcsb.org/>).¹⁴²

1.3.1 Structural biology of GPCRs

In the early days of GPCR structural biology, the inherent instability of GPCRs in a detergent solution and the required amounts displayed major bottlenecks for their crystallization.¹⁴³ The research group of Gebhard Schertler achieved the first insights into GPCR structures in the 1990s. They obtained two-dimensional crystals of the bovine rhodopsin in a lipid bilayer environment. For the first time, scientists demonstrated the fundamental orientation of the TM segments in a membrane-like environment on a 9 Å projection density map.¹⁴⁴ The next crucial step was the invention of a novel technique utilizing lipidic cubic phases (LCPs) in a bicontinuous system which allowed to obtain well-ordered crystals of the integral membrane protein bacteriorhodopsin (also see Section 1.3.6).¹⁴⁵ Then, in 2000, the first high-resolution crystal structure (2.8 Å) of a GPCR, rhodopsin, was elucidated by employing multi-wavelength anomalous diffraction methods.¹⁴⁶ Rhodopsin could be purified from its natural source of bovine rod outer segment membranes due to its high abundance and thus avoiding the bottleneck of recombinant expression.¹⁴⁷ In the following years, the methods needed to be further improved to finally result in the next GPCR structure of the β_2 AR in complex with the partial inverse agonist carazolol in 2007.^{143;} ^{148–150} In 2012, Brian Kobilka and Robert Lefkowitz were jointly rewarded with the Nobel Prize for their groundbreaking work on

the structural basis of GPCR signaling. Recombinant expression methods, receptor engineering, insertion of fusion partners, and improved lipidic cubic phases displayed key advancements for successful crystallization.^{151; 152}

Receptor modification focused on the ICL3, which up to then hindered structural elucidation by its disordered structure. Replacement of the ICL3 with the T4-lysozyme (T4L) as a soluble fusion partner led to better conformational homogeneity and improved crystal diffraction, reaching a resolution of 2.4 Å.^{148; 150} The complex of the β_2 AR and a Fab5 antibody recognizing the ICL3 was derived from the same idea and yielded a 3.4/3.7 Å resolved β_2 AR structure.¹⁴⁹ In general, fusion partners are compact, small, and stable proteins that replace inherent flexible parts such as N/C-termini or ICL2/3 while providing essential polar contacts for crystal lattice formation.^{152; 153} The same applies to antibodies binding to the ICL3, which stabilize the receptor and increase the polar surface area accessible to crystal contacts.¹⁵² In 2008, the A_{2A} AR in complex with the inverse agonist ZM241385 was structurally resolved by employing the T4L insertion method. Purification and solubilization were carried out in the presence of the CLR analog cholesteryl hemisuccinate (CHS), high concentrations of sodium chloride, and the nonspecific AR antagonist theophylline, all of which contributed to further increased stability.¹⁵⁴ In the same year, the structure of the turkey β_1 adrenergic receptor (β_1 AR) was solved by employing single amino acid mutations that increased the receptor's apparent melting temperature T_M by 21°C while stabilizing the receptor in its inactive state.^{155; 156} The idea of thermostabilizing mutations also assisted in solving the structure of the NECA- and adenosine-bound A_{2A} AR, which contained four thermostabilizing point mutations L48^{2.46}A, A54^{2.52}L, T65^{2.63}A, and Q89^{3.37}A. L48^{2.46}A and Q89^{3.37}A (superscripts refer to the Ballesteros-Weinstein numbering system¹⁵⁷) that were found to stabilize the NECA-bound A_{2A} AR potentially by affecting the transition between different conformational states R and R*.¹⁵⁸

Binding of downstream transducers such as G proteins are often necessary to obtain the fully activated receptor state. Since ICL3 modification sterically impedes proper G protein binding, and a G protein-GPCR complex is even more challenging to crystallize, published structures are mainly inactive or intermediate active structures. So far, the β_2 AR- G_s and the dopamine D1 receptor- G_s complexes display the only GPCR-G protein structures solved by X-ray crystallography.^{23; 29; 159} Workaround solution with transducer mimetics such as conformation-specific nanobodies and mini-G proteins have been

developed but remain demanding.^{30; 160} Cryogenic electron microscopy (cryo-EM) has filled this gap in recent years and demonstrated its value for obtaining GPCR-G protein and GPCR-arrestin complex structures.¹⁴³ In total, there are three major approaches to achieving crystallization of an antagonist-bound GPCR: a) truncation of the N/C terminal domains, b) introduction of point mutations, and c) insertion of soluble fusion partners (also see Figure 9 and Figure 63).¹⁵² Amino acid exchanges can provide stability (for example, by locking the receptor in a distinct state), enhance expression, or avoid post-translational modifications (PTM), especially glycosylation.¹⁵² Undoubtedly, it is crucial to be aware that these approaches artificially engineer the receptors in ways that may affect proper receptor function.¹⁵² These effects need to be carefully monitored and evaluated based on the specific question of the research project. Thus, ICL3 fusion partners may affect agonist affinities but might not alter antagonist binding.

1.3.2 Structural biology in the field of drug discovery

The traditional way of target-based drug discovery can be divided into the following steps: target identification, target validation, hit identification, and subsequent hit to lead and lead optimization.¹⁶¹ This procedure is traditionally applied for the development of small molecules as drugs. The atomic structure of a target protein can be of immense value in increasing the efficiency of the tedious drug development process. This approach was termed “structure-based drug design” (SBDD) and described a way to benefit from structural information to accelerate the determination of suitable drug candidates.¹⁶² Already in 1986, Wim G. J. Hol discussed the fruitful collaboration between medicinal chemistry and structural biologists, which can greatly facilitate drug discovery based on a rational working strategy.¹⁶³ Targets cover a vast and diverse group of proteins ranging from membrane proteins such as ion channels and GPCRs to manifold enzymes.¹⁶⁴ SBDD seeks to identify, characterize and interpret ligand binding sites and elucidate operating principles of receptors and enzymes.¹⁶¹ GPCRs display an exceptionally important target group for small molecule drugs, and hence structural insights can also assist in this field of drug discovery. The exact impact of solved GPCR structures on drug development is hard to evaluate since it is a highly complex and interdisciplinary process. However, it is safe to say that the impact is substantial.¹⁶⁵ GPCRs often possess a well-defined orthosteric ligand binding pocket that can be targeted by small molecules. Structures of GPCRs in complex with ligands of different potency and efficacy can help medicinal chemists to optimize

compounds systematically and tune their pharmacological profiles.¹⁶⁵ Moreover, structures, which were determined experimentally, can complement and improve computer-aided modeling and docking studies.¹⁶⁶ One example of a successful SBDD project is the compound AZD4635. X-ray crystal structures of the A_{2A}AR revealed a hydrophobic sub-pocket that was not occupied by any of the known antagonists. This void was previously not occupied by the inverse agonist ZM241385 (4EIY) and led to the exploration of a new compound class.¹⁶⁵ The dimethylpyridine moiety of the AZD4635-related compound is able to interact with the ribose binding pocket formed by H278^{7.43} and S277^{7.42} (3UZA).¹⁶⁷ Further optimization led to the antagonist AZD4635, which is currently under investigation in anti-tumor cancer therapy.¹⁶⁸

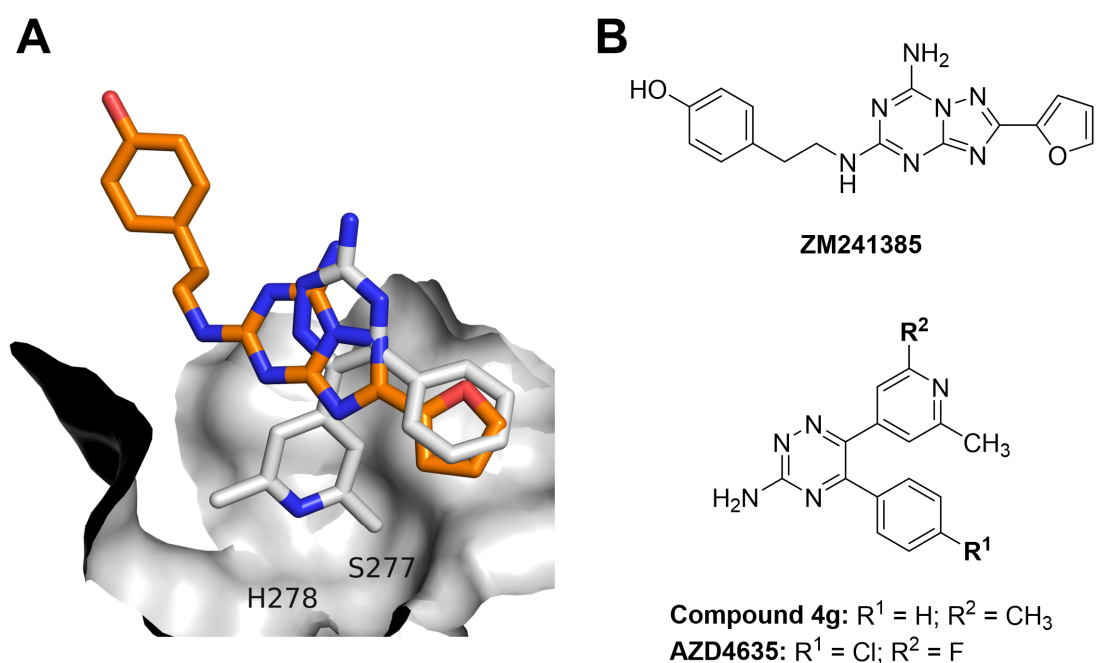


Figure 6. Comparison between binding modes of ZM241385 (4EIY) and compound 4g (3UZA).

A: Surfaces of residues close to the dimethylpyridine moiety are shown in grey. The A_{2A}AR-compound 4g structure (3UZA) was solved employing the A_{2A}-StaR2 construct bearing the mutation S277^{7.42}A. ZM241385 and compound 4g are depicted in orange and light grey, respectively. B: Chemical structures of ZM241385, compound 4g and AZD4635.

1.3.3 Cryogenic electron microscopy

Methods to solve 3D structures of macromolecules like proteins include X-ray crystallography, cryo-EM, and nuclear magnetic resonance (NMR) spectroscopy. Cryo-EM tries to directly image a macromolecule using transmission electron microscopy with no need for crystallization. Since the electrons of the beam which hit the biological

specimen are scattered by any atoms, EM requires a working environment devoid of any matter.^{169; 170} The use of a high vacuum impedes the direct work with aqueous solutions and requires special sample preparation. In early experiments, dehydration processes and the fixation of the sample to matrices disturbed the natural integrity and harbored the danger of introducing artifacts.¹⁶⁹ Further crucial developments in the 1980s led to the implementation of a vitrification step to transform the surrounding water into non-crystalline amorphous or vitreous ice, which could be maintained by cooling the sample in liquid nitrogen (“cryo”-EM).^{171; 172} This technique preserved the sample and reduced radiation damage inflicted by the electrons.¹⁷³ Results of cryo-EM studies are arrays of 2D images in which the protein of interest is randomly orientated, resulting in snapshots from different points of view of the same macromolecule.¹⁷⁰ These noisy low-dose 2D images are then combined and display the starting point for complex calculations to achieve a 3D reconstitution called single-particle reconstruction/processing. Combining multiple images of the same molecule can only be successful if two principles are fulfilled.¹⁷⁴ Firstly, the information on the location of atoms must be highly consistent between the different copies/particles, allowing superimposition of the images (sample homogeneity). Secondly, the information must be sufficient to identify the orientation of the molecule.¹⁷⁴ The main limitation of early cryo-EM studies was their low resolution, but since 2013 remarkable progress has been made to achieve even low atomic resolution in the same range as X-ray crystallography (<10 Å). A new generation of electron detectors and progress in developing processing algorithms greatly facilitated this breakthrough.¹⁶⁹

1.3.4 X-ray crystallography

Underlying theory and laws of X-ray crystallography that bridge the gap between a diffraction image and a 3D model are extremely complex and will be described only briefly (for detailed literature, see references ^{175; 176}). Crystals are built upon a unique crystal lattice that contains atoms/(macro) molecules in a highly ordered arrangement. The smallest repeating unit within the crystal is called the “unit cell”. Thus, the unit cell reflects the whole crystal lattice by repetitive translational operations.^{177; 178} The concept of Bravais lattices is applied to describe the geometry of these crystal lattices.¹⁷⁹ If a monochromatic X-ray beam hits the crystal, it will be scattered by the electrons surrounding the atoms and create a specific pattern on a detector, the “diffraction image”.^{177; 180} The diffracted waves appear as specific spots on the detector, whose intensity is proportional to the square of

their amplitudes.¹⁷⁷ There are many waves scattered in multiple directions, which interfere with each other destructively or constructively. Bragg's law determines the requirements for the constructive interference of a set of waves.^{178; 181} If the additionally traveled path length of a wave that went deeper into the crystal equals an integer of their wavelength, they will be added constructively and create a diffraction spot. Consequently, the diffraction pattern contains structural information about the spacing of the atoms within the lattice.¹⁷⁷ Once well-diffracting crystals are obtained, the next task is to compute an electron density map, which is then filled with an initial model. The problem is that a wave is characterized by its amplitude and its phase, but detectors are only capable of measuring its intensity.^{177; 180} Thus, the information about the phase of a wave is completely lost. Phases and amplitudes are not related to each other apart from the electron density map, which links them.¹⁸⁰ The "phase problem" is one of the central difficulties to overcome on the way to a 3D model. There are several methods to recover the phase information and subsequently create an initial model. If a close homolog, like a receptor family member, has already been structurally solved, the technique of molecular replacement will be employed in most cases.¹⁷⁷ The idea of Patterson maps is applied to bypass the lack of phases and to calculate a vector map based on intensities.¹⁸⁰ Using these vector maps, the relative and not the absolute position of atoms in the unit cells matters. Similarly, a Patterson map can be calculated based on the amplitudes from a close homolog. The Patterson map of the new crystal is then oriented by rotation and translation to overlap closely with the Patterson map of a close homolog.^{177; 178; 180} This process results in an initial model that is further refined to fit the measured data. After several rounds of refinement, it agrees with the obtained diffraction data and elucidates the atomic structure of the target protein.^{177; 178; 180}

1.3.5 Structural biology of membrane proteins: general approach and workflow

Every technique that aims to experimentally investigate the structure of a macromolecule, like a protein, requires the purified target protein. No matter how advanced a technique might be, without a purified protein, there will be no success. The standard procedure consists of two steps: recombinant expression and subsequent purification and concentration of the protein of interest. The unique difficulty with membrane proteins, such as GPCRs, is that they are located in a membrane built by a lipid bilayer and need to be

extracted or solubilized from their native membrane environment upon purification. Consequently, a solubilization step needs to be added between expression and purification.^{44; 152}

1.3.5.1 Expression

Despite tremendous progress and improvement, producing a sufficient amount of correctly folded GPCR has been and still is a major bottleneck for structural studies. In general, there are four common and well-established expression systems for the recombinant production of proteins: a) *Escherichia coli* (*E. coli*), b) insect cells, c) mammalian cell lines, and d) yeast.⁴⁴

E. coli displays a well-known and diverse expression system that has been improved and used for decades.¹⁸² However, heterologous expression of eukaryotic proteins in prokaryotic organisms like *E. coli* raises several concerns. *E. coli* possesses a significantly less evolved protein biosynthesis machinery, including inferior quality control, membrane insertion, and post-translational modifications (e.g., glycosylation) of proteins.^{182; 183} Misfolded and aggregated GPCRs, as well as low yields in general, are consequences.¹⁸⁴ Nevertheless, strategies to overcome these problems have been developed. Using a fusion partner and introducing stabilizing point mutations aim to enhance the inherent low stability and expression levels of GPCRs.^{183–186} The idea is to “lock” the GPCR in a distinct conformation and thus assist the less evolved machinery in coping with more complex proteins.¹⁸² Despite these hurdles, several GPCRs have been expressed successfully in *E. coli*, e.g., the A_{2A}AR and the β₁AR.^{184; 187; 188} One advantage of the expression in *E. coli* is that the bacteria are relatively easy to utilize for isotopic labeling experiments required for NMR studies.^{182; 183}

The most commonly used method to achieve sufficient quantities of recombinant protein is the expression in insect cell lines. The larger part of structural studies uses *Sf9* or *Sf21* insect cells, but the efficiency and yield of different proteins may vary between cell lines of *Sf9/21* and *Trichoplusia ni* (*Tni*).^{182; 189; 190} In general, insect cells combine the advantages of low culturing costs, easy scale-up possibility and the ability to perform most of the mammalian PTMs. The expression strategy is based on a viral infection with a modified form of the baculovirus *Autographa californica* multiple nucleopolyhedrovirus (AcMNPV), often under the control of a polyhedrin promoter.^{44; 189} Once the correct virus has been generated, infection and expression can easily be done within a few days as long

as cells are already scaled up. One point to consider is the membrane composition of insect cells compared to that of mammalian cells since protein function might be dependent upon the lipid environment.⁴¹ Insect cell membranes are characterized by high levels of phosphatidylinositol, but low levels of CLR and the absence of phosphatidylserine.^{44; 191} Lipid concentrate or CLR-cyclodextrin inclusion complexes might be used for supplementation as described for the turkey β_1 AR and human dopamine D₃ receptor.^{192; 193}

The three yeast species *Schizosaccharomyces pombe*, *Saccharomyces cerevisiae* (*S. cerevisiae*), and *Pichia pastoris* (*P. pastoris*) have been successfully utilized for the recombinant expression of GPCRs.^{44; 182} The methylotrophic *P. pastoris* is the most suitable one for structural studies since expression levels are high, but *S. cerevisiae* might be used for the fast screening of potential constructs.^{44; 182} Sufficient yields of the A_{2A} adenosine, serotonin 5-HT_{5A}, β_2 adrenergic, and M₂ muscarinic receptors were obtained based on a *P. pastoris* expression system.^{194–196} Moreover, high-resolution crystal structures of the A_{2A}AR and the histamine H₁ receptor in complex with the Fab antibody were obtained.^{197; 198} The fast growth rate, high cell densities, and cost-effective medium make yeast attractive expression systems. Moreover, they can perform most mammalian PTMs, including disulfide bond formation and N-/O-linked glycosylation.^{44; 182} N-linked glycosylation can nevertheless result in hypermannosylation or occur at unnatural positions.¹⁹⁹ One crucial point to consider is that yeasts contain significantly lower CLR levels in their membranes but, in return, high levels of the steroid ergosterol as compared to mammalian cells.^{44; 182} Genetically engineered strains of *P. pastoris* that can synthesize CLR or CHS supplementation might be potential workaround solutions.^{182; 200}

Mammalian expression systems are, of course, the most obvious choice when trying to express human GPCRs. Mammalian cell lines possess all necessary enzymes within the protein biosynthesis machinery, which take care of proper folding, processing, and trafficking.^{44; 182} Moreover, the lipid composition of their membranes is the most native-like option among the described expression systems. Nevertheless, expensive culture media, low protein yields, and transfection procedures with limited efficiency display major disadvantages. Transient transfection requires large amounts of DNA, while stable transfection is significantly more time-consuming.⁴⁴ Moreover, overexpression might induce an overload of the cellular protein biosynthesis capacity and result in undesired heterogeneous glycosylation or misfolded protein.⁴⁴ Proteins for the crystal structures of the human cannabinoid CB₁ as well as the human angiotensin AT₁ receptors were expressed

in suspension cultures of the immortalized human cell line embryonic kidney 293 (HEK293F, Expi293F).^{201; 202}

1.3.5.2 Solubilization

After successful expression, the next step is to extract the GPCR from its native membrane environment by solubilization. The goal is to solubilize the receptor without disrupting its folding or functionality. Amphiphilic detergents above their critical micelle concentration (CMC) are able to form micelles that can interact with the native membrane bilayer and incorporate the receptor molecule into their micelle. Unfortunately, detergents do not solubilize the GPCR with all membrane interaction partners and are not fully capable of recreating an environment with the same properties.^{44; 182} However, lipids can be essential for correct receptor conformation either as an allosteric modulator or as a supporter of the lateral pressure applied by the surrounding membrane.^{182; 203} In most cases, the non-ionic detergent *n*-dodecyl- β -D-maltoside (DDM) was used as a detergent for subsequent crystallographic studies.²⁰⁴ Other detergents such as ionic (sodium dodecyl sulfate, SDS) or zwitterionic (*n*-dodecyl-*N,N*-dimethylamine-*N*-oxide) are too harsh and might cause destabilization of the GPCR.⁴⁴ CHS can be added to the DDM solution to further stabilize the GPCR molecule within the micelle and mimic native CLR but with the advantage of improved solubility.^{44; 187} Lauryl maltose neopentyl glycol (LMNG) might be a suitable alternative to DDM, which possesses a lower CMC and can even provide superior stability.²⁰⁵ In contrast to the ellipsoid micelles of DDM, LMNG tends to assemble in more rod-like micelles.²⁰⁶ A computational study of the dynamics within detergent micelles harboring GPCR revealed less flexibility in the LMNG environment. Due to its branched structure, hydrophobic chains of LMNG can occupy the space between transmembrane helices more efficiently, enhancing interactions while reducing flexibility, which ultimately correlates with improved stability.²⁰⁷

1.3.5.3 Purification

Crystallographic studies require highly concentrated and pure protein solutions. Therefore, the obtained protein sample, which contains the solubilized GPCR, needs to undergo additional purification steps to remove impurities and reduce the detergent concentration as well as the overall volume. Suitable standard techniques are affinity, ion

exchange, and size-exclusion chromatography (SEC). In most cases, immobilized metal-affinity chromatography (IMAC) is carried out as a first-choice purification process.⁴⁴ IMAC depends on the affinity between Co^{2+} or Ni^{2+} ions and an N- or C-terminal polyhistidine-tag inserted in the protein construct. Co^{2+} and Ni^{2+} are bound to a carboxymethylaspartate (CMA) or nitriloacetic acid (NTA) matrix, respectively.⁴⁴ Co^{2+} -CMA (TALON resin) is preferred for GPCR purification because of low non-specific binding and high elution purity.²⁰⁸ Affinity chromatography can also be based on FLAG M1 antibody resin or resin carrying a ligand, which then assures that the eluted protein is still intact.^{29; 149; 209–212} A FLAG tag is often already present for determining expression levels. Furthermore, SEC can be added as a final purification step after deglycosylation or proteolytic cleavage to further fine-tune the purity.^{29; 149; 158; 210; 213; 214} However, SEC requires a more complex instrumental equipment and is often only used as an analytical method to investigate protein purity and monodispersity.

1.3.6 Crystallization within the lipidic cubic phase

Crystallization of membrane proteins is not as simple as that of soluble proteins and displays a challenging task in structural biology. Membrane proteins are extremely vulnerable once removed from their native environment; they tend to lose their structural integrity by aggregation and denaturation. Additionally, their anisotropic orientation impedes the achievement of a well-ordered homogenous 3D crystal required for X-ray crystallography.²¹⁵ In the course of method development, the major hurdle was to find a medium or an artificial environment that provided pseudo-native quasi-solid properties and was capable of generating a matrix incorporating sufficient amounts of protein, detergents, and precipitating agents.^{216; 217} This matrix then should create a pseudo-native environment and facilitate crystallization by its structured yet flexible nature.²¹⁵ Water-lipid systems build various phases depending on temperature and lipid concentrations and are suitable to fulfill these requirements. Especially the two cubic phases, micellar and bicontinuous, show the desired quasi-solid properties.²¹⁶ In the micellar cubic phase, the spherical micelles are packed in a well-ordered cube-like shape. Although there is a well-ordered array, the lack of a dynamic lateral diffusion that feeds a growing crystallization nucleus hinders proper crystallization. In contrast to the micellar phase, the bicontinuous cubic phase, in which both phases extend continuously in all spatial directions, enables free diffusion of protein

molecules (Figure 7). The continuous aqueous phase forms a communicating channel system allowing protein molecules to migrate to the crystallization nucleus.²¹⁷

The so-called syringe method can be employed to mix the pure and concentrated aqueous protein solution with a monoacylglycerol (MAG) such as 1-oleoyl-*rac*-glycerin (monoolein) solution to generate the mesophase.²¹⁸ As monoolein is an uncommon membrane lipid, the lipid phase can be doped with phosphatidylcholine, phosphatidylethanolamine, or CLR to create an environment as native as possible.²¹⁹ Subsequently, various distinct phase states occur, depending on temperature and composition. The protein-laden mesophase is then dispensed onto glass sandwich plates and covered with varying precipitant solutions.²¹⁷ The surrounding precipitants diffuse into the mesophase inducing locally the formation of a lamellar phase, which is meant to facilitate nucleation and crystal growth. This local crystallization area is fed with protein molecules by the bulk protein reservoir in the cubic phase, slowly supporting the slow increase of crystal size.²¹⁶

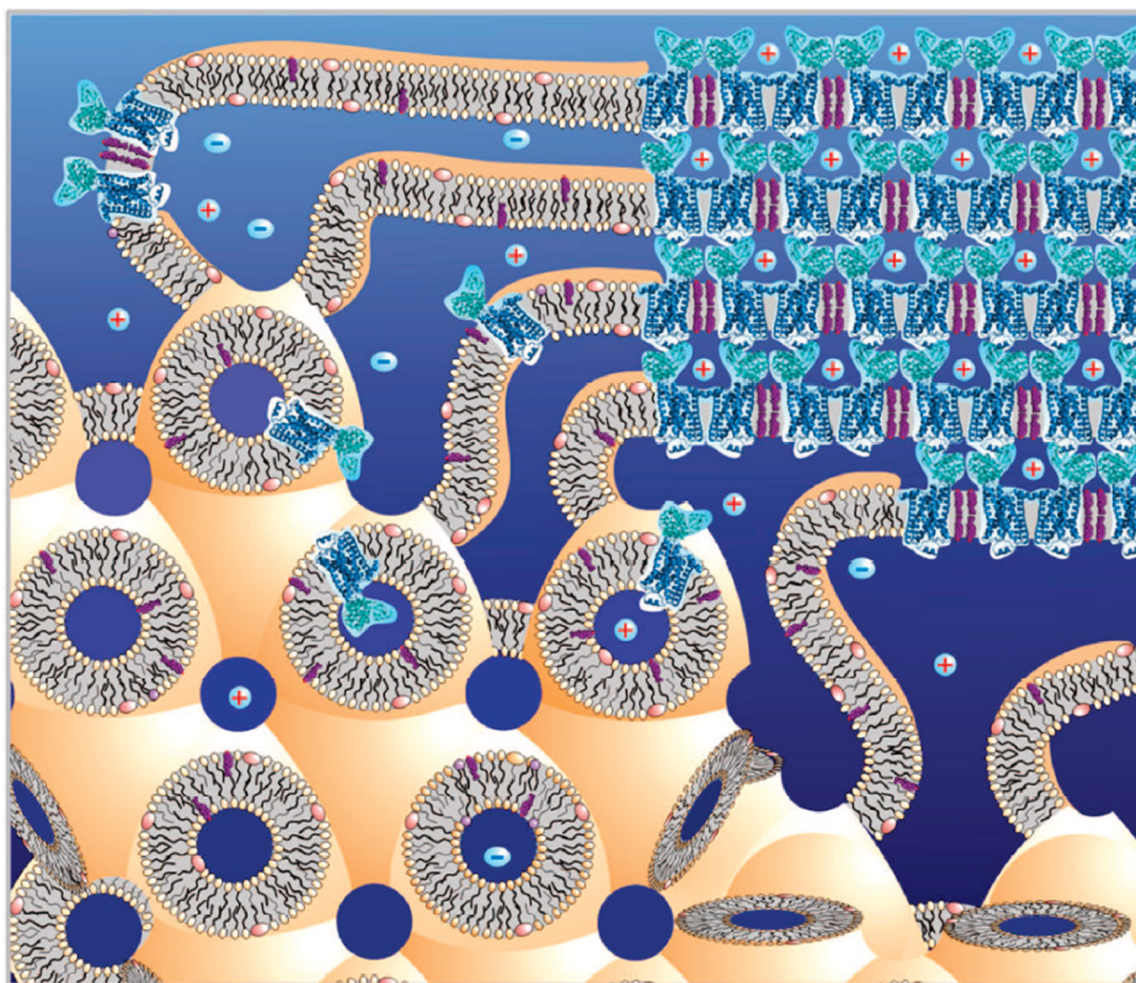


Figure 7. Schematic illustration of the mesophase crystallization processes.
(image taken from Caffrey²¹⁶).

1.4 The A₃AR from a structural point of view

Until now, the A₃AR has not yet been structurally solved, neither utilizing X-ray crystallography nor based on the rising cryo-EM technique. Out of the AR family, the A₁- and the A_{2A}ARs were already solved in 2017 and 2008, respectively.^{154; 214; 220} The A_{2A}AR represents a model receptor within the field of GPCR structural biology with 58 published X-ray structures in the PDB database. In contrast, just two X-ray structures, which were both released in 2017, and three additional cryo-EM structures (complexes with G_{i2}) are currently listed for the A₁AR.^{221; 222} Despite the lacking of an A₃AR structure, homology models, molecular docking, and site-directed mutagenesis studies (SDM) revealed crucial structural information of A₃AR over the past years.

As a member of the GPCR family, the A₃AR consists of 7 TM α -helices spanning through the cell membrane, an extracellular N-terminus, and an intracellular C-terminus, including helix VIII. ECL2 and the tip of TM3 are connected via a disulfide bond between C83^{3.25}-C166^{45.50}, which is well conserved among class A GPCRs.²²³ This disulfide bridge is crucial for the general architecture and rigidity of a GPCR. Thus, corresponding serine mutations had a devastating effect on ligand binding to the A₁- and A_{2B}ARs.^{116; 224} Ligand binding to the A_{2A}AR is less severely affected by disruption of the conserved C^{3.25}-C^{45.50} connection probably because it possesses two other disulfide bridges between C71-C159 and C74^{3.22}-C146 which might compensate for the disruption.^{114; 225} The A₃AR contains four potential and accessible N-glycosylation sites meeting the consensus motif Asn-X-Thr/Ser, with X being any amino acid except for proline.²²⁶ Apart from the N-glycosylation site within ECL2, which is similarly present in the A₁-, A_{2A}-, and A_{2B}ARs, the A₃AR possesses three additional glycosylation sites within its N-terminus. The attachment of the 16-carbon long, saturated palmitic acid, called “palmitoylation”, can occur as a PTM of GPCRs besides N-glycosylation. Targets of transferases catalyzing this reaction are intracellular cysteine residues, which are often located 10–14 amino acids after TM7 at the cytoplasmic tail.²²⁷ C300^{8.61} and C303^{8.64} represent the two cysteine residues within the C-terminal tail of the A₃AR that qualify for palmitoylation sites.

1.4.1 The ligand binding pocket

The core of the orthosteric binding pocket is well conserved among ARs, as expected for a receptor family sharing a common endogenous ligand. Jespers et al. (2018) published a comprehensive review that summed up all available data from SDM studies

targeting ARs to this date.²²³ They stated a core pocket consisting of 7 amino acids in helices III, VI, VII, and ECL2. The bidentate N250^{6.55} is one of the key residues within this binding pocket and forms important hydrogen bonds, e.g., with an exocyclic amino group and a heterocyclic nitrogen atom. In the case of Cl-IB-MECA, hydrogen bonds of N250^{6.55} with N⁶ and N7 of the adenine core fix the ligand within the binding pocket.²²⁸ Consequently, the N250^{6.55}A mutant led to a complete loss of agonist and antagonist binding.^{229; 230} A₁AR and A_{2A}AR structures confirmed the central role of these hydrogen bonds formed by the conserved N^{6.55.38}; ²¹⁴ F168^{ECL2} in the ECL2 represents a crucial binding partner interacting with the ligand core scaffold via $\pi - \pi$ stacking. Exchanging it for alanine, resulting in the mutation F168^{ECL2}A, abolished agonist-induced receptor activation.²²⁸ Similar to the A₃AR, aromatic stacking with the triazolo-triazine scaffold of ZM241385 and the xanthine scaffold of DU172 was observed in the A₁AR and A_{2A}AR structures, respectively.^{154; 214}

The neighbor of the pivotal F168^{ECL2}, V169^{ECL2}, is also meant to be part of the conserved binding pocket, according to Jespers et al.²²³ The A₁-, A_{2A}-, and A_{2B}ARs possess glutamate in this position. In most A_{2A}AR structures, E169^{ECL2} forms a salt bridge with H264^{ECL3} in ECL3, connecting ECL2 and ECL3. This salt bridge is not present in the so far published A₁AR antagonist structures.^{214; 220} V169^{ECL2} in the A₃AR seems to be able to interact via van der Waals forces with antagonists since V169^{ECL2}A reduced affinity of the antagonist Compound 18.²³¹ However, quite surprisingly, V169^{ECL2}E showed an unaltered affinity for Compound 18.²³¹ Contrary, V169^{ECL2}E unexpectedly increased the potency of IB-MECA and NECA. Their iodobenzyl moiety is thought to occupy a hydrophobic area around V169^{ECL2}, which contradicts this finding at first glance but might point towards more complex interactions. Nevertheless, V169^{ECL2} is critical for agonist and antagonist binding.²²⁸ A detailed mutagenesis study of residue Q167^{ECL2} revealed its important contribution to ligand binding. Mutation to alanine, arginine, and glutamate decreased the affinity of all tested adenosine derivatives. However, ligands bearing C2 moieties with an oppositely charge to arginine and glutamate showed an increased affinity for the respective mutant compared to the other mutants.²³²

Functional inactivity was caused by the mutations T94^{3.36}A, L246^{6.51}A, I268^{7.39}A, S271^{7.42}A and H272^{7.43}A. T94^{3.36}, S271^{7.42} and H272^{7.43} coordinate the ribose moiety of agonists via direct or water-mediated hydrogen bonds.²²⁸ Interestingly, alanine mutations of T94^{3.36} and H272^{7.43} impaired activation by an agonist, but still showed basal activity.²²⁸ Moreover, S271^{7.42}A and H272^{7.43}A led to a complete loss of high affinity binding of the

agonist [¹²⁵I]-AB-MECA and the antagonist [³H]PSB-11.²³³ The mutant T94^{3.36}A was still able to bind both ligands but with a 4- to 10-fold lower affinity.²³³ Mutation of H272^{7.43} to glutamate did not cause such a drastic effect, but agonist and antagonist affinity was also reduced.²³⁴ The two hydrophobic residues L246^{6.51}A and I268^{7.39}A seem to form required van der Waals interactions for ligand-induced receptor activation.²²⁸

S247^{6.52}, which is histidine in all other ARs, is located deeper within the ligand binding pocket. The A₃AR might therefore be more open toward larger substituents advancing deeper into the pocket since serine displays a less bulky residue.²²³ S247^{6.52} is not as pivotal as it is for the A_{2A}AR because mutation to alanine did not affect agonist binding and only slightly decreased antagonist binding. In contrast, the corresponding H250^{6.52} abolished ligand binding to the A_{2A}AR.^{229; 233; 235}

A229^{6.34}E and R108^{3.50}K/A are two interesting mutations that are not meant to interact with ligands directly but impact basal activity (basal activity in cAMP accumulation assay: A229^{6.34}E > R108^{3.50}A > R108^{3.50}K). These specific mutations create a particular receptor species called constitutively active mutants (CAMs).²³⁶ Molecular dynamics studies revealed that different patterns and persistency of the “inactive state signatures”, salt bridges D107^{3.49}–R108^{3.50} and E225^{6.30}–R111^{3.53}, might be contributing factors.²³⁷

The role of W^{6.48}, which is part of the conserved CWxP motif, is often described as a “transmission” or “toggle switch” within the agonist-induced TM rearrangements.^{238; 239} In the A₃AR, serine replaces cysteine in the first position of this motif, creating the amino acid sequence S^{6.47}W^{6.48}L^{6.49}P^{6.50} identical to that of the A₁AR. The introduction of the alanine mutant W243^{6.48}A did not significantly influence agonist binding but significantly decreased antagonist binding.^{229; 233; 240} This mutation discriminates against nonnucleoside-based antagonists since nucleoside-based antagonists are not as affected.²⁴⁰ The same effect was determined for W243^{6.48}F but to a smaller extent.²²⁹ Despite unaltered agonist binding, mutation of W243^{6.48} to either alanine or phenylalanine impaired receptor activation, proving its crucial role in conformational rearrangements.^{229; 238} L244^{6.49} (X in CWxP) is less critical for ligand binding, and thus L244^{6.49}A resulted in no significant change of agonist and antagonist affinities.²³³ However, exchange to alanine diminished the potency of Cl-IB-MECA in a PLC activity assay by 36-fold, indicating that this residue is involved in signal transduction.²³³

H95^{3.37}, which is glutamine in all other ARs, is located similarly to T94^{3.36} at the bottom of the ligand binding pocket. It was found to be directly involved in ligand

recognition because H95^{3.37}A markedly decreased agonist and antagonist affinity. Interestingly, H95^{3.37}A exhibited no significant decrease in the potency of Cl-IB-MECA determined by IP₃ production as it was shown for, e.g., W243^{6.48}A.²²⁹

Further positions of SDM are K152^{ECL2} and hydrophobic interaction partners like L90^{3.32}, M174^{5.35}, M177^{5.38}, V178^{5.39}, F182^{5.43}, I249^{6.34}, and L264^{7.34}. However, these residues are less crucial for ligand binding.^{229; 231; 233; 241}

1.4.2 Conserved motifs

1.4.2.1 NPxxY motif

The NPxxY motif is a highly conserved GPCR motif located at the end of helix VII, starting with N^{7.49}, followed by P^{7.50}, two variable residues, and Y^{7.53}. The two spacing amino acids are isoleucine/valine in the A₁-, A_{2B}-, and A₃ARs and phenylalanine/isoleucine in the A_{2A}AR. NPxxY is involved in conformational rearrangements upon receptor activation and is often termed one of the activation “microswitches”.²²³ Activation causes the tip of TM7 to move inwards, which is mediated by a reorganization of residues within the NPxxY motif. Y^{7.53} undergoes a rotameric switch by moving upwards and connecting with the conserved Y^{5.58} in TM5 via a water-mediated hydrogen bond, as seen in the G protein-bound A_{2A}- and A₁ARs structures.^{222; 242} The Y^{5.58}-Y^{7.53} link, often named “tyrosine toggle switch”, and the TM7 inward movement in combination with the large outward shift of TM6 ultimately facilitate G protein binding by forming a binding cavity, which can be approached by the $\alpha 5$ helix of G proteins.^{243; 244}

1.4.2.2 DRY motif

The DRY motif consists of D^{3.49}, R^{3.50}, and Y^{3.51} and is located at the bottom of TM3. It connects TM3 with the end of TM6 in the inactive state, preventing its outward tilt upon activation.²⁴⁴ In the A₁AR inactive state structure, 5UEN, D^{3.49} and R^{3.50} are too distant to build a salt bridge but are linked indirectly through H-bonds to T^{2.39}.²¹⁴ In this case, the common ionic interactions can be observed between E^{6.30} and R^{3.50} as well as R^{3.53}.²¹⁴ D^{3.49} links the DRY motif with the ICL2 via a hydrogen bond to Y^{3.60}.²¹⁴ In contrast to that, the A_{2A}AR inactive state structure 4EIY revealed a slightly different arrangement, especially a change in the rotamer of E^{6.30}. R^{3.50} and E^{6.30} appear not to form a direct ionic lock but rather form hydrogen bonds with an extensive water molecule network. Similarly,

the first A_{2A}AR structure from Jaakola et al. showed that D^{3.49} forms hydrogen bonds with Y112^{ICL2} and T^{2.39}, located in the ICL2 and the cytosolic part of helix II.¹⁵⁴ Both receptors have in common that the DRY motif is additionally links helix VI to the ICL2 and helix III. However, details, like the rotamer of E^{6.30}, and the presence of an ionic lock, differ significantly. It has been assumed that the presence of a short helical section in the ICL2 might be the reason for the interaction between D^{3.49} and the tyrosine in ICL2.¹⁵⁴ Receptor activation leads to a disruption of the (ionic) “lock” between helix III and VI allowing helix VI to undergo its characteristic outward movement.²⁴⁴ Overall, the DRY motif is a signature for the inactive state and is well conserved among GPCRs, but its detailed architecture can differ even among receptor family members.²⁴⁴

1.4.2.3 PIF motif

P^{5.50}, I^{3.40}, and F^{6.44} are organized to form the PIF motif, which is identical within the AR family. These three hydrophobic residues are located close to the bottom of the orthosteric ligand binding pocket and participate in the ratchet-like propagation of rearrangements, causing larger movements of helices at the cytoplasmic site. Sansuk et al. (2011) described the interaction between P^{5.50} and I^{3.40} as a fulcrum/lever setup. I^{3.40} functions as a lever, which uses P^{5.50} as a fulcrum to induce the unwinding of TM5.²⁴⁵ These relatively small local structural changes around P^{5.50} are also linked to F^{6.44} in helix VI and thus are associated with the large helical movement of helix VI.^{3; 245; 246} A detailed analysis of F^{6.44} suggested that I^{3.40} acts as a gate, allowing F^{6.44} to pass into the hydrophobic pocket between helix III and V when activation occurs.²⁴⁶ Moreover, interaction partners of F^{6.44} in TM3 and TM5 seem to be conserved. In the A_{2A}AR inactive state structure (4EIY), residues in close proximity are: T^{3.36}, I^{3.40}, L^{3.43} in TM3, as well as V^{5.47} and L^{5.51} in TM5. Interestingly, the β₂ receptor shows the same composition in this hydrophobic cavity apart from phenylalanine in position 5.47.²⁴⁶ This area is well conserved within the AR family and differs only in position 5.47, which is occupied by isoleucine in the A₃AR. Superimposition of the two inactive state structures of the A₁- (5UEN) and A_{2A}ARs (4EIY) demonstrated that the architecture is highly similar except for a different rotamer of I^{3.40}. The second A₁AR inactive state structure (5N2S) conforms to the A_{2A}AR structure and reveals the same rotamer of I^{3.40}.

1.4.2.4 CWxP motif

Closely above the PIF motif, W^{6.48} is located as part of the CWxP motif. This motif extends from position 6.47 to the highly conserved position 6.50, which is a proline in 98% of all class A GPCRs.²⁴⁷ C^{6.47} is less conserved (70 %) and is exchanged by similar residues like serine or threonine in 10 % and 4 % of all sequences.²⁴⁷ The occupation of 6.47 differs even within the AR family. A₁AR and A₃AR possess serine in this position, whereas the A_{2A}- and A_{2B}ARs feature the more common cysteine. Rearrangements of these residues assist in transmitting the conformational changes originating from the orthosteric binding pocket to the cytoplasmic areas of TM5 and 6. This mechanism is similar to that of the PIF motif, to which it is functionally coupled, and sometimes combined to one larger motif.²³ Overall, these two motifs determine the changes in the interface between helices III, V, and VI upon receptor activation.²³ The most prominent result of these changes is the large outward tilt of helix VI. P^{6.50} displays a central role in this helix, which causes its characteristic kink and functions as a pivot for this outward movement.²⁴⁷ The role of C^{6.47} was investigated by Olivella et al. in 2013. They concluded that C^{6.47} functions as a “gatekeeper” of the hydrogen bond network involving D^{2.50}, N^{7.44}, and N^{7.45} and thus influences the NPxxY motif. Inactive state structures exhibit hydrogen bonds between N^{7.44}/N^{7.45} and N^{7.45}/C^{6.47}, allowing C^{6.47} to affect the orientation of N^{7.44}. This hydrogen network is disrupted in the active state structures, thereby freeing N^{7.44} to interact with D^{2.50}.²⁴⁷ The role of W^{6.48}, which occupies the space at the bottom of the ligand binding pocket, is slightly less universal. It was demonstrated that agonists and the inverse agonist ZM241385 are able to interact with W^{6.48}. In the active state, this interaction stabilizes the shift of W^{6.48} and the accompanying swing of helix VI.^{158; 242; 248} On the contrary, the link between ZM241385 and W^{6.48} prevents this shift in the inactive state.^{154; 248}

1.4.2.5 Sodium binding pocket

It was discovered almost 50 years ago that Na⁺ acts as an allosteric modulator at most of the class A GPCRs.^{249; 250} At a concentration of 100 mM, NaCl inhibited [¹²⁵I]-AB-MECA binding to the wt A₃AR by around 80 % and significantly decreased the dissociation rate of [³H]PSB-11.^{233; 251} Na⁺ binds to a pocket which is highly conserved within class A GPCRs and is located in the middle of the seven TM regions.²⁵² High-resolution structures further proved and elucidated its composition. This structural information revealed that it comprises 16 residues and is anchored at the negatively charged D^{2.50}.^{38; 253} 15 out of 16

residues are identical within the AR family except for L^{3.35} being replaced by phenylalanine in the A₃AR (Figure 8). Rearrangement of the TM regions upon receptor activation leads to a partial collapse of the sodium binding pocket, preventing high-affinity binding of Na⁺. Residues D^{2.50} and S^{3.39}, which coordinate Na⁺ in the inactive state structures, are now directly connected by a hydrogen bond, leaving no space for Na⁺.²⁵³ Therefore, Na⁺ bound to its pocket is a key linchpin for stabilizing the inactive receptor state.²⁵⁴ Thus, mutagenesis of residues within the pocket can be utilized to disrupt the binding pocket and consequently stabilize distinct receptor states.^{255; 256} The sole mutation of S^{3.39} to lysine recently enabled A_{2A}AR co-crystallization with so far elusive Preladenant derivatives and even exceeded the properties of A_{2A}-StaR2, which bears nine mutations.^{257; 258} The highly conserved composition of the binding pocket suggests that successful residue exchanges, which have already facilitated successful crystallization, might be transferable to other GPCRs.

Receptor	Position														
	1.50	1.53	2.46	2.47	2.49	2.50	3.35	3.39	3.43	6.48	7.45	7.46	7.49	7.50	7.53
hA ₁ AR	N	V	L	A	A	D	L	S	L	F	W	N	S	N	Y
hA _{2A} AR	N	V	L	A	A	D	L	S	L	F	W	N	S	N	Y
hA _{2B} AR	N	V	L	A	A	D	L	S	L	F	W	N	S	N	Y
hA ₃ AR	N	V	L	A	A	D	F	S	L	F	W	N	S	N	Y

Figure 8. Sequence alignment of the residues forming the sodium binding pocket of AR subtypes.

2. Aim of this thesis

The A₃AR was the last discovered AR subtype and, besides the A_{2B}AR, is one of the two members within the AR family for which no X-ray or cryo-EM structure has been published so far. Its closest relative, the A₁AR, and the A_{2A}AR were successfully crystallized, and their structures were elucidated by X-ray crystallography for the first time in 2017 and 2008.^{154; 214} The A₃AR is widely expressed in the human body and plays a crucial role in various types of cancer, inflammatory and autoimmune diseases, and different kinds of pain including chronic pain.^{57–59; 70–74; 87–89} Several clinical trials have been conducted or are currently ongoing, proving the relevance of the A₃AR as a novel drug target.^{57; 70; 75; 259} However, the characterization of the A₃AR, which still appears enigmatic, is less advanced compared to the related, well-studied A₁- and A_{2A}ARs.^{241; 260} Therefore, after the successful implementation of the structural biology research unit within the research group of Professor Christa Müller that initially focused on the A_{2A}AR, research efforts were expanded towards a new GPCR that is related to the A_{2A}AR but has been structurally elusive so far. This put the A₃AR into the spotlight. In order to prepare the A₃AR for crystallization, the following aims were pursued:

- Design, cloning, and expression of A₃AR constructs
- Comprehensive analysis and characterization of purified proteins
- Identification of potential A₃AR crystallization constructs
- Conducting initial crystallization experiments
- Extensive construct validation

X-ray crystallography of membrane proteins, such as GPCRs, have undergone tremendous advances over the past years but still remain challenging. Inherent protein instability, low expression levels, and low yields often impede their investigation by structural biology techniques. To date, no research studies have been published that tried to pave the way for the structural biology of the A₃AR.²⁶⁰ Development of a sufficiently stable A₃AR crystallization construct that fulfills the requirements regarding yield, purity, and homogeneity would mean enormous progress and could significantly facilitate structure elucidation efforts. Moreover, a comprehensive validation of such a

crystallization construct would test the applicability of common approaches in structural biology for the A₃AR or might reveal A₃AR-specific pitfalls that need to be considered. The results of this work are expected to provide valuable information that will contribute to decrypting the structure of the poorly explored A₃AR.

3. Results and Discussion

3.1 Construct design

The fundamental approach was to design and generate a wide variety of human A₃AR constructs and subsequently express, purify and analyze the properties of these proteins. Since human and rodent A₃ARs display striking differences in ligand binding, the mouse A₃AR was also included in this investigation. As described in Section 1.3.1, there are three principles to stabilize a GPCR for crystallographic studies: a) N/C terminal truncation, b) point mutations, and c) insertion of fusion partners (Figure 9). The cleavable signal sequence from the influence hemagglutinin (HA) protein is commonly employed to enhance the expression and was inserted at the N-terminus of the A₃AR constructs.²⁶¹ A FLAG-tag following the HA-tag enabled the evaluation of the expression by flow cytometry. A C-terminal deca-histidine tag was employed to purify the proteins.

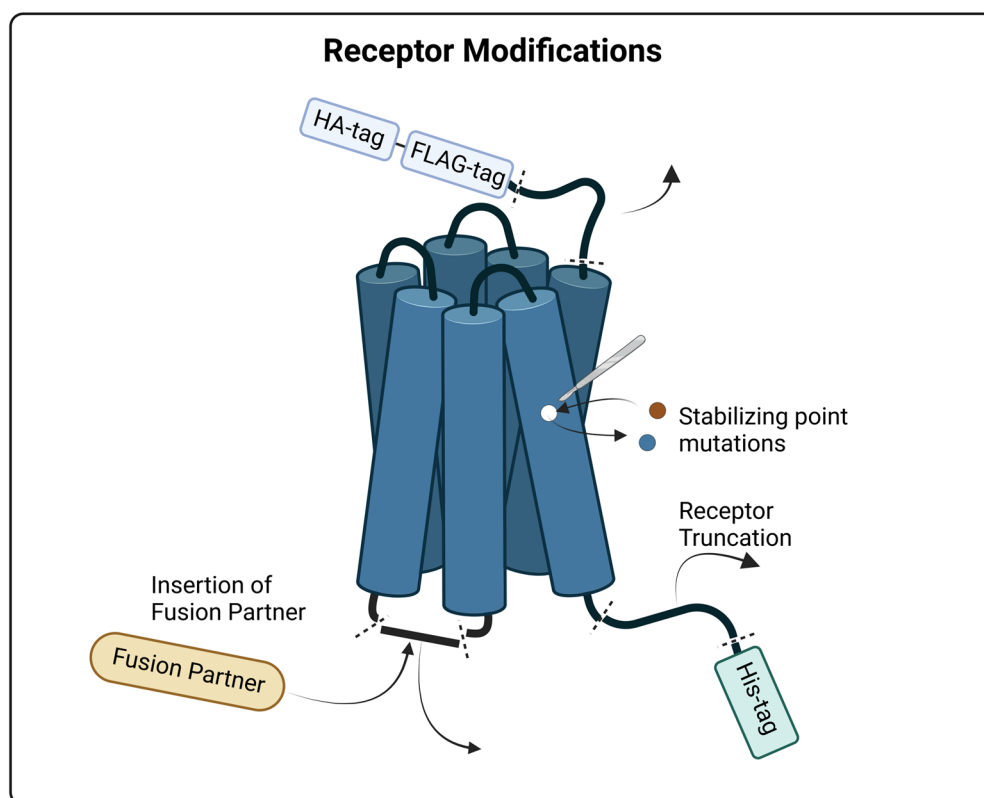


Figure 9. Overview of employed receptor modifications.
Created with BioRender.com

The following sections will present the results of various approaches explained at the beginning of each section. Expressed and purified proteins were analyzed by SEC and

checked for their thermal stability by the *N*-[4-(7-diethylamino-4-methyl-3-coumarinyl)phenyl]maleimide (CPM) thermostability assay, which was used to determine the protein's melting temperature (T_M).²⁶² The CPM-based thermostability assay is a technique to examine the biophysical properties of ligand binding at solubilized receptors. Upon heating, the protein gradually unfolds, and buried cysteine residues become accessible to interact with the CPM dye to form CPM-thiol adducts resulting in an increased fluorescence signal.²⁶² The T_M value was defined as the inflection point of the unfolding curve as determined by non-linear regression. In the SEC chromatogram, a peak at around 4 min was considered to correspond to the A₃AR protein and was used to evaluate the overall protein yield. An example of typical results is given in Figure 10, which presents the complete SEC chromatogram and thermostability assay results of the already published A_{2A}AR-bRIL- Δ C crystallization construct.³⁸ Since the area of interest is at around 4 min, the SEC chromatogram will be shortened in most cases, and the time between 3–5 min will be shown. A normalized SEC chromatogram is employed to illustrate the peak shape and assess the size of the plateau before the protein peak, which corresponds to protein aggregates.^{201; 263} In some cases, protein samples were incubated at higher temperatures (50–60°C) to induce thermal stress and accelerate protein aggregation. Afterward, the protein samples were again analyzed by SEC to assess the degree of protein aggregation (“thermal SEC”, dashed lines, for an example see Figure 20). The protein peaks will be decreased, and protein aggregates of higher molecular weight will cause an elevation of the shoulder between 3–4 min. The more stable the protein is, the less aggregation is induced by this stress test. Thermal SEC and the CPM thermostability assay complement each other for evaluating the stability parameters of the subjected protein constructs. The principal objective was to find constructs with improved protein yield and higher T_M values (see Table 18 for a detailed overview of all constructs).

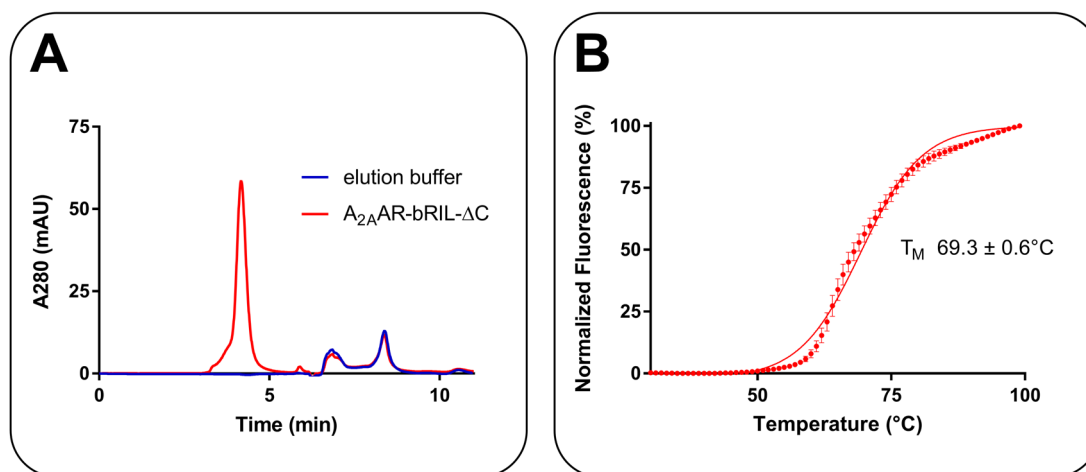


Figure 10. Analysis of the A_{2A}AR-bRIL-ΔC protein.³⁸

A: Complete SEC chromatogram of the A_{2A}AR-bRIL-ΔC protein and the corresponding elution buffer as a control. B: CPM thermostability assay. The protein was purified in the presence of the antagonist ZM241835.

3.2 Introduction of fusion partners

In order to create a starting point for the crystallization of the A₃AR, constructs were generated whose ICL3 or N-terminus were replaced by fusion partners (see Figure 11). The N- and C-termini of the receptor were truncated right before S9^{1,29} and right after S308^{8,69}. L208^{5,69}–G219^{6,24} was chosen as the standard junction site for the insertion of fusion partners into the ICL3, based on other GPCR crystallization constructs.^{38; 214} In total, nine different fusion partners were taken into account: the thermostabilized apocytochrome b₅₆₂ (mutations M7W, H102I, R106L, bRIL), chain A of the T4 lysozyme with and without cysteine residues (residues 2–161, dsT4L, T4L), a longer C-terminal fragment of the T4 lysozyme (residues 60–164 followed by Ser(Gly)₄Ala linker and residues 1–12, lyso fragment), flavodoxin, rubredoxin, xylanase, a fragment of the helical histidine phosphotransferase domain P1 from the chemotaxis kinase CheA of *Ter motoga maritima* (residues 4–104, PTD) and the C-domain of the glycogen synthase from *Pyrococcus abyssi* (residues 218–413, PGS).^{153; 264–267} When inserting a fusion partner into the ICL3, it is crucial that the folding of helices V and VI and the fusion partner itself is not disrupted.¹⁵³ Therefore, fusion partners with different distances between their N- and C-termini and varying molecular structures were tested to find a suitable candidate that fits into the ICL3 of the A₃AR.

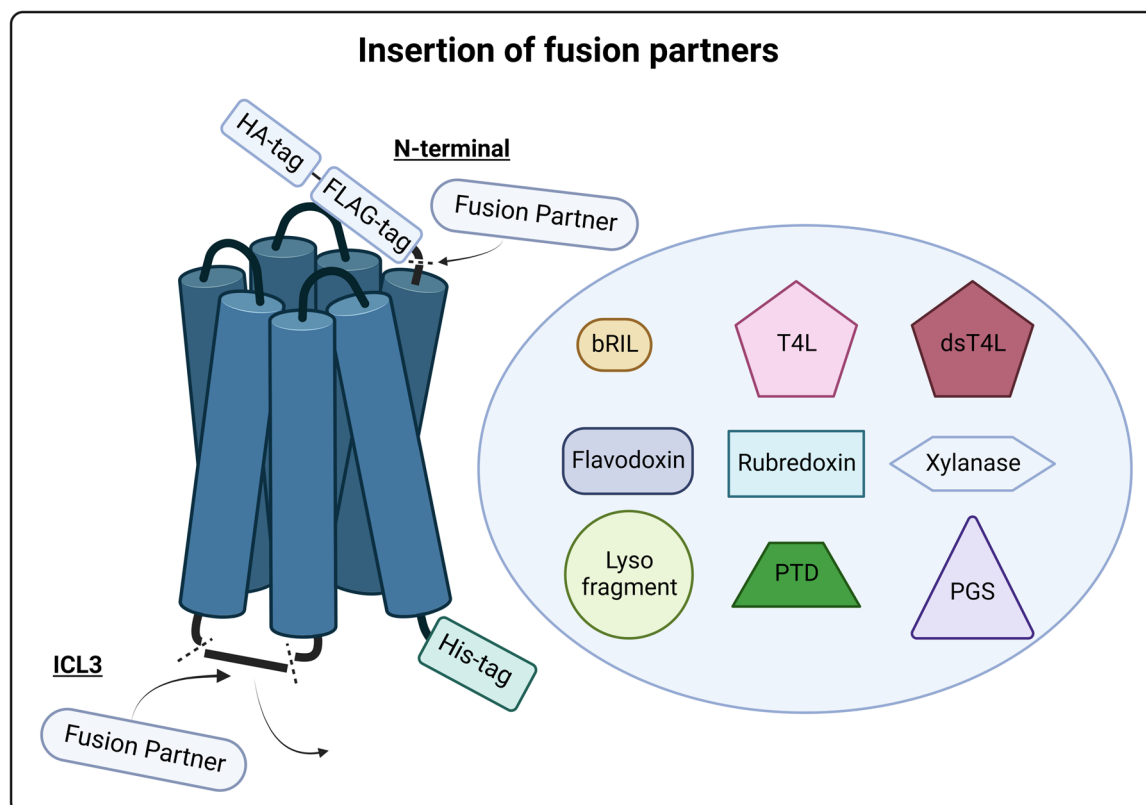


Figure 11. Schematic illustration of the insertion of fusion partners.
For abbreviations of fusion partners see Section 3.2. Created with BioRender.com

3.2.1 Fusion partner inserted into the ICL3

Insertion of various fusion partners into the ICL3 of the A₃AR resulted in no considerably improved protein yields compared to the wt A₃AR. As shown in Figure 12, every construct displayed a small shoulder to different extents at the retention time of the A_{2A}AR control peak, which represented the desired A₃AR protein. Interestingly, the wt receptor and the wt receptor plus bRIL revealed a minimally better protein yield, which is surprising since the wt construct was expected to be the most unstable construct. The corresponding truncated constructs did not reveal any distinctively pronounced shoulder, and thus this observation might have been caused by the absence of the N- or C-terminus, which will be of interest later on. Nevertheless, these differences occurred on an extremely small scale and were, therefore, hard to analyze reliably.

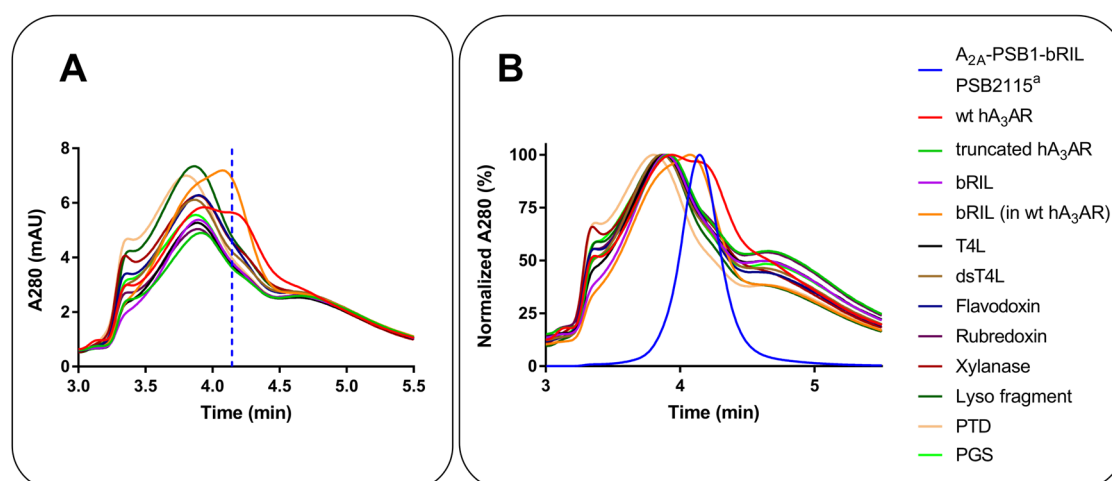


Figure 12. Fusion partner inserted into the ICL3.

Constructs represent truncated hA₃ARs with indicated fusion partner replacing the ICL3 (N-truncation M1–L8, C-truncation L309–E318; insertion site L208^{5,69}–G219^{6,24}). A: Shortened SEC chromatogram (3–5.5 min). The dashed line represents the peak of the A_{2A}-PSB1-bRIL protein. B: Normalized SEC chromatogram (3–5.5 min). All proteins were purified in the presence of TK-OT-018. ^asee reference ²⁵⁷

3.2.2 N-terminal fusion partner

Similar to fusion partners inserted into the ICL3 of the truncated A₃AR, no construct bearing an N-terminal fusion partner yielded a significantly increased protein amount (Figure 13). Again, the shoulder at 4.1 min most likely indicated the presence of some A₃AR protein, but in extremely low amounts. The obtained peak heights resembled the peak heights of constructs with fusion partners in the ICL3. However, the shoulders were, on average, slightly more pronounced than that of constructs with ICL3 fusion partners, similar to the untruncated wt constructs. This observation indicated that instead of the absent C-terminus of truncated constructs, the presence of the N-terminus could be responsible for the improved results of untruncated constructs. Moreover, this effect did not depend on the nature of the N-terminal amino acids.

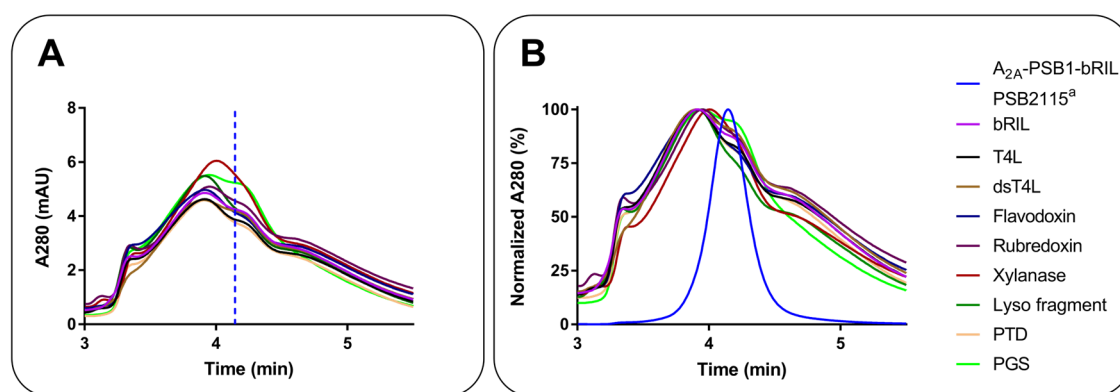


Figure 13. N-terminal fusion partner.

Fusion partner inserted N-terminally into the truncated hA₃AR (N-truncation M1–L8, C-truncation L309–E318). A: Shortened SEC chromatogram (3–5.5 min). The dashed line represents the peak of the A_{2A}-PSB1-bRIL protein. B: Normalized SEC (3–5.5 min). All proteins were purified in the presence of TK-OT-018. ^asee reference²⁵⁷

3.3 Further construct modifications

Variation of fusion partners which replaced the ICL3 or the N-terminus did not lead to significantly improved protein yields, and thus the approach was extended to find a starting point to build upon. Since a fusion partner will most likely be present in a final crystallization construct, bRIL was set as the standard fusion partner and was inserted into the ICL3 by replacing residues S209^{5.70}–T218^{6.23}. Two constructs were designed in which the two most commonly used fusion partners, bRIL and T4L, replaced one further amino acid of TM6, resulting in a junction site of L208^{5.69}–A220^{6.25}. Moreover, the common N-glycosylation site in the ECL2 was mutated to glutamine resulting in the N160^{ECL2}Q mutant.

In order to assess the effect of larger N- and C-terminus truncation compared to the standard truncation before helix I and right after helix VIII, constructs were designed whose N-terminus truncation increased gradually by one amino acid. The A₃AR was truncated maximally up to T14^{1.34}, resulting in a construct that started with Y15^{1.35}. Moreover, two constructs were truncated after A299^{8.60} and P305^{8.66} to investigate the outcome of a larger C-terminal truncation. A299^{8.60} was chosen because it cut off the two cysteines C300 and C303, which is S-palmitoylated during PTM.

Until this point, the transcription of all constructs was controlled by the polyhedrin promoter, which induces the expression in the late phase of the baculovirus infection.²⁶⁸ Selected constructs were cloned into a plasmid controlled by the gp64 promoter in order to evaluate the effect of different promoters.²⁶⁹ The truncated A₃AR, the truncated A₃AR fused to bRIL, an A₃AR construct that possessed 22 amino acids of the

human M₄ muscarinic acetylcholine receptor (M₄ mAChR) N-terminus and bRIL, and the truncated mA₃AR were subjected to this plasmid change (for further information about the M₄ mAChR N-terminus see Sections 3.8 and 3.9).

A_{2B}AR crystallization approaches showed that exchanging TM1 with the corresponding A_{2A}AR TM1 was beneficial. Therefore, the complete A₃AR TM1 was replaced by A_{2A}AR's TM1, as illustrated in Figure 14. Moreover, only the first 11 or 7 amino acids of A_{2A}AR's TM1 replaced the corresponding A₃AR's TM1 residues to reduce the total number of amino acid exchanges and to assess whether fewer amino acids will potentially lead to the same result. Y9^{1.35} and E19^{1.39} were set as intermediate points for the partial TM1 exchange because they are conserved among all ARs (for alignment, see Figure 14).

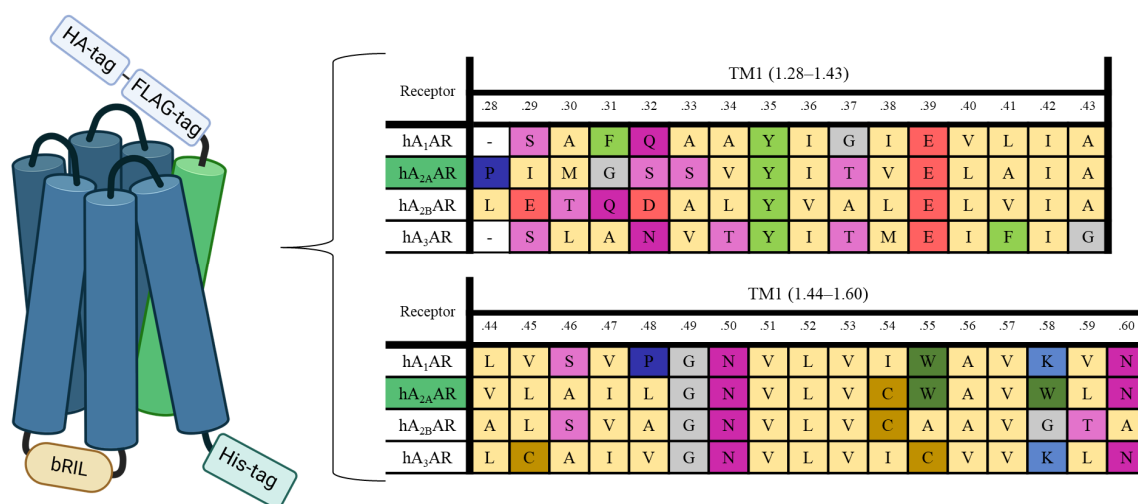


Figure 14. The design of the TM1 exchange.

Left: Schematic illustration of an A₃AR construct bearing bRIL in the ICL3 and the TM1 (green) of the A_{2A}AR. This figure was created with BioRender.com. Right: TM1 sequence alignment of all members of the human AR family.

3.3.1 Results of further construct modifications

General conclusions stated in Sections 3.2.1 and 0 apply to most results of further construct modifications (Figure 15). Unfortunately, the insertion of the 22 amino acids of the M₄ mAChR N-terminus, which had been utilized to increase the expression of the A₁AR crystallization construct, did not lead to considerably larger amounts of the desired A₃AR protein.²¹⁴ The chromatogram did not reveal a noticeably higher protein peak even though the shoulder between 3–4 min was slightly higher. An A_{2B}AR construct, which did not possess any C-terminal His-tag, was expressed as a control. Since the His-tag is missing,

no receptor protein should be purified by Co²⁺-based IMAC. Consequently, the resulting SEC chromatogram represented a baseline or background noise caused by buffer ingredients and protein impurities bound unspecifically to the resin. The differences between this control and the investigated constructs represented the A₃AR protein. Therefore, it was concluded that the higher the peak at 4.1 min and the smaller the extent of absorption between 3–4 min, the better the yield of correctly folded GPCR protein. Most of the investigated constructs showed higher peaks than the control without His-tag, proving that there was indeed A₃AR protein present, although in minimal amounts. Moreover, most purified proteins were aggregated since the major differences compared to the red chromatogram (no His-tag) appeared before 4 min.

Adapting the junction site to L208^{5,69}–A220^{6,25} or modifying the receptor truncation did not cause any improvements. The purple chromatogram revealed a second peak at around 4.5 min, which was even later eluted than the A_{2A}AR peak and was considered an artifact. Moreover, the TM1 exchange strategy, which occurred to be beneficial for the A_{2B}AR, seemed not transferable to the A₃AR. The mutation N160^{ECL2}Q, which prevents heterogeneous glycosylation and is present in many crystallization constructs, neither improved protein stability nor increased protein yield. Nevertheless, this mutation will be considered for initial crystallization trials once a stable construct has been established.

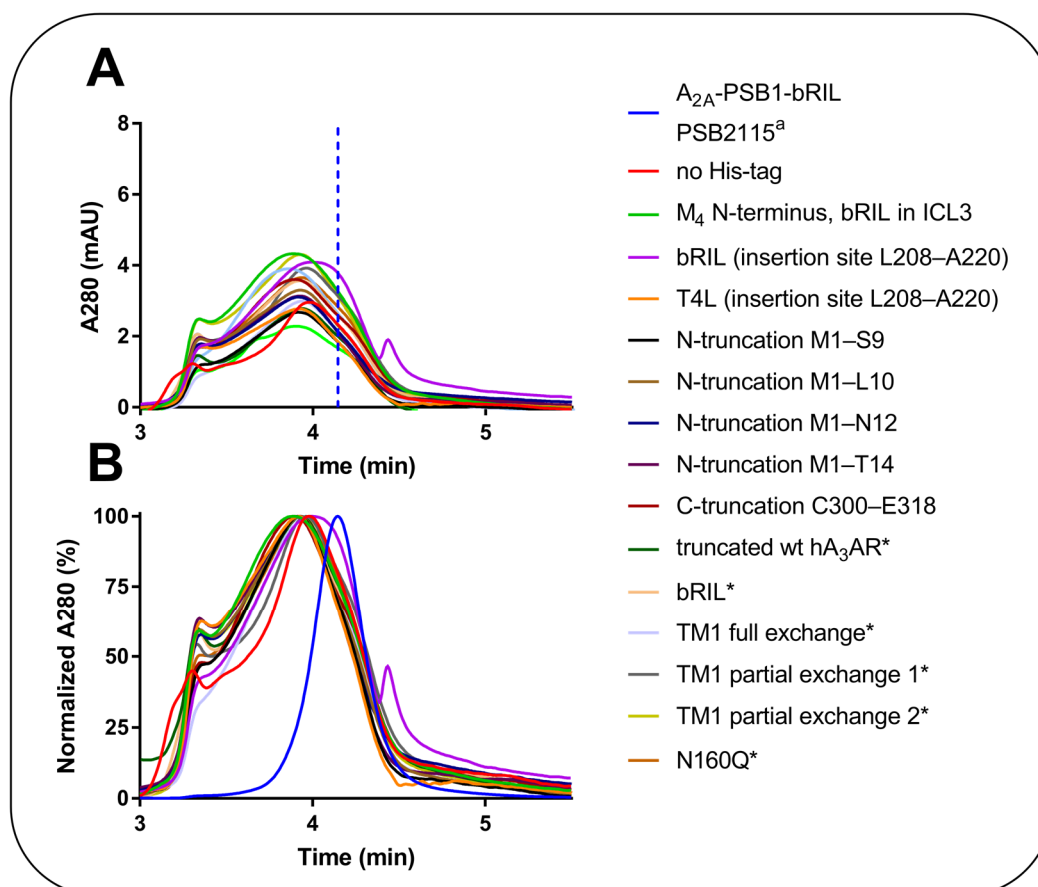


Figure 15. Results of further construct modifications.

A: Shortened SEC chromatogram (3–5.5 min). The dashed line represents the peak of the A_{2A} -PSB1-bRIL protein. B: Normalized SEC chromatogram (3–5.5 min). Unless stated otherwise, constructs are based on the truncated A_3 AR bearing bRIL in its ICL3 (N-truncation M1–L8, C-truncation L309–E318; insertion site L208^{5.69}–G219^{6.24}). TM1 full exchange: S9^{1.29} to N40^{1.60} replaced by A_{2A} AR residues P2^{1.28} to N34^{1.60}. TM1 partial exchange 1: S9^{1.29} to E19^{1.39} replaced by A_{2A} AR residues P2^{1.28} to E13^{1.39}. TM1 partial exchange 2: S9^{1.29} to Y15^{1.35} replaced by A_{2A} AR residues P2^{1.28} to Y9^{1.35}. All proteins were purified in the presence of TK-OT-018. *Constructs expressed under the control of the gp64 promoter. ^asee reference ²⁵⁷

3.4 Analysis of initial A_3 AR protein constructs

3.4.1 Thermostability of initial A_3 AR constructs

Due to inadequate protein amounts, the construct's thermostabilities could not be evaluated precisely. Nevertheless, these results provided useful information, as seen in Figure 16. A_{2A} -PSB1-bRIL and the elution buffer were included in all three figures as controls.²⁵⁷ The A_{2A} -PSB1-bRIL protein possessed a steep slope with a clear inflection point caused by the gradually unfolding receptor. In contrast, the elution buffer displayed the baseline without any protein present. The differences between the elution buffer and the investigated A_3 AR protein constructs proved that A_3 AR protein was present. However, the protein appeared unstable, and the overall protein amount was relatively small. Even

graphs of poorly expressed constructs showed a slight plateau and an initial inflection point in the range of 0–25 % normalized fluorescence (rectangle, Figure 16). However, inflection points were substantially less pronounced than that of the $A_{2B}AR$ control. The untruncated A_3AR with bRIL in its ICL3 (orange graph, Figure 16, B) showed a slightly better protein yield in the SEC (Figure 12). The corresponding thermostability assay revealed an elevated fluorescence signal correlating well with its SEC results. All other constructs behaved similarly with no significantly improved properties. Nonlinear regression curve fit to obtain the T_M values could not be reliably carried out because inflection points were not sufficiently pronounced. Efforts to exclude the upper part (normalized fluorescence >60 %) to correctly examine the protein's melting curve were unsuccessful. Nevertheless, visual evaluation implied that T_M s of A_3AR proteins harboring ICL3 fusion partner, N-terminal fusion partner, and further modifications were around 50°C. In the end, a precise assessment of thermostability will be enabled as soon as the A_3AR is successfully stabilized.

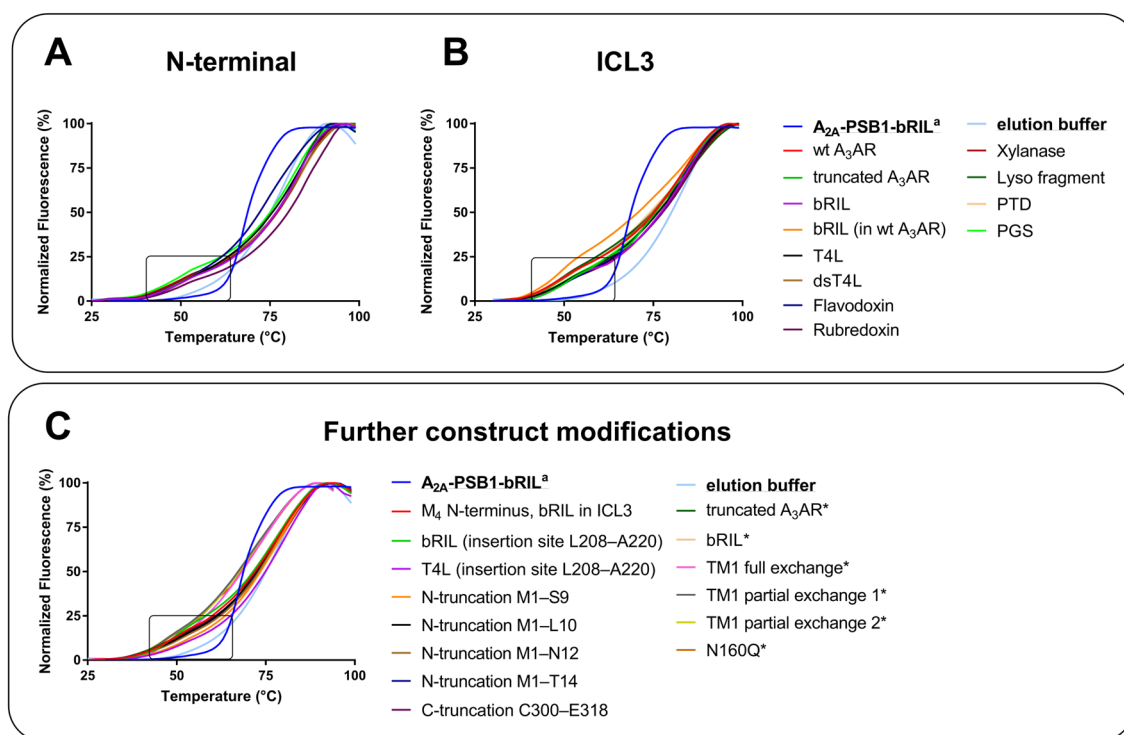


Figure 16. CPM thermostability assay results of initial A_3AR constructs.

A: N-terminal fusion partner. B: Fusion partner inserted into the ICL3. C: Further construct modifications. TM1 full exchange: S9^{1.29} to N40^{1.60} replaced by $A_{2A}AR$ residues P2^{1.28} to N34^{1.60}. TM1 partial exchange 1: S9^{1.29} to E19^{1.39} replaced by $A_{2A}AR$ residues P2^{1.28} to E13^{1.39}. TM1 partial exchange 2: S9^{1.29} to Y15^{1.35} replaced by $A_{2A}AR$ residues P2^{1.28} to Y9^{1.35}. *Constructs expressed under the control of a gp64 promoter. ^asee reference ²⁵⁷

3.4.2 Protein analysis of initial A₃AR protein constructs

All constructs were investigated by SDS-polyacrylamide gel electrophoresis (SDS-PAGE), whereas selected proteins were checked by western blotting. Coomassie-stained SDS-PAGE gels revealed faint bands of the corresponding protein constructs at around 40 kDa (Figure 17, red rectangle), agreeing well with the size of the A₃AR constructs (~36 kDa plus the size of the fusion partner). Protein constructs that contained rather large fusion partners could clearly be distinguished from those possessing smaller fusion partners (PTD, 105 amino acids, 11.85 kDa; PGS, 588 amino acids, 21.83 kDa). Although protein bands were detected for all constructs, the intensity was weak due to low protein quantities. Unfortunately, SDS-PAGE gels illustrated that purified protein solution contained many impurities besides the A₃AR protein. Overall, the samples shared a similar band pattern with several dominant bands at 20, 30, 50, and 90 kDa additionally to the A₃AR protein band. The small amount of receptor protein and the added imidazole concentration during purification were insufficient to prevent unspecific binding at the Co²⁺-resin beads. Therefore, it left space for the unspecific binding of various other proteins. The A_{2A}AR-bRIL-ΔC crystallization construct indicated that the purification method could remove interfering proteins as soon as the GPCR protein amount had been increased. Of course, it has to be kept in mind that the volume of the A_{2A}AR protein solution loaded into the gel was lower than that of the A₃AR samples. Moreover, a second band at around 80 kDa occurred for all investigated constructs and the A_{2A}AR control, which is commonly observed for GPCRs and might be caused by unspecific protein aggregation during sample preparation or receptor dimerization.^{153; 257; 270} Nevertheless, western blot analysis employing an anti-His antibody and SDS-PAGE proved the presence of the A₃AR protein, which is essential for further investigations. The purification process was further optimized by adding a short centrifugation step between the individual washing steps to remove residual impurities of the previous step improving the purification grade, as described in Section 3.7.

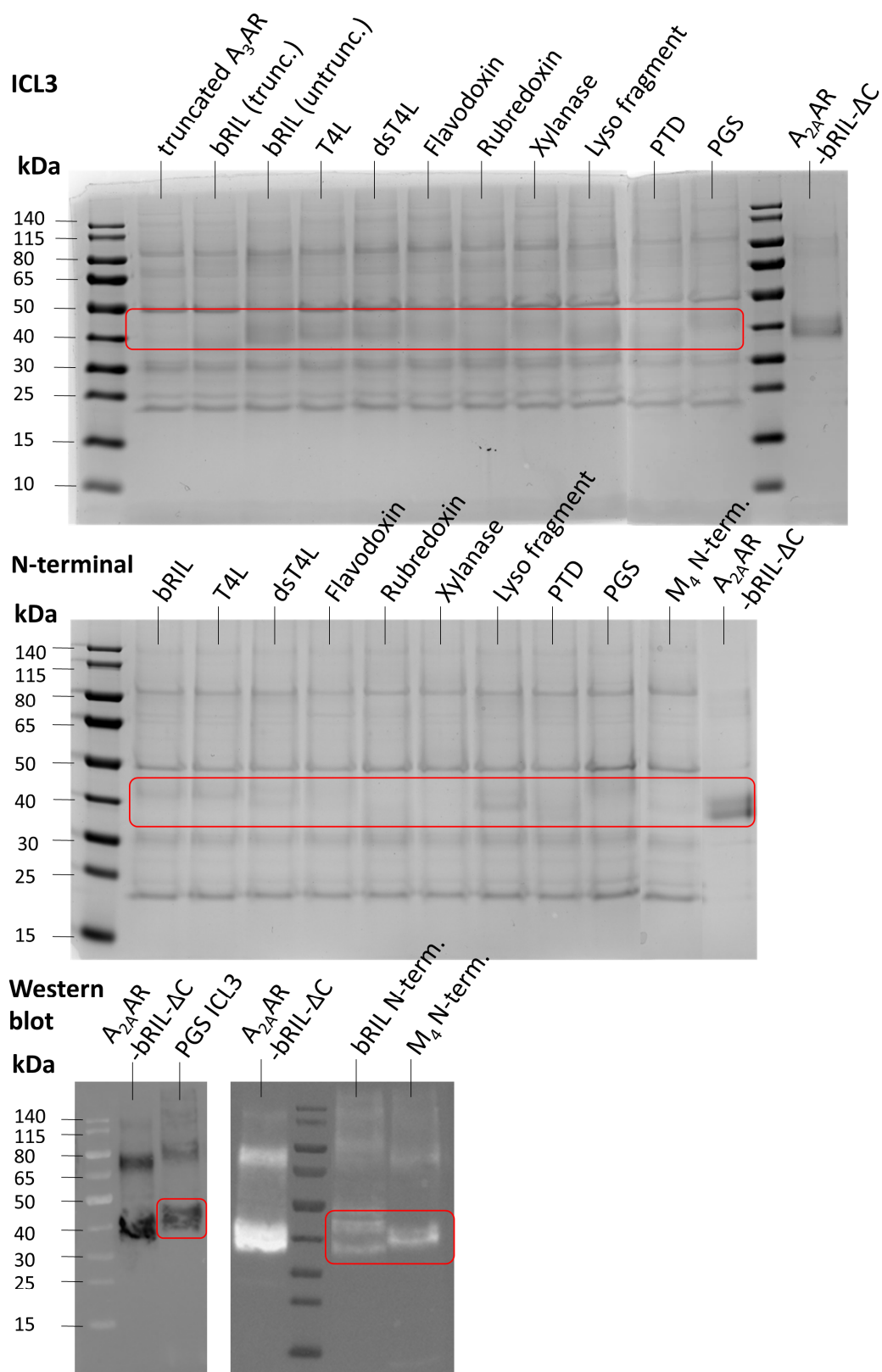


Figure 17. Coomassie-stained SDS-PAGE gels and western blots of initial A₃AR constructs.

Top: Fusion partner inserted into the ICL3. Middle: N-terminal fusion partner. Bottom: Western blot of selected constructs. Sample lanes were loaded with 22.5 μ L protein solution or 4 μ L of the A_{2A}AR-bRIL- Δ C crystallization construct as a positive control.³⁸ Bands which represent the A₃AR constructs are highlighted by red rectangles.

3.5 Introduction of the S97^{3.39}K mutation within the sodium binding pocket

The S97^{3.39}K mutation was introduced to evaluate its potentially stabilizing effect on the inactive receptor state by stabilizing the sodium binding pocket via a hydrogen bond and preventing its collapse during receptor activation. This mutation was introduced into the truncated A₃AR construct with bRIL replacing the ICL3. Recently, this mutation proved its highly beneficial effect on the A_{2A}AR, which allowed to solve previously inaccessible co-crystal structures employing just this mutation.²⁵⁷

Mutation of S97^{3.39} to lysine increased the peak height at 4.1 min, and consequently, the protein yield by approximately 3-fold (Figure 18 A). Now, the SEC chromatogram showed a clear and distinct peak, which was significantly more pronounced than the previously described shoulder of the wt A₃AR and the wt A₃AR plus bRIL (see Section 3.2.1). Thus, the small shoulder actually represented a minimal amount of the A₃AR protein (Figure 12). Moreover, the increased protein yield was also observed in the thermostability assay resulting in a higher fluorescence signal between 55–80°C (Figure 18 C). An exact determination of the T_M by non-linear regression remained challenging, but the inflection point of the green graph was shifted to higher temperatures. Subsequently, the technique “thermal SEC” was applied to investigate the thermostability differently. After a heat shock of 42°C for 5 min, the protein was again injected onto the SEC column. The normalized SEC chromatogram revealed that temperature-induced stress caused an elevation of the shoulder before the protein peak, resulting from protein aggregates of higher molecular weight (Figure 18 B). Nevertheless, the heat shock did not destroy all of the protein, and intact protein was still present since the protein peak at 4.1 min was still existent. These results demonstrated that A₃AR constructs benefitted hugely from the S97^{3.39}K mutation and that the increased stability correlated with an improved protein yield. Introducing a single point mutation into the highly conserved sodium binding pocket significantly improved protein stability and yield. In conclusion, stabilizing mutations in conserved motifs are transferable to other GPCRs as long as these motifs are present. Since the mA₃AR harbors an identical composed sodium binding pocket, the probability is high that mA₃AR constructs will also benefit from the S^{3.39}K mutation (see Section 3.15).

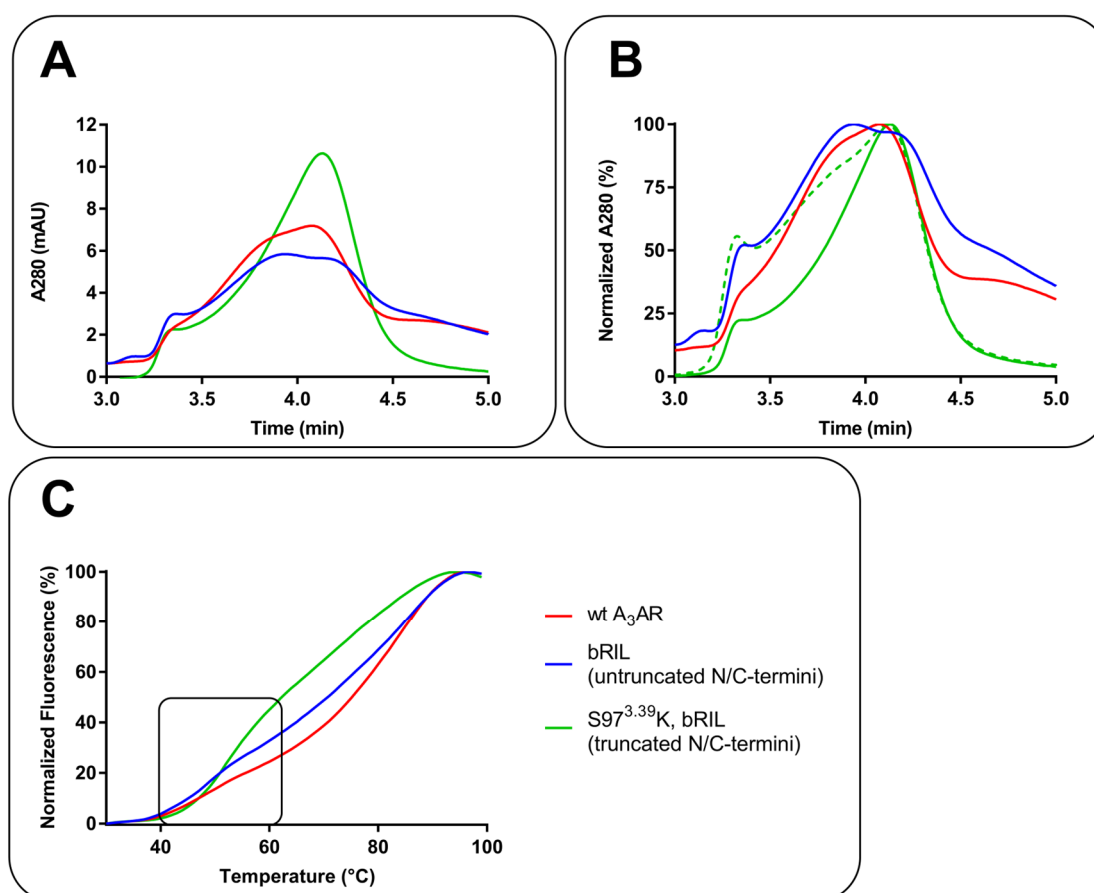


Figure 18. Results obtained by introducing the S97^{3,39}K mutation.

A: SEC chromatogram (3–5 min). B: Normalized SEC chromatogram (3–5 min). SEC after a heat shock of 42°C for 5 min is presented as dashed line. C: CPM thermostability assay results.

3.6 Construct optimization by junction site modifications

How fusion partners are inserted into the ICL3 of GPCRs plays a crucial role in the overall structural arrangement and stability. The goal is to adapt the junction site so that the fusion partner and the adjacent helices V and VI can form their native structures without getting compressed or stretched. An extension of the junction sites of bRIL and T4L was not favorable (see Section 3.3). Therefore, a comprehensive study on junction site modifications was required. In the A₁AR crystallization construct, the junction site was adapted to the one of A_{2A}AR crystallization constructs by replacing residues 220–228 for those of the A_{2A}AR.²¹⁴ TM6 of ARs are quite diverse up to position 6.29; after that, they display high similarity (Figure 19, bottom panel). Interestingly, the A₁- and A₃ARs are similar at the beginning of TM6 with an acidic and two aromatic residues in positions 6.22, 6.26, and 6.27, respectively. To transfer this approach to the A₃AR, the amino acids that directly follow bRIL were exchanged piece by piece to the corresponding A₁AR's and

A_{2A}AR's residues. This approach resulted in three changes in the junction site (Figure 19): a) insertion of 7 A_{2A}AR amino acids (E219^{6.21}–Q226^{6.28}), “A_{2A} partial”, b) insertion of 7 A_{2A}AR (E219^{6.21}–Q226^{6.28}) and 5 A₁AR amino acids (K228^{6.29}–I232^{6.33}), “A_{2A}/A₁ hybrid”, and c) insertion of A_{2A}AR amino acids (E219^{6.21}–A231^{6.33}) up to position 6.34 from which A₃AR and A_{2A}AR sequences continue identically, “A_{2A} full”. Moreover, 22 amino acids of the human M₄ mAChR were inserted N-terminally into each of these three constructs in analogy to the A₁AR crystallization construct.

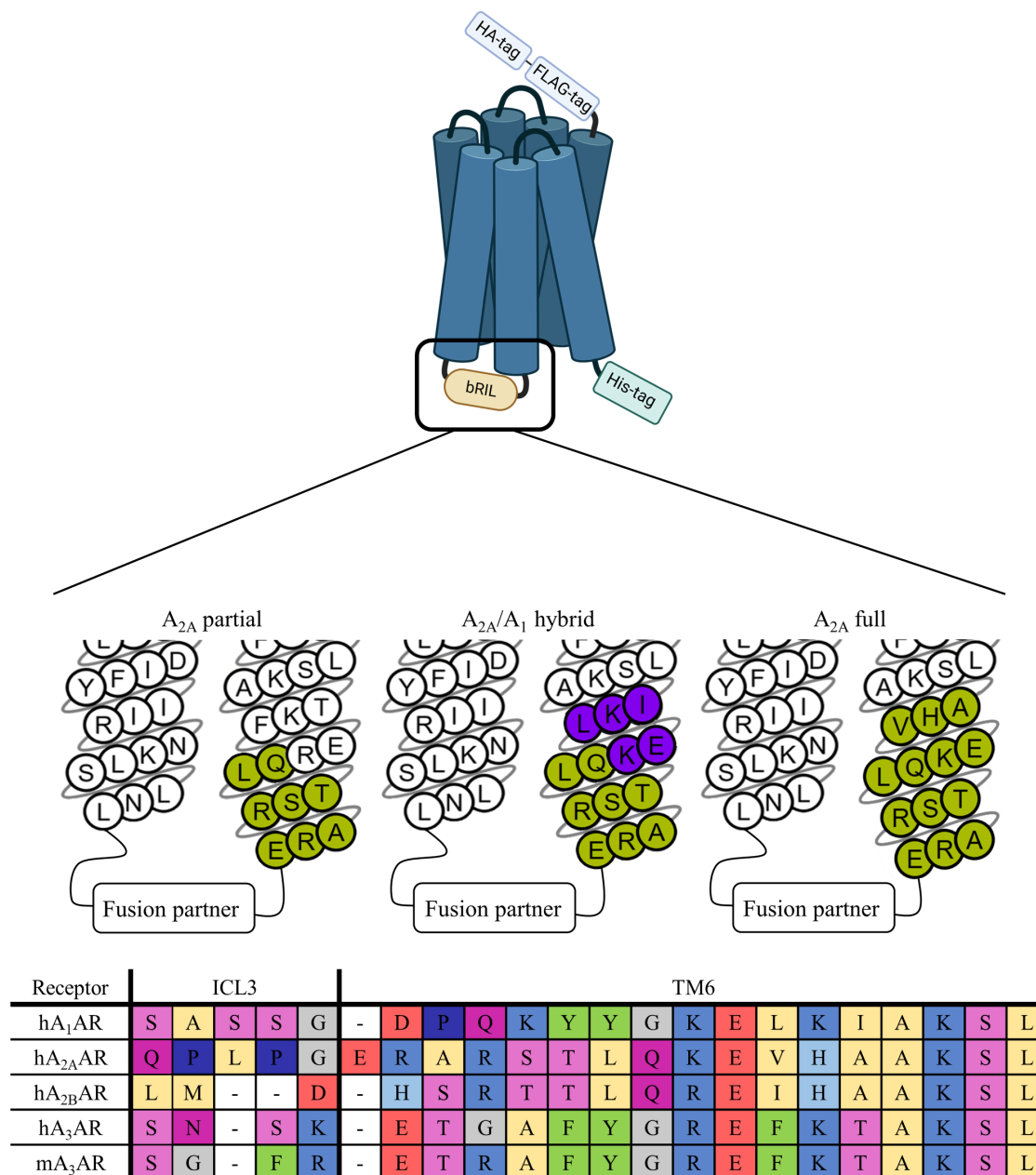


Figure 19. Junction site modifications.

Top: Schematic illustration of a GPCR construct carrying bRIL in its ICL3, created with BioRender.com. Middle panel: Detailed view of junction sites of A₃AR constructs. Snake plot was generated by gpcrdb.org.²⁷¹ Amino acids that are right behind the fusion partner were exchanged for the corresponding A_{2A}AR (yellow-green) and A₁AR (purple) amino acids. Bottom panel: ICL3 and TM6 sequence alignment with all members of the AR family including the mA₃AR.

Figure 20 shows the SEC profile of constructs with junction site modifications: A_{2A} partial junction site, A_{2A}/A₁ hybrid junction site, and A_{2A} full junction site with and without N-terminal insertion of the M₄ mAChR N-terminus. The A_{2A} partial and the A_{2A}/A₁ hybrid junction sites improved the overall protein yield, whereas the A_{2A} full junction site was less beneficial. When comparing constructs with and without the M₄ mAChR N-terminus, it was striking that these 22 amino acids bearing three N-glycosylation sites were able to increase the peak height at 4.1 min by at least 2-fold for every construct, even for the A_{2A} full junction site, which did not perform well without the M₄ mAChR N-terminus. Consequently, the A_{2A} full junction site provided some stability since the M₄ mAChR N-terminus alone seemed insufficient as long as there was no fundamental stability (see Section 3.3). The best overall protein yield was obtained by combining the M₄ mAChR N-terminus and the A_{2A} partial junction site, reaching a peak height of over 20 mAU. Interestingly, the retention time of the A_{2A}/A₁ hybrid junction site + M₄ mAChR N-terminus (purple graph, Figure 20 C) was slightly lower than the retention time of the corresponding peak without the M₄ mAChR N-terminus (green graph, Figure 20 C). It is well known that the presence of N-glycans can influence the migration of proteins in SEC and SDS-PAGE.²⁷² Consequently, this difference was probably caused by the increased molecular weight and the larger hydrodynamic volume due to the M₄ mAChR N-terminus with its three N-glycosylation sites.

Figure 20 D provides the SDS-PAGE gels of the corresponding constructs. The constructs with M₄ mAChR N-terminus migrated slightly less far on the gel compared to constructs without this alteration, which was in agreement with the observation of lower retention times. The M₄ mAChR N-terminus with the following tobacco etch virus protease cleavage site weighs 3.06 kDa. Additionally, each N-glycan consists of three mannose molecules, two *N*-acetylglucosamine (GlcNAc), and one or two fucose molecules, which amount to 1.1 or 1.2 kDa for each N-glycosylation site.²⁷³ In total, the 22 amino acids of the M₄ mAChR N-terminus, the subsequent protease cleavage site, and approximately 1 kDa per glycosylated N-glycosylation site sum up to ~9 kDa. Of course, it is unknown how many potential asparagine residues are actually glycosylated and whether glycosylation occurs completely and homogeneously. Nevertheless, long chains of N-glycans influence the geometric shape and affect migration through the porous SEC column. An exact molecular weight determination is difficult since poor SDS-glycan interactions may impact migration.²⁷² Nevertheless, the difference of approximately 10 kDa could be explained by the molecular weight of the 29 amino acids and the attached

oligosaccharides. Moreover, the band intensities correlated well with the corresponding peak height at 4.1 min, proving that the peak height displays an appropriate parameter for the overall protein yield. After a heat shock of 42°C for 5 min, SEC was carried out to investigate the thermostability. The heat shock caused protein aggregation and hence increased the shoulder right before the GPCR peak. The M₄ mAChR N-terminus seemed not to drastically influence the thermostability since the shoulder elevation occurred in a similar ratio between constructs with and without M₄ mAChR N-terminus.

It is important to note that constructs with these junction site modifications possess a TM6 of 41 amino acids compared to the junction site L208^{5,69}–G219^{6,24} and to the wt A₃AR, whose TM6 consists of 38 and 40 amino acids, respectively. Therefore, an elongation of TM6 maintaining the correct folding of bRIL could be a conceivable reason for their enhanced performance. All in all, the A_{2A} partial and the A_{2A}/A₁ hybrid junction site modifications in combination with the M₄ mAChR N-terminus tremendously enhanced the protein yield, exceeding 20 mAU for the first time.

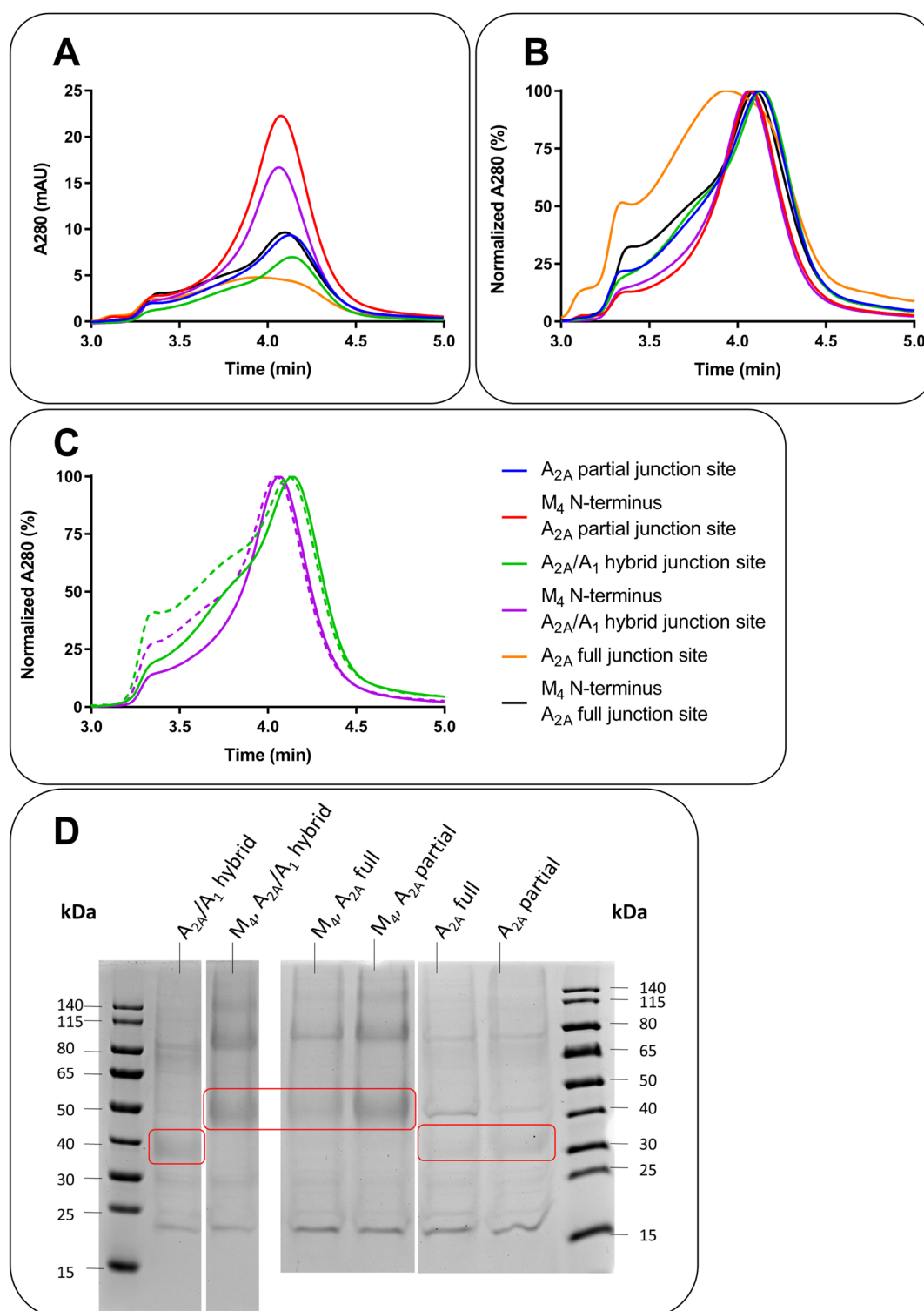


Figure 20. Junction site modifications I.

A: SEC chromatogram (3–5 min). B: Normalized SEC chromatogram (3–5 min). C: Normalized SEC chromatogram (3–5 min) of A_{2A}/A_1 hybrid junction site constructs before (solid line) and after (dashed line) a heat shock of 42°C for 5 min. D: Coomassie stained SDS-PAGE gel. Equal volumes of purified protein solutions were loaded onto the gel. Bands that represent the A_3AR construct are highlighted by a red rectangle.

3.7 Combination of the S97^{3.39}K mutation and junction site modifications

The next step was to combine successful approaches of junction site modifications with the S97^{3.39}K mutation and investigate their potentially synergistic effects. The A_{2A} partial and the A_{2A}/A₁ hybrid junction site, as well as the M₄ mAChR N-terminus, were combined with the S97^{3.39}K mutation. The A_{2A} full junction site was not considered due to its inferior performance.

In both cases, the introduction of the S97^{3.39}K mutation enhanced the peak height at 4.1 min, but to a greater extent for the A_{2A}/A₁ hybrid junction site (Figure 21). Interestingly, the A_{2A} partial junction site + S97^{3.39}K was no longer superior to the corresponding A_{2A}/A₁ hybrid junction site construct, contrary to the results reported in Section 3.6. In combination with S97^{3.39}K, both junction site modifications showed similar SEC profiles with almost identical peak heights at 4.1 min, even exceeding 30 mAU. However, after a heat shock of 50°C for 5 min (Figure 21 B, dashed red and blue graphs), normalized SEC revealed differences in their thermostability. The hybrid junction site combined with S97^{3.39}K was slightly more stable as assessed by the smaller plateau right before the protein peak, representing aggregated or unfolded protein after the heat shock. A comparison of the partial junction site with and without S97^{3.39}K (Figure 21 B purple and red dashed graphs) nicely visualized the thermostabilizing effect of the S97^{3.39}K mutation. The protein without S97^{3.39}K was almost entirely destroyed by the temperature-induced stress, whereas most of the protein harboring S97^{3.39}K was still intact. After the heat shock, the extent of aggregated protein reached over 80 %, in contrast to less than 20 % aggregated protein of the receptor stabilized by restraining it in the inactive state.

The beneficial effect of the M₄ mAChR N-terminus, which was already implied in Section 3.6, was supported by a construct possessing the A_{2A}/A₁ hybrid junction site and S97^{3.39}K but no M₄ mAChR N-terminus (Figure 21 orange graph). This construct displayed approximately half the peak height compared to the corresponding construct carrying the M₄ mAChR N-terminus. Moreover, the orange chromatogram was again minimally shifted to higher retention times. This phenomenon has already been observed previously and was caused by the lower molecular weight.

The TM6 of constructs with these kinds of junction site modifications consists of 41 amino acids, and thus their superior performance might be imitated by the shortened A₃AR insertion site L208^{5.69}–K216^{ICL3} (Figure 21 D). This insertion site did not introduce any further amino acid exchanges but possessed 41 amino acids after the C-terminus of the

fusion partner up to the beginning of ECL3. In a second construct, amino acids between L208^{5.69}–E217^{6.22} were replaced by bRIL. Additionally, T218^{6.23} was exchanged by arginine and alanine (RA) in order to obtain 41 amino acids and align the first three amino acids following bRIL to the ones of the A_{2A}AR (Figure 21 D).

Both approaches resulted in a clear peak at 4.1 min, which indicated that a substantial amount of the A₃AR constructs was present (black and brown graphs, Figure 21). The A₃AR junction site L208^{5.69}–K216^{ICL3} exhibited a slightly higher peak and superior stability than the junction site L208^{5.69}–E217^{6.22} + RA. Moreover, their peak height was even comparable to that obtained with the hybrid junction site. Incubation at 50°C for 5 min caused complete destruction, similar, but still less than that of the construct with the partial junction site without S97^{3.39}K (purple graph). Therefore, the overall performance of these two A₃ junction sites was akin to the junction site modifications but with a significantly reduced number of amino acid exchanges. The junction site L208^{5.69}–K216^{ICL3} completely removed any non-native residues at the beginning of helix VI.

Protein size and purity were again assessed by SDS-PAGE analysis (Figure 21 C). All investigated constructs showed an adequate purity degree and a similar band pattern, with one band at approximately 40 kDa and a second band at 80 kDa, agreeing well with previous results and commonly observed band patterns of purified GPCRs.^{153; 257; 270} The purity grade could be significantly improved by higher protein amounts and an additional centrifugation step to remove residual washing buffers and impurities (Figure 17; Figure 20). Only the construct harboring the A₃ junction site L208^{5.69}–E217^{6.22} + RA exhibited a strangely broadened band which could not be reasonably explained.

In conclusion, a necessary but not the only contributing factor to increased protein yields was the prolonged TM6 in constructs with the A_{2A} partial and the A_{2A}/A₁ hybrid junction sites. The combination of the junction site L208^{5.69}–K216^{ICL3} and the S97^{3.39}K mutation will provide further progress and might even reach similar properties as the hybrid junction site. These results must be kept in mind because they constitute an appropriate starting point to reduce the artificiality of the final crystallization construct.

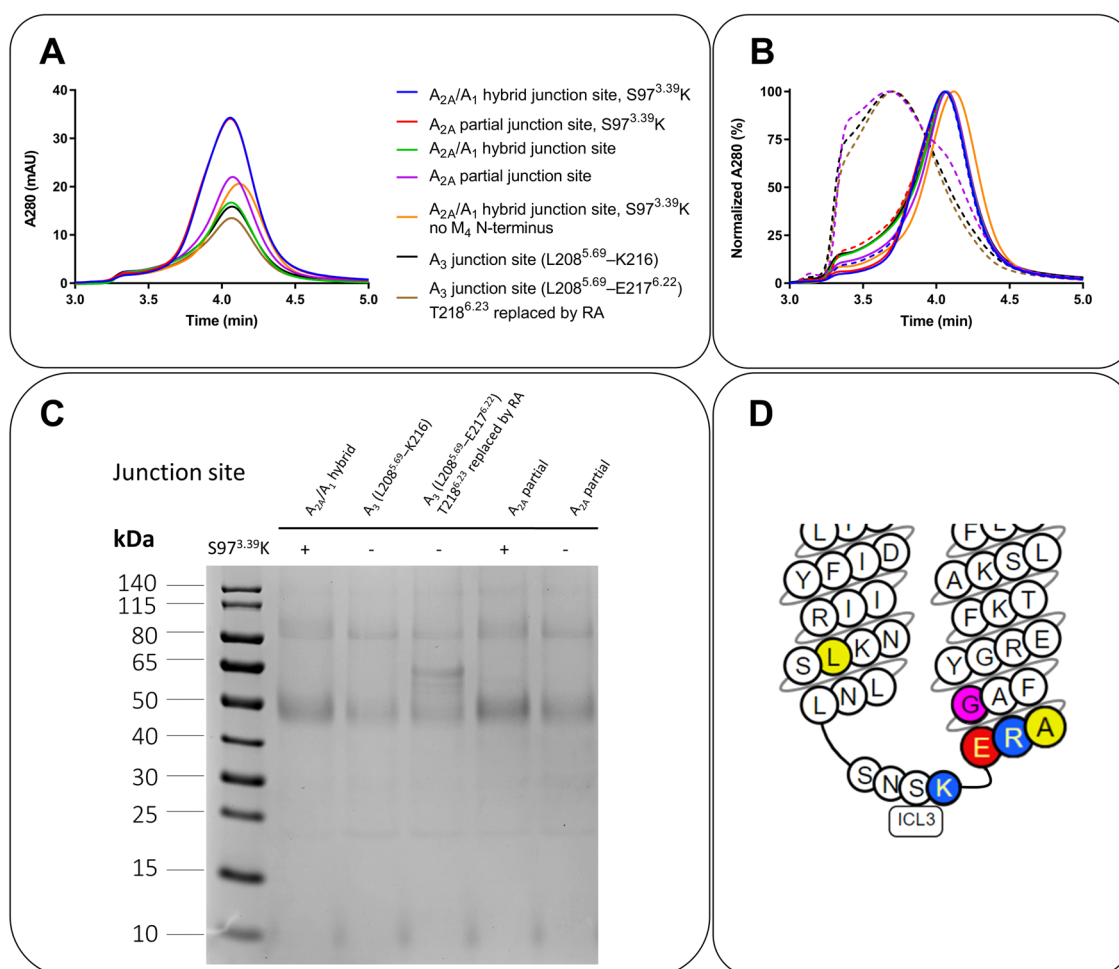


Figure 21. Combination of S97^{3.39}K and junction site modifications.

A: SEC chromatogram (3–5 min) B: Normalized SEC chromatogram (3–5 min). SEC after a heat shock of 50°C, 5 min is presented as dashed line. C: SDS-PAGE gel of selected constructs. All constructs possess an N-terminal M₄ mAChR N-terminus if not stated otherwise in the legend. D: Schematic illustration of A₃ junction sites. L208^{5.69} & A220^{6.25} (yellow), K216^{ICL3} (blue) and G219^{6.24} (pink). E (red) and R (blue) are corresponding amino acids of the A_{2A}AR (E219^{6.21} and R220^{6.22}). Snake plot was taken from gpcrdb.org and subsequently modified.²⁷¹

3.7.1 Insights into the effects of junction site modifications

In order to reduce the artificiality of the junction site modifications (Figure 19), constructs were designed to understand their beneficial effect. Constructs with the A_{2A}/A₁ hybrid junction site possessed the A_{2A}AR sequence ERARSTLQ followed by the A₁AR sequence KELKI at the beginning of TM6. Subsequently, their TM6 consisted of 41 amino acids compared to the wt A₃AR, whose TM6 was formed by only 40 amino acids. Two constructs with A₃ junction sites that imitated this prolonged TM6 revealed promising results (see Section 3.7 and Figure 21). Next, constructs were designed to elucidate the effect of the A₁AR sequence KELKI (alignment in Figure 19), which was partially changed back to KEFKT (JS69, corresponding hA₃AR sequence REFKT) and

KELHI (JS70, corresponding A_{2A}AR sequence KEVHA). KEFKT aimed to return to a sequence similar to that of the wt A₃AR since the A₃AR possesses the aromatic amino acid phenylalanine and the hydrophilic threonine in positions three and five of this sequence in contrast to non-aromatic, aliphatic amino acids in A₁-, A_{2A}-, and A_{2B}ARs. KELHI investigated the effect of histidine in the second last position of the partial sequence, which is present in the A_{2A}- and A_{2B}ARs (Figure 19). Additionally, the two constructs that carry an A₃ junction site were combined with the S97^{3.39}K mutation and the A₁AR amino acid sequence KELKI, separately or collectively (JS71–76, see Table 5).

Table 5. Overview of constructs to investigate junction site modifications.

All constructs display the truncated hA₃AR with bRIL in its ICL3 and an N-terminal M4 mAChR N-terminus.

No.	Junction site	S97 ^{3.39} K	A ₁ AR sequence KELKI
JS71	L208 ^{5.69} –K216 ^{ICL3}	✗	✓
JS72	L208 ^{5.69} –E217 ^{6.22} T218 ^{6.23} replaced by RA	✗	✓
JS73	L208 ^{5.69} –K216 ^{ICL3}	✓	✗
JS74	L208 ^{5.69} –E217 ^{6.22} T218 ^{6.23} replaced by RA	✓	✗
JS75	L208 ^{5.69} –K216 ^{ICL3}	✓	✓
JS76	L208 ^{5.69} –E217 ^{6.22} T218 ^{6.23} replaced by RA	✓	✓

Results of approaches to further understand the consequences of the junction site modifications are depicted in Figure 22. First, results proved once again that S97^{3.39}K was crucial for the thermostability and protein yield, which had already been observed (see Section 3.7). All constructs carrying S97^{3.39}K resulted in significantly higher amounts of protein than those without S97^{3.39}K (green and purple graphs). Moreover, the thermostability correlated well with the protein yield. T_M values and thermal SEC (heat shock of 55°C for 5 min; Figure 22 B, C) revealed that the two constructs without S97^{3.39}K were by far the two most unstable ones (T_M of 55.0° and 59.1°C) and thus exhibited the lowest yields. Therefore, thermostability and protein yield were probably and meaningfully causally linked. The more stable the protein construct was, the more robust it was against destruction caused by stress during expression, solubilization, and purification. The

construct that possessed the A_{2A} partial junction site (ERARSTLQ) followed by the A_{2A}-like KELHI and S97^{3.39}K displayed the most stable protein of this series (T_M 72.1°C). The A₃-like sequence KEFKT was slightly less stable since the shoulder in the thermal SEC profile and its T_M were slightly higher or lower, respectively. As a result, the aromatic phenylalanine in position three and a polar threonine in position five were inferior to non-polar, aliphatic residues like leucine (A₁AR), valine (A_{2A}AR), and isoleucine (A_{2B}AR) in position three as well as isoleucine (A₁AR), and alanine (A_{2A}AR, A_{2B}AR) in position five. The kind of basic amino acid in position 4 (KELHI) had less impact on the stability since the exchange to histidine affected the performance less than the A₃AR-like changes.

Insertion of the A₁AR sequence KELKI slightly increased the protein stability when combined with S97^{3.39}K compared to the S97^{3.39}K mutation alone (JS73 vs. JS75, JS74 vs. JS76). The determined T_M values of these four constructs were all in a similar range of 64.1–65.8°C, but thermal SEC disclosed differences. Comparing the orange (JS73) and brown (JS75) as well as the black (JS74) and dark blue (JS76) graphs, constructs with KELKI possessed a less elevated shoulder before the protein peak, indicating superior stability. Another important finding was that the A₃ insertion sites combined with the A₁AR sequence KELKI and S97^{3.39}K could not wholly mimic the stabilizing effect of the A_{2A}AR sequence. Therefore, the elongation of TM6 was not the only decisive factor, and the quite unlike residues between 6.22–6.28 profited from the A_{2A}AR residues. Nevertheless, the A₃ insertion site L208^{5.69}–K216^{ICL3}, which does not harbor any amino acid exchanges at the beginning of TM6, in combination with S97^{3.39}K, resulted in a remarkably stable protein (T_M 64.1°C).

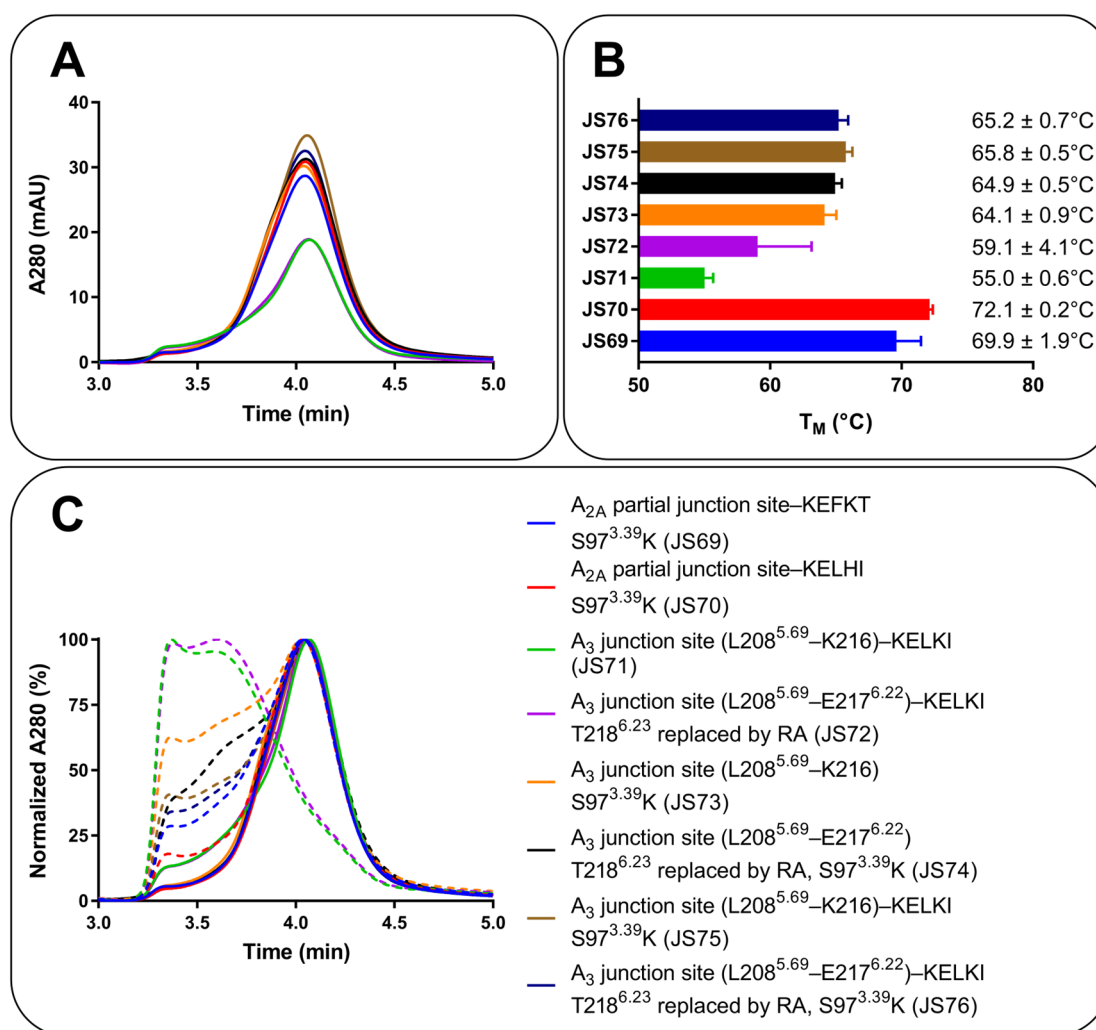


Figure 22. Insights into the effects of junction site modifications.

A: SEC chromatogram (3–5 min). B: T_M values of investigated proteins obtained by the CPM thermostability assay. Data represent mean ± SEM from 2–4 different experiments. C: Normalized SEC chromatogram (3–5 min). SEC after a heat shock (55°C, 5 min) is presented as dashed lines. All constructs possess the M₄ mAChR N-terminus (see Table 5).

3.8 The role of N-terminal N-glycosylation sites

Results proved that the presence of the 22 amino acids from the M₄ mAChR N-terminus containing three potential N-glycosylation sites increased the overall protein yield by 2-fold without significantly changing the thermostability (see Section 3.6). This approach had already been utilized for the structural elucidation of the A₁AR.²¹⁴ The choice to particularly insert the M₄ mAChR N-terminus might be based on the presence of N-glycosylation sites due to their involvement in receptor trafficking and folding.²⁷⁴ Interestingly, the hA₃AR (and also the mA₃AR) is the only member of the AR family that possesses the motif N-X-S/T in its N-terminus (X any amino acid except proline, for sequence alignment, see Figure 23 A), which may indicate that N-glycosylation plays a

specific role for the A₃AR. The relevance of N-glycans could thus explain the positive effect of the M₄ mAChR N-terminus insertion. If native N-terminal N-glycosylation sites are required for this effect, the A₁AR would not have benefited from the M₄ mAChR N-terminus since it does not natively possess N-terminal glycosylation sites. The result would then be based on a more general mechanism and would not be caused by any A₃AR-specific properties. Moreover, the exact sequence of the M₄ mAChR N-terminus might not be decisive for its effect and might even be replaceable by the only 7-residues-long native A₃AR N-terminus (without methionine). Therefore, untruncated constructs that still carry the A₃AR N-terminus were combined with junction site modifications and the S97^{3.39}K mutation to comprehensively investigate the role of N-terminal N-glycosylation sites in the receptor expression.

The A_{2A} partial junction site alone and the A_{2A}/A₁ hybrid junction site together with S97^{3.39}K were investigated in combination with the M₄ mAChR N-terminus but without the A₃AR N-terminus and without M₄ mAChR N-terminus but with the A₃AR N-terminus instead. Figure 23 B presents the SEC results of this construct series. Constructs with the A₃AR N-terminus (blue, green) lead to higher peaks in the chromatogram than the corresponding constructs with the M₄ mAChR N-terminus (red, purple). Moreover, the peaks of untruncated constructs were slightly shifted towards higher retention times since the 7-amino acid-long hA₃AR N-terminus contains just two N-glycosylation sites. On the contrary, the M₄ mAChR N-terminus and the subsequent protease cleavage site comprise 29 amino acids and three glycosylation sites, resulting in a larger hydrodynamic volume. Less bulky proteins migrate further into the porous SEC column and are consequently eluted later. In addition, the combination of the hybrid junction site plus S97^{3.39}K revealed an improved shoulder (blue vs. green graph) before the protein peak indicating superior stability and homogeneity.

In conclusion, the M₄ mAChR N-terminus was not superior to the native A₃AR N-terminus. Presumably, N-glycosylation sites are generally required without the need for any specific sequence.

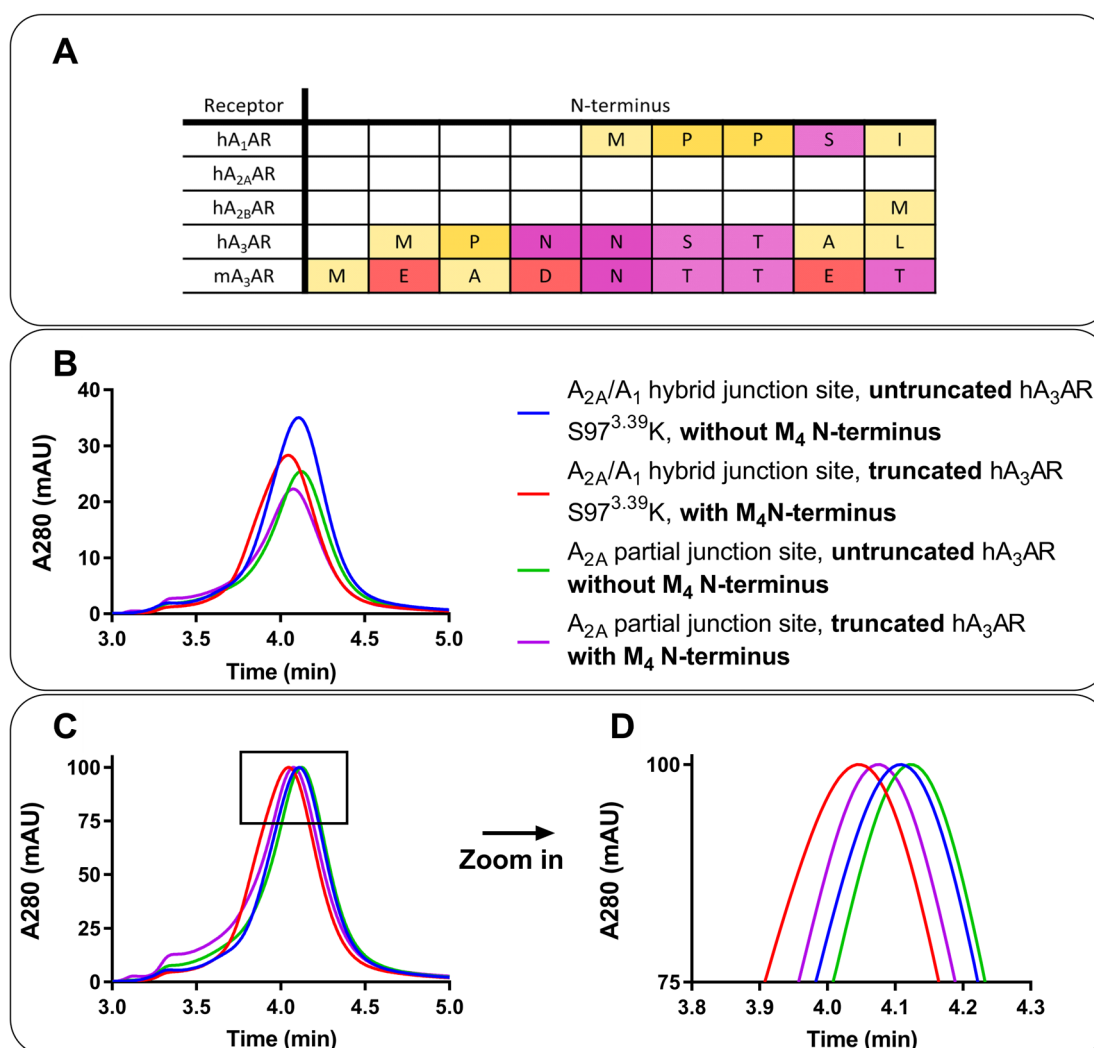


Figure 23. The role of N-terminal N-glycosylation sites.

A: Sequence alignment of N-termini of all human ARs including the mA₃AR. B: SEC chromatogram (3–5 min). C: Normalized SEC chromatogram (3–5 min). D: Enlarged, normalized SEC chromatogram (x: 3.8–4.3 min; y: 75–100 %).

3.8.1 Enzymatic deglycosylation of N-terminal N-glycans

First evidence indicated that N-glycans might be beneficial for obtaining increased protein yields (see Section 3.6). Therefore, the actual glycosylation state of the construct JS53 (M₄ mAChR N-terminus, S97^{3.39}K, A_{2A}/A₁ hybrid junction site) was elucidated. Different glycosylation states can result in multiple receptor bands or band broadening, which can be consolidated upon deglycosylation by enzymatic digestion.¹⁵³ The purified protein was treated with the mannosyl-glycoprotein endo-β-N-acetylglucosaminidase (Endo H), which hydrolyses the glycosidic bond between two GlcNAc molecules within high-mannose glycopeptides. Consequently, the N-glycan is cleaved, and one GlcNAc molecule remains linked to the asparagine of N-glycosylation sites.

In a second experiment, the corresponding construct harboring the A₃AR N-terminus (JS68) was, on the one hand, expressed in the presence of tunicamycin and, on the other hand, treated with N-glycosidase F (PNGase F). This approach allowed to examine the glycosylation state from two different directions. Tunicamycin blocks the first step of the attachment of N-glycans by inhibiting the UDP-*N*-acetylglucosamine—undecaprenyl-phosphate *N*-acetylglucosaminophosphotransferase, which is involved in the initial *N*-acetylglucosamination of glycoproteins.²⁷⁵ PNGase F, on the other hand, cleaves the glycosidic bond between the innermost GlcNAc molecule and the asparagine residue of glycoproteins.²⁷⁶ Consequently, tunicamycin completely prevents the synthesis of glycoproteins in general, while PNGase F only attacks the final protein after expression and purification.

3.8.2 Glycosylation of JS53

JS53 was expressed, purified, and subsequently treated with Endo H. The SEC chromatogram and the SDS-PAGE gels are presented in Figure 24. After Endo H treatment, a second faint band occurred below the main band (red arrow). Additionally, a new band at just below 30 kDa appeared, which could unequivocally be allocated to the added Endo H, whose molecular weight is 29 kDa. After Endo H treatment, the second band right below the main band of JS53 indicated that N-glycans were successfully cleaved off and caused altered migration in the SDS-PAGE gel. Nevertheless, the main band was still predominant, implying that the digestion was not complete and only a small fraction was deglycosylated. Prolongation of the incubation time might have improved completeness and thus increased the intensity of the second band. The corresponding construct JS68 containing the untruncated hA₃AR with the native A₃AR N-terminus instead of the M₄ mAChR N-terminus showed the protein band at a slightly lower molecular weight. The longer M₄ mAChR N-terminus possessed a 2.3 kDa higher molecular weight than the shorter A₃AR N-terminus. With an additional N-glycosylation site, JS53's molecular weight was increased by around 3 kDa, which explained the different migration distances well. A second construct with the M₄ mAChR N-terminus (JS74, see Table 5) supported this observation by showing a band at a similar height as JS53. JS68's protein band appeared as a double band rather than a fuzzy and blurry single band upon closer inspection. This double band characteristic indicated that glycosylation occurred heterogeneously, meaning that the second band below represents either mono-glycosylated or not

glycosylated protein. During this investigation, it must be noted that JS53 and JS68 still possessed the conserved N-glycosylation site N160^{ECL2} in their ECL3, which might also carry attached N-glycans. In the SEC chromatogram of JS53 after Endo H treatment, a second sharp peak was eluted at 5.1 min, correlating well with the SDS-PAGE band at 29 kDa of the Endo H. Moreover, the peak of JS53 was minimally right-shifted, which could be due to the presence of a deglycosylated receptor species. However, since the majority remained glycosylated, this shift occurred only partially. Altogether, Endo H sensitivity proved that JS53 was indeed glycosylated, even if the actual state of each N-glycosylation site remained unclear.

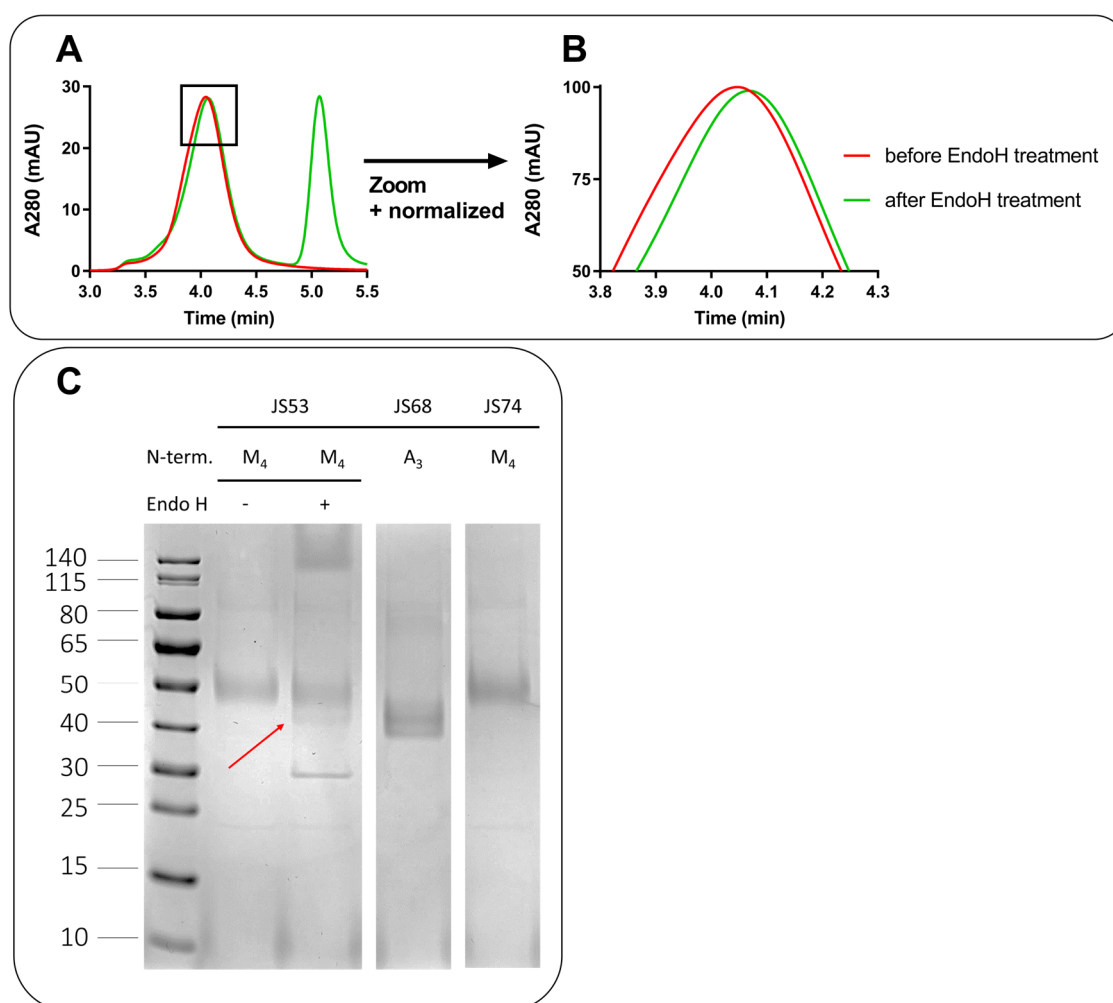


Figure 24. Enzymatic deglycosylation of JS53.

A: SEC chromatogram of JS53 (M₄ mAChR N-terminus, S97^{3.39}K, A_{2A}/A₁ hybrid junction site) before and after EndoH treatment (30 min, 37°C). B: Normalized and enlarged SEC chromatogram (x: 3.8–4.3 min; y: 50–100 %). C: SDS-PAGE gel. JS68 (untruncated termini, S97^{3.39}K, A_{2A}/A₁ hybrid junction site) and JS74 (M₄ mAChR N-terminus, S97^{3.39}K, bRIL, also see Table 5) were added as controls.

3.8.3 Glycosylation state of JS68

JS68 was expressed with and without tunicamycin present in the growth medium. Subsequently, proteins were simultaneously purified and analyzed according to the standard procedure. Purified proteins were then divided up into two batches. One batch was not further processed, while the other was treated with PNGase F, resulting in four protein batches that were then analyzed by SDS-PAGE. The untreated batch was handled the same way as the treated batch, but without PNGase F. Both expressions yielded a decent protein amount up to 20–30 mAU (Figure 25 A). However, the protein yield with tunicamycin was approximately one-third less. Tunicamycin is known to induce stress in the endoplasmic reticulum, which potentially caused the decreased protein yield.²⁷⁷ Subsequent SDS-PAGE elucidated the glycosylation state of JS68. Proteins were pure and migrated similarly up to the 40 kDa marker band. SEC and SDS-PAGE indicated that tunicamycin did not drastically alter the GPCR because the apparent molecular weight and the SEC retention times were similar. Nevertheless, the protein with tunicamycin was resistant to PNGase F digestion since its band remained unchanged. The band of JS68 without tunicamycin appeared blurry and broad before deglycosylation. After PNGase F treatment, the band was sharper and more compressed, identical to the tunicamycin protein band. Lanes of proteins treated with PNGase F showed an additional band between 30–40 kDa for the PNGase F, whose molecular weight is approximately 36 kDa.²⁷⁶ Both protein lanes without tunicamycin occurred slightly more intensely, probably caused by the higher protein amount since equal volumes of the protein solution were loaded onto the gel.

In conclusion, tunicamycin successfully blocked the attachment of N-glycans and led to JS68, free of any N-glycans. The inhibition of N-glycosylation did not cause a complete loss of expression, indicating that N-glycans are not absolutely necessary for the biosynthesis of the A₃AR. On the other hand, this observation proved that JS68 was, in fact, natively glycosylated but heterogeneously and not wholly. It remained elusive which of the four potential N-glycosylation sites (N3, N4, N12, N160^{ECL2}) carried glycans. Additionally, this experiment validated the applied PNGase F digestion and confirmed that cleavage was successful and even complete, which will be helpful for further studies.

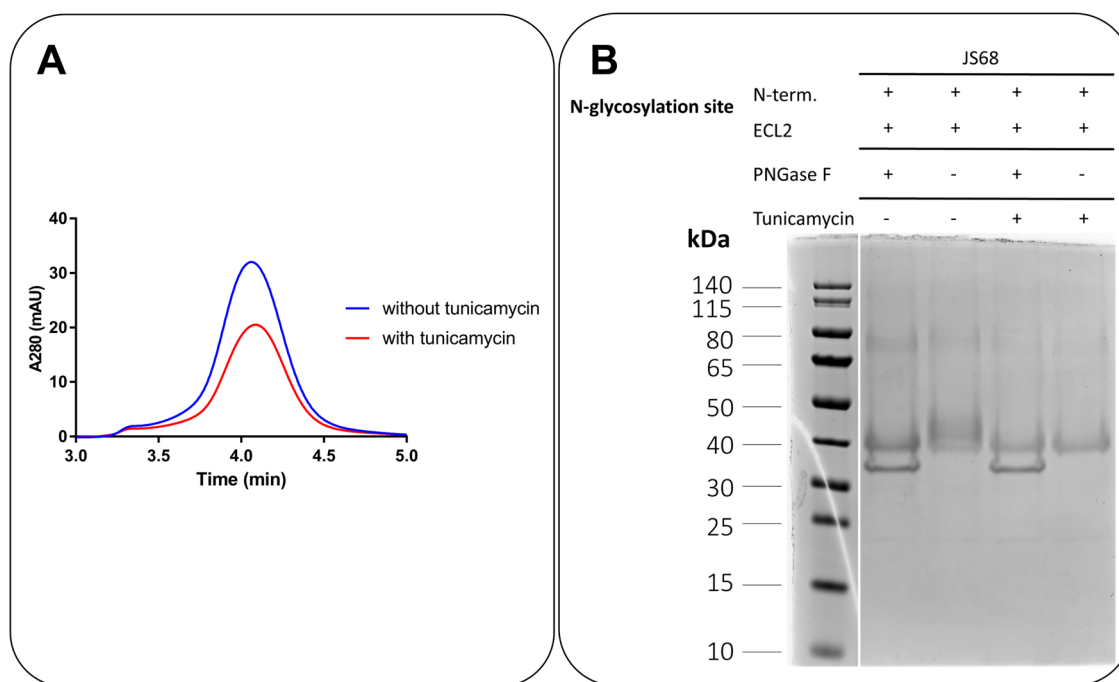


Figure 25. Glycosylation state of JS68.

A: SEC chromatogram (3–5 min) of JS68 (untruncated termini, S97^{3,39}K, A_{2A}/A₁ hybrid junction site) with and without tunicamycin present during expression (1 μg/mL). B: SDS-PAGE gel after overnight digestion with PNGase F. N-terminal N-glycosylation sites: N3, N4, N12. ECL2 glycosylation site: N160^{ECL2}.

3.9 Optimization of the N-terminal construct sequence

The development of an optimized A₃AR crystallization construct led to the finding that an untruncated N-terminus improved the protein yield, similar to the insertion of 22 amino acids of the M₄ mAChR N-terminus. The A₃AR possesses two N-terminal glycosylation sites (sequence “NNST”), which is unique within the AR family (Figure 23 A). Therefore, N-terminal glycosylation sites seemed crucial for the improved protein yield, potentially by increasing the expression. Glycosylation may occur incompletely and inconsistently and thus cause microheterogeneity of the glycoprotein. Moreover, the presence of N-glycans further enhances the flexibility, which may impede proper crystal formation together with the heterogeneity of N-glycans.⁴⁴ To avoid these unnecessary obstacles, N-glycosylation sites are often removed and mutated to alanine or glutamine by site-directed mutagenesis.⁴⁴ The A₃AR contains four asparagine residues that fulfill the rule N-X-S/T (X≠P) and potentially get glycosylated. Three of the four, N3, N4, and N12 are located at the N-terminus and beginning of TM1 and will be called N-terminal glycosylation sites. The fourth one, N160^{ECL2}, can be found in the ECL2. Each asparagine was mutated to the closely related glutamine to prevent any attachment of glycosides.

Three constructs were generated to examine the performance of proteins without N-glycans at the N-terminus, ECL2, or all sites: JS94 without N-terminal glycosylation sites (N3Q, N4Q, N12Q), JS95 without the ECL2 N-glycosylation site (N160^{ECL2}Q) and JS97 without any N-glycans (N3Q, N4Q, N12Q, N160^{ECL2}Q). All constructs were based upon JS68, which combined untruncated termini, bRIL inserted into the A_{2A}/A₁ hybrid junction site, and S97^{3.39K}.

Figure 26 A shows that N-glycosylation sites did not alter the protein yield. Constructs with and without N-glycosylation sites exhibited virtually identical protein yields as determined by their protein peak height. Moreover, surface expression of corresponding constructs revealed no apparent decrease in the absence of N-glycans (Figure 26 D). All tested constructs possessed a high surface expression of >80 %. T_M values were determined to be above >70°C and in the range of ±1°C to JS68's T_M for all constructs implying that N-glycans did not affect protein thermostability (Figure 26 B).

Subsequently, PNGase F digestion and SDS-PAGE analysis with purified proteins were utilized to assess their degree of glycosylation. If a protein possesses N-glycans, the protein band will shift to a lower apparent mass on an SDS-PAGE gel (also see Section 3.8). On the other hand, if the protein does not possess any N-glycans, the band will occur unaltered. Figure 26 C proves that the digestion affected constructs with either intact N-terminus (JS94) or intact ECL2 glycosylation sites (JS95) and thus harbored N-glycans. In contrast, the protein without any glycosylation sites (JS97) was resistant to PNGase F digestion and displayed one sharp band. Prior to digestion, the protein bands of JS94 and JS95 seemed blurrier and even appeared as a double band (JS95). PNGase F digestion removed the upper band and led to a sharper band at the same height as the unglycosylated JS97. Before digestion, the double band indicated that glycosylation was heterogeneous, and the protein was also present without N-glycans. Moreover, each lane corresponding to digested samples showed an additional band between 30–40 kDa for the PNGase F, whose molecular weight is approximately 36 kDa.²⁷⁶

In parallel, the beneficial effect of untruncated constructs was approached from a different perspective. Since the effect was neither dependent on the type of the inserted N-terminus nor the actual presence of N-glycans, it might just be caused by a linker before the GPCR. In order to further pursue this idea, the sequence “NNST” of the A₃AR N-terminus was inserted between the HA- and FLAG-tag, initially still possessing N-glycosylation sites (JS96, purple graph, Figure 26 A). JS96 possessed no N-terminal glycosylation sites (N3Q, N4Q, N12Q) but carried N160^{ECL2} in its ECL2. Insertion of the

amino acid sequence NNST between the HA- and FLAG-tag noticeably increased the overall protein yield compared to the other constructs of this series (Figure 26 A). On the other hand, thermostability and surface expression were in the same range (Figure 26 B, D).

SDS-PAGE analysis revealed that the band of JS96 did not show the characteristic double band, in contrast to JS95. PNGase F digestion shifted JS96's band to the height of corresponding proteins without N-glycans. Moreover, the unglycosylated species seemed absent before digestion since there was no apparent stain at the height of the corresponding deglycosylated proteins. This absence suggested that glycosylation occurred homogeneously and completely compared to JS94 and JS95. The inserted glycosylation sites could be more accessible for glycosylation enzymes because they were located further away from the transmembrane regions.

In general, the employed PNGase F digestion was complete as all proteins revealed bands at the height of JS97 after digestion without any faint band above, representing the glycosylated receptor. The sequence NNST further increased the protein yield indicating that the performance of untruncated constructs was based on the presence of a linker. Since N-glycans are not crucial, NNST might be replaceable by any sequence, e.g., QQST or the common GSGS linker. Moreover, other GPCR constructs could potentially benefit from inserting a linker as the underlying mechanism seems more general and not A₃AR-specific.

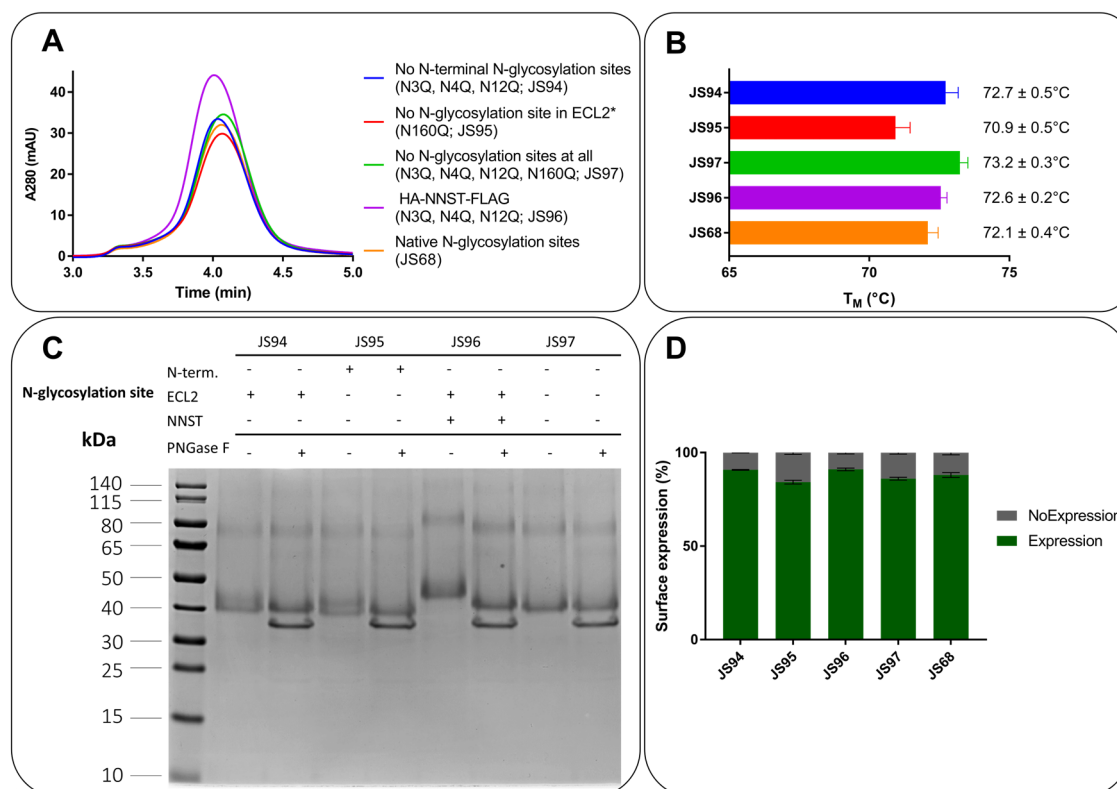


Figure 26. Optimization of the N-terminal construct sequence.

A: SEC chromatogram (3–5 min). *Construct does not possess amino acids L309–E318. B: Determined T_M values. Data represent mean ± SEM from three experiments. Statistical evaluation was carried by one-way ANOVA. No statistically significant difference could be determined (compared to JS68). C: SDS-PAGE gel of protein samples. D: Surface expression determined by flow cytometry. Data represent mean ± SD. Experiment was repeated twice independently with the same cells. JS68 (untruncated termini, bRIL in A_{2A}/A₁ hybrid junction site, S97^{3.39}K) was added as a control.

3.9.1 Transfer and improvement of the NNST sequence

The sequence HA-NNST-FLAG was transferred to an A_{2A}AR (JS98) and a mA₃AR (JS100) construct to investigate whether this approach is transferable to other GPCR constructs. JS98 was derived from the A_{2A}-PSB1-bRIL construct, which displays the A_{2A}AR truncated after A317 and bearing bRIL in its ICL3 in combination with S97^{3.39}K.²⁵⁷ JS100 was based on the truncated mA₃AR (M1–T9; L310–E319) with bRIL in its ICL3 (L209^{5.69}–A221^{6.25}) and S98^{3.39}K.

In both cases, insertion of the four amino acids NNST between the HA- and FLAG-tag considerably increased the overall protein yield (Figure 27 A). The improvement of the A_{2A}AR construct was remarkable since its performance had already been outstanding. The protein quantity of the mA₃AR construct was enhanced but still lacked stability and homogeneity compared to the symmetrical A_{2A}AR peak. The T_M of A_{2A}-PSB1-bRIL and JS98 were within 1°C and were consequently considered virtually identical, proving that NNST did not affect the protein's thermostability (Figure 27 D). The

idea of the NNST insertion was indeed transferable to other GPCR constructs and hence might act as a universal approach to increase the protein yield.

Since the presence of N-glycans was not required, the NNST sequence was changed to the corresponding QQST and the common GSGS linker. QQST and GSGS no longer fulfill the rule for N glycosylation. Hence, digestion before crystallization will not be necessary, saving time and avoiding unnecessary protein loss. All three possibilities were assessed using JS97 (untruncated A₃AR; N3Q, N4Q, N12Q, N160^{ECL2}Q; S97^{3.39}K; bRIL in ICL3, A_{2A}/A₁ hybrid junction site).

Constructs with the sequences NNST, QQST, or GSGS all resulted in similar peak heights of just below 60 mAU and exceeded that of the unmodified prime example A_{2A}-PSB1-bRIL (Figure 27 B). Consequently, the protein yield could be further enhanced even though all constructs already possessed the favorable untruncated A₃AR N-terminus. The protein peak of the glycosylated NNST protein was slightly shifted to lower retention times due to the large glycan chains at its N-terminus. Again, T_M values did not differ significantly and were within 1.5°C (Figure 27 D). PNGase F digestion proved that the construct carrying NNST was completely glycosylated, whereas the corresponding construct with QQST was unaffected by enzymatic deglycosylation (Figure 27 C).

As a result, NNST led to glycosylation, but N-linked glycans were not required for an increased protein yield. It did not depend on the sequence type or N-glycans since even the common GSGS linker resulted in the same effect. Of course, one needs to consider that these kinds of insertions lead to an elongation of the flexible N-terminus, which might be unfavorable for later crystallization. Nevertheless, using the GSGS linker removes the flexible A₃AR N-terminus and still achieves a sufficient amount of protein without any N-glycans attached.

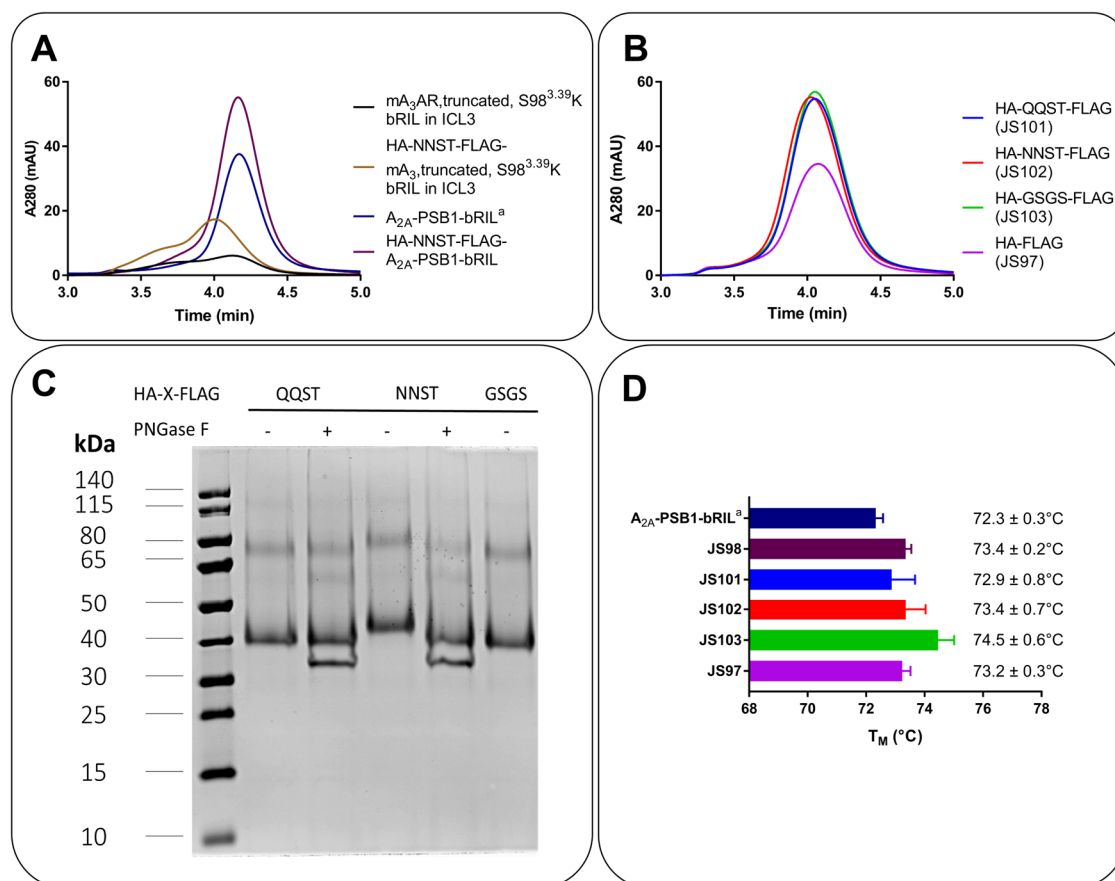


Figure 27. Transfer and improvement of the NNST sequence.

A: SEC chromatogram (3–5 min). B: SEC chromatogram (3–5 min) of constructs with various linkers between the HA- and FLAG-tag (X=QQST, NNST, GSGS) in comparison to their template JS97. C: SDS-PAGE gel after overnight PNGase F digestion. D: Bar chart of determined T_M values. Data represent mean \pm SEM from three experiments. Statistical evaluation was carried by one-way ANOVA. No statistically significant difference could be determined compared to their templates A_{2A} -PSB1-bRIL and JS97. ^asee reference²⁵⁷

3.10 The helix VIII exchange

Jain et al. (2020) increased the expression of functional hA₃AR in yeast by replacing the A₃AR C-terminus with the A_{2A}AR C-terminus.²⁷⁸ They created a chimeric receptor protein consisting of the N-terminus and transmembrane regions of the A₃AR (residues 1–284) fused to the helix VIII and the C-terminus of the A_{2A}AR (291–412).²⁷⁸ The A_{2A}AR crystallization constructs A_{2A} -stabilized receptor 2-bRIL (A_{2A} -StaR2-bRIL) and A_{2A} -PSB1-bRIL were truncated after residue 316 but were still well expressed and yielded sufficient protein amounts.^{257; 258; 279} Thus, helix VIII rather than the C-terminus might be critical for ensuring correct trafficking of the A_{2A}AR. Interestingly, the A_{2A}AR is the only member of the AR family that lacks a cysteine residue in position 8.64 of helix VIII, which is palmitoylated upon receptor synthesis. Moreover, the extra 96 amino acids would insert a highly flexible part which would be unfavorable for later crystallization. Consequently,

only helix VIII (K285^{7.56}-S308^{8.69}) of the A₃AR was exchanged for helix VIII (R291^{7.56}-A316) of the A_{2A}AR (JS83). Moreover, optimized constructs bearing favorable modifications (S97^{3.39}K, A_{2A}/A₁ hybrid junction site) in combination with the M₄ mAChR- (JS80) and the A₃AR N-terminus (JS81) were included in this investigation (Figure 28). In addition, the constructs A_{2A}-StaR2-bRIL and A_{2A}-PSB1-bRIL were added as reference constructs. In order to examine the effect of S97^{3.39}K and bRIL (standard insertion site L208^{5.69}-G219^{6.24}), corresponding constructs were also considered for this experiment series.

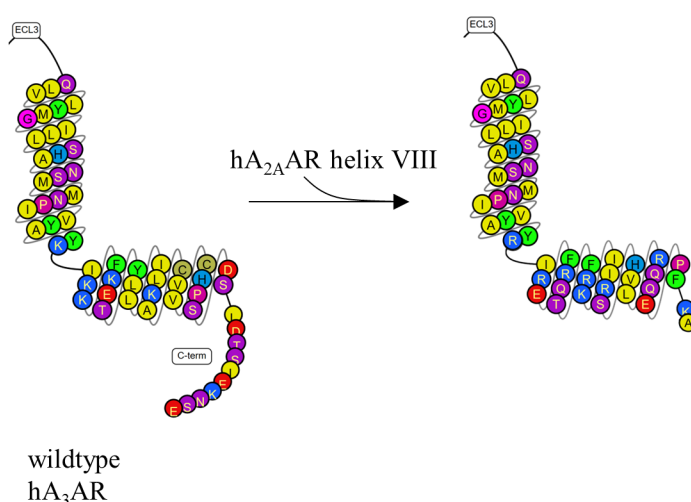


Figure 28. The helix VIII exchange.

Left: Snake plot of TM7, helix VIII and the C-terminus of the hA₃AR. Right: Snake plot of the hA₃AR whose TM7 is fused to helix VIII of the A_{2A}AR. Both images were created with online tools from gpcrdb.org and subsequently modified.²⁷¹

Expression and protein purification were analyzed with flow cytometry and SEC, respectively (Figure 29). The wt A₃AR showed low surface expression levels of below 25 %. Both, bRIL (standard insertion site L208^{5.69}-G219^{6.24}) and the S97^{3.39}K mutation, increased the receptor expression up to 40 % and just over 60 %, respectively. The effect of the single S97^{3.39}K mutation was remarkably high since it increased the expression by almost 4-fold compared to the wt receptor, proving its exceptional value. The two positive controls, A_{2A}-StaR2-bRIL and A_{2A}-PSB1-bRIL, revealed high expression levels of 75 % on average. The helix VIII exchange increased the surface expression as long as the surface expression of the parent construct was below 70 %. Inserted into the wt A₃AR, the A_{2A}AR-H8 enhanced the expression similarly to bRIL up to 34 %. The expression of JS53 (optimized + M₄ mAChR N-terminus) was slightly improved, whereas the expression of

JS68 (optimized + A₃AR N-terminus) was already slightly higher (~75 %) without the helix VII of the A_{2A}AR and could not be improved further. In general, maximal expression levels reached a plateau at around 75-80 % surface expression.

After the expression, A₃AR proteins were purified and analyzed by SEC (Figure 29 A and B). In both cases, the helix VIII exchange slightly increased the overall protein yield (red and purple graph). Constructs carrying the A₃AR N-terminus were superior and yielded higher peaks compared to the corresponding constructs with the M₄ mAChR N-terminus. However, the improved expression did not inevitably correlate with higher protein yields. The A₃-A_{2A} chimera without any stabilizing modifications revealed higher expression than the wt A₃AR, but purification led to almost no detectable protein (orange graph). Consequently, improving the expression levels can only be beneficial if the investigated construct already possesses inherent high stability. Investigation of expression levels can provide valuable additional information, but purification and subsequent protein analysis will always be decisive. Altogether, the helix VIII exchange was beneficial, but the extent of improvement may not outweigh the high degree of introduced changes.

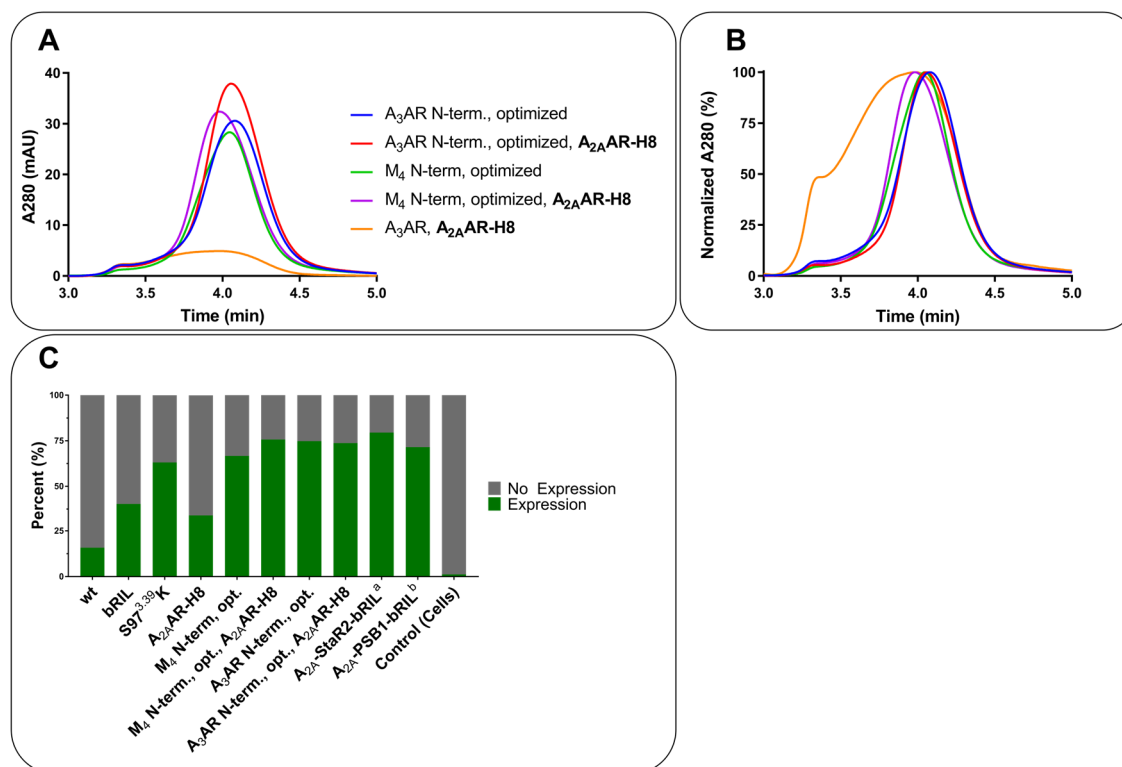


Figure 29. The helix VIII exchange — results.

A: SEC (3–5 min) chromatogram. B: Normalized SEC chromatogram (3–5 min). C: Surface expression levels. Expression was determined flow cytometry using an anti-FLAG antibody conjugated to fluorescein isothiocyanate (FITC). Optimized constructs carry the mutation S97³⁻³⁹K as well as bRIL in the A_{2A}/A₁ hybrid junction site.^asee references^{258; 279}, ^bsee reference²⁵⁷.

3.11 Investigation of point mutations

Introducing point mutations is often essential for a stable and homogeneous protein suitable for crystallization. Seven point mutations were selected based on the state-stabilizing mutation tool (inactive state, gpcrdb.org), the construct design tool (mutation scan, inactive state, gpcrdb.org mutations), and mutations of the A₁- and A_{2A}ARs crystal constructs.^{271; 280} Moreover, mutations should not interfere with conserved motifs, which are crucial for the overall architecture of the A₃AR. Applying these criteria, the mutations A69^{2.61}S, F48^{2.40}N, F233^{6.38}A, M99^{3.41}W, S242^{6.47}S, L101^{3.43}A/ I104^{3.46}A, and S271^{7.42}A were chosen. Moreover, point mutations that aim to interact with or stabilize the sodium binding pocket were excluded since S97^{3.39}K already locks this pocket in the inactive state. Listed point mutations were introduced into the template construct JS86. JS86 displayed the untruncated hA₃AR with bRIL in its ICL3 (A₃ insertion site L208^{5.69}–K216^{ICL3}) combined with S97^{3.39}K. Despite the superior stability of the A_{2A}/A₁ hybrid junction site, it was not used as a template to potentially enhance the thermostabilizing effect of investigated point mutations. Ideally, point mutations assist in arresting the receptor in the inactive state, which can, for example, be achieved by blocking conformational changes upon activation or improving the overall rigidity of receptor domains.

The following section briefly describes the literature describing the effects of changes in targeted positions. In TM2, two positions were chosen for point mutations. A69^{2.61} was mutated to serine (**A69^{2.61}S**). The corresponding alanine (A419) in the follicle-stimulating hormone receptor was found to abolish cAMP signaling when mutated to threonine, but did not generally interfere with ligand binding.²⁸¹ Moreover, this mutation occurs naturally and is involved in primary ovarian failure.²⁸¹ Mutation of N89^{2.61} of the neurokinin receptor-1 to alanine and serine caused loss of high-affinity binding for Substance P and reduced ligand efficacy (EC₅₀) in a phosphatidylinositol hydrolysis assays.²⁸² F48^{2.40}, whose corresponding amino acid had already been investigated for its effect on ligand binding in the C-X-C chemokine receptor 2, was exchanged for the residue of the A_{2A}- and A_{2B}ARs (**F48^{2.40}N**).²⁸³ Position 6.38 had already been utilized to introduce thermostabilizing mutations into the A_{2A}AR and is alanine in the A₁-, A_{2A}-, and A_{2B}ARs.²⁸⁴ Contrary, position 6.38 is occupied by the aromatic phenylalanine in the A₃AR. Interaction partners close to position 6.38 are highly conserved among ARs, indicating that exchanging it for a smaller hydrophobic amino acid, like alanine, might tweak A₃AR's stability

(**F233^{6.38}A**). Mutation in position 3.41 to tryptophan was found to increase the protein yield of functional β_2 receptor by potentially stabilizing the interface between helices III, IV, and V.^{36; 285} The presence of bulky hydrophobic residues was beneficial, and thus the corresponding smaller hydrophobic M99^{3.41} in the A₃AR was mutated to tryptophan (**M99^{3.41}W**). S242^{6.47} was mutated to the more common cysteine in this position (**S242^{6.47}S**). Position 6.47 is part of the conserved CWxP motif (see Section 1.4.2.4) and participates in the transduction of conformational changes originating from the orthosteric binding site.²³ The double mutant **L101^{3.43}A/I104^{3.46}A** might be able to interfere indirectly with the NPxxY motif in helix VII or play a role in constitutive active receptor mutants.^{149;}²⁸⁶ The polar residues threonine and serine at position 7.42 are involved in binding the ribose moiety of agonists at the bottom of the binding pocket. Thus they have already been mutated to alanine and utilized for stabilizing the A₁- and A_{2A}ARs in the StaR approach.^{158; 220; 242; 258} Consequently, **S271^{7.42}A** was also selected for stabilizing the A₃AR.

3.11.1 Introduction of point mutations

M99^{3.41}W and the double mutant L101^{3.43}A/I104^{3.46}A showed decreased overall protein yields (Figure 30 A). The double mutant L101^{3.43}A/I104^{3.46}A even noticeably impaired the protein yield, whereas M99^{3.41}W only slightly decreased the overall protein amount compared to the employed template JS86. All other mutations improved the overall peak height at 4.1 min. The two mutations F233^{6.38}A and S271^{7.42}A revealed the highest protein peak heights, while F48^{2.40}N, A69^{2.61}S, and S242^{6.47}C resulted in protein quantities of similar magnitude.

Besides the peak height, the peak shape provided valuable information about the homogeneity of the protein samples. Figure 30 C provides a detailed analysis of the normalized SEC chromatogram, which is enlarged in the area of the shoulder before the protein peak. The double mutant L101^{3.43}A/I104^{3.46}A showed the greatest extent of elevation relative to the protein peak. The mutations A69^{2.61}S, F233^{6.38}A, M99^{3.41}W, S242^{6.47}C, and S271^{7.42}A were able to reduce the shoulder compared to the template JS86 to a similar extent, which is favorable in terms of protein homogeneity. Figure 30 D compares the best mutations, F233^{6.38}A and S271^{7.42}A, with their respective template, JS86 and JS104. JS104 is a C-terminally truncated version of JS86 without N-glycosylation sites, the C-terminus, and the protease cleavage site and additionally carrying the A_{2A}/A₁ hybrid junction site. JS104 benefited from removing the flexible C-terminal region, improving

homogeneity and peak shape (see Section 3.16.6). Both mutations revealed a similar reduction of the shoulder as JS104. Interestingly, the sequence alignment of position 6.38 and its close environment (Figure 30 B) revealed that this area is conserved among ARs except for the A₃AR, which might explain the benefit of this mutation.

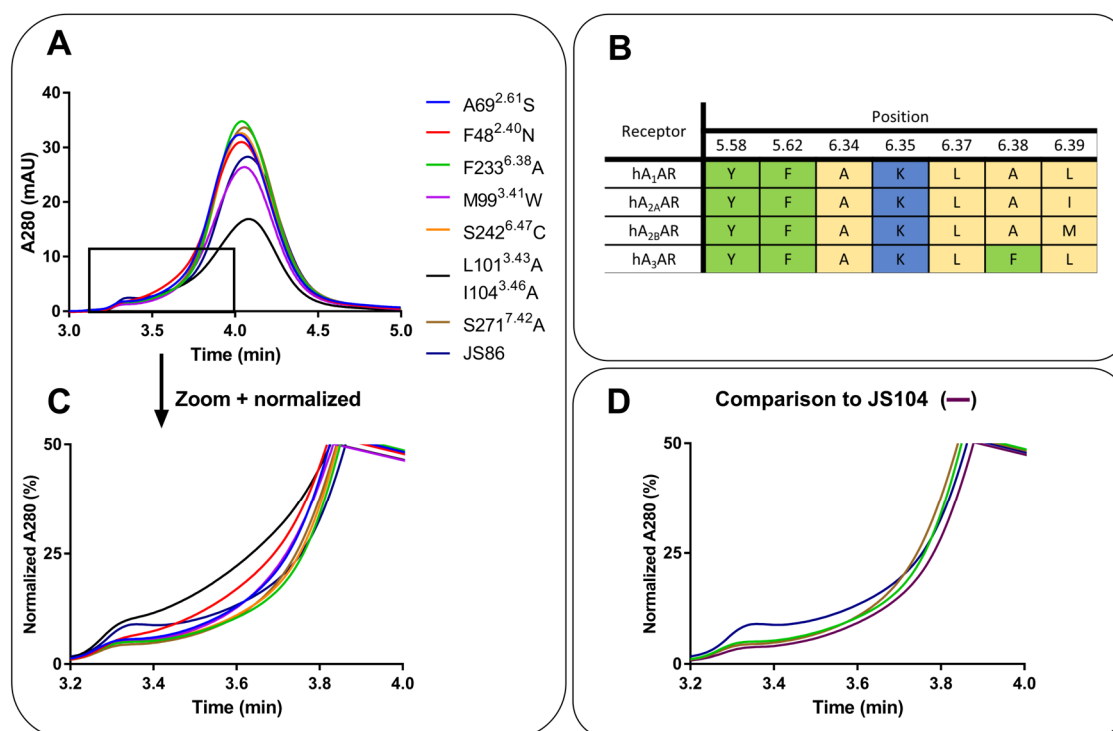


Figure 30. Investigation of point mutations I.

A: SEC chromatogram (3–5 min). B: Sequence alignment of residues in position 6.38 and their close environment (5 Å, based on the inactive state homology model of gpcrdb.org) of human ARs. C: Normalized SEC chromatogram (3.2–4.0 min). D: Normalized SEC chromatogram (3.2–4.0 min) of F233^{6.38}A, S271^{7.42}A in detailed comparison with their template JS86 and JS104.

Next, thermal SEC (heat shock 55°C, 5 min) and the CPM-based thermostability assay were utilized to determine the thermostabilizing effects of the seven investigated point mutations (Figure 31). The results of SEC, thermal SEC, and CPM assay were well in agreement with each other. High peaks in the SEC corresponded to high T_M values and reduced effects of the heat shock. The order of mutations ranked by the extent of the shoulder elevation after the heat shock was almost identical to the order of decreasing T_M values. Only A69^{2.61}S and F48^{2.40}N swapped positions. Therefore, thermal SEC and CPM assay results were suitable to complement each other, providing a comprehensive stability characterization. Moreover, a general rule can be derived from comparing the extent of protein aggregation (shoulder elevation) after the heat shock and the determined T_M values relative to the applied temperature. Proteins whose T_M was 5°C higher than the heat shock

temperature were almost entirely aggregated afterward (L101^{3.43}A/ I104^{3.46}A). A T_M of 10°C above the heat shock temperature caused approximately 50 % protein aggregation (M99^{3.41}W, A69^{2.61}S, F233^{6.38}A), and a T_M of 15°C above the heat shock temperature resulted in only one-tenth of protein aggregation (S271^{7.42}A). As a general rule, the heat shock temperature should be set around 10°C lower than the corresponding T_M to ensure that the stress test causes aggregation appropriately for further analysis. Otherwise, the thermal SEC will lose valuable information, if the temperature is too high or too low. In that case, no further differentiation can be examined between constructs that are either entirely destroyed or not altered by the applied heat shock.

The double mutant L101^{3.43}A/ I104^{3.46}A, whose protein peak was the lowest, also displayed the least stability reaching a T_M of 59.6°C, which was 10°C lower than the T_M of the S271^{7.42}A (69.2°C) mutant. Mutations A69^{2.61}S, F48^{2.40}N, F233^{6.38}A, and M99^{3.41}W possessed T_M values in a similar range around 65.0 ± 0.9 °C. S242^{6.47}C showed a T_M value of 66.8°C, the second-highest in this series of constructs. S271^{7.42}A revealed the highest T_M of 69.2°C and withstood the heat shock without extensive damage. F233^{6.38}A displayed the third-highest T_M of 65.9°C, slightly in contrast to its best overall protein yield determined by the SEC peak height. In conclusion, the two mutations, S242^{6.47}C and S271^{7.42}A, stood out from the group of tested mutants. Especially S271^{7.42}A significantly increased the thermal stability and showed a T_M of just below 70°C, making this mutation a suitable candidate for further consideration.

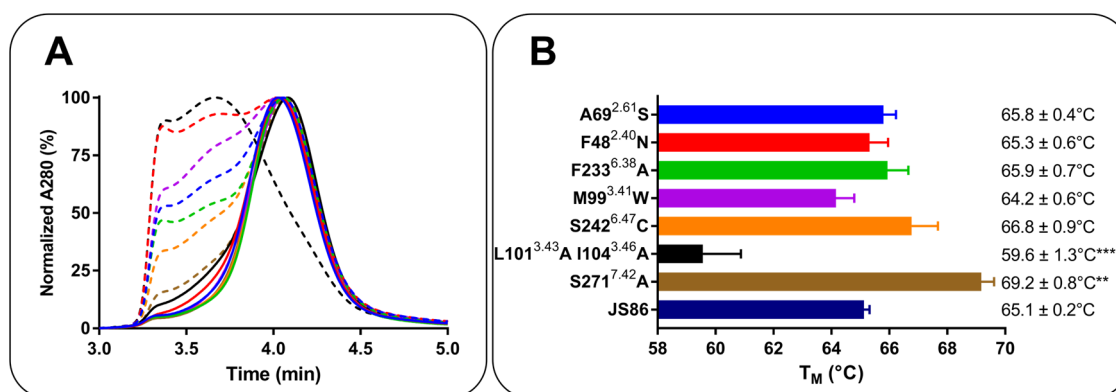


Figure 31. Investigation of point mutations II.

A: Normalized SEC chromatogram (3–5 min). Dashed lines represent SEC chromatograms after a heat shock of 55°C, 5 min. B: Bar chart of T_M values. Data represent mean \pm SEM from three experiments. Statistical evaluation was carried by one-way ANOVA with Dunnett's post hoc test (ns $p \geq 0.5$ ns; * $0.05 > p > 0.01$; ** $0.01 \geq p > 0.001$; *** $0.001 \geq p > 0.0001$; **** $p < 0.0001$).

3.11.2 Combination of point mutations

F233^{6.38}A, which yielded the highest protein yield, and S271^{7.42}A, whose T_M was the highest among the tested mutations, were combined with the so-far best construct JS104 (untruncated N-terminus, S97^{3.39}K, A_{2A}/A₁ hybrid junction site, C-terminal truncation, no N-glycosylation sites). Both mutations were introduced into JS104 separately and collectively. Figure 32 presents the construct series' SEC chromatograms, T_M values, and thermal SEC (heat shock 55°C, 5 min). The overall protein yield was similar for all constructs, except for S271^{7.42}A, which was lower. However, the insertion of the S271^{7.42}A mutation increased the T_M value of JS104 by 2.3°C. F233^{6.38}A even decreased the T_M value by 1.4°C resulting in 71.7°C. Consequently, the combination of F233^{6.38}A and S271^{7.42}A improved the stability, but to a smaller extent than S271^{7.42}A alone, which was probably due to the destabilizing effect of F233^{6.38}A. This observation was supported by thermal SEC, proving that F233^{6.38}A was inferior to S271^{7.42}A. Nevertheless, the combination with JS104's modifications achieved an increase of the T_M value by 5.7°C and 6.2°C for F233^{6.38}A (65.9°C vs. 71.7°C) and S271^{7.42}A (69.2°C vs. 75.4°C), respectively. This effect was most likely caused by the advantageous A_{2A}/A₁ hybrid junction site rather than the C-terminal truncation or the removal of N-glycosylation sites. For the first time, the T_M of an A₃AR construct exceeded 75°C, resulting in a prime candidate for further application.

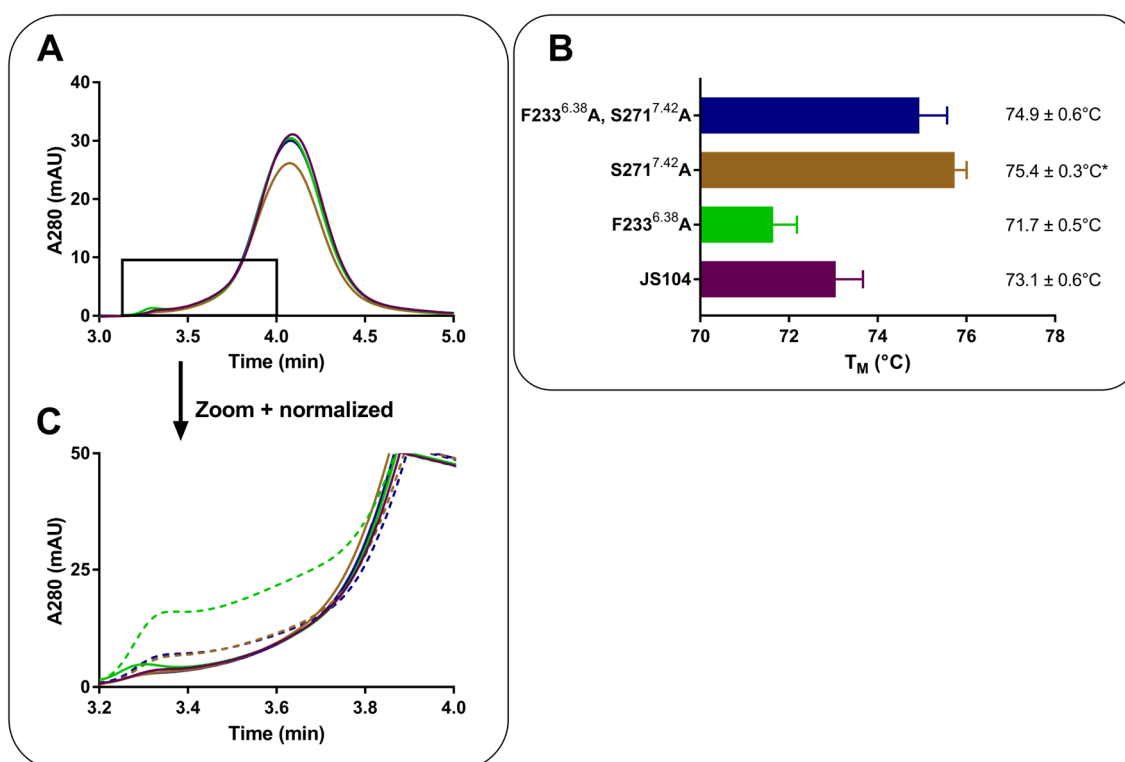


Figure 32. Combination of point mutations.

A: SEC chromatogram (3–5 min). B: Determined T_M values. Data represent mean ± SEM from three experiments. Statistical evaluation was carried by one-way ANOVA with Dunnett's post hoc test (ns $p \geq 0.5$ ns; * $0.05 > p > 0.01$; ** $0.01 \geq p > 0.001$; *** $0.001 \geq p > 0.0001$; **** $p < 0.0001$). C: Normalized SEC chromatogram (x: 3.2–4.0 min; y: 0–50 %). SEC after a heat shock (55°C, 5 min) is presented as dashed lines.

3.12 Investigation of the conserved disulfide bond connecting ECL2 and TM3

The highly conserved disulfide bond between C166^{45.50} in ECL2 and C83^{3.25} in TM3 is most likely also present in the wt A₃AR and hence must be present in the expressed A₃AR construct subjected to crystallization. This disulfide bond displays a common feature of most GPCRs and plays a crucial role in receptor folding, localization, and ligand binding.^{116; 287} However, no study has explored this essential connection in the A₃AR. Therefore, both cysteine residues were mutated to serine to validate the connection between C83^{3.25}–C166^{45.50}. C88^{3.30}, which displays a second cysteine residue at the top of TM3, was also included in this investigation. C166^{45.50}S was introduced into JS68, which combined the untruncated hA₃AR with bRIL inserted into the A_{2A}/A₁ hybrid junction site and S97^{3.39}K. C83^{3.25}S and C88^{3.30}S were introduced into JS68 without N-glycosylation sites, the C-terminus, and the C-terminal protease cleavage site, corresponding to JS104. These changes do not alter the thermostability properties but slightly reduce the shoulder in the SEC chromatogram as described in Section 3.16.6. Parent constructs JS68 and JS104 are included as references in the figures. The Transfection and expression of C83^{3.25}S and

C88^{3.30}S mutants were repeated once and are named C83^{3.25}S II and C88^{3.30}S II, respectively.

The mutations C166^{45.50}S and C83^{3.25}S substantially decreased the T_M compared to the corresponding constructs with potentially intact disulfide bond (Figure 33 B). On average, the T_M values of both constructs were approximately 65°C, which was 8°C lower than the average T_M value of both reference constructs (mean 73°C). Moreover, disruption of C83^{3.25}–C166^{45.50} at each end affected the thermostability virtually identically (average of C83^{3.25}S I/II 65.5°C vs. C166^{45.50}S 65.4°C). The conserved disulfide bond C83^{3.25}–C166^{45.50} was assumed to be correctly formed since the respective constructs without serine mutations and potentially intact connection, JS68, JS104, and the C88^{3.30}S mutant, displayed superior stability. The construct carrying C88^{3.30}S, which was not expected to participate in the disulfide bond formation, revealed a T_M of 72°C (C88^{3.30}S I 71.5°C; C88^{3.30}S II 72.5°C). This T_M was about the same magnitude as JS104 (73.1°C) and indicated that C88^{3.30} did not interact with the connection between ECL2 and TM3.

Thermal SEC (heat shock 55°C, 5 min) further proved the effect and the presence of the connection of C83^{3.25}–C166^{45.50} (Figure 33 D). Most of the protein harboring C83^{3.25}S was aggregated after the heat shock, as seen in the substantial elevation of the shoulder in the SEC chromatogram. In contrast, the C88^{3.30}S mutant was more stable, and only a tiny portion was destructed, matching its 7°C higher T_M . Repetition of constructs bearing C83^{3.25}S and C88^{3.30}S resulted in very similar thermostability (T_M , thermal SEC) but slightly lower protein yield (Figure 33 B, C). Interestingly, the overall protein yield was remarkably similar to constructs without serine mutations C83^{3.25}S and C166^{45.50}S (Figure 33 A).

Protein constructs with mutations disrupting the overall architecture are often retained in the cell and not correctly expressed anymore. However, these receptor mutants (C83^{3.25}S, C166^{45.50}S) seemed not to be recognized by the quality control system of the *Sf9* insect cells and were still expressed and trafficked in an unaltered way. The quality control system of insect cells is known to be less developed, but that receptor mutants with disrupted architecture can slip through this system is probably less well-known. Therefore, it cannot generally be assumed that receptor constructs that are well expressed and yield sufficient amounts of protein possess all necessary features, such as disulfide bonds.

Protein validation by thermostability assessment and thermal SEC was suitable for detecting changes in the overall protein structure. An intact conserved disulfide bond was crucial for the overall rigidity and stability of the A₃AR. Disruption of C83^{3.25}–C166^{45.50}

by serine mutations had a devastating effect on ligand binding at the A₁- and A_{2B}ARs, but less detrimental effects at the A_{2A}AR, which possesses two additional disulfide bonds providing additional stability.^{114; 116; 224} All mutants were checked for binding of the A₃-selective antagonist [³H]PSB-11. The C83^{3.25}S and C166^{45.50}S mutations showed no specific binding of [³H]PSB-11, similar to the corresponding mutations in the A₁- and the A_{2B}ARs. Thus, the conserved disulfide bond is most likely essential for the overall stability and potentially for efficient ligand binding at the A₃AR. Incubating membrane preparations from CHO-S cells expressing the wt A₃AR with 10 mM of the reducing agent dithiothreitol (DTT) for 30 min at room temperature reduced the specific binding by ~30 % (n=2) but did not alter the affinity of the antagonist radioligand. The amount of reduced disulfide bonds is unknown, but similar experiments indicated that not all disulfide bonds are reduced under these conditions.^{114; 116; 288; 289} A₃ARs with a reduced disulfide bond might consequently be unable to bind [³H]PSB-11, whereas A₃ARs with intact disulfide bond can still bind [³H]PSB-11 with high affinity, which potentially explains the reduced specific binding but the unaltered affinity. Decreased ligand binding but unaltered high-affinity binding after DTT incubation was also observed for the dopamine D₂ receptor or the serotonin 5-HT_{1A} receptor, which both possess just one disulfide bond between TM3 and ECL2 or in ECL2 similar to the A₃AR.^{290; 291} However, when the disulfide bond is not crucial for the ligand binding, which would explain the unaltered affinity, the reduced specific binding must be a result from a different effect of the DTT incubation.

Surprisingly, the C88^{3.30}S mutant also failed to bind [³H]PSB-11 implying that this cysteine residue might also play a role in ligand binding. Previous mutagenesis studies at this position showed that C88^{3.30}F decreased the affinity for [¹²⁵I]-AB-MECA by 7-fold.²³⁶ Similarly, C85^{3.30}S reduced the affinity for R-PIA by 4-fold but did not affect antagonist binding ([³H]DPCPX) at the A₁AR.²²⁴ At this point, it needs to be kept in mind that A₃AR constructs expressed in *Sf9* insect cells generally revealed altered binding properties (see Section 3.18.1). Consequently, amino acid exchanges, such as C88^{3.30}S, that potentially affect ligand binding might further impede the detection of specific binding. Nevertheless, the data provided here validates the presence and importance of the conserved C83^{3.25}–C166^{45.50} for the A₃AR, proving its similarity to the A₁- and A_{2B}ARs in concern of disulfide bonds. Expression of the three cysteine mutants (C83^{3.25}S, C88^{3.30}S, C166^{45.50}S) in CHO-S cells and subsequent investigation by agonist and antagonist radioligand binding will ultimately examine their effect on ligand binding at the A₃AR.

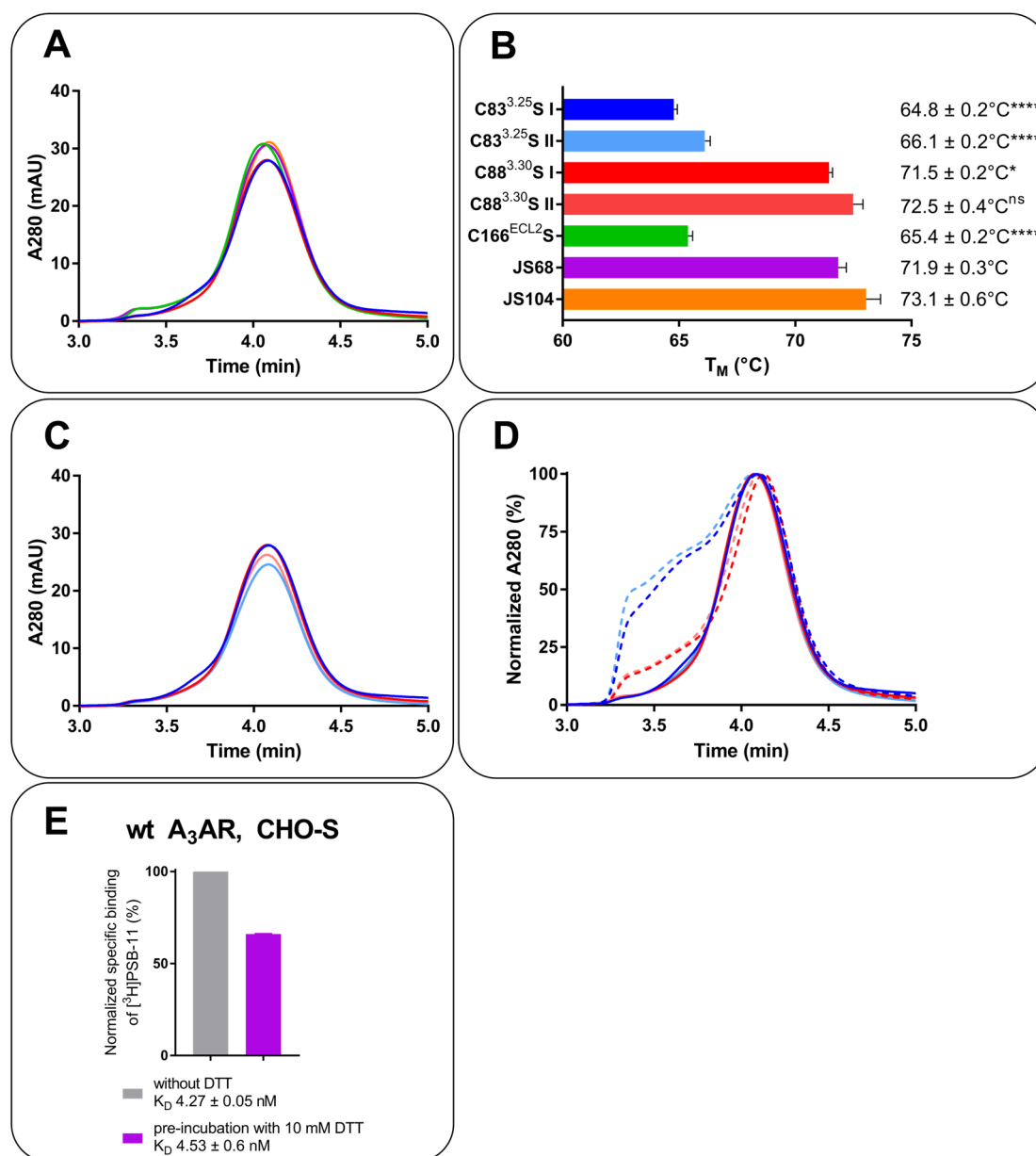


Figure 33. Investigation of the conserved disulfide bond C83^{3.25}-C166^{45.50}.

A: SEC chromatogram (3–5 min). B: Determined T_M values. Data represent mean ± SEM from three experiments. Statistical evaluation was carried out by a two-tailed student's *t* test (JS68 vs. C166^{ECL2}S) and one-way ANOVA with Dunnett's post hoc test (JS104 vs. C83^{3.25}S I/II, C88^{3.30}S I/II; ns $p \geq 0.5$ ns; * $0.05 > p > 0.01$; ** $0.01 \geq p > 0.001$; *** $0.001 \geq p > 0.0001$; **** $p < 0.0001$). C: SEC chromatogram (3–5 min) of C83^{3.25}S I and C88^{3.30}S I together with C83^{3.25}S II and C88^{3.30}S II. D: Normalized SEC chromatogram (3–5 min) of C83^{3.25}S I/II and C88^{3.30}S I/II including SEC chromatograms after a heat shock of 55°C, 5 min, which are presented as dashed lines. E: DTT pre-incubation. The membrane preparation (A₃AR wt, CHO-S) was pre-incubated with 10 mM DTT at room temperature for 30 min before used in the homologous competition binding ([³H]PSB-11 vs. PSB-11). Specific counts were normalized to a control treated the same way but without DTT (n=2).

3.13 Optimization of expression and purification conditions

Ligands can be added to the growth medium to assist as a pharmacological chaperone in receptor trafficking and folding. High-affinity orthosteric ligands such as

antagonists/inverse agonists can stabilize the receptor and thus can be added during solubilization and purification to maintain proper receptor folding. The two antagonists CGS 15943 and TK-OT-018, with K_i values of 51 nM and 2.8 nM at the hA₃AR, were considered (for structures, see Figure 5).^{119; 125} In order to assess their effects on the protein yield and stability when being present during expression and purification/solubilization, JS53 (M₄ mAChR N-terminus, truncated hA₃AR, A_{2A}/A₁ hybrid junction site, S97^{3.39}K) was expressed and purified in four different ways:

- 1) Expression with CGS 15943 (1 μ M) + purification/ solubilization with TK-OT-018 (25 μ M)
- 2) Expression without CGS 15943 + purification/solubilization with TK-OT-018 (25 μ M)
- 3) Expression with CGS 15943 (1 μ M) + purification/solubilization without TK-OT-018
- 4) Expression without CGS 15943 + purification/solubilization without TK-OT-018

All expression approaches resulted in a clear and sharp peak at around 4.1 min with similar overall protein yields (see Figure 34). Detailed analysis revealed that the protein yield was lower when CGS 15943 was present during expression. Since the addition of CGS 15943 to the growth medium did not lead to a significantly improved yield, the presence of a ligand will not be used as standard procedure. The peaks of proteins purified with TK-OT-018 were marginally shifted towards higher retention times and possessed a slightly steeper slope. This shift indicated that the ligand might have improved the receptor homogeneity and rigidity, resulting in a sharper peak. Nevertheless, the effect of TK-OT-18 during solubilization and purification could not be unambiguously proven since differences occurred to an insufficient extent.

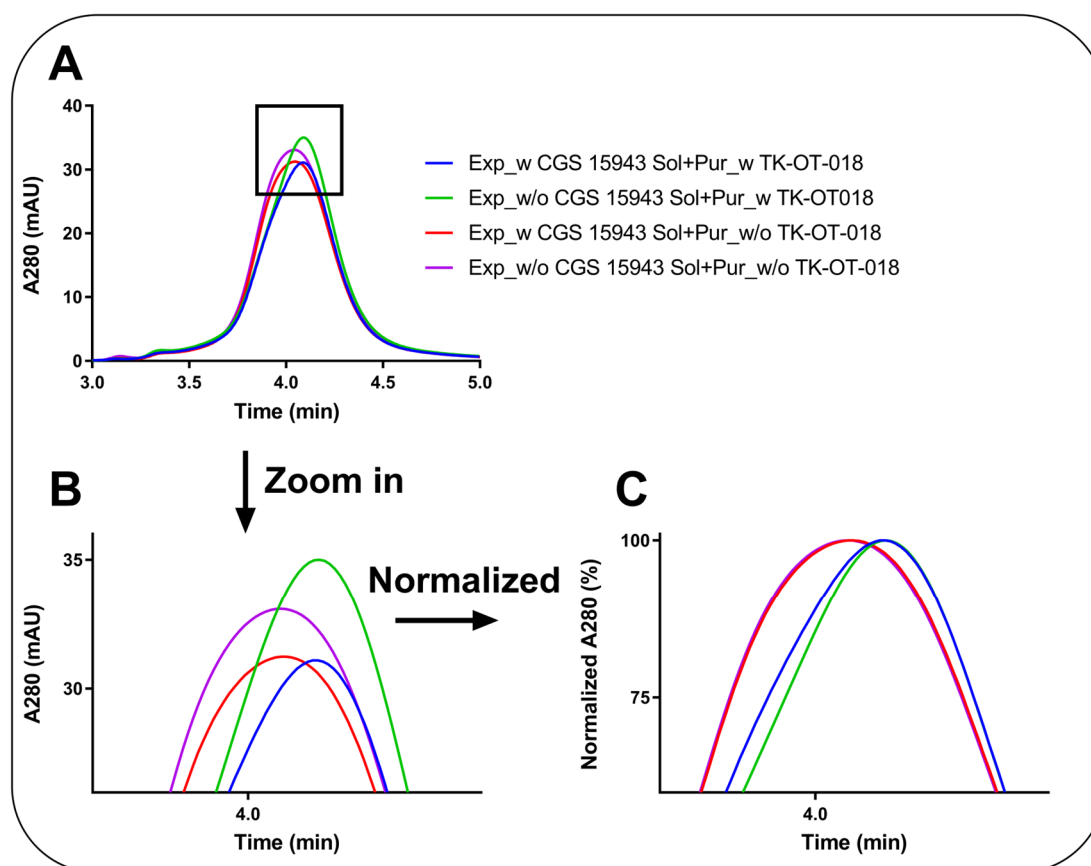


Figure 34. Optimization of expression and purification conditions.

A: SEC chromatogram (3–5 min) of JS53 (M₄ mAChR N-terminus, S97^{3.39}K, A_{2A}/A₁ hybrid junction site). Exp=Expression, Sol+Pur=solubilization and purification, w=with, w/o=without. B: Enlarged SEC chromatogram (x: 3.8–4.3 min; y: 26–36 mAU). C: Normalized, enlarged SEC chromatogram (x: 3.8–4.3 min; y: 60–101 %).

3.13.1 Purification in the presence of various A₃AR ligands

The construct JS54 (truncated hA₃AR, S97^{3.39}K, bRIL in ICL3, A_{2A}/A₁ hybrid junction site) was solubilized and purified in the presence of six different ligands, including antagonists (high and low affinity) and one agonist (NECA). On the one hand, this experiment aimed to find a stabilizing ligand, and on the other hand, it tried to prove proper ligand binding indirectly. In theory, different ligands should stabilize or even destabilize the investigated GPCR differently, resulting in altered protein yields or T_M values. A stabilizing ligand might increase the overall protein yield since the GPCR-ligand complex might be more resistant to destruction during solubilization and purification. Therefore, the antagonists TK-OT-008, TK-OT-018, MRS1523, caffeine, and CGS 15943, as well as the agonist NECA were employed in this experiment (see Figure 4 and Figure 5 for structures of these compounds).

All approaches resulted in a clear peak with a similar height of around 20 mAU (Figure 35 A). No ligand was able to increase the overall protein yield significantly. Since the protein yield seemed identical, a heat shock of 55°C for 5 min was applied to find any differences between the performance of tested ligands (Figure 35 B). As already described, the extent of protein aggregation can be evaluated based on the shoulder size before the protein peak. Again, no favorable ligand could be identified. Caffeine and NECA revealed a similar shoulder elevation, whereas MRS1523 resulted in a slightly lower shoulder. Surprisingly, the three high-affinity antagonists TK-OT-008, TK-OT-018, and CGS 15943 performed even worse than the apo GPCR. The obtained T_M values revealed a similar picture (Figure 35 C). Only NECA showed a T_M slightly lower than the antagonists and the apo GPCR, which were around 68°C.

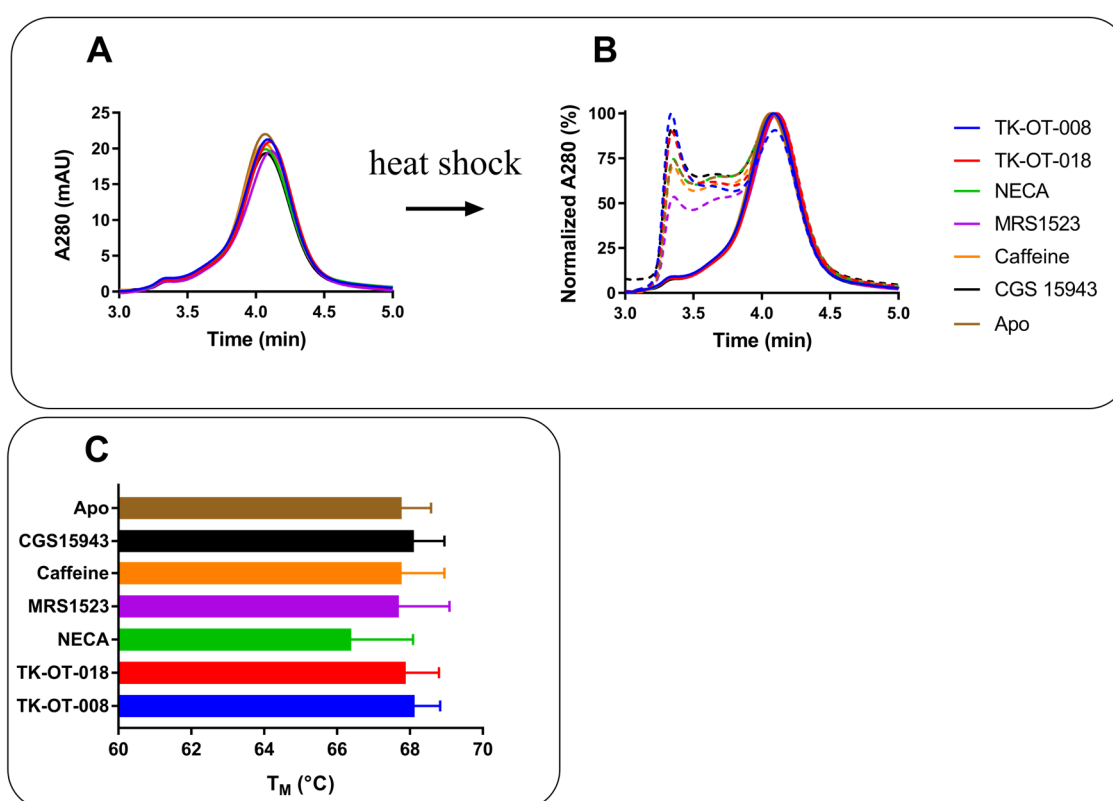


Figure 35. Solubilization and purification of JS54 in the presence of various ligands.

A: SEC chromatogram (3–5 min). B: Normalized SEC chromatogram (3–5 min). SEC chromatograms of proteins after a heat shock (55°C, 5 min) are shown as dashed lines. C: Bar chart of T_M values. Data represent mean \pm SEM from three experiments. Statistical evaluation was carried by one-way ANOVA. No statistically significant difference could be determined.

3.13.2 Solubilization and purification with LMNG and the irreversible A₃AR antagonist LUF7602

LMNG is a suitable detergent used for solubilization, which might provide superior performance compared to the current gold standard detergent DDM. LMNG interacts with the GPCR molecules more efficiently and intensively due to its branched architecture resulting in improved stability or functionality (see Section 1.3.5.2). Therefore, experiments in this section compared the standard solubilization with 1%/0.2% DDM/CHS with the use of 1%/0.1% LMNG/CHS. Additionally, the subsequent purification was performed in the presence of the irreversible A₃AR antagonist LUF7602 (1 μM, see Figure 43 and Table 7).

The subject of this experiment was JS68, expressed at a medium scale (250 mL). Subsequent membrane preparation was divided into equal batches, which were then processed individually but simultaneously to maintain comparability. Overall, LMNG/CHS-solubilized proteins were eluted later than the corresponding DDM/CHS samples, probably caused by the different micelle sizes and forms (Figure 36). Moreover, protein yields provided by the solubilization with LMNG were less, whereas stability was improved. After a heat shock of 58°C for 5 min, the SEC chromatogram revealed almost no protein aggregation for the LMNG/CHS-solubilized samples (Figure 36 C). DDM/CHS-solubilized samples were slightly more susceptible to temperature-induced stress but still preserved the majority of stable GPCR molecules. In both cases, the presence of LUF7602 increased the protein yield, but to a greater extent for the LMNG solubilization. Moreover, the peak of the sample DDM/CHS + LUF7602 was slightly shifted and appeared sharper than the corresponding DDM/CHS peak without LUF7602. LUF7602's effect on the thermostability of LMNG/CHS-solubilized samples could not be reliably examined since the heat shock was too mild to distinguish differences, and the CPM assay data could not be analyzed. In contrast, the combination of DDM/CHS + LUF7602 revealed less protein aggregation after the heat shock and exhibited a 1.9°C higher T_M than observed with DDM/CHS without LUF7602 being present (Figure 36 B, C).

In conclusion, LMNG was suitable to solubilize the A₃AR and provided higher native stability. Nevertheless, the protein yield was only half that obtained with DDM/CHS. The additional thermostability aspect of LMNG might not be needed since DDM/CHS samples were already extraordinarily stable (T_M > 70°C).

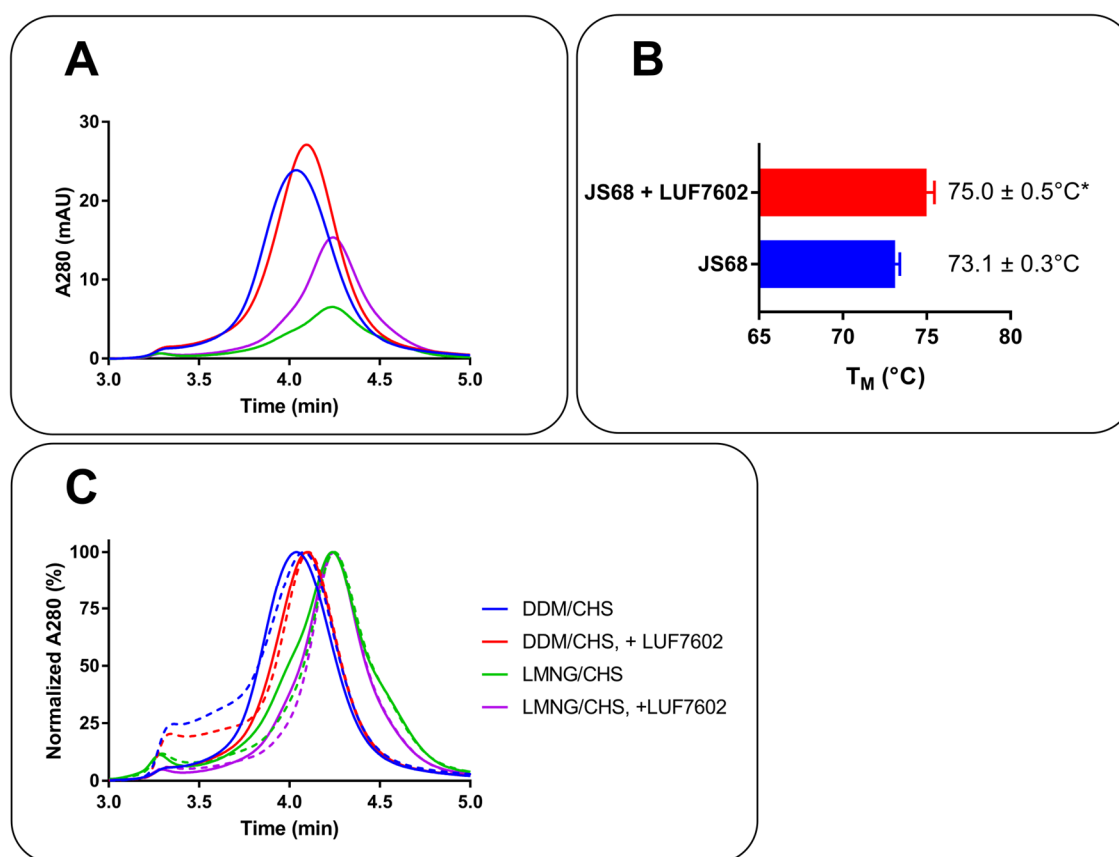


Figure 36. Solubilization and purification with LMNG and the irreversible A_3AR antagonist LUF7602.

A: SEC chromatogram (3–5 min) of JS68 solubilized and purified with DDM/CHS (1%/0.2%, w/v) or LMNG/CHS (1%/0.1%, w/v) with and without LUF7602 (1 μM) being present. B: Determined T_M values. Data represent mean ± SEM from three experiments. Statistical evaluation was carried out by a two-tailed student's t test (ns $p \geq 0.5$ ns; * $0.05 > p > 0.01$; ** $0.01 \geq p > 0.001$; *** $0.001 \geq p > 0.0001$; **** $p < 0.0001$). C: Normalized SEC chromatogram (3–5 min). Dashed lines represent SEC after a heat shock of 58°C for 5 min.

3.14 Assessment of ligand binding by the CPM-based thermostability assay

Typically, crystallization projects of GPCRs include assessing ligand-induced thermostabilizing effects on the solubilized GPCR. On the one hand, ligands that can increase receptor stability are favorable to shorten the long way to successful crystallization since protein stability and crystallization success correlate.^{262; 292} On the other hand, investigation of ligand binding indirectly validates the correct folding of the GPCR. The absence of any ligand effect in the thermostability assay might indicate that the receptor is misfolded. Various proteins were expressed, solubilized, and purified without any ligand (apo). Subsequently, these proteins were tested in the thermostability assay in the presence of different ligands, including nonselective and selective A_3AR agonists and antagonists, to determine their T_M values (Figure 37). In order to thoroughly investigate ligand binding, five screening campaigns were carried out, each utilizing a different approach.

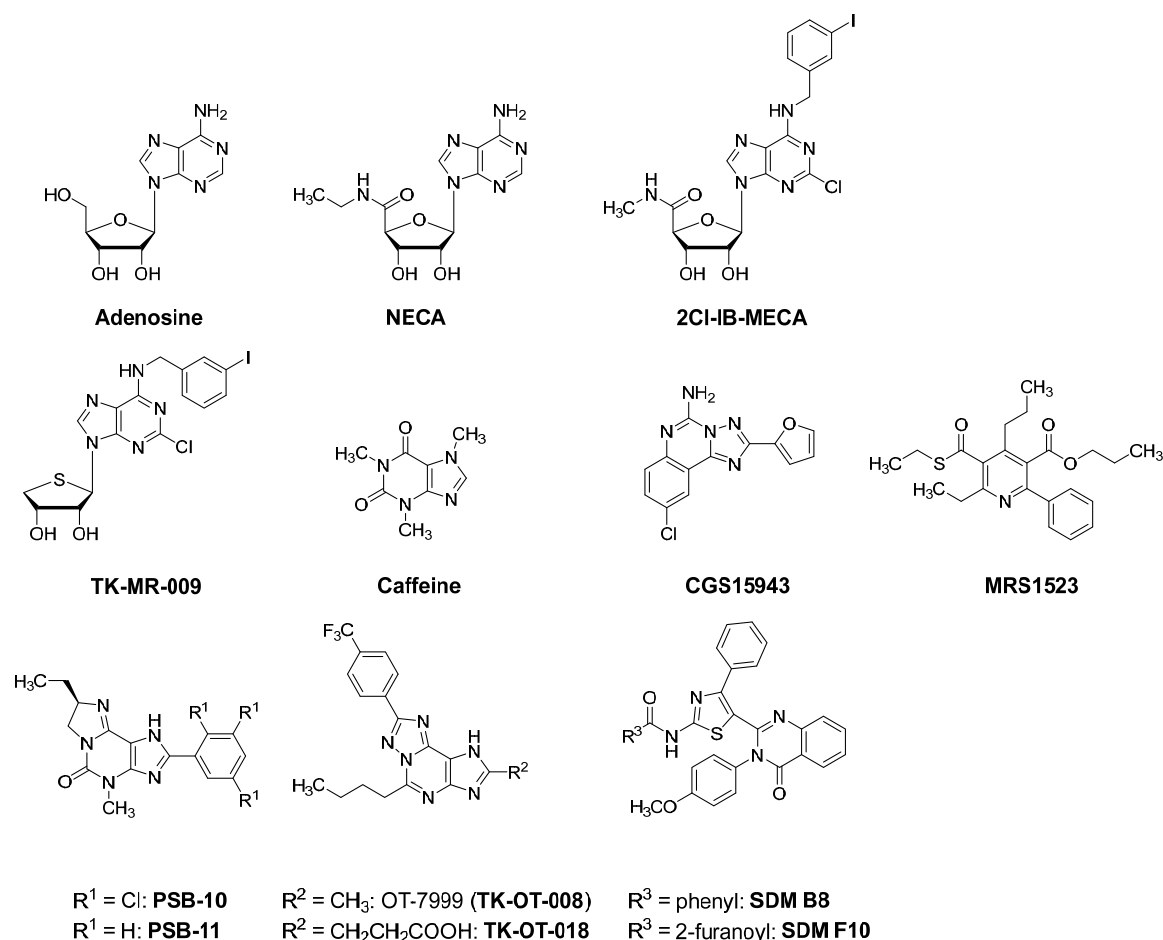


Figure 37. Structures of ligands tested in the CPM thermostability assay campaigns.

3.14.1 Ligand screening campaign I

Three A₃AR constructs were subjects of the first ligand screening campaign. JS53 and JS54, only differing in the presence of the M₄ mAChR N-terminus, and JS73, which possesses the A₃ junction site instead of the A_{2A}/A₁ hybrid junction site, were investigated.

Investigated constructs

JS53: truncated hA₃AR, N-terminal M₄ mAChR N-terminus, bRIL in A_{2A}/A₁ hybrid junction site, S97^{3.39}K

JS54: truncated hA₃AR, bRIL in A_{2A}/A₁ hybrid junction site, S97^{3.39}K

JS73: truncated hA₃AR with combined with the N-terminal M₄ mAChR N-terminus, bRIL in A₃ junction site (L208^{5.69}–K216^{1CL3}), S97^{3.39}K

Overall, T_M values of JS53 and JS54 were around 75°C and in the range of 71–75°C, respectively (Figure 38). Different protein concentrations might have caused the observed differences instead of any effect of the M₄ mAChR N-terminus on ligand binding.

T_M values of JS73 were shifted by 5°C to 65–70°C, demonstrating that the A_3 junction site was inferior to the hybrid junction site. Unfortunately, none of the tested ligands at any investigated constructs resulted in either a destabilizing or a stabilizing effect.

Ligand screening campaign I

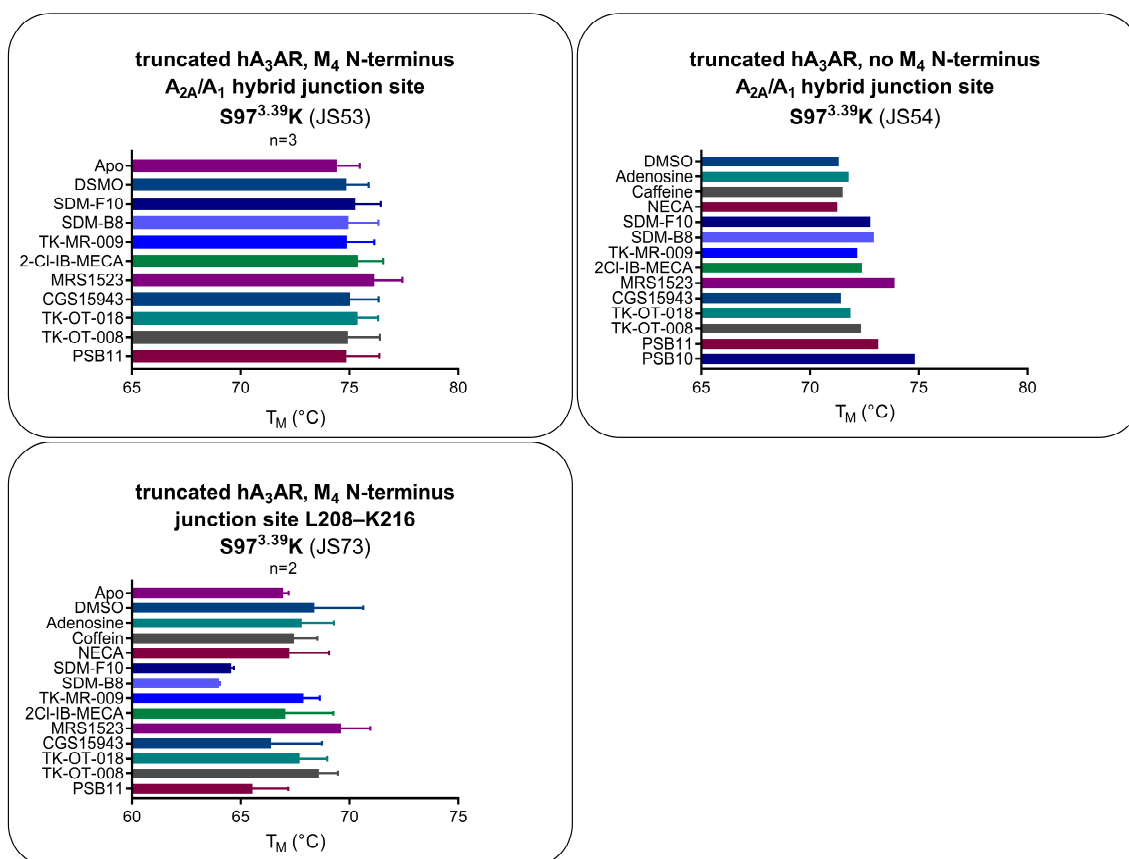


Figure 38. Ligand screening campaign I.

T_M values of JS53, JS54 and JS73 determined in the presence of various ligands (10 μ M). When error bars are given, data represent mean \pm SEM from n different experiments. Number of experiments (n) is stated in each subheading.

3.14.2 Ligand screening campaign II

Two A_3 AR constructs (JS53, JS68) were subjects of the second ligand screening campaign. In this campaign, melting curves were baseline-corrected to further enhance the detection of the effect caused by the protein-ligand complex and account for fluorescence signals caused by the ligand and the elution buffer. Therefore, the baseline was defined by the corresponding sample with elution buffer instead of the purified protein. Additionally, the two tested constructs, JS68 and JS53, will compare the A_3 AR N-terminus and the M₄ mAChR N-terminus (JS53).

Investigated constructs

JS53: truncated hA₃AR, N-terminal M₄ mAChR N-terminus, bRIL in A_{2A}/A₁ hybrid junction site, S97^{3.39}K

JS68: untruncated hA₃AR, bRIL in A_{2A}/A₁ hybrid junction site, S97^{3.39}K

All T_M values were within the range of 70–75°C, fluctuating around 72–73°C (Figure 39). Consequently, the native A₃AR and the M₄ mAChR N-terminus seemed not to alter the melting curves. In both cases, the highest T_M was obtained in the presence of MRS1523 (JS68 73.8°C JS53 74.0°C). Nevertheless, no significant ligand effect could be observed.

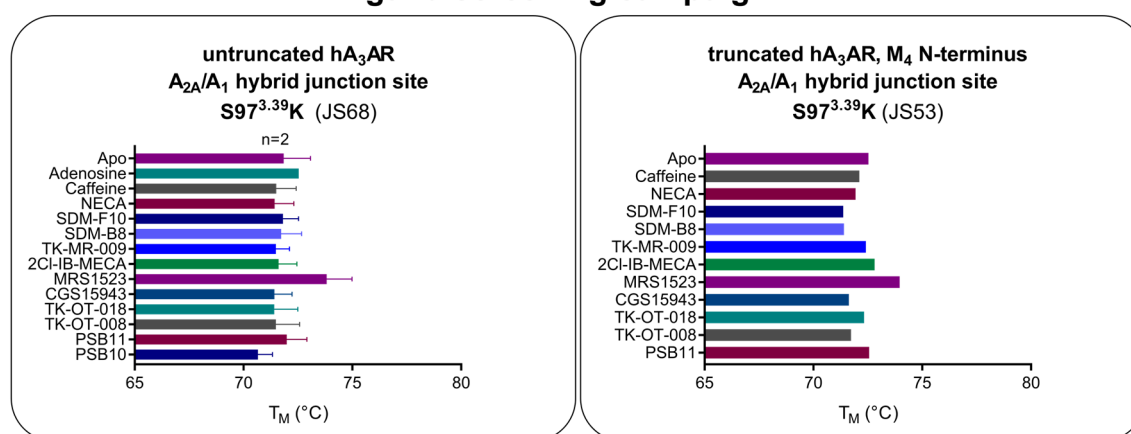
Ligand screening campaign II

Figure 39. Ligand screening campaign II.

T_M values of JS68 and JS53 determined in the presence of various compounds (10 μM). When error bars are given, data represent mean ± SEM from n different experiments. Number of experiments (n) is stated in each subheading.

3.14.3 Ligand screening campaign III

In the third campaign, constructs JS68, JS77, JS80, and JS81 were considered. JS77, not possessing any fusion partner, was meant to clarify whether the presence of a fusion partner might impede proper ligand-induced stabilization. In JS80 (A₃AR N-terminus) and JS81 (M₄ mAChR N-terminus), helix VIII was exchanged for the helix VIII of the A_{2A}AR (also see Section 3.10). Moreover, JS68 was included as a reference to screening campaign II.

Investigated constructs

JS68: untruncated hA₃AR, bRIL in A_{2A}/A₁ hybrid junction site, S97^{3.39}K

JS77: untruncated hA₃AR, S97^{3.39}K

JS80: truncated hA₃AR, N-terminal M₄ mAChR N-terminus, bRIL in A_{2A}/A₁ hybrid junction site, S97^{3.39}K, A_{2A}AR helix VIII (residues K285^{7.56}–S308^{8.69} are replaced by R291^{7.56}–A316)

JS81: untruncated hA₃AR, bRIL in A_{2A}/A₁ hybrid junction site and S97^{3.39}K, A_{2A}AR helix VIII (residues K285^{7.56}–S308^{8.69} are replaced by R291^{7.56}–A316)

Results are depicted in Figure 40. The determined T_M values of JS68 were around 73°C, similar to the second campaign. The absence of a fusion partner decreased the protein stability resulting in T_M values of below 60°C. Exchanging helix VIII did not alter the melting curves of the tested ligand-protein complexes, which resulted in similar T_M values to those of JS80, JS81, and JS68. As in previous screening experiments, no significant ligand effect could be identified, and the highest T_M was obtained for MRS1523. However, only JS77 showed this observation.

Ligand screening campaign III

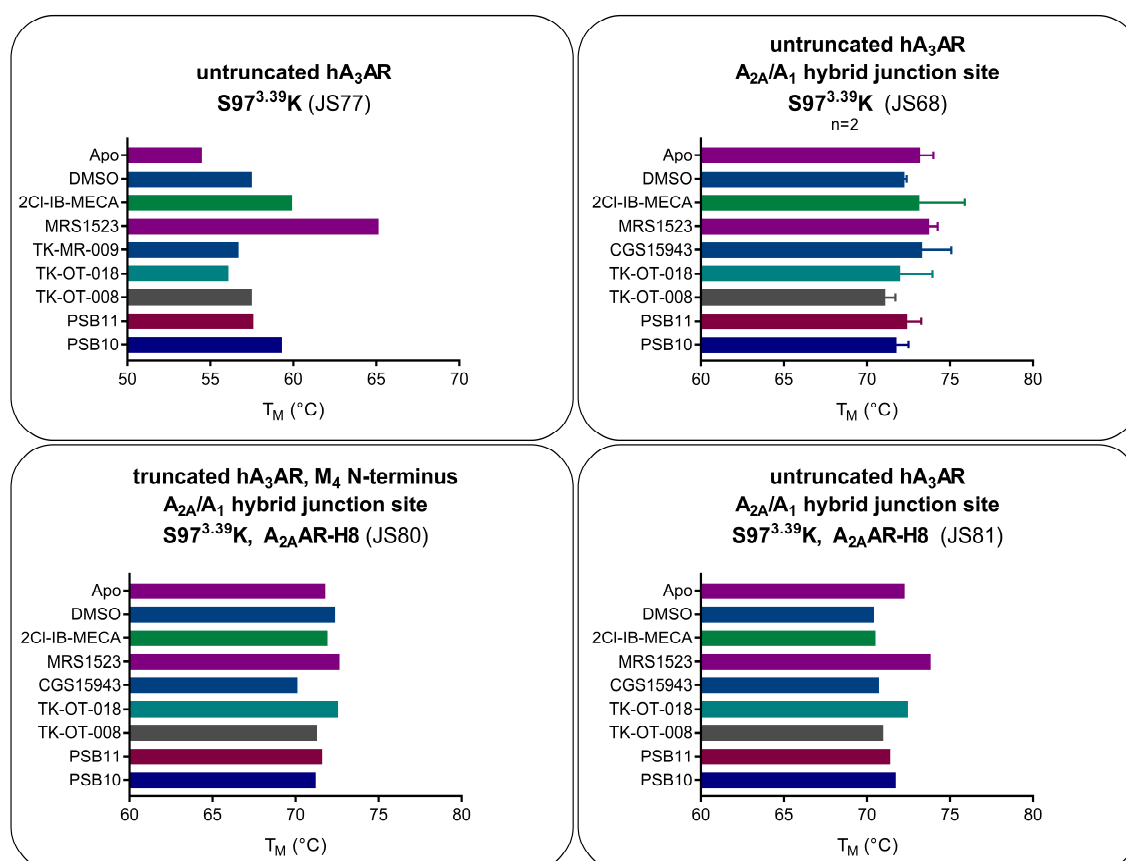


Figure 40. Ligand screening campaign III.

T_M values of JS77, JS68, JS80 and JS81 determined in the presence of various compounds (10 μ M). When error bars are given, data represent mean \pm SEM from n different experiments. Number of experiments (n) is stated in each subheading.

3.14.4 Ligand screening campaign IV

So far, all investigated constructs harbored a mutated sodium binding pocket. The mutation S97^{3.39}K locks the receptor in its inactive state and thus can provide a substantial increase in stability. However, this mechanism might prevent observing a ligand effect in the CPM-based thermostability assay. Therefore, the two constructs, JS40 and JS79, which did not possess the S97^{3.39}K mutation, were subjects of the fourth ligand screening campaign.

Investigated constructs

JS40: truncated hA₃AR, N-terminal M₄ mAChR N-terminus, bRIL in A_{2A}/A₁ hybrid junction site

JS79: untruncated hA₃AR, bRIL in A_{2A}/A₁ hybrid junction site

Both constructs only differed in their N-terminus and were equally stable (Figure 39). All T_M values were within 60–65°C and fluctuated around 63°C, which is 10°C lower than corresponding constructs with the S97^{3.39}K mutation, proving the crucial benefit of this mutation (Figure 41). Moreover, results indicated that the S97^{3.39}K mutation was not the reason for the absence of any ligand effect in the CPM-based thermostability assay. Like in previous campaigns, no clear ligand-mediated effect could be observed.

Ligand screening campaign IV

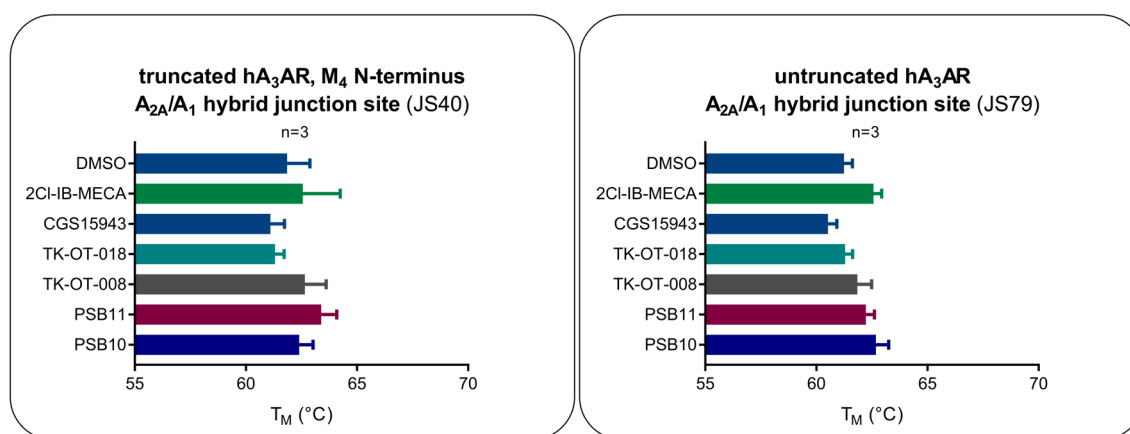


Figure 41. Ligand screening campaign IV.

T_M values of JS40 and JS79 determined in the presence of various compounds (10 μ M). When error bars are given, data represent mean \pm SEM from n different experiments. Number of experiments (n) is stated in each subheading.

3.14.5 Ligand screening campaign V

In the following campaign, the effect of a promoter exchange, the insertion of the sequence NNST between the HA- and the FLAG-tag, as well as the combination of an A_3 junction site and untruncated N/C-termini were tested. Moreover, the construct JS89 was included, whose conserved disulfide bond between C83^{3.25}–C166^{45.50} was disrupted by the mutation C166^{45.50}S. Corresponding mutations abolished ligand binding at all ARs with just one disulfide bond like the A_3 AR. Thus, this mutant displayed a well-suitable control to assess the properties of a construct that is likely unable to bind ligands. Indeed, the mutation C166^{45.50}S did not show any specific [³H]PSB-11 binding (also see Section 3.12). Subsequently, the results of JS89 can be used as a reference to classify further the results obtained so far.

Investigated constructs

JS85: p10 promoter, untruncated hA₃AR, bRIL in A_{2A}/A₁ hybrid junction site, S97^{3.39}K

JS86: untruncated hA₃AR, bRIL in A₃ junction site (L208^{5.69}–K216^{1CL3})

JS89: untruncated hA₃AR, bRIL in A_{2A}/A₁ hybrid junction site, S97^{3.39}K, C166^{45.50}S

JS90: truncated hA₃AR, HA-NNST-FLAG, bRIL in A_{2A}/A₁ hybrid junction site, S97^{3.39}K

The promoter exchange to the p10 promoter showed similar results compared to the corresponding construct with the polyhedrin promoter (JS68), yielding T_M values around 73°C (Figure 42). The less stable construct JS86, which possessed the A₃ insertion site instead of the hybrid junction site, resulted in similar T_M values compared to its close relative JS73 (Figure 38). The protein with the short linker NNST between the HA- and FLAG tag exhibited high T_M values (70–75°C) that were slightly lower than those of JS85 on average. In all three cases, the highest T_M was obtained in the presence of MRS1523. The ligand screening of the construct JS89, which lacks the conserved disulfide bond, revealed interesting results. The T_M values were approximately 8°C lower than that of JS85, which possessed an intact disulfide bond (also see Section 3.12). Apart from the overall decreased stability, the results of JS89 were highly similar to those of all previous screening campaigns. This similarity was surprising since the protein was known to be unable to bind ligands properly. Conversely, this indicated that the ligands might not bind at the investigated constructs. On the other hand, the tested ligands could bind properly but were incapable of further stabilizing the protein. Moreover, the observation of higher T_M values in the presence of MRS1523 might thus be a non-specific effect rather than any binding-mediated effect since this effect could be similarly observed for the loss-of-binding mutant C166^{45.50}S (JS89), disrupting the highly conserved disulfide bond between the top of TM3 and ECL2.

Ligand screening campaign V

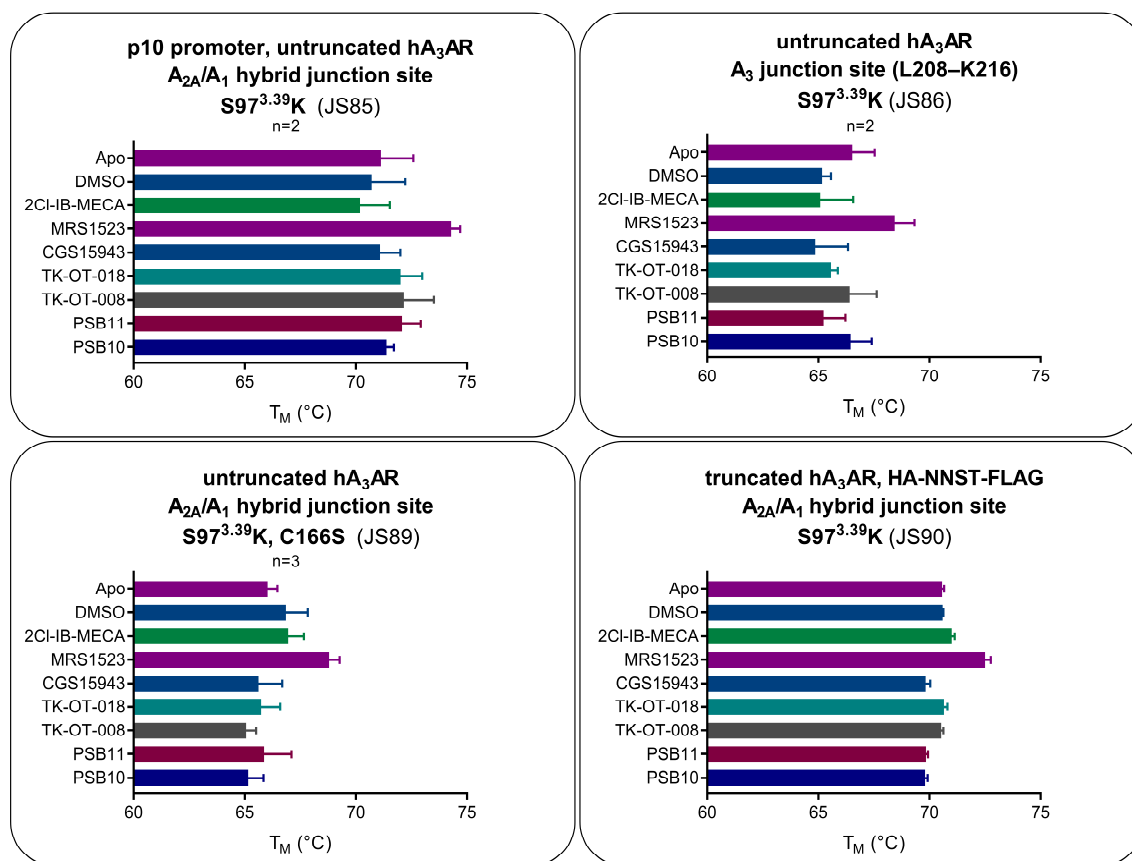


Figure 42. Ligand screening campaign V.

T_M values of JS85, JS86, JS89 and JS90 determined in the presence of various compounds (10 μ M). When error bars are given, data represent mean \pm SEM from n different experiments. Number of experiments (n) is stated in each subheading.

3.14.6 The antagonists LUF7602 and AT563

Due to their extremely slow dissociation and long residence time, covalent ligands can be crucial for providing a significant increase in stability and for the success of crystallization.²⁹³ The crystal structure of the A₁AR had been successfully solved by employing the covalent antagonist DU172. DU172 and the second investigated covalent antagonist, FSCPX, were able to stabilize the crystallization construct the most, leading to a significant thermostability shift with ΔT_M of $\sim 16^\circ\text{C}$.²¹⁴ Therefore, investigating the binding properties of a covalent A₃AR antagonist was of high interest to eventually observe a thermostability shift. The only available covalent A₃AR antagonist was the xanthine-based LUF7602, which targets a tyrosine residue in helix VII (Y265^{7.36}) with its reactive fluorosulfonyl warhead. Additionally, the triazoloprunine-based AT563, which possesses the highest affinity of the tested antagonists and potentially binds irreversible to the A₃AR ($K_i 0.28 \pm 0.01$ nM), was included in this investigation (also see Section 3.17)

The purified A₃AR construct JS104 was incubated with 10 μM and 100 μM of LUF7602 and 10 μM of AT563. Results are shown in Figure 43. LUF7602 was able to slightly increase the T_M at both concentrations (ΔT_M 10 μM 0.8°C, ΔT_M 100 μM 1.0°C). The effect of AT563 was minimally larger, resulting in an increment of ΔT 1.9°C. Irreversible ligands usually lead to a significant shift of the unfolding curve and increase the protein's T_M by a larger margin.^{214; 262} Since LUF7602's covalent binding mode is well-proven, these findings indicated that it was questionable whether LUF7602 bound covalently to the investigated A₃AR protein.¹³¹ LUF7602 stabilized the A₃AR construct, but the observed effects occurred to a rather small extent. Of course, it must be kept in mind that the tested A₃AR construct JS104 was already extremely stable on its own (T_M 71.9°C), which potentially narrowed the margin for a ligand-induced thermostability shift. However, the absence of any superiority of a covalent ligand could point to a fundamental problem in receptor folding and proper ligand binding, especially together with the previous ligand screening campaigns.

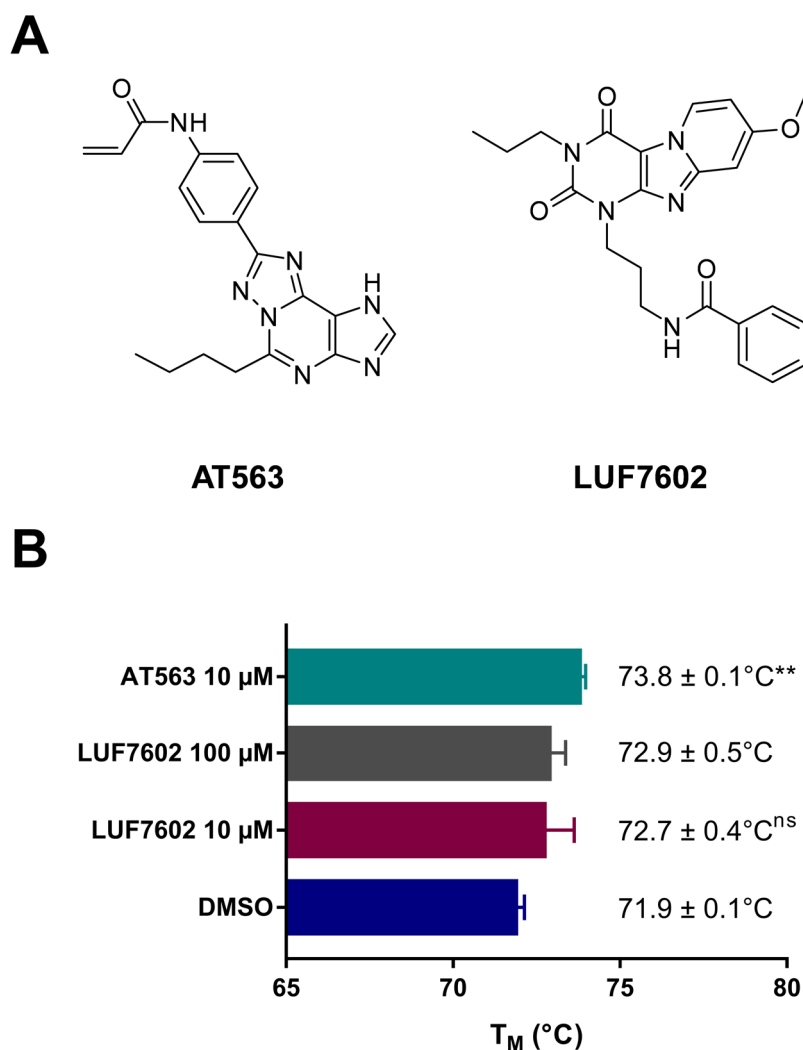


Figure 43. Thermostability in the presence of A₃AR antagonists LUF7602 and AT563.

A: Structures of LUF7602 and AT563. B: T_M values of JS104 determined in the presence of LUF7602 (10 μ M, 100 μ M) and AT563 (10 μ M). Data represent means \pm SEM from *n* different experiments (*n*=4: DMSO, LUF7602 10 μ M; *n*=3: AT563; *n*=2: LUF7602 100 μ M). Statistical evaluation was carried by one-way ANOVA with Dunnett's post hoc test comparing values of AT563 and LUF7602 (10 μ M) with that of the DMSO control (ns $p \geq 0.5$ ns; * $0.05 > p > 0.01$; ** $0.01 \geq p > 0.001$; *** $0.001 \geq p > 0.0001$; **** $p < 0.0001$).

3.14.7 Thermostability — conclusion

Extensive effort was put into several thorough ligand screening campaigns to track down the best candidate to be employed in crystallization experiments. In the initial screening campaigns, no distinct ligand-mediated effect could be observed. Several approaches to elucidate this observation were pursued to rule out potentially contributing factors. The mutation S97^{3.39}K, the presence of a fusion partner, the A_{2A}/A₁ hybrid junction site, and the M₄ mAChR N-terminus were ruled out as parameters that might have affected ligand binding or interfered with the detection of ligand binding in the CPM-based

thermostability assay. Moreover, the inherently high stability of optimized constructs ($T_M > 70^\circ\text{C}$) did not prevent the detection of a ligand effect since less stable constructs ($T_M < 70^\circ\text{C}$) showed similar behavior. In the end, the absent ligand effect might result from testing unfavorable ligands. However, even the covalent ligand LUF7602, which should have the highest probability of resulting in a noticeable shift, did not provide a significantly increased T_M value. Only the novel $A_3\text{AR}$ antagonist AT563 provided a significant stabilization, which resulted in the highest T_M increment of 1.9°C . In conclusion, the assessment of ligand binding by the CPM-based thermostability assay might hint towards an altered ligand binding to the solubilized $A_3\text{AR}$ constructs, which need to be further investigated.

3.15 Mouse $A_3\text{AR}$ constructs

Mouse and human $A_3\text{AR}$ s display striking interspecies differences in ligand binding. Hence, structural comparison of these receptors by X-ray crystallography would be of great value in elucidating this divergence. At first, the wt, the N-/C-terminally truncated wt, and the truncated wt plus bRIL replacing the ICL3 (insertion site L209^{5.69}–A221^{6.25}) were generated, expressed, purified, and analyzed. Additionally, the successful approaches of the A_{2A}/A_1 hybrid junction site and the N-terminal insertion of the M_4 mAChR N-terminus were transferred to $mA_3\text{AR}$ constructs. Consequently, amino acids between L209^{5.69}–A230^{6.34} were replaced by bRIL, followed by the $A_{2A}\text{AR}$ sequence ERARSTLQ and the $A_1\text{AR}$ sequence KELKI. The hybrid junction site was then further combined with the M_4 mAChR N-terminus.

Figure 44 A and B provide the results of this initial construct series. Similar to the first $hA_3\text{AR}$ constructs, initial $mA_3\text{AR}$ constructs featured low protein yield. Only the wt $mA_3\text{AR}$ (blue graph), the only construct with untruncated termini, revealed a small protrusion at around 4.2 min. This observation had already been observed for the untruncated $hA_3\text{AR}$ constructs, and deeper investigation initially identified N-glycosylation sites as a cause. Sequence alignment proves that N-terminal N-glycosylation sites, according to the pattern N-X-S/T ($X \neq P$), are conserved among rodent and mammalian $A_3\text{AR}$ s (Figure 23 A). Thus, truncation of the N-terminus might also be counterproductive for $mA_3\text{AR}$ constructs. SDS-PAGE analysis confirmed the presence of $mA_3\text{AR}$ protein with the correct size of ~ 40 kDa (Figure 44 E, red rectangle). Unfortunately, none of the modifications (insertion of bRIL, use of hybrid junction site)

improved the stability or yielded any decent protein quantity. Utilizing the M₄ mAChR N-terminus increased the protein yield as long as there was fundamental stability. This effect could also be observed for the mA₃AR constructs. Although the construct, possessing the hybrid junction site combined with the M₄ mAChR N-terminus, showed an elevated signal in the SEC chromatogram, a clear protein peak was still not present (orange graph). In conclusion, the mA₃AR probably has a slightly different architecture of the interface between TM5, ICL3, and TM6 than the hA₃AR since it did not benefit from the A_{2A}/A₁ hybrid junction site. Variation of the starting and end points of the insertion site could be promising to achieve correctly merged and aligned helices of the receptor and bRIL.

The mutation S98^{3.39}K within the highly conserved sodium binding pocket has already been proven to stabilize the receptor by arresting it in the inactive state. S98^{3.39}K would likely be advantageous for the mA₃AR since the mA₃AR sodium binding pocket is identical to that of the hA₃AR. The more conserved the stabilizing mutation or its close environment is, the more likely a transfer from another species or receptor is successful. Of course, such a mutation should not fundamentally change the GPCR and thus nullify the informative value of a X-ray structure.

Figure 44 C and D show that S98^{3.39}K successfully yielded a small peak at around 4.2 min and proved its transferability to the mA₃AR. For the first time, a mA₃AR construct reached a small but substantial amount of protein. As mentioned above, the M₄ mAChR N-terminus was utilized to increase the expression and, subsequently, the protein yield once fundamental stability was achieved. The corresponding construct, carrying the M₄ mAChR N-terminus, exhibited a 5-fold increased peak height in the SEC chromatogram (brown graph). The protein peak was slightly shifted to lower retention times, which could be explained by the increased hydrodynamic radius. Based on the findings in Section 3.9, the M₄ mAChR N-terminus was replaced by the short amino acid sequence NNST, inserted between the N-terminal HA- and FLAG-tag. This short sequence, which possesses two potential N-glycosylation sites, was capable of increasing the protein peak height by more than 3-fold. The construct carrying NNST (blue) was eluted shortly after the construct that bears the M₄ mAChR N-terminus (brown) and before the construct with a truncated N-terminus (black). The sequence NNST comprises only four amino acids in contrast to 29 additional residues in the construct carrying the M₄ mAChR N-terminus. In Section 3.9, the potential need for N-glycans was analyzed, and it was concluded that the beneficial effect of this kind of sequence might just be caused by its role as a “linker” between the N-terminal HA-tag and the GPCR itself.

In comparison to the hA₃AR construct JS104, it was noticeable that the peak shape differed significantly. Despite a peak height above 20 mAU, the peak was less steep and possessed a pronounced shoulder, as seen in the normalized SEC chromatogram, indicating that the protein was less homogenous and less stable. Nevertheless, the combination of S98^{3.39}K and the modified short sequence NNST resulted in a substantial amount of mA₃AR protein and displayed an appropriate starting point to build upon. The obvious next steps would be to improve homogeneity and enhance stability, for example, by investigating point mutations or optimizing the insertion site.

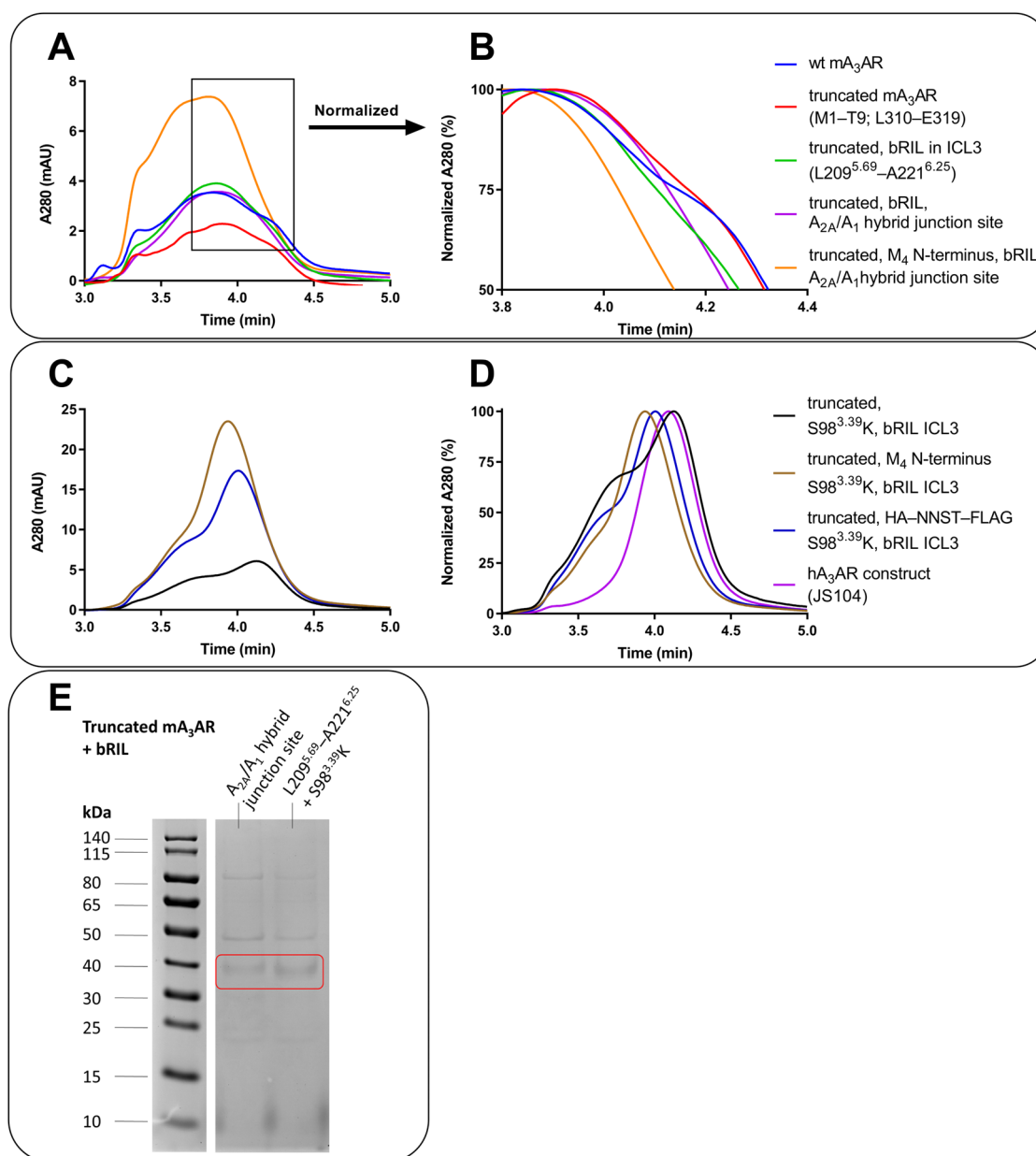


Figure 44. Mouse A₃AR constructs.

A: SEC chromatogram of initial mA₃AR constructs (3–5 min) B: Enlarged and normalized SEC chromatogram of initial constructs (x: 3.8–4.4 min; y: 50–100 %). C: SEC chromatogram of further mA₃AR constructs (3–5 min). D: Normalized SEC chromatogram of further mA₃AR constructs. hA₃AR construct JS104 (purple) is included for comparison. E: SDS-PAGE gel of two mA₃AR constructs corresponding to the purple and black graph, respectively.

3.16 Crystallization experiments

After achieving sufficient amounts of stable and homogenous hA₃AR protein, the next step was to conduct initial LCP crystallization experiments. For crystallization experiments, A₃AR constructs were expressed at a larger scale (900 mL *Sf9* cells), solubilized, purified, and subsequently concentrated. Solubilization and purification was performed in the presence of 25 μM TK-OT-018 since it combines appropriate solubility with high affinity. In contrast to small-scale purification, a concentration step was necessary to obtain a small volume of highly concentrated protein suitable for crystallization. Subsequently, two parts of protein were mixed with three parts of a monoolein:cholesterol (9/1) mixture using two Hamilton micro-syringes connected by a narrow-bore coupler. This protein-loaded mesophase was then dispensed onto glass sandwich plates and covered with varying precipitant solutions. In initial experiments, screening plates containing many different salts in different solutions were used to cover a broad spectrum of conditions. The composition of a well with initial crystal hits was subsequently used to build upon and create conditions to screen a narrower range of concentrations and additives.

3.16.1 First crystallization experiment of JS68

JS68, which combines untruncated N/C-termini, S97³⁻³⁹K, and bRIL in the A_{2A}/A₁ hybrid junction site, was chosen as the first protein construct to be used in crystallization experiments. JS68 was successfully expressed at a larger scale of 900 mL *Sf9* cells while maintaining high surface expression > 85 % (Figure 45 D). Half of the membrane preparation, corresponding to 450 mL biomass, was used for a single crystallization experiment. Protein purification in the presence of TK-OT-018 was successful and resulted in a decent protein yield (SEC peak height ~ 40 mAU, Figure 45 A, B). The purified protein was eluted in 4 steps of 500 μL elution buffer each. The 5th elution fraction exhibited only a low protein concentration and was, therefore, not added to the final protein solution. The subsequent concentration procedure of the first four fractions successfully increased the protein concentration ~80-fold while keeping a good peak shape in the SEC chromatogram. The shoulder right before the protein peak, indicating the degree of homogeneity, was in an acceptable range (Figure 45 B). Protein purity was confirmed by SDS-PAGE analysis (Figure 45 E), proving high purity. Only the protein-overloaded sample lane of the highly concentrated protein revealed minor impurities. The thermostability assay resulted in a

steep unfolding curve with a well-pronounced inflection point at $73.2 \pm 0.5^\circ\text{C}$ (Figure 45 C). The concentrated protein solution was then employed to conduct the first A₃AR LCP crystallization experiment. Various screening plates containing a vast spectrum of salt concentrations at pH values of 5.0–7.4 were used as precipitant solutions.

Table 6 shows promising wells with the corresponding precipitant conditions, which were based on 30 % PEG400 and 400/100 mM sodium citrate buffer at pH 5.6 (StockOptions Salt, Hampton Research). In these wells, small and gradual changes were observed over time. A comparison of day 0 and day 8 revealed that a fine sand of potential microcrystals started to grow. Examination under a microscope equipped with polarization filters supported the presence of crystals. Unfortunately, crystals remained small and rare. However, obtaining small crystal hits in the very first experiment is already a massive success since initial crystallization experiments screen a broad spectrum of crystallization conditions. Further optimization based on these conditions might improve crystal growth and quality. One aspect to consider is that JS68 still possessed all native N-glycosylation sites in its N-terminus (N3, N4, N12) and its ECL2 (N160^{ECL2}). Glycosylation of JS68 was shown to be incomplete and thus increased the heterogeneity of the protein sample, which might have interfered with crystal formation. Heterogenic glycosylation was determined to be the reason for the slightly blurry and not completely sharp protein band on the SDS-PAGE gel (see Section 3.8.3). All in all, the first crystallization experiment proved that the A₃AR construct JS68 met the requirements for crystallization, i.e., sufficient protein amount, purity, and stability, and it was able to form initial crystal hits.

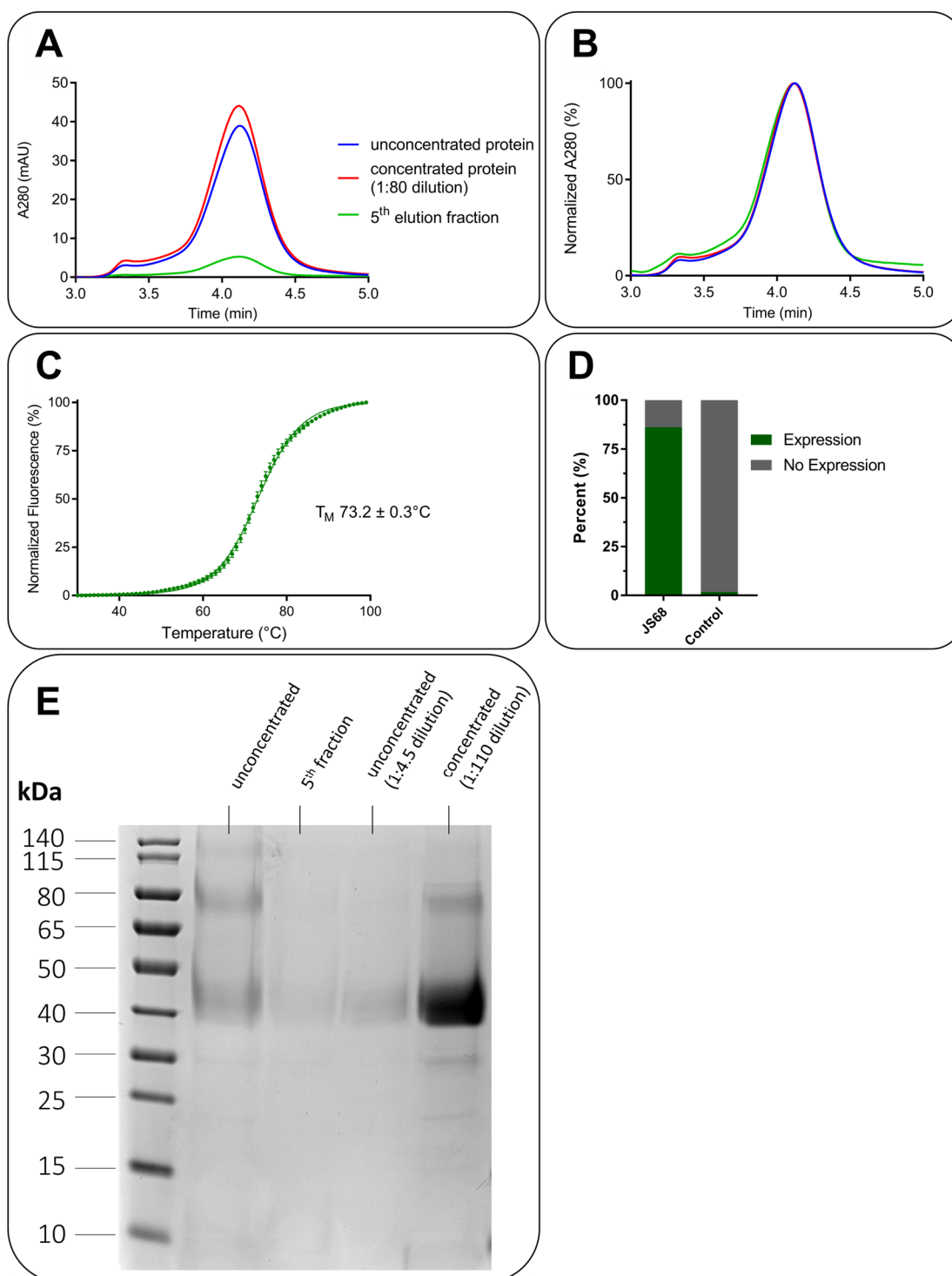
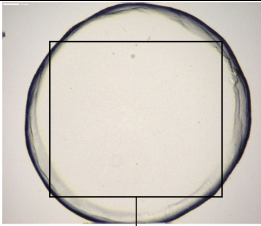
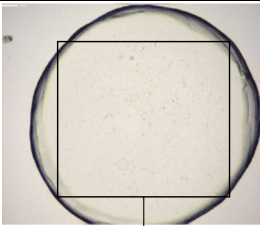
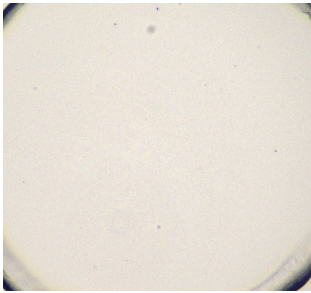
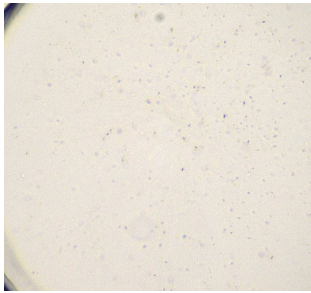
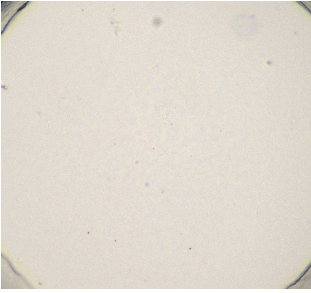
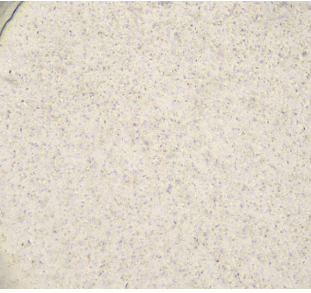
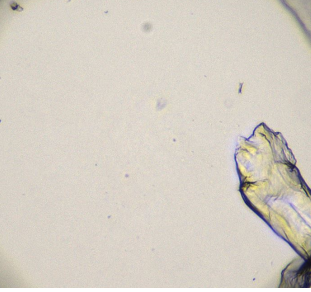
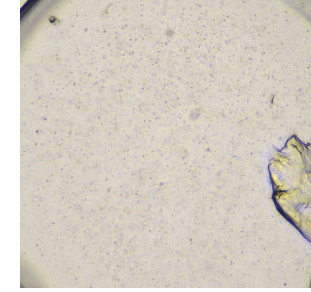
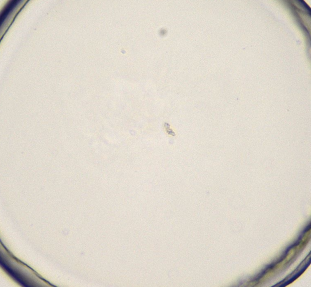
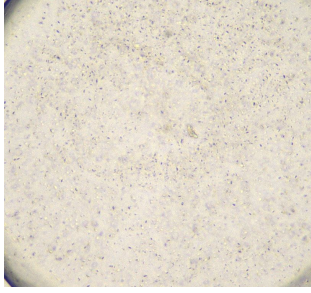
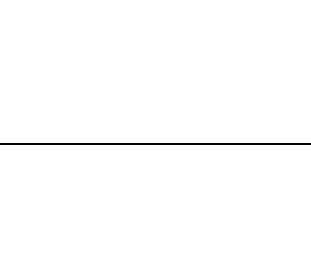
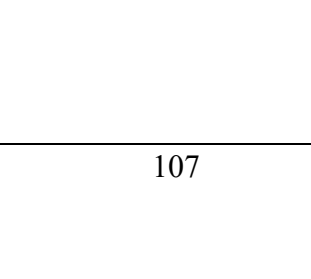


Figure 45. Protein analysis of JS68 (crystallization I).

A: SEC chromatogram (3–5 min). B: Normalized SEC chromatogram (3–5 min). C: Protein melting curve determined by the CPM thermostability assay. Data represent mean ± SEM from three experiments. D: Bar chart of the surface expression levels (single measurement). Non-infected *Sy9* insect cells were used as a control. E: SDS-PAGE gel. Total volume per lane was 30 μ L.

Table 6. Images of the first A₃AR crystallization experiment.

Images of wells with crystal hits at day 0 and day 8 (JS68, first crystallization experiment). Composition of the precipitant solution is listed in the right column.

Image		Crystallization condition
Day 0	Day 8	
		30 % PEG 400, 100 mM sodium citrate pH 5.6
		images are enlarged in the area of the droplets
		+ 50 mM ammonium formate
		+ 50 mM ammonium tartrate
		+ 50 mM sodium tartrate
		+ 200 mM potassium formate

3.16.2 Second crystallization of JS68

In the first crystallization experiment, the protein yield estimated by the protein peak height amounted to about 40 mAU. For comparison, A_{2A}AR crystallization experiments in our laboratory often yielded double the amount of protein, reaching up to 80–120 mAU. Since the subsequent concentration procedure was conducted identically, the final protein solution of JS68 might have had an insufficient protein concentration.

Therefore, double the amount of membrane preparation compared to the first experiment was employed in the second crystallization experiment (2x25 mL membrane preparation, in total 900 mL of *Sf9* insect cells). JS68 from both batches was solubilized and purified simultaneously but independently. Both proteins were eluted with 3x500 μ L of elution buffer and combined before concentration, which amounted to \sim 3 mL of purified protein solution. Figure 46 provides the analytical data of the purified protein. The protein concentration of the unconcentrated sample was similar to the first run, but the total volume was \sim 3 mL instead of 2 mL, which indicated that the overall protein amount could be increased by 50 %. The SEC chromatogram of the concentrated protein sample further proved this observation and yielded a peak height of \sim 60 mAU (compared to 40 mAU in the first crystallization experiment). Since concentration steps were conducted identically to those in the first experiment, the final protein solution displayed a 50 % higher concentration in this crystallization experiment. The 4th and 5th elution fractions still contained small amounts of protein. However, including these fractions was not worthwhile. The protein stability (T_M $71.9 \pm 0.3^\circ\text{C}$) was high and comparable to the first crystallization experiment (Figure 46 D). SDS-PAGE analysis revealed a single band and proved the crystallization-grade purity of the protein sample (Figure 46 C).

Crystallization conditions were partly screening-based and partly optimized based on the conditions which harbored initial crystal hits in the first crystallization experiment. Unfortunately, crystals remained rare and small with no clear further crystal evolution. Nevertheless, the protein concentration used for the crystallization was successfully increased by \sim 1.5-fold.

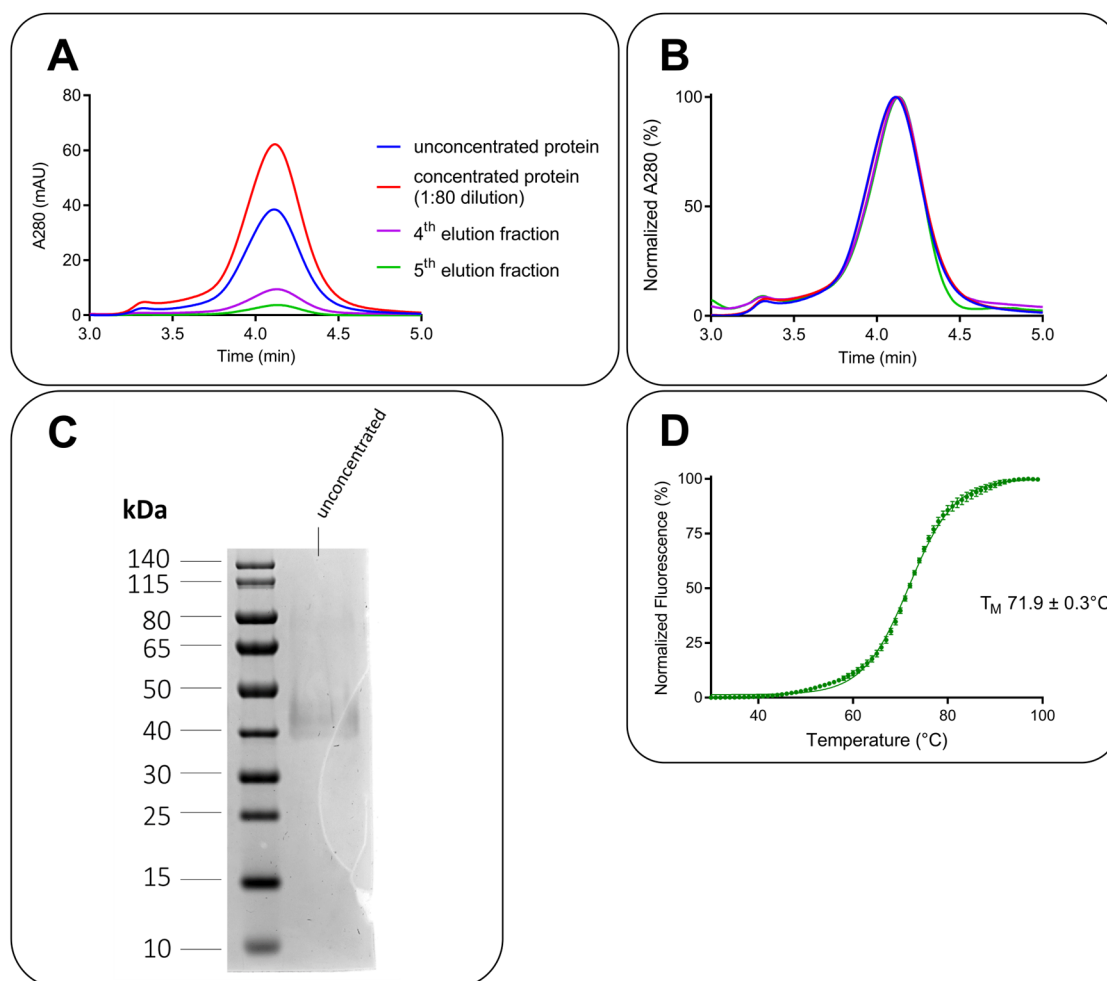


Figure 46. Protein analysis of JS68 (crystallization II).

A: SEC chromatogram (3–5 min). B: Normalized SEC chromatogram (3–5 min). C: SDS-PAGE gel. 2.5 times less volume of the unconcentrated protein solution was loaded onto the gel compared to Figure 45. Total volume per lane was 30 μL . D: Protein melting curve determined by the CPM thermostability assay. Data represent mean \pm SEM from three experiments.

3.16.3 Crystallization of JS68 — conclusion

The first two crystallization attempts were technically successful, and the final protein solutions fulfilled the fundamental requirements for purity, stability, and quantity. Even minor crystal hits could be observed. However, robust reproduction and significant improvement of initial crystal hits failed despite higher protein concentration and optimized precipitant conditions. Therefore, possibilities to further adjust the crystallization construct should be pursued and exploited first. The determined T_M value of $>70^\circ\text{C}$ demonstrated that the stability of JS68, which combines S97^{3.39}K and the A_{2A}/A₁ hybrid junction site, was most likely sufficient (also see Figure 65). However, protein homogeneity and flexibility were points worth targeting. SDS-PAGE analysis of JS68 revealed that the band

was slightly blurred and broadened. Moreover, the slope steepness and overall sharpness of the protein peak in the SEC chromatogram could be improved further.

JS68 still possesses four potential N-glycosylation sites, three N-terminal ones (N3, N4, N12) and one in the ECL2 (N160^{ECL2}). Heterogeneous glycosylation and the presence of N-glycans might have impeded the formation of ordered crystal lattices and are consequently removed in many cases of successful crystallization. Detailed investigation of the glycosylation state indicated that this also caused band and peak broadening in SDS-PAGE and SEC. Interestingly, the removal of N-glycans did not affect the performance of the constructs, nor did it reveal any disadvantages. Therefore, one could prevent N-glycosylation by mutating the corresponding asparagine residues to glutamine. Moreover, JS68's C-terminus is not truncated and carries a protease cleavage site before the 10xHis-tag, which is currently not needed. C-terminal residues L309–E318, the following EcoRI recognition site (amino acids glutamate and phenylalanine), and the protease cleavage site (sequence LEVLFQGP) sum up to 21 dispensable residues. Removing flexible parts is one of the central ideas for creating GPCR crystal constructs. Hence, truncation of these 21 amino acids might be beneficial. These two approaches were realized with the new constructs JS97 and JS104, which will be the following two subjects for crystallization experiments. JS97 equals JS68 without any N-glycosylation sites (additional mutations N3Q, N4Q, N12Q, N160^{ECL2}Q), and JS104 equals JS97 without the A₃AR C-terminus (L309–E318), and the EcoRI as well as the protease cleavage site.

3.16.4 Crystallization of JS97

As described above, crystallization of JS97 (untruncated termini, S97^{3.39}K, bRIL in A_{2A}/A₁ junction site, no N-glycosylation sites) was performed to investigate the effect of N-glycans on crystal formation.

Corresponding analytical results are depicted in Figure 47. The overall protein yield and concentration were in between the two attempts with JS68 (Figure 47 A, B). However, the unconcentrated sample revealed a significantly less pronounced shoulder in the SEC chromatogram. The thermostability was determined to be equivalent to that of JS68, resulting in a T_M of $73.0 \pm 0.3^\circ\text{C}$, which demonstrated that high stability did not depend on the presence of N-glycans (Figure 47 D). SDS-PAGE analysis illustrated the positive effect of removing N-glycans (Figure 47 C). The protein band occurred sharper and more concentrated than the slightly blurry band of JS68 while maintaining an excellent degree

of purity. These results proved that intact N-glycosylation sites were not crucial for the expression and the resulting protein yield, which contradicts a previous working hypothesis and the literature (see Section 3.3 and reference²¹⁴). However, the absence of glycans did not improve crystal formation.

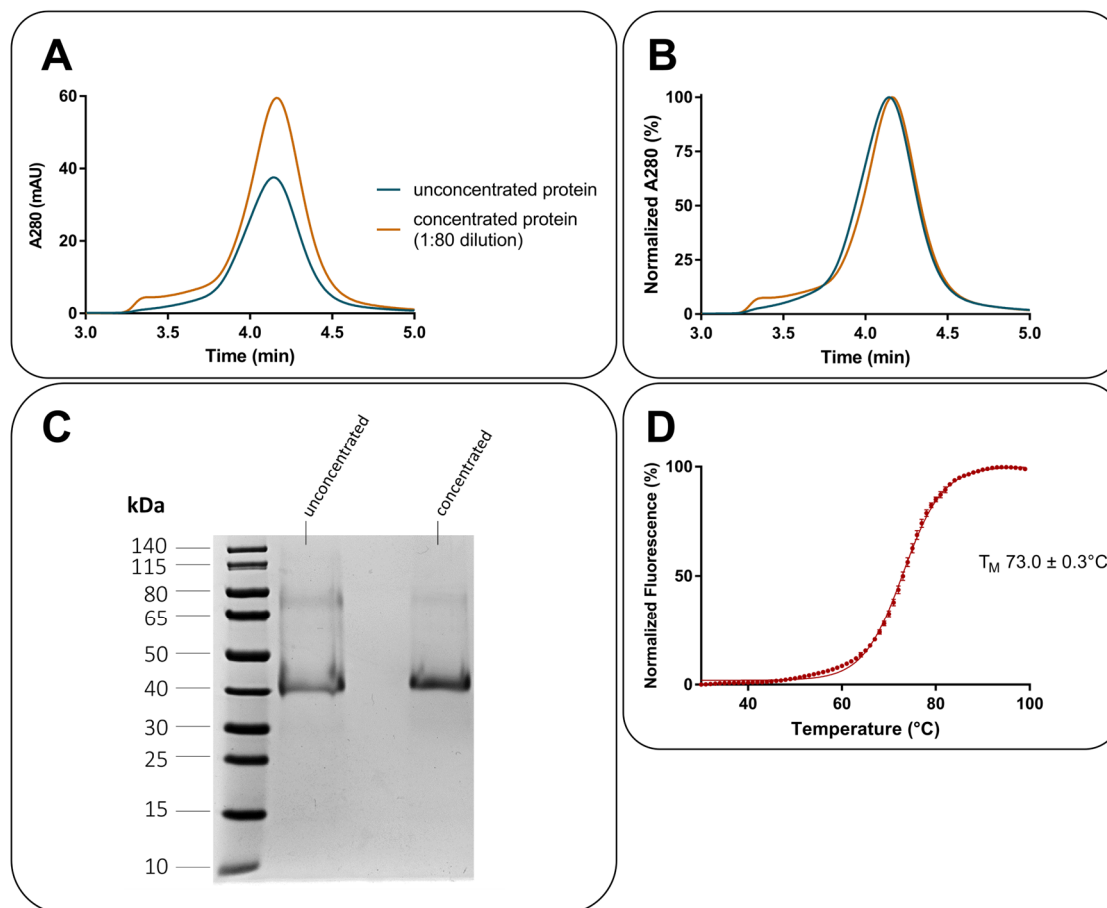


Figure 47. Protein analysis of JS97 for crystallization.

A: SEC chromatogram (3–5 min). B: Normalized SEC chromatogram (3–5 min). C: SDS-PAGE gel. Total volume per lane was 30 μ L. The concentrated sample was taken from the empty concentrator which was rinsed with 100 μ L of water. D: Protein melting curve determined by the CPM thermostability assay. Data represent mean \pm SEM from three experiments.

3.16.5 Crystallization of JS104

JS104 was the subject of the fourth A₃AR crystallization trial. JS104 combines the absence of N-glycans with the removal of flexible C-terminal parts (untruncated N-terminus, N3Q, N4Q, N12Q, N160^{ECL2}Q, S97^{3.39}K, bRIL in A_{2A}/A₁ hybrid junction site).

Similar to JS68 and JS97, JS104 displayed a decent protein yield resulting in a peak height of \sim 40 mAU of the unconcentrated protein sample (Figure 48, A). Interestingly, the protein concentration was more efficient and almost reached 100 mAU; the highest protein concentration ever achieved employing an A₃AR crystallization construct. JS104's protein

stability was $72.3 \pm 0.5^\circ\text{C}$, which was agreed with T_M values obtained in the first three crystallization experiments (Figure 48 D). SDS-PAGE analysis proved that the final protein was crystallization-grade with virtually no impurities (Figure 48 C). Moreover, the peak shape was flatter at the beginning and revealed a less pronounced shoulder, precisely the idea behind the removal of flexible parts. A detailed comparison of all crystallization attempts is provided in the next section. Unfortunately, this advancement did not yet substantially improve crystal growth or crystal quality.

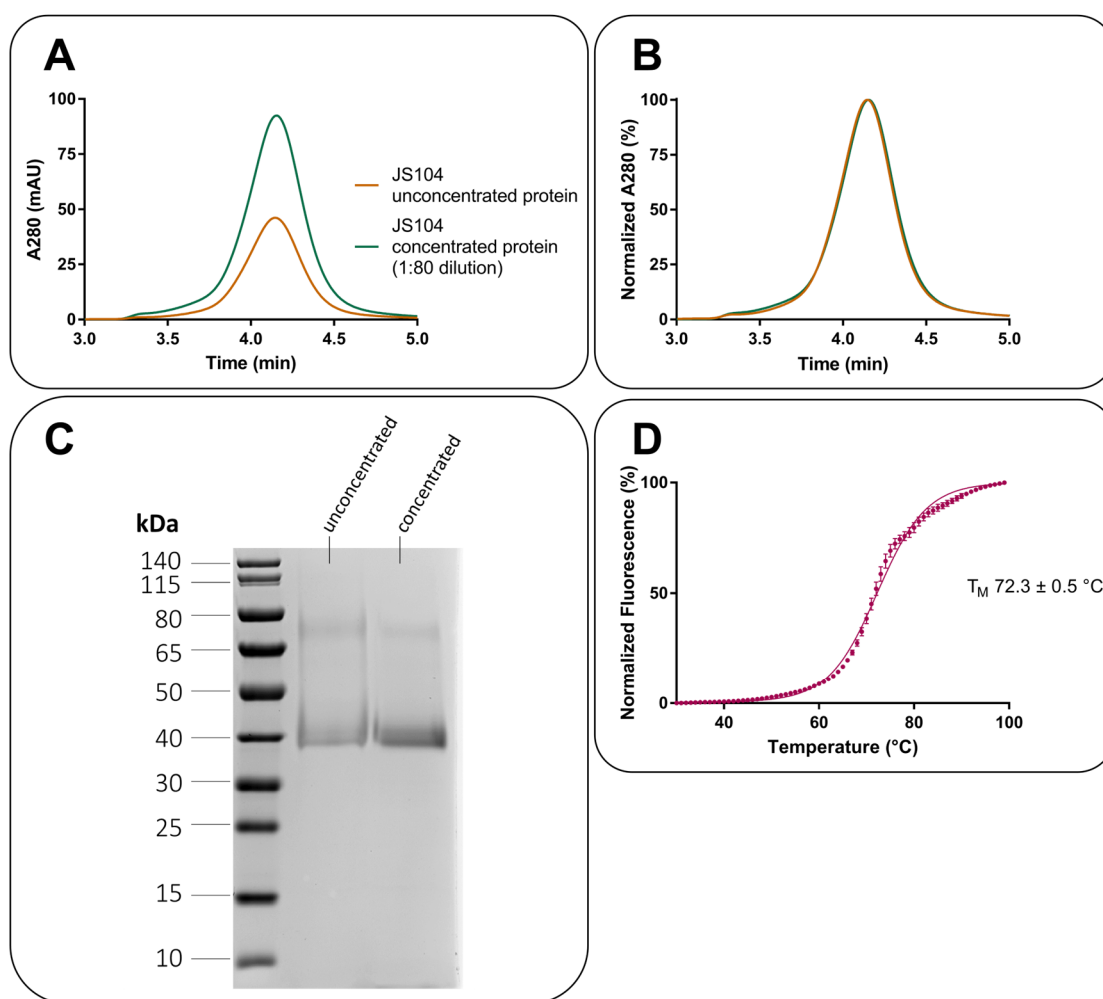


Figure 48. Protein analysis of JS104 for crystallization.

A: SEC chromatogram (3–5 min). B: Normalized SEC chromatogram (3–5 min). C: SDS-PAGE gel. The total volume per lane was $30\ \mu\text{L}$. The concentrated sample was taken from the empty concentrator which was rinsed with $100\ \mu\text{L}$ of water. D: Protein melting curve determined by the CPM thermostability assay. Data represent mean \pm SEM from three experiments.

3.16.6 Crystallization experiments — conclusion

The first crystallization experiments with A₃AR constructs were carried out using three different constructs (JS68, JS97, JS104). All constructs possessed the untruncated A₃AR N-terminus in combination with bRIL inserted into the A_{2A}/A₁ hybrid junction site and the S97^{3.39}K mutation. In addition, the native N-glycosylation sites were disrupted in JS97 and JS104 by mutation of the corresponding asparagine residues to glutamine. Furthermore, JS104's C-terminal region was trimmed to remove unfavorable flexible parts.

Purified protein solutions contained sufficient quantities of highly stable and pure proteins. Initial promising crystal hits could not be validated and improved. However, gradual progress was made in the protein characteristics. Figure 49 compares all four A₃AR crystallization attempts with the previously crystallized and published A_{2A}-PSB1-bRIL construct.²⁵⁷ The prime A_{2A}AR protein showed an exceptionally sharp and steep peak with almost no detectable shoulder. These characteristics might also play a role in the fact that the A_{2A}AR was the first AR to be crystallized and has provided an extraordinarily high number of crystal structures. Therefore, the results of the A₃AR crystallization attempts were compared to the A_{2A}-PSB1-bRIL protein. The detailed comparison showed that JS68 was eluted slightly earlier (Figure 49 B) and still possessed a relatively pronounced shoulder before the protein peak (Figure 49 C). JS97 and JS104, on the other hand, were eluted closer to the A_{2A}AR protein. These differences were conceivably caused by the presence of N-glycans in JS68, which increased its hydrodynamic radius. A comparison of SDS-PAGE gels nicely illustrated the effect of N-glycans on the width and sharpness of a protein band (Figure 49 D). Bands of JS97 and JS104 were significantly sharper and more compressed. The blur of JS68 might even indicate that heterogeneous glycosylation states are present. The constructs JS97 and JS104 entirely bypassed this problem. Moreover, JS104 revealed a reduced extent of the initial shoulder due to the removal of 21 surplus amino acids in the C-terminal region (Figure 49C). This observation supported the hypothesis that more rigid and less flexible proteins result in a steeper and sharper peak, potentially favorable for crystallization.

The progress toward characteristics of the A_{2A}-PSB1-bRIL construct indicated that modifications on a molecular basis could still further optimize the A₃AR construct for crystallization, leaving room for improving crystallization chances.

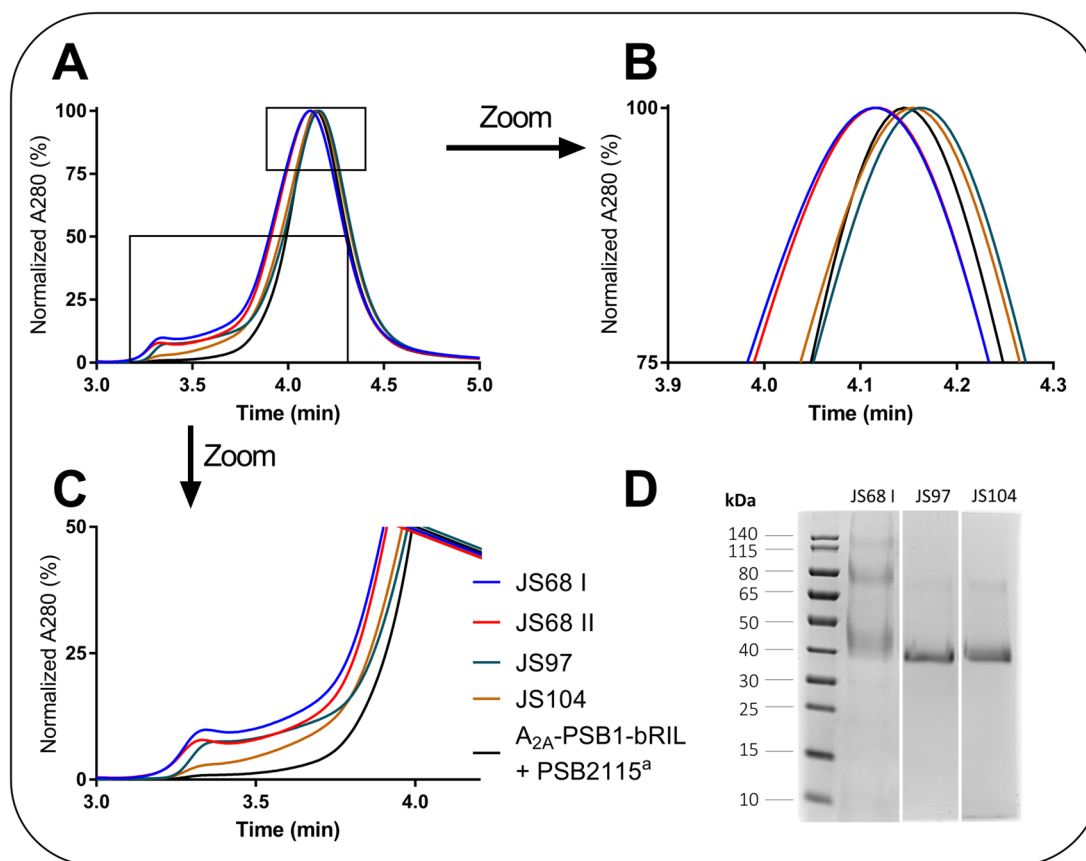


Figure 49. Comparison of A₃AR crystallization experiments.

A: Normalized SEC chromatogram (3–5 min) of listed proteins (concentrated samples). B: Enlargement of A (x: 3.9–4.3 min; y: 75–101 %). C: Enlargement of A (x: 3.0–4.2 min; y: 0–50 %). ^asee reference²⁵⁷ D: Composited SDS-PAGE gel.

3.17 Development of irreversible A₃AR antagonists

Covalent antagonists can be of great value in X-ray crystallography (also see Section 3.14.6). Until this point, the xanthine-based LUF7602 displays the only suitable and well-validated irreversible A₃AR antagonist, targeting Y265^{7,36}. In this side-project, the question of whether other residues are accessible for covalent antagonist binding and/or whether a change to other scaffolds might be beneficial will be investigated. The pyrazolo[3,4-*d*]pyrimidine (scaffold a), the 1,2,4-triazolo[5,1-*i*]purine (scaffold b) as well as the pyrido[2,1-*f*]purin-2,4-dione (scaffold c) scaffolds were taken into consideration. Compounds were designed together with Dr. Ahmed Temirak, who synthesized all investigated compounds and subsequently characterized together with Christin Vielmuth. Furthermore, it was tried to determine whether nucleophilic residues at the bottom of the orthosteric ligand binding pocket are accessible attack points. Previous studies revealed that asparagine N250^{6,55} forms two key hydrogen bonds with N1 and N9 of the

triazolopurine scaffold.^{125; 228–230} This crucial interaction orientates these compounds so that substituents in position 8 are directed towards the bottom of the ligand binding pocket. Consequently, insertion of reactive warheads at this position might lead to the possibility of covalent interaction, for example, with S181^{5.42} at the bottom of the ligand binding pocket. Additionally, a change of the reactive warhead was assessed. Determined K_i values are listed in Table 7, together with values of related compounds from the literature.

Both compounds of the pyrazolo-pyrimidine series, AT518 and AT519, did not reveal high-affinity binding at the A_{1-} , A_{2A-} , and A_{2B} ARs. AT518 showed only medium binding affinity (K_i 220 nM) at the A_3 AR in contrast to AT519, which was inactive at all AR subtypes. AT519's inactivity is surprising since the closely related compound 2b, which possesses a methoxy group instead of the fluorosulfonyl moiety, has already been determined to bind with high affinity to the A_3 AR (K_i 0.18 nM).¹²⁸ Thus, a fluorosulfonyl group in this position is not tolerated and abolishes binding to the A_3 AR.

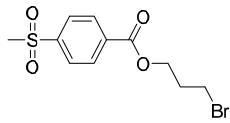
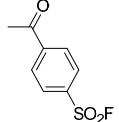
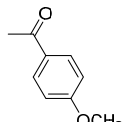
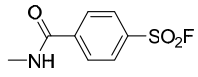
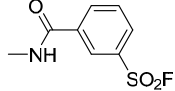
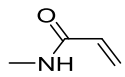
Based on the triazolopurine scaffold of OT-7999, the compounds AT515, AT527, AT529, AT531, AT553, and AT563 were investigated. In compounds AT515, AT527, and AT529, the trifluoromethyl group of OT-7999 is replaced by a bromo-, nitro- and amino-substituent. K_i values of all three compounds are \sim 0.2 nM at the A_3 AR. Bromo (AT515) and nitro (AT527) substituents maintain high receptor subtype selectivity (>400 -fold A_1/A_3 ; >1000 -fold A_{2A}/A_3 ; >1000 -fold A_{2B}/A_3), whereas the amino-substituted analog (AT529) is less selective and revealed binding to all AR subtypes with K_i values of <60 nM. Due to its high affinity for the A_3 AR (K_i 0.145 nM), the selectivity of AT529 remains decent and is >50 -fold vs. each other AR subtypes. In AT531 and AT553, the larger fluorosulfonylphenyl group is attached via an amide-linker to position 4 of the phenyl ring. The reactive fluorosulfonyl group was placed in the *para*- (AT531) and *meta*-position (AT553). Both compounds showed weak binding with K_i values \geq 1000 nM at the A_{1-} , A_{2A-} , and A_{2B} ARs and moderate affinity for the A_3 AR (AT531 K_i 21.2 nM; AT553 K_i 134.2 nM). Consequently, the *para*-substituted AT531 was superior to the *meta*-substituted AT553 with an approximately 6-fold lower K_i value. A second moiety for irreversible interactions was investigated with AT563, in which the reactive fluorosulfonyl group was replaced by an acrylamide function acting as a Michael acceptor. Together with the adjacent phenyl ring, it forms the *N*-phenylprop-2-enamide group, a less reactive warhead than the sulfonyl fluoride.²⁹⁴ AT563 showed subnanomolar affinity for the A_3 AR (K_i 0.28 nM) and moderate affinity for the A_1 AR (K_i 123 nM) while maintaining high selectivity towards the A_{2A-} and A_{2B} ARs ($K_i > 1000$ nM). The K_i ratio A_1/A_3 was \sim 440,

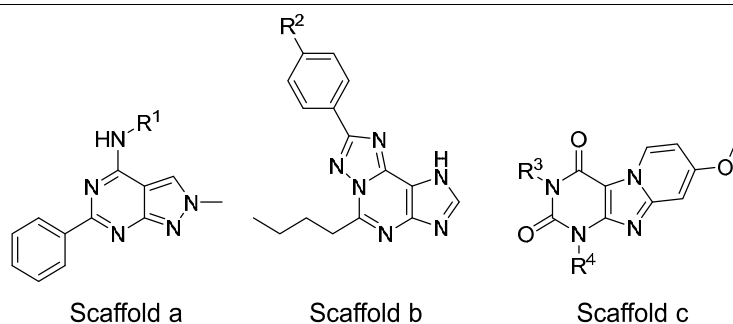
similar to that of AT515 and AT527. Compared to the parent compound OT-7999, the affinity is increased by ~5-fold, but the selectivity towards the A₁AR is decreased. Overall, smaller substituents are superior in affinity and selectivity, but larger moieties still preserve decent affinity, allowing the insertion of a fluorosulfonylphenyl moiety. This conclusion only partially applies to the amino substituent, which maintains a high affinity for the A₃AR but substantially lacks selectivity towards the other ARs.

Next, LUF7602 and its related compound AT562 (compound 17a) were resynthesized as positive controls, e.g., for use in the CPM thermostability assay (see Section 3.14.6), as a reference compound to validate further compounds or to be employed in crystallization experiments. AT562 failed to bind to any AR, whereas LUF7602 revealed an apparent K_i of 14.8 nM for the A₃AR, which is in agreement with the literature value of 10 nM. A shorter incubation time (1 h instead of 2 h) might be the reason for a slightly lower affinity because of the time-dependent affinity shift of irreversible ligands. A C₂ linker between the pyridopurinone scaffold (AT562) and the reactive moiety is unsuitable, coinciding with previous findings.¹³¹ Interestingly, an assay with overnight (~16 h) incubation time revealed an apparent K_i value of 2.9 nM for LUF7602, which can be used as an additional indicator for its covalent binding mode and might represent its “equilibrium” K_i value. Replacing the propyl chain with a cyclopropylmethyl moiety in position 1 was superior and improved affinity and kinetic parameters for a closely related compound.²⁹⁵ This idea was transferred to LUF7602 resulting in the cyclopropyl analog AT622. In fact, this modification resulted in a ~4-fold increased A₃AR affinity and an ~2-fold improved selectivity vs. the A₁AR.

All in all, AT563 could be a novel irreversible A₃AR antagonists, possessing moderate to high A₃-affinity and subtype selectivity. AT563's potential interaction partners are located down at the bottom of the binding pocket, which displays a novel target point that has not yet been employed. Moreover, LUF7602 was improved by modification of position 1, resulting in increased affinity and selectivity. Changing the pyrido[2,1-*f*]purin-2,4-dione scaffold to an imidazole-based imidazo[2,1-*f*]purin-2,4-dione scaffold might further tweak the properties of AT563 since compounds based on such scaffolds appeared to be slightly more selective and potent.¹³⁰

Table 7. Affinity novel A₃AR antagonists, including related compounds from the literature.

Name	Scaffold	R ¹ /R ² /R ³ /R ⁴	hA ₁ AR ^a	hA _{2A} AR ^b	hA _{2B} AR ^c	hA ₃ AR ^d
			K _i ± SEM (nM)			
			or (% inhibition ± SEM at 1 μM)			
AT518	a		>1000 (7 ± 6, n=2)	>1000 (17 ± 5)	>1000 (18 ± 12, n=3)	220 ± 16.9
AT519	a		>1000 (15 ± 2 n=2)	>1000 (4 ± 5)	>1000 (14 ± 0)	>1000 (24.8 ± 5.6)
2b ^f	a		1037.0 ± 105.0 ^f	3179.0 ± 315.0 ^f	-	0.18 ± 0.02 ^f
AT515	b	-Br	61.7 ± 7.2	>1000 (37 ± 4)	~1000 (49 ± 4 n=3)	0.146^c ± 0.016
AT527	b	-NO ₂	98.8 ± 5.5	~1000 (43 ± 8, n=3)	299 ± 84 extrapolate	0.213^c ± 0.028
AT529	b	-NH ₂	7.71 ± 0.61	54.3 ± 11.4	25.3 ± 5.3	0.145^c ± 0.018
AT531	b		>1000 (15 ± 11, n=2)	1070 ± 210	~1000 (43 ± 8, n=3)	21.2 ± 4.3
AT553	b		>1000 (4 ± 6, n=2)	>1000 (14 ± 6, n=2)	>1000 (-9 ± 16, n=2)	134.2 ± 18.3
AT563	b		123 ± 20	>1000 (27 ± 1, n=2)	>1000 (21 ± 0, n=2)	0.28 ± 0.01
OT-7999 ^g	b	-CF ₃	(4 at 10 μM) ^g	(31 at 10 μM) ^g	(6 at 10 μM) ^g	0.95^g



Name	Scaffold	R ¹ /R ² /R ³ /R ⁴	hA ₁ AR ^a	hA _{2A} AR ^b	hA _{2B} AR ^c	hA ₃ AR ^d
			K _i ± SEM (nM) or (% inhibition ± SEM at 1 μM)			
AT562 (17a ^h)	c	R ³ = propyl R ⁴ =	>1000 (7 ± 0 at 0.1 μM, n=2)	>1000 (10 ± 5, n=2)	>1000 (9 ± 6, n=2)	>1000 (16.7 ± 5.0)
LUF7602 ^g	c	R ³ = propyl R ⁴ =	794 ± 232	>1000 (25 ± 14, n=2)	>1000 (31 ± 13, n=2)	14.8 ± 1.5
AT622	c	R ³ = R ⁴ =	1810 ± 750	>1000 (27 ± 4, n=2)	>1000 (15 ± 3, n=2)	3.43 ^e ± 0.29

Experiments at A₁-, A_{2A}-, A_{2B}ARs were performed by Christin Vielmuth

^aDisplacement of specific [³H]CCPA binding to CHO-S cells transiently expressing the hA₁AR.

^bDisplacement of specific [³H]MSX-2 binding to CHO-S cells transiently expressing the hA_{2A}AR.

^cDisplacement of specific [³H]PSB-603 binding to CHO-S cells transiently expressing the hA_{2B}AR.

^dDisplacement of specific [³H]PSB-11 binding to CHO-S cells transiently expressing the hA₃AR.

^eExperiments performed by Christin Vielmuth ^fsee reference ¹²⁸ ^gsee reference ¹⁰⁶ ^hsee reference ¹³¹ ^{a,b,c,d}Data represent mean ± SEM from three experiments unless stated otherwise.

3.17.1 Wash-out experiments

Wash-out experiments can be utilized to examine the binding mode of potentially irreversible ligands. Covalently bound ligands, e.g., antagonists, possess an extremely slow dissociation rate. Once these ligands are bound to a receptor, they can barely be removed, contrary to reversible ligands. Precisely this property was exploited in the following wash-out experiments. hA₃AR membrane preparations were incubated with A₃AR antagonists at concentrations corresponding to 10-fold their K_i values for 2 h at room temperature. After a thorough washing procedure, the remaining binding capacity for [³H]PSB-11 was determined. The irreversible A₃AR antagonist LUF7602 and the reversible analog of AT563, TK-OT-018, were included as positive and negative control, respectively (for structures see Table 7).

The irreversible antagonist LUF7602 almost completely prevented the specific binding of [³H]PSB-11 and showed high inhibition of specific radioligand binding (>90 %) even after the wash-out procedure, proving its irreversible binding mode. In contrast, the reversible antagonist TK-OT-018 resulted in an inhibition of 50 % without the wash-out procedure and was almost entirely washed out, resulting in just below 10 % inhibition. Membranes incubated with the potentially irreversible antagonist AT563 were still able to bind 20 % of the radioligand compared to the controls, and the subsequent wash-out further decreased the inhibition. Although AT563 was washed out to a larger extent than LUF7602, the inhibition of specific radioligand binding remained at approximately 65 %, which significantly differs from the results of its reversible analog TK-OT-018. The acrylamide function of AT563 might react slower than the fluorosulfonyl moiety of LUF7602 resulting in less bound ligand after 2 h incubation time. Moreover, the covalent linkage between AT563 and the A₃AR might be more prone, leading to a larger effect of the reverse reaction. Further investigation by site-directed mutagenesis, exchanging potential interaction partners located at the bottom of the ligand binding pocket, will assist in determining its binding mode ultimately.

The same wash-out experiment but employing membrane preparations of the A₃AR-S97^{3.39}K-bRIL (JS68) construct expressed in *Sf9* insect cells revealed that incubation with the compounds AT563 and LUF7602 resulted in clearly less inhibition of specific [³H]-PSB-11 binding compared to the experiment using wt A₃AR membrane preparation of A₃AR-expressing CHO-S cells. Moreover, LUF7602 appeared to be removed entirely by the washing procedure resulting in an inhibition of radioligand binding below 1 %.

These altered antagonist binding might be caused by introduced modification or the expression in *Sf9* insect cells, which will be discussed in the following sections.

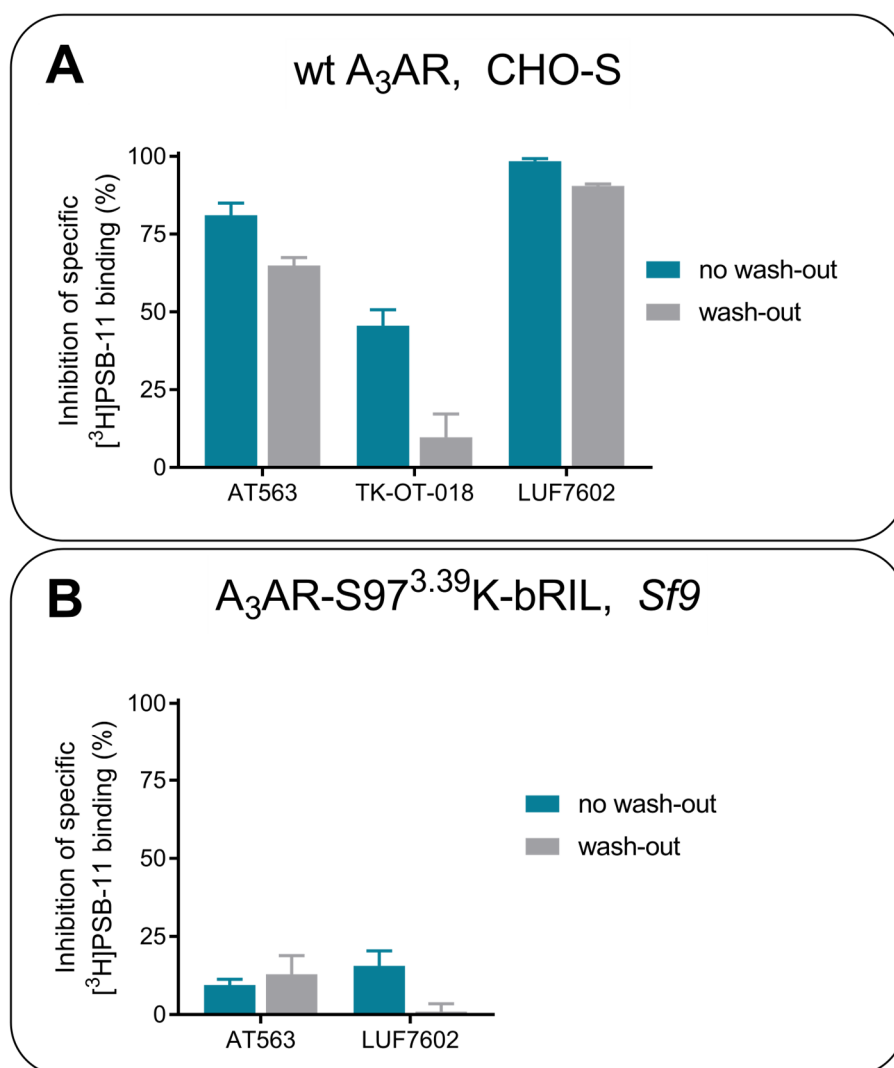


Figure 50. Wash-out experiments.

A: Data represent mean \pm SEM from three (AT563), and two (TK-OT-018, LUF7602) experiments performed in duplicates. B: The construct A₃AR-S97^{3.39}K-bRIL possessed bRIL as a fusion partner inserted into the A_{2A}/A₁ hybrid junction site, an N-terminal HA-tag, and a C-terminal 10xHis-tag. Data represent mean \pm SEM from a single experiment performed in duplicates.

3.18 Construct validation

3.18.1 Ligand binding at constructs expressed in *Sf9* insect cells

Validation of the modified construct for crystallization displays a crucial checkpoint for increasing the chances to obtain a meaningful X-ray structure. Therefore, constructs listed in Table 8 were expressed in *Sf9* cells (small-scale, 40 mL), and their membrane preparations were investigated by homologous competition binding of PSB-11 vs. [³H]PSB-11 (K_D 4.9 nM) to determine their K_D values.¹²⁶ Competition binding curves and K_D values are depicted in Figure 51 and Table 8, respectively.

None of the investigated constructs resulted in a low nanomolar K_D value. Even JS1 (K_D 26.5 ± 11.2 nM), which corresponds to the wt A_3AR with N-terminal HA- and FLAG-tag and a C-terminal His-tag, revealed a 5-fold lower affinity compared to the wt A_3AR expressed in CHO-S cells (K_D 4.2 ± 0.1 nM). Interestingly, the membrane preparation of a small-scale expression did not result in sufficient specific binding of [³H]PSB-11. Only the medium-scale expression of JS1 and, consequently, the higher concentrated membrane preparation produced just sufficient specific binding to be measurable. The introduction of the stabilizing S97^{3.39}K mutant (JS79) and the combination with the fusion partner bRIL (JS78) further increased the K_D value. JS68, which was already employed in first crystallization experiments, showed a 51-fold lower affinity than the wt A_3AR expressed in CHO cells (K_D 250 ± 14 nM). A chimeric $A_3AR/A_{2A}AR$ construct comprising the A_3AR (residues 1–284) fused to the C-terminus of the $A_{2A}AR$ (residues 219–412) revealed a 2-fold improved expression of functional receptor protein compared to the wt A_3AR .²⁷⁸ However, the replacement of helix VIII by the corresponding $A_{2A}AR$'s helix VIII did not improve the affinity to PSB-11 (JS81). Moreover, removing all N-glycosylation sites did not crucially affect ligand binding (JS97).

A precise comparison of the determined K_D values was not possible since the radioligand did not provide the essential high-affinity binding anymore. Nevertheless, the assessment of ligand binding revealed that the optimized construct JS68 bearing S97^{3.39}K and bRIL within the A_{2A}/A_1 hybrid junction site failed to bind PSB-11 with low nanomolar affinity. Each modification, which improved the construct's stability, appeared to further impair the binding of PSB-11. The wt A_3AR construct (JS1) already indicated altered binding properties when expressed in *Sf9* cells as compared to the wt A_3AR expressed in CHO-S cells. As the increased stability of constructs typically correlates with higher amounts of receptor protein incorporated into the *Sf9* cell membranes, the observed

correlation between stability and reduced affinity might be caused by the relative depletion of a membrane component and or not exclusively by the modifications themselves.

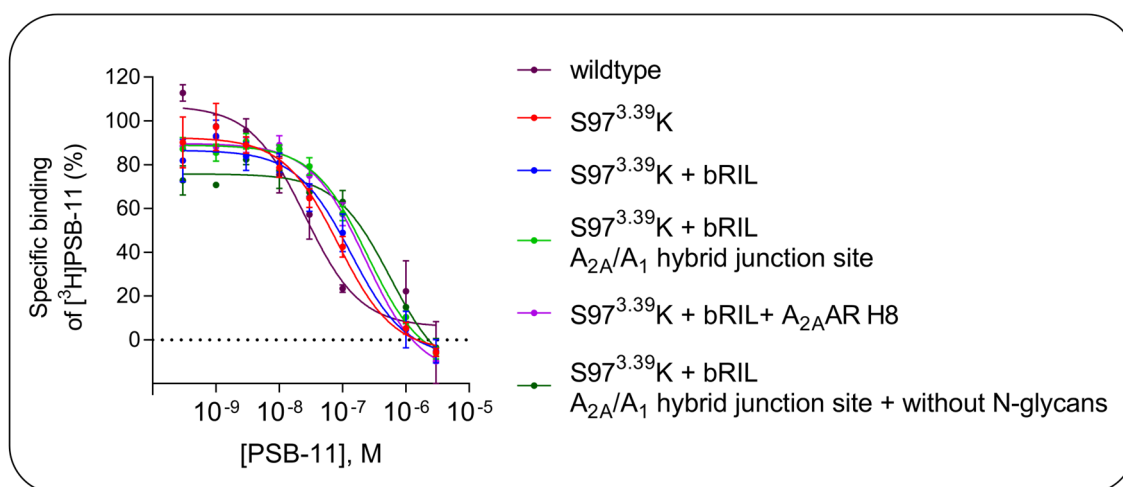


Figure 51. Competition binding studies at A_3AR constructs expressed in *Sf9* insect cells. Data represent means \pm SEM from three independent experiments.

Table 8. Affinity of PSB-11 at various A_3AR constructs expressed in *Sf9* cells.

Constructs were expressed in *Sf9* insect cells and possess an N-terminal HA-and FLAG-tag as well as a C-terminal His-tag.

hA ₃ AR constructs — <i>Sf9</i> expression	PSB-11 vs. [³ H]PSB-11 K _D \pm SEM [nM] (n=3)
wt (JS1) ^a	26.5 \pm 11.2
S97 ^{3.39} K (JS77)	85.7 \pm 16.6
S97 ^{3.39} K + bRIL (JS78)	141 \pm 26
S97 ^{3.39} K + bRIL (A _{2A} /A ₁ hybrid junction site, JS68)	250 \pm 14
S97 ^{3.39} K + bRIL (A _{2A} /A ₁ hybrid junction site) + A _{2A} AR helix VIII (JS81)	243 \pm 62
S97 ^{3.39} K + bRIL (A _{2A} /A ₁ hybrid junction site) + without N-glycans (JS97)	609 \pm 246
wt A ₃ AR (expressed in CHO cells)	4.2 \pm 0.1 (4.9 ^b)

^amedium-scale expression (250 mL); ^bsee reference¹²⁶

3.18.2 Ligand binding at constructs expressed in CHO-S cells

Radioligand competition assays at A₃AR constructs expressed in *Sf9* insect cells had revealed altered binding properties. Thus, constructs carrying the same modifications were transiently expressed in CHO-S cells and subsequently subjected to the homologous competition binding assay of PSB-11 vs. [³H]PSB-11 to determine their K_D values (Figure 52, Table 9).

In general, all constructs without an N-terminal HA-tag exhibited low nanomolar K_D values similar to the K_D value of [³H]PSB-11 previously determined by saturation binding or with the employed homologous competition binding assay.¹²⁶ S97^{3,39}K and bRIL alone or in combination with and without a C-terminal His-tag resulted in K_D values of 4.7 nM, 7.9 nM, 5.4 nM, and 6.3 nM, respectively. The obtained K_D values prove that neither the mutated sodium binding pocket nor bRIL within the A_{2A}/A₁ hybrid junction site or a C-terminal His-tag significantly decreased the affinity of PSB-11. Only the N-terminal insertion of the HA signaling peptide resulted in a 2–3-fold shift of the K_D value compared to those constructs without HA-tag. Constructs carrying the HA-tag and bRIL without and with the S97^{3,39}K mutation showed a significantly decreased K_D value of 16.5 and 18.1 nM, respectively. Interestingly, the HA-tag increased the specific counts and thus B_{max} by several fold indicating that it improved the expression. This observation could suggest a similar tendency as observed after the expression in insect cells: higher levels of A₃AR appeared to be associated with a lower affinity to PSB-11. Removal of any N-glycosylation sites seemed to abolish the expression since no specific [³H]PSB-11 binding could be measured. Even a medium-scale expression did not yield a membrane preparation that showed specific radioligand binding, indicating that N-glycosylation might be essential for the biosynthesis of the A₃AR. All in all, the expression in mammalian cells provided a different picture than the expression in *Sf9* insect cells and demonstrated that stabilizing modifications did not significantly affect the binding of the A₃AR-selective antagonist [³H]-PSB-11.

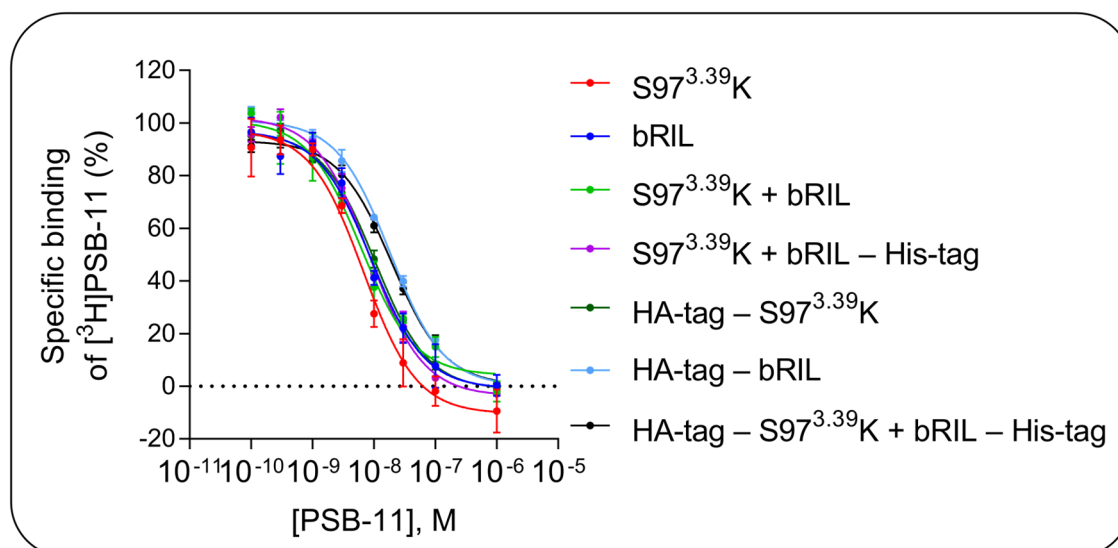


Figure 52. Competition binding studies at A_3AR constructs expressed in CHO-S cells. Data represent means \pm SEM from three independent experiments.

Table 9. Affinity of PSB-11 at various A_3AR constructs expressed in CHO-S cells.

All constructs possess an N-terminal FLAG-tag. One-way ANOVA of corresponding pK_D values was employed to assess statistical significance compared to the wt A_3AR (ns $p \geq 0.5$ ns; * $0.05 > p > 0.01$; ** $0.01 \geq p > 0.001$; *** $0.001 \geq p > 0.0001$; **** $p < 0.0001$).

hA_3AR constructs — CHO-S expression	PSB-11 vs. [3H]PSB-11 $K_D \pm$ SEM [nM] (n=3)
wt	4.2 \pm 0.1 (4.9 ^a)
S97 ^{3.39} K	4.7 \pm 1.4
bRIL (A_{2A}/A_1 hybrid junction site)	7.9 \pm 3.6
S97 ^{3.39} K + bRIL (A_{2A}/A_1 hybrid junction site)	5.4 \pm 2.2
S97 ^{3.39} K + bRIL – His-tag (A_{2A}/A_1 hybrid junction site)	6.3 \pm 0.8
HA-tag – S97 ^{3.39} K	8.3 \pm 0.6
HA-tag – bRIL (A_{2A}/A_1 hybrid junction site)	16.5 \pm 1.2*
HA-tag – S97 ^{3.39} K + bRIL – His-tag (A_{2A}/A_1 hybrid junction site)	18.1 \pm 1.2**

^asee reference¹²⁶

3.18.3 NECA binding

Homologous competition binding of the agonist NECA vs. [3H]NECA was carried out to further characterize the S97^{3.39}K mutation and bRIL insertion, as well as the differences observed between A_3AR constructs expressed in mammalian as compared to insect cells. Therefore, A_3AR constructs bearing the modified sodium binding pocket or

the fusion partner were transiently expressed in CHO-S cells. An N-terminal HA-tag was inserted to enhance expression. On the other hand, the wt A₃AR and A₃AR constructs bearing the same modifications were expressed in *Sf9* insect cells. Moreover, the corresponding wt A₃AR construct, JS1, was co-expressed with hGβ₁γ₂ and hGα_{i1} to ensure sufficient amounts of the cognate G protein interaction partners, which are likely required for high-affinity agonist binding.^{13; 296; 297} hGα_{i1} was co-expressed with hRic8A acting as a GEF and a chaperone.²⁹⁸ K_D values of 6.2 nM (saturation binding of [³H]NECA) and 26 nM (competition binding vs. [¹²⁵I]ABA) had been reported for NECA in the literature.^{60; 107} Competition binding curves and determined K_D values are presented in Figure 53 and Table 10, respectively.

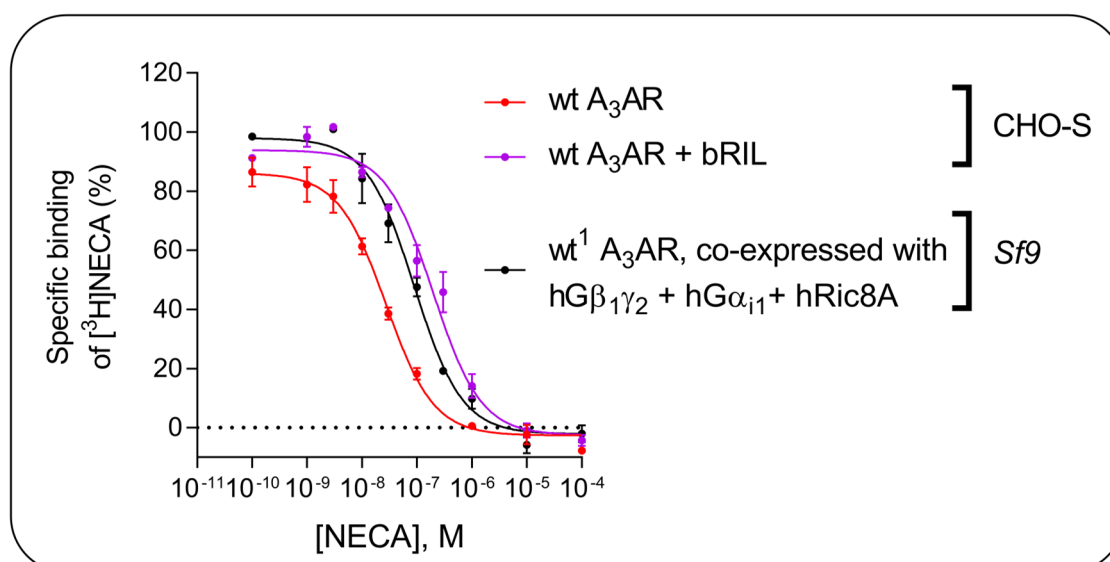


Figure 53. Homologous competition binding of NECA vs [³H]NECA.

Data represents mean ± SEM from three experiments. ¹Construct: HA-FLAG-wt A₃AR-His.

Table 10. Affinity of A₃AR constructs for the agonist NECA.

Expression system	hA ₃ AR construct	NECA vs. [³ H]NECA K _D ± SEM [nM] (n=3)
CHO-S	wt	14.3 ± 1.4
	bRIL ^{1,2}	197 ± 56***
	S97 ^{3,39} K ¹	No high-affinity binding detectable
<i>Sf9</i>	wt ³	>1000 ⁴
	wt ³ + hGβ ₁ γ ₂ + hGα _{i1} + hRic8A	92.9 ± 14***
	bRIL ^{2,3}	>1000 ^{4,5}
	S97 ^{3,39} K ³	No high-affinity binding detectable ⁵

¹N-terminal HA-tag ²A_{2A}/A₁ hybrid junction site ³construct: HA-FLAG-A₃AR-His ⁴Specific [³H]NECA binding was not sufficient to determine a K_D value. ⁵Preliminary results from two experiments. Statistical evaluation was carried using the corresponding pK_D values by one-way ANOVA with Dunnett's post hoc test (ns p ≥ 0.5 ns; * 0.05 > p > 0.01; ** 0.01 ≥ p > 0.001; *** 0.001 ≥ p > 0.0001; **** p < 0.0001). Means were compared to the pK_D value of the wt A₃AR expressed in CHO-S cells.

The wt A₃AR, expressed in CHO-S cells, resulted in a K_D of 14.3 nM, which corresponds well with the literature values. The S97^{3,39}K mutation completely abolished specific [³H]NECA binding. Replacement of the ICL3 by bRIL and thus prevention of G protein coupling decreased the affinity by ~14-fold (K_D 197 nM) but did not completely block NECA binding.

The wt A₃AR (HA-FLAG-wt A₃AR-His, JS1), expressed in *Sf9* cells, displayed a K_D value of 92.9 nM for NECA when co-expressed with G proteins hGβ₁γ₂ and hGα_{i1}. Without its G protein interaction partners, NECA binding was extremely weak and insufficient for determining an exact K_D value. Similarly, only weak NECA binding was observed for the A₃AR-bRIL construct indicating only low-affinity binding. No binding could be observed for the A₃AR construct carrying the S97^{3,39}K mutation.

The S^{3,39}K mutation is known to prevent any detectable NECA binding presumably by modifying the conserved sodium binding pocket and thus impeding the rearrangement of key activation switches, which are required for agonist binding.²⁵⁷ Insertion of fusion partners (bRIL, T4L) into the ICL3 of GPCRs is commonly used for optimizing a receptor

for structural studies. This insertion prevents functional G protein coupling but does not prevent agonist binding in general. Characterization of the β_2 AR-T4L crystallization construct showed that agonists (isoproterenol, epinephrine, salbutamol, formoterol) could still bind with high affinity and that the affinity was even increased by at least 2-fold (competition binding vs. the antagonist [3 H]DHA). The authors stated that the insertion of T4L might have changed the arrangement of helix V and VI at the intracellular side and consequently caused a shift towards a partially constitutively active receptor species that had a higher affinity for agonists. Interestingly, all constructs investigated in those binding studies were expressed in *Sf9* insect cells proving that insect cells are capable of providing all requirements for high-affinity agonist binding to the G_s -coupled β_2 AR.¹⁵⁰ Similarly, the A_{2A} -T4L crystallization construct expressed in HEK293T cells displayed a 3-fold increased affinity to the A_{2A} AR agonist CGS21680 (competition binding vs. the antagonist [3 H]ZM241385).¹⁵⁴ The analogous crystallization construct (A_{2A} -bRIL- Δ C) bearing bRIL instead of T4L revealed a 1.5-fold increased affinity for the agonist UK432,097 (competition binding vs. [3 H]ZM241385).³⁸ Moreover, the A_{2A} - Δ C-bRIL construct expressed in *Sf9* insect cells did not show a significantly reduced NECA affinity as determined in competition binding experiments vs. the A_{2A} AR antagonist [3 H]MSX-2.²⁵⁷ Similar results were obtained for the G_i -coupled A_1 AR, A_3 AR's closest relative in the AR family. The A_1 -bRIL crystallization construct expressed in FlpIn-CHO cells displayed a 3-fold increased affinity for NECA (competition binding vs. the antagonist [3 H]DPCPX).²¹⁴ These studies indicated that GPCRs whose ICL3 is replaced by a fusion partner can still bind their agonists, even with increased affinity and even when expressed in insect cells.

In contrast, bRIL insertion into the ICL3 of the A_3 AR caused a significantly reduced affinity for the agonist NECA (14-fold, 14.3 nM vs. 197 nM) when expressed in CHO-S cells. This observation suggests that interaction between the ICL3 of the A_3 AR and its G proteins is likely important for high-affinity agonist binding. Consequently, the potential lack of sufficient amounts of G proteins in insect cells might cause a decreased NECA affinity for the wt A_3 AR when expressed in insect cells. Since bRIL prevents G protein interaction with the ICL3, the potential lack of G proteins in insect cells should not affect NECA binding to the A_3 AR-bRIL construct. The A_3 AR-bRIL construct expressed in *Sf9* insect cells exhibited only weak NECA binding, which was not even sufficient for determining a K_D value. Moreover, the wt A_3 AR required co-expression with the $G\beta_1\gamma_2$ and $G\alpha_{i1}$ proteins to bind NECA with moderate affinity implying that G proteins play a role for

agonist binding at the A₃AR in general. Nevertheless, the discrepancy in ligand binding between A₃AR constructs expressed in insect and mammalian cells was also observed for the agonist NECA since even co-expression with the cognate G proteins resulted in a 6.5-fold decreased affinity for NECA as compared to the wt A₃AR expressed in CHO-S cells. However, co-expression enabled moderate NECA binding in the first place. In conclusion, these data suggest that G proteins could play a role for ligand binding to the A₃AR in general which is clearly different compared to other GPCRs, e.g., the β₂AR or the A_{2A}AR.

3.18.4 Cholesterol depletion

The altered binding properties of A₃AR constructs expressed in *Sf9* cells could result from lower CLR levels since low CLR levels are typical for insect cell membranes.^{44;} ¹⁹¹ CLR can be depleted from cell membranes by incubation with cyclodextrins, such as methyl-β-cyclodextrin (MβCD).²⁹⁹ Thus, wt A₃AR-expressing CHO-S membrane preparations were incubated with increasing concentrations of MβCD and subsequently washed thoroughly by a 4-step washing procedure to remove any residual MβCD. The CLR-depleted membranes were then investigated by a homologous competition binding assay employing PSB-11 vs. [³H]PSB-11 (Figure 54).

Figure 54 B demonstrates that increasing MβCD concentrations caused decreased specific binding. After incubation with 25 mM MβCD, the remaining specific binding was below 15 % of the specific binding obtained after incubation with only 0.1 mM MβCD, thus preventing any reliable K_D determination. In general, the determined K_D values increased with increasing MβCD concentrations as follows: 4.6 ± 0.3 nM, 7.4 ± 1.9 nM, and 15.4 ± 1.0 nM for 0.1 mM, 1 mM, and 10 mM MβCD, respectively. 0.1 mM MβCD led to a virtually identical K_D value compared to the K_D value of [³H]PSB-11 at the wt A₃AR (4.2 ± 0.1 nM see Table 8, 4.9 nM according to literature), whereas 10 mM MβCD resulted in a significantly decreased affinity, showing a 3-fold higher K_D value.¹²⁶ The determined B_{max} values were slightly decreased and determined to be 2348 ± 128 cpm and 1326 ± 435 cpm for membranes incubated with 0.1 mM and 10 mM MβCD, respectively.

The same method was applied for JS68 expressed in *Sf9* cells. JS68 was chosen to be the subject of this investigation since the corresponding wt construct JS1 was not stable

enough and did not provide a sufficient assay window. After incubation of JS68 with 10 mM M β CD, the specific binding was not decreased to the extent observed with the wt A₃AR CHO-S preparation, and K_D values were in a similar magnitude as without M β CD treatment (control 599 \pm 239 nM vs. 758 \pm 341 nM, 10 mM M β CD). Specific binding remained at ~90 % in contrast to the 4-fold reduction of specific [³H]PSB-11 binding to wt A₃AR CHO-S membranes treated with 10 mM M β CD.

In contrast to the A₃AR results, CLR depletion studies at the A_{2A}AR revealed that the affinity of [³H]ZM241385 to A_{2A}AR-containing membrane preparations from cells treated with 5 mM M β CD was not affected. Investigated membrane preparations were shown to contain 50 % less CLR compared to that of untreated cells.⁴⁷ Similarly, a study on rat striatal membrane preparations, which natively express the rat A₁- and A_{2A}Rs, revealed no change in affinity for the A₁AR-selective antagonist [³H]DPCPX (K_D values 6.2 \pm 1.0 vs. 3.9 \pm 0.7 nM) and the A_{2A}AR-selective antagonist [³H]ZM241385 (K_D 2.2 \pm 0.6 vs 2.4 \pm 0.8 nM) when CLR was depleted by incubation with 10 mM M β CD. However, affinities of the A₁AR-selective agonist [³H]CCPA (1.17 \pm 0.03 nM vs. 0.87 \pm 0.03 nM) and the A_{2A}AR-selective agonist [³H]CGS21680 (24.7 \pm 2.7 vs. 34.3 \pm 1.5 nM) were significantly increased or reduced, respectively. Incubation with 10 mM M β CD decreased the CLR content of the rat striatal membrane preparations by 50 % and significantly reduced specific binding of all tested radioligands. This effect was larger for the A_{2A}AR ligands [³H]CGS21680 and [³H]MSX-2 (75 % and 56 % specific binding after incubation with 10 mM M β CD) than the A_{2A}AR antagonist [³H]ZM241385 (83 %) and the A₁AR-selective ligands [³H]CCPA (86 %) and [³H]DPCPX (82 %). Nevertheless, the specific binding still remained at >50 % for all ligands compared to those of the controls. After CLR depletion with 10 mM M β CD, rat striatal membranes showed significantly reduced B_{max} values for [³H]CCPA, [³H]DPCPX and [³H]ZM241385 as determined by saturation binding studies, but the B_{max} value for the agonist [³H]CGS21680 remained unchanged.³⁰⁰

No such studies have yet been published describing CLR's role on the A₃AR. These data suggest unique CLR interactions impacting antagonist binding at the A₃AR, which significantly differ from those observed for the A₁- and A_{2A}AR. On the other hand, low levels of CLR in insect cell membrane might not be the sole reason for the reduced affinity of PSB-11 at A₃AR constructs expressed in *Sf9* cells. Although CLR depletion drastically reduced specific binding of [³H]PSB-11 to CHO-S cell membranes and significantly

decreased its affinity, the determined K_D values remained below 20 nM and thus several fold lower than those of A₃AR crystallization constructs. If CLR acts as an allosteric modulator at the A₃AR and is required for high specific [³H]PSB-11 binding, A₃AR crystallization constructs expressed in *Sf9* cells should not be able to bind [³H]PSB-11 to a great extent. In fact, the wt A₃AR construct (JS1) revealed extremely low specific binding, and a K_D value of 26.5 nM, which does not significantly differ from the K_D value obtained using A₃AR-CHO-S membrane preparations treated with 10 mM M β CD (K_D 15.4 nM). However, introducing stabilizing modifications further decreased the affinity, which ultimately resulted in K_D values of >250 nM. Interestingly, binding to these stabilized A₃AR constructs was not affected by incubation with M β CD, which might be due to the natively low CLR levels in insect cell membranes.

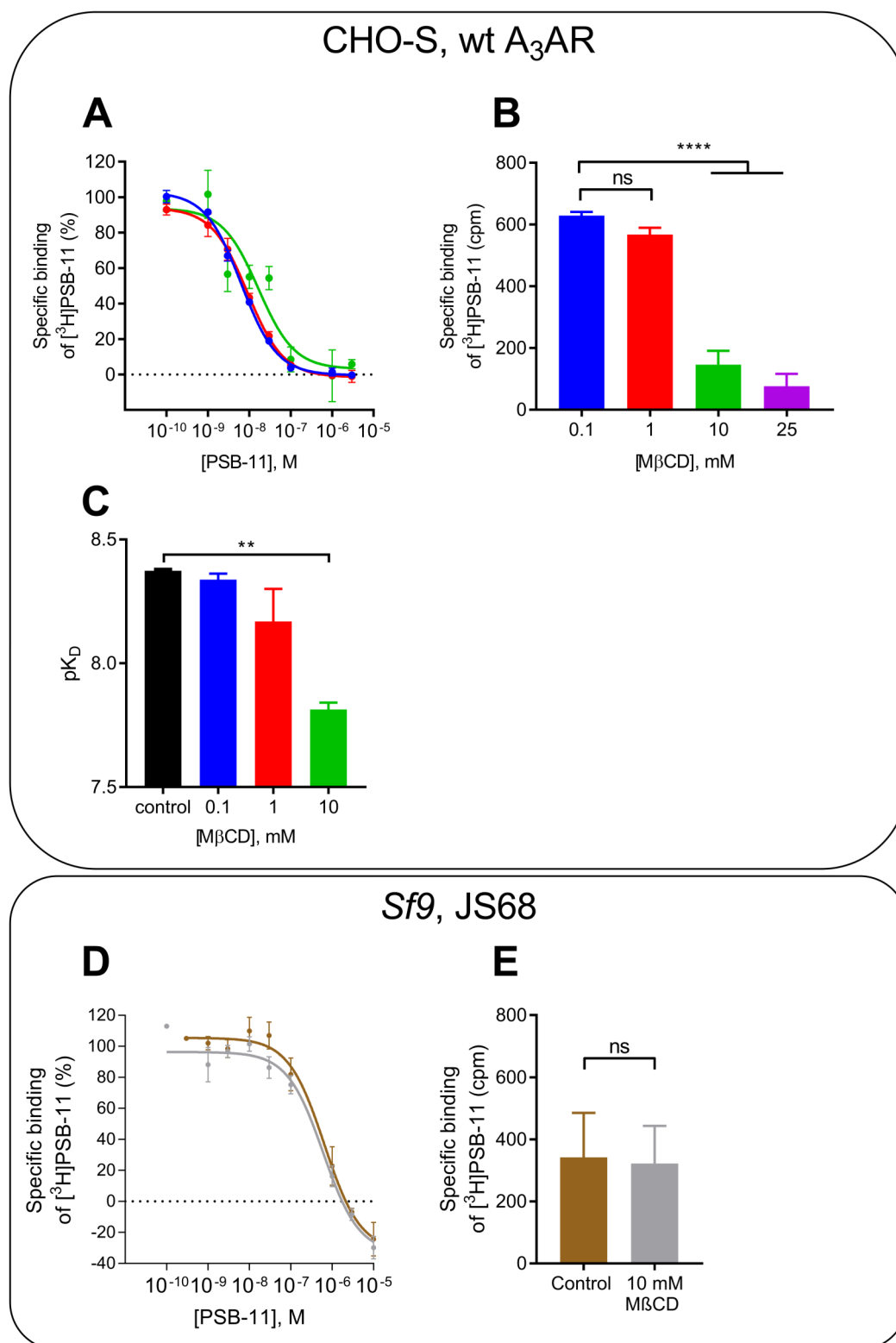


Figure 54. Assessment of ligand binding after cholesterol depletion.

A–C: wt A₃AR expressed in CHO-S cells. **D + E:** A₃AR construct JS68 (S97³⁻³⁹K, bRIL, A_{2A}/A₁ hybrid junction site). **A, D** Competition binding studies [³H]PSB-11 vs PSB-11. **B, E** Specific binding of [³H]PSB-11. **C:** pK_D values obtained after incubation with indicated MβCD concentrations (control: without MβCD). All data represent means ± SEM from three independent experiments. Statistical evaluation was carried by one-way ANOVA with Dunnett's post hoc test (ns p ≥ 0.5 ns; * 0.05 > p > 0.01; ** 0.01 ≥ p > 0.001; *** 0.001 ≥ p > 0.0001; **** p < 0.0001).

3.18.5 Cholesterol replenishment

M β CD-CLR inclusion complexes can be utilized to restore CLR levels in CLR-depleted membranes or to increase naturally low CLR levels, e.g., in *Sf9* insect cell membranes.⁴³ Moreover, CLR supplementation during expression potentially compensates for the low CLR abundance in *Sf9* cells. Therefore, two constructs, JS68 and JS104, were expressed under CLR-increasing conditions. JS104 was expressed with CLR supplemented by an inclusion complex according to Gimpl et al., 2002.³⁰¹ Additionally, bovine serum albumin (BSA) was added as a carrier.³⁰² JS68 was expressed in growth medium supplemented with 3X final concentration of Cholesterol Lipid Concentration 250X Gibco™. Competition binding curves and determined K_D values are presented in Figure 55 and Table 11, respectively. CLR supplementation failed to restore high-affinity binding for both tested constructs and expression conditions. However, JS104's affinity to PSB-11 could be increased by 2-fold, but the obtained results might be hampered by the generally observed low-affinity binding. Again, a precise statistical comparison of the determined K_D values was not possible since the radioligand itself did not provide the essential high-affinity binding anymore. The K_D value of [³H]PSB-11 at JS68 + 3X CLR was determined to be 285 ± 59 nM. Thus, CLR supplementation did not further improve the affinity, which remained at a similar magnitude compared to expression without any supplementation.

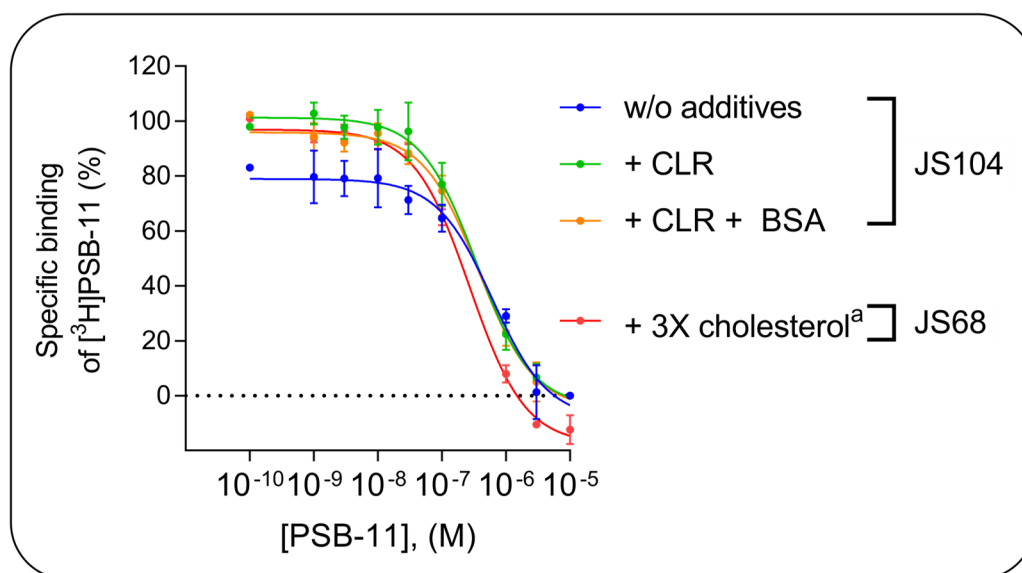


Figure 55. Homologous competition binding after CLR supplementation during expression. Data represents mean \pm SEM from three experiments. ^aCholesterol Lipid Concentration 250X Gibco™

Table 11. Affinity of PSB-11 to A₃AR constructs expressed with CLR supplementation.

JS104: N3Q, N4Q, N12Q, N160Q, S97^{3.39}K, bRIL A_{2A}/A₁ hybrid junction site, truncated after S308. JS68: S97^{3.39}K, bRIL A_{2A}/A₁ hybrid junction site.

hA₃AR construct	Expression condition	PSB-11 vs. [³H]PSB-11 K_D ± SEM [nM] (n=3)
	Without additives	1001 ± 198
JS104	+ CLR	363 ± 106
	+ CLR + BSA	418 ± 73
	Without additives	250 ± 14
JS68	+ 3X cholesterol	
	(Cholesterol Lipid Concentration 250X Gibco™)	285 ± 59

Next, membrane preparations of JS68 (*Sf9*) were incubated with increasing concentrations of CLR (as M β CD-CLR inclusion complex, 37°C 30 min, gentle shaking) and subsequently checked for their affinity to PSB-11 in a radioligand competition assay (Figure 56). The determined K_D values did not reveal a clear trend, but the values seemed to be slightly lower than those of the control (272 nM) of the same batch of membrane preparation and also compared to the previously determined K_D value of 250 nM (Table 8). However, incubation with CLR-supplementing inclusion complexes led to an increased specific binding, which was observed for every concentration. Incubation with 1 mM CLR more than doubled the specific binding compared to incubation with 0.01 mM CLR. These data is in agreement with CLR-depletion studies (see Section 3.18.4) indicating that CLR is important for the specific binding of [³H]PSB-11 but is not able to restore high-affinity binding.

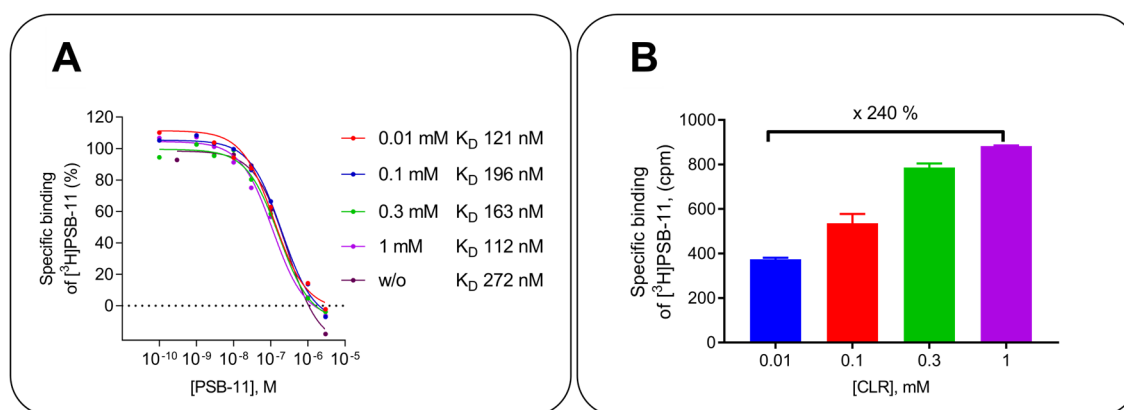


Figure 56. CLR replenishment.

A: Homologous competition binding curves after incubation with increasing CLR concentrations. CLR was provided as M β CD-CLR complex. Indicated concentrations refer to the CLR concentration. **B:** Specific binding of [³H]PSB-11. Values are normalized to specific binding after incubation with 0.01 mM CLR. Presented data originate from a single experiment. Total and non-specific binding were determined in duplicates.

3.18.6 Transferring potential interaction partners

Just recently, in 2020, Mao et al. solved the cryo-EM structure of the γ -amino butyric acid receptor B (GABA_B) in a complex with G_{i1} and the G_i-binding protein scFv16. They expressed both subunits of the heterotrimeric GABA_B receptor, GB1 and GB2, in HEK293F cells. In contrast to that, the heterotrimeric G_{i1} protein and scFv16 were expressed in *Sf9* and *Tni* insect cells, respectively. Mammalian cells expressing the GPCR subunits were then disrupted together with the insect cells expressing the G_{i1} subunit. The final complex was formed after adding the purine diphosphohydrolase apyrase and the scFv16 protein, proving that proteins of different expression systems can interact when cells are disrupted in one batch. After incubation, the complex was solubilized with LMNG supplemented with CHS, purified, and subjected to the subsequent cryo-EM procedure.³⁰³ Apyrase is commonly used to hydrolyze GDP released from the G protein and GTP, which can interfere with the high-affinity binding between a GPCR and its G protein, with the aim to obtain a nucleotide-free GPCR-G protein complex.^{29; 31}

At first, *Sf9* insect cell membrane preparations of JS94 were mixed with membrane preparations of native CHO-S cells and wt A_{2A}AR-expressing CHO-S cells by incubation at 37°C with occasional vortexing. Initial disruption of the *Sf9* insect cells was performed with the hypoosmotic 5/2 buffer containing 5 mM tris(hydroxymethyl)aminomethane (Tris) and 2 mM ethylenediaminetetraacetic acid (EDTA) instead of the low osmotic buffer (10 mM 4-(2-hydroxyethyl)-1-piperazineethanesulfonic acid (HEPES) pH 7.5, 10 mM

MgCl₂, 20 mM KCl), which was usually used as the standard lysis buffer for membrane preparations of *Sf9* insect cells.

Moreover, *Sf9* insect cells expressing JS68 were suspended and disrupted with an equal amount of native CHO-S cells. This procedure aimed at providing potential interaction partners present in mammalian CHO-S cells or attached to their membranes, which might be missing in insect cells but are necessary for high-affinity ligand binding. Subsequently, homologous competition binding (PSB-11 vs. [³H]PSB-11) was employed to determine the K_D values. Results (Figure 57) show that membrane preparations from *Sf9* insect cells disrupted by the 5/2 buffer lack high-affinity binding. Furthermore, the mixtures of mammalian and insect cell membranes failed to increase the affinity, displaying unaltered low-affinity binding of PSB-11 with K_D values of ~400–800 nM (Figure 57). Moreover, the joint disruption of insect cells expressing the A₃AR construct JS68 and native CHO-S cells did not restore high-affinity binding. Thus, low-affinity PSB-11 binding is not the result of missing interaction partners required for high-affinity binding that can be easily transferred by the applied procedures. It is also important to note that modified G_{i1} and G_{γ2} proteins that lack cysteine residues essential for membrane targeting were used for obtaining the GABA_B-G protein complex.³⁰³ Consequently, joint cell lysis of native CHO-S cells together with *Sf9* insect cells expressing A₃AR constructs might only reconstitute soluble intracellular interaction partners. Moreover, this approach requires the correct biosynthesis and folding of the A₃AR in insect cells so that soluble interaction partners can facilitate high-affinity ligand binding after the A₃AR traffics to the cell membrane.

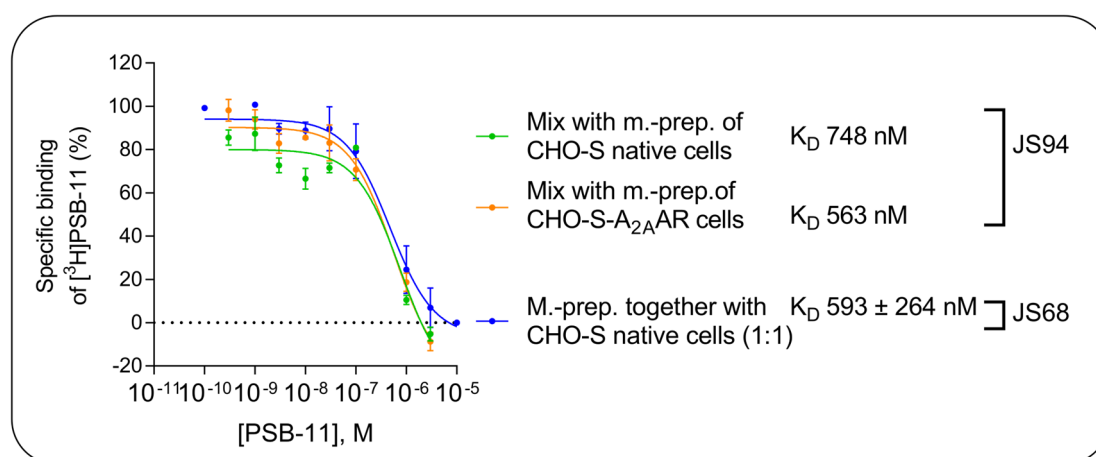


Figure 57. Competition binding curves of *Sf9*-CHO-S membrane preparations.

Membrane preparation of JS94, which equals JS68 without any N-terminal N-glycosylation sites, was carried out according to the standard CHO-S protocol with initial cell lysis using the 5/2 buffer (5 mM Tris, 2 mM EDTA, pH 7.4) but with homogenization by a dounce homogenizer instead of an Ultra Turrax (see Section 5.3.1). Data were obtained in one and three experiment(s) for JS94 and JS68 (mean ± SEM), respectively.

3.18.7 Ligand binding at solubilized A₃AR receptor constructs

Next, radioligand binding studies were performed employing A₃AR receptor constructs solubilized from CHO-S and *Sf9* insect cell membranes expressing the respective construct. Solubilization was achieved by extracting the receptor constructs from the membranes with 1 % of the zwitterionic detergent CHAPS or 1 % of the non-ionic detergent DDM supplemented with 0.2 % CHS. Subsequently, the solubilized receptor preparations were investigated by homologous competition of PSB-11 vs. [³H]PSB-11 to determine the K_D.

Solubilization of the wt A₃AR and the A₃AR-bRIL construct from CHO-S membranes, as well as all experiments trying to solubilize A₃AR constructs from *Sf9* insect cell membranes, including stabilized receptor mutants, failed, and no sufficient specific radioligand binding was detected. Only the stabilized A₃AR-S97^{3.39}K construct expressed in CHO-S cells was successfully solubilized by 1 % CHAPS and 1 %/0.2 % DDM/CHS and yielded specific [³H]PSB-11 binding. The CHAPS-solubilized A₃AR-S97^{3.39}K construct revealed a 10-fold decreased affinity compared to the membrane-bound receptor (82.8 nM vs. 8.3 nM). Contrary, the same receptor construct solubilized by DDM/CHS showed a K_D value of 11.5 nM. Interestingly, the A₃AR-S97^{3.39}K-bRIL construct solubilized by DDM/CHS revealed a 15-fold decreased affinity compared to the membrane-bound construct (270 nM vs. 18.1 nM) and only a 1.5-fold higher affinity compared to the CHAPS-solubilized construct (270 nM vs. 406 nM). Thus, the insertion of the fusion partner bRIL appeared to affect the solubilization process, resulting in the loss of high-affinity binding.

Analog studies had been conducted with the wt A₁- and A_{2A}ARs but revealed different results compared to those of the A₃AR.³⁰⁴⁻³⁰⁶ Both receptors were solubilized identically with 1 % CHAPS from rat striatal membranes. The solubilized A₁AR maintained high affinity for the tested agonists and showed slightly increased antagonist affinity as determined by competition binding vs. the agonist [³H]R-PIA.³⁰⁴ Similarly, the A_{2A}AR solubilized by CHAPS showed almost identical high antagonist affinity in competition binding studies vs. the antagonists [³H]ZM241385 and [³H]XAC.^{305; 306}

In contrast to the A₁- and A_{2A}ARs, CHAPS-solubilization of the A₃AR constructs resulted in a significantly decreased affinity for the A₃-selective antagonist PSB-11. The combination of the mild, non-ionic detergent DDM and the CLR derivative CHS efficiently preserved the A₃AR-S97^{3.39}K construct upon extraction and maintained almost identical

high-affinity binding compared to the membrane-bound construct. The detergent DDM is known to disrupt protein-lipid interactions rather than protein-protein interactions, whereas the zwitterionic detergent CHAPS possesses intermediate effects.³⁰⁷ Moreover, a study that investigated the solubilization of the 5-HT_{1A} receptor by various detergents revealed that CHAPS and DDM solubilized membrane lipids differently and that CHAPS extracted less CLR compared to DDM, which might explain the observed affinity differences.^{308; 309} The CLR analogue CHS could also contribute to the successful solubilization process. In conclusion, the A₃AR seems to require a specific membrane environment for efficient ligand binding that differs from that of the A₁- and A_{2A}ARs.

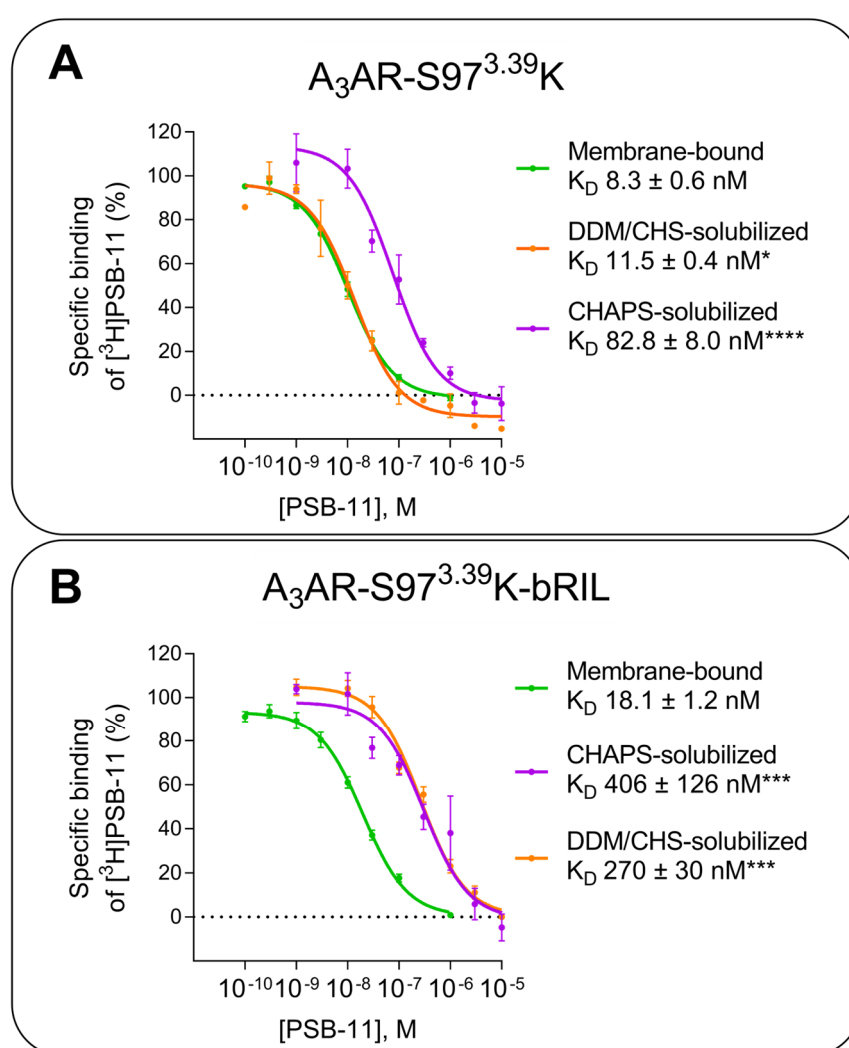


Figure 58. Ligand binding at solubilized A₃AR constructs.

Constructs carried an N-terminal HA-tag and were expressed in CHO-S cells. The construct A₃AR-S97^{3.39}K-bRIL possessed bRIL as a fusion partner inserted into the A_{2A}/A₁ hybrid junction site and a C-terminal His-tag. Solubilization was carried out by 1 % CHAPS and 1 %/0.2 % DDM/CHS. Data represents the mean ± SEM from three independent experiments. Statistical evaluation was carried out based on the corresponding pK_D values by one-way ANOVA with Dunnett's post hoc test comparing the solubilized receptor constructs with the membrane-bound receptor constructs. (ns p ≥ 0.5 ns; * 0.05 > p > 0.01; ** 0.01 ≥ p > 0.001; *** 0.001 ≥ p > 0.0001; **** p < 0.0001).

3.18.8 Purification of A₃AR constructs expressed in CHO-S cells

Extensive investigation of ligand binding revealed that A₃AR constructs expressed in *Sf9* insect cells failed to bind PSB-11 and NECA with high affinity. Contrary, the same constructs provided high-affinity binding when expressed in CHO-S cells. Therefore, JS68 with and without HA-tag was expressed in CHO-S cells and subsequently purified to assess the efficiency and yield of mammalian cell expression. At first, JS68 without HA-tag was expressed on a small-scale (50 mL), and subsequent membrane preparations were carried out according to the insect cell and the CHO-S cell protocols (see Sections 5.2.8 and 5.3.1). Secondly, small- and medium-scale (175 mL) expressions of JS68 with HA-tag were employed to increase the overall protein yield.

Results obtained by SEC and SDS-PAGE are provided in Figure 59. Batches without HA-tag showed no characteristic protein peak in the SEC but exhibited a faint band between 40–50 kDa on the SDS-PAGE gel. Consequently, the A₃AR protein seemed to be present in both membrane preparations (red rectangle), and no protein remained in the initial pellet (P1) of the CHO-S membrane preparation (see Section 5.3.1). The protein obtained after membrane preparation according to the CHO-S cell protocol was slightly less pure, as seen by several additional bands. Insertion of the HA-tag significantly increased the overall protein yield and resulted in a well-visible protein peak at around $t = 4$ min. Upscaling led to an even higher protein amount, although the increment was not proportional to the employed biomass. Interestingly, the protein band occurred at the height of the unglycosylated A₃AR protein used as a control, which was expressed in *Sf9* insect cells (JS101). However, the expression of the corresponding construct without any N-glycosylation sites failed. N-glycans might thus be essential for efficient production of the A₃AR. Expression in CHO-S cells was successfully implemented and provided A₃AR protein of high purity. Nevertheless, the overall efficiency of the transient mammalian cell expression was inferior and yielded less protein than baculovirus-based expression in *Sf9* insect cells.

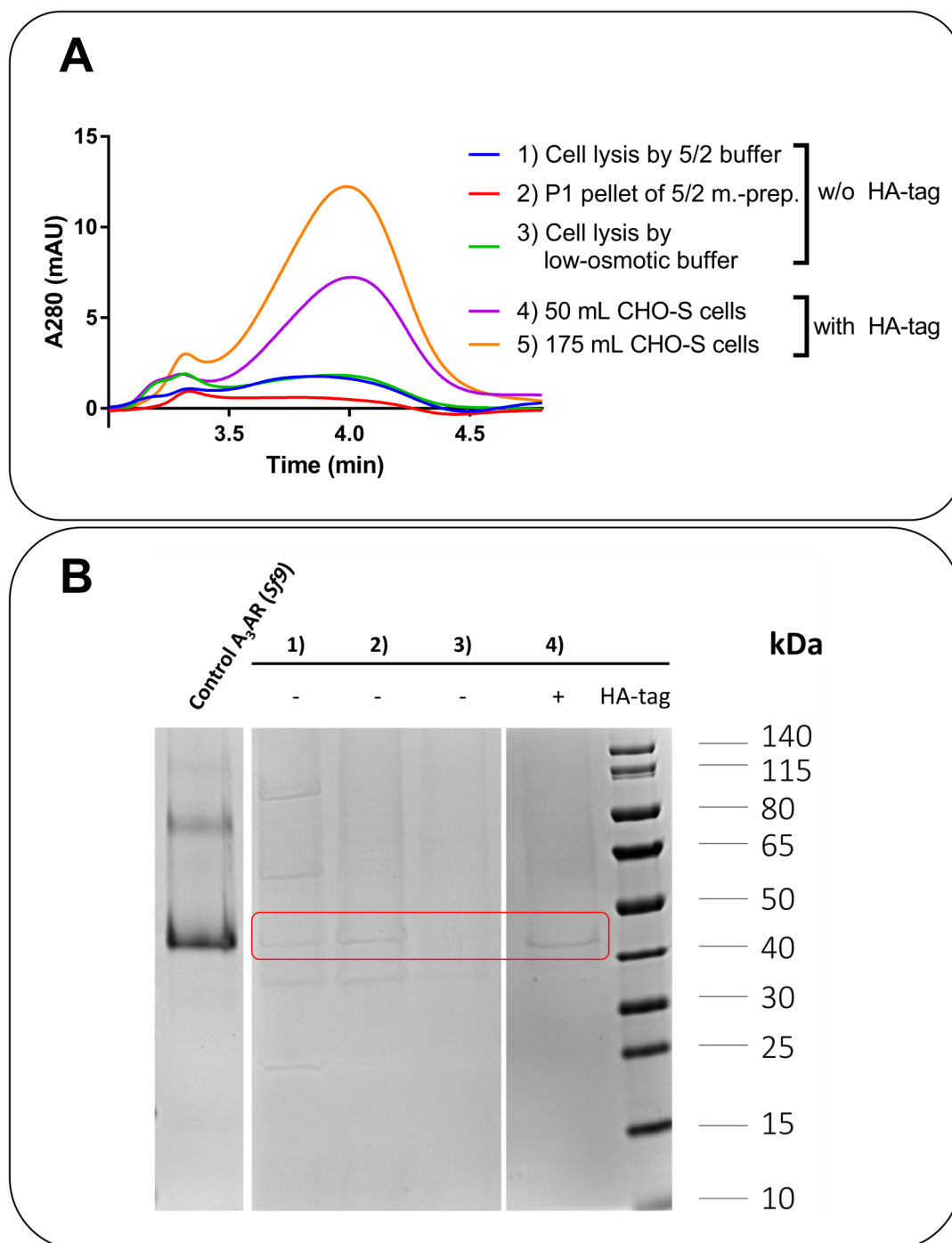


Figure 59. Purification of the A₃AR crystallization construct JS68 expressed in CHO-S cells.

A: SEC chromatogram (3–4.8 min) of purified proteins. Cell lysis was achieved by the 5/2 buffer (5 mM Tris, pH 7.4, 2 mM EDTA), which is the standard lysis buffer for CHO-S cell membrane preparation employed in ligand binding testing, or by the low-osmotic buffer (10 mM HEPES pH 7.5, 10 mM MgCl₂, 20 mM KCl). For details see Sections 5.2.8 and 5.3.1. **B:** SDS-PAGE of purified proteins. Equal volumes of the protein samples were loaded onto the gel. JS101, which was expressed in *Sf9* cells, was employed as a control.

3.18.9 Ligand binding at purified A₃AR constructs expressed in CHO-S cells

After successful expression in CHO-S cells, the obtained membrane preparations were checked for their ligand binding affinity by the homologous competition assays (PSB-11 vs. [³H]PSB-11) before solubilization and after purification (Figure 60 A). All three membrane preparations resulted in high-affinity binding with K_D values of 1) 4.7 nM, 2) 14.5 nM, and 3) 22.7 ± 1.6 nM, proving their ability to bind PSB-11 efficiently when incorporated into a mammalian membrane. After solubilization and purification, thermostability was assessed by the CPM-based thermostability assay (Figure 60 B, C). The protein was similarly stable compared to the same protein expressed in insect cells, resulting in T_M values in the range of 70–75°C and melting curves with a sharp inflection point. Moreover, thermostability was investigated in the presence of the A₃AR antagonists TK-OT-018, AT563, and the irreversible antagonist LUF7602 (for structure see Table 7). No apparent ligand-mediated effects could be observed compared to the DMSO control (71.8°C). However, TK-OT-018 appeared to result in a slightly lower T_M (70.4 ± 0.3°C) than AT563 (72.4 ± 0.2°C) and LUF7602 (72.0 ± 0.4°C).

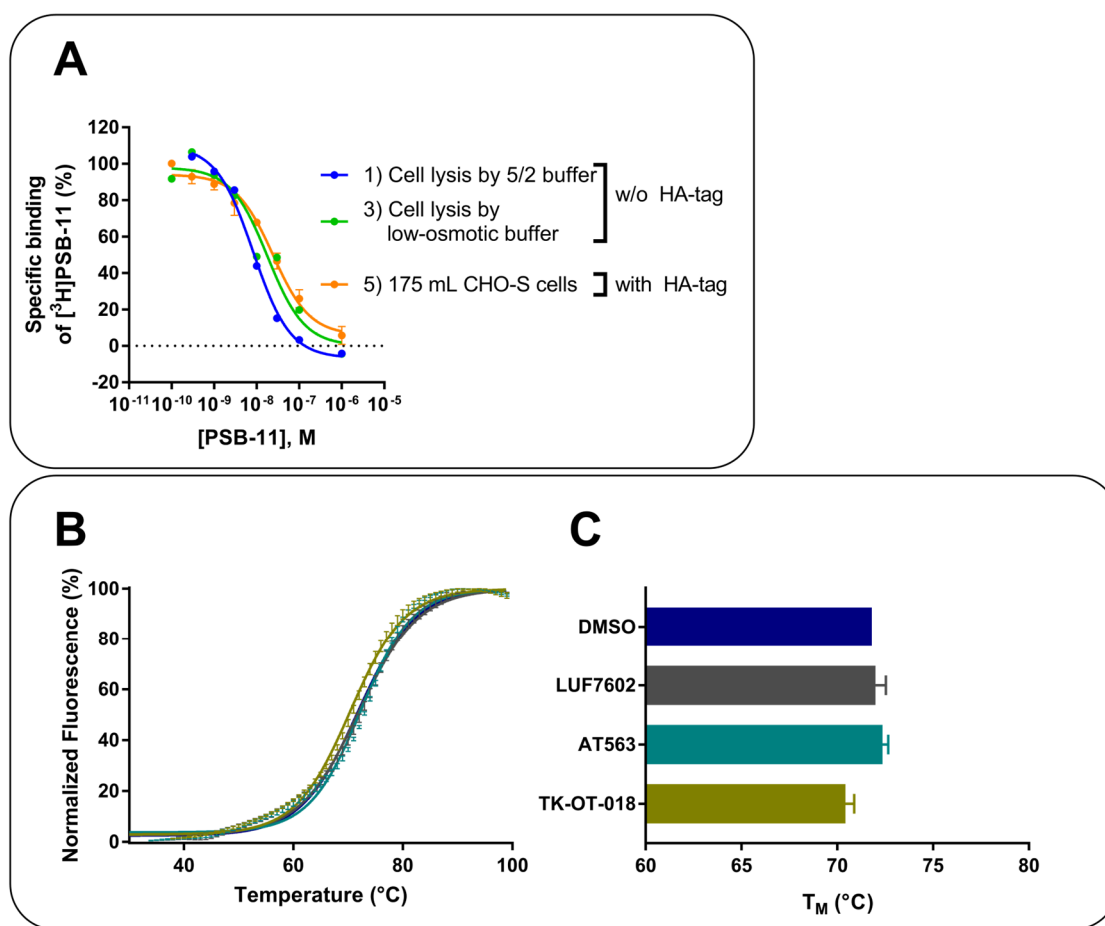


Figure 60. CHO-S expression of JS68 — ligand binding.

A: Homologous competition binding. Cell lysis was achieved by the 5/2 buffer (5 mM Tris, pH 7.4, 2 mM EDTA), which is the standard lysis buffer for CHO-S cell membrane preparation employed in ligand binding testing, or by the low-osmotic buffer (10 mM HEPES pH 7.5, 10 mM MgCl₂, 20 mM KCl). For details see Sections 5.2.8 and 5.3.1. **B:** Melting curves of the purified protein (orange graph, No. 5 in Figure 59) in the presence of DMSO, TK-OT-018, AT563, and LUF7602. **C:** Determined T_M values. **A, B, C:** When error bars are presented data represents mean \pm SEM from two experiments, otherwise data were obtained in one experiment.

3.18.10 The BODIPY-labeled ligand TK-OT-024

High-affinity ligands can be attached to fluorophores such as boron-dipyrromethene derivatives (BODIPY) to obtain tool compounds for imaging or for developing novel pharmacological assay systems, e.g. nanoBRET assays.^{310; 311} Just recently, SEC with a detection wavelength of 495 nm was used to prove the presence of the fluorophore-labeled ligand PSB-2115 bound to the A_{2A}-PSB1-bRIL protein.²⁵⁷ Detection at 495 nm ensured that only the fluorophore-labeled ligand was explicitly detected. In general, the ligand added to the protein solution should bind to the solubilized GPCR just as to the GPCR within a membrane environment. Thus, the ligand should be co-eluted with the GPCR protein peak at approximately 4.1 min. Ligands without the protein will be eluted

significantly later since small molecules extensively enter the pores of the stationary phase. In most cases, it is impossible to reliably prove that the ligand is bound to a GPCR by SEC since absorption of the ligand is superimposed by the absorption of the protein itself. An additional detection wavelength of 495 nm enables the simultaneous detection of both protein and ligand since only the fluorophore-labeled ligand will cause absorption at such a long wavelength. The correlation between the absorption at 495 nm (A₄₉₅) and 280 nm (A₂₈₀) consequently allows the conclusion of whether the ligand is correctly bound to the GPCR.

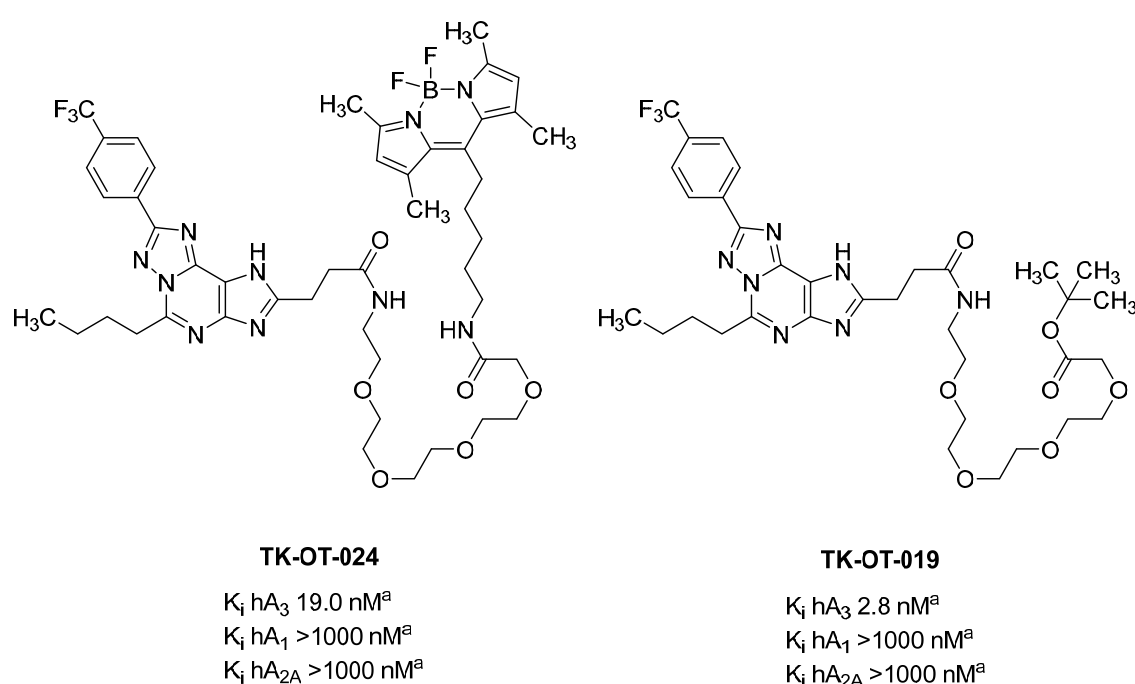


Figure 61. Structures of TK-OT-024 and TK-OT-019.

^asee Ref¹²⁵

In this case, the ligand TK-OT-024, obtained by coupling of the selective A₃AR antagonist TK-OT-019 with an amino alkyl-functionalized BODIPY fluorophore, was utilized to assess its binding to the solubilized and purified A₃AR protein JS104 (Figure 61). JS104 possessed no N-glycosylation sites, bRIL inserted into the A_{2A}/A₁ hybrid junction site, a truncated C-terminus after residue S308, and the stabilizing mutation S97^{3.39}K. Moreover, an A_{2B}AR protein construct was employed as a negative control to examine any artificial or unspecific binding that might be misinterpreted as specific binding. Both constructs were expressed at a small scale of 40 mL of *Sf9* insect cells.

Additionally, JS116, which corresponded to JS104 but with intact N-glycosylation sites and untruncated C-terminus, was expressed in CHO-S cells (50 mL) and tested for its ability to bind TK-OT-024.

Proteins were purified without any ligand present and incubated with 25 μ M of TK-OT-019 or the BODIPY-labeled TK-OT-024. Subsequently, all proteins were analyzed by SEC (Figure 62). After the incubation, the proteins of JS104 and the A_{2B}AR construct showed the commonly observed clear protein peak at approximately 4.1 min elution time (280 nm). JS104 + TK-OT-019 revealed no absorption at 495 nm at the elution time of the protein, demonstrating that this wavelength selectively detected TK-OT-024. In contrast, JS104 + TK-OT-024 showed a clear peak at 495 nm representing the bound ligand since TK-OT-024 alone showed a significantly smaller peak at this elution time. The negative control A_{2B}AR + TK-OT-024 revealed a similar peak than TK-OT-024 alone, proving the selective binding of TK-OT-024 to the A₃AR construct (Figure 62 B). However, the amount of ligand bound to the A₃AR protein JS104 is less than 10 % compared to a previously reported analog experiment employing the A_{2A}-PSB1-bRIL protein and the antagonist PSB-2115, which harbored the same BODIPY fluorophore as TK-OT-024.²⁵⁷ However, in that study, the A_{2A}-PSB1-bRIL protein was purified in the presence of the fluorescent ligand PSB-2115 and not, like in the present case of the A₃AR protein, purified in its apo form and subsequently incubated with the ligand. Nevertheless, the smaller extent of bound TK-OT-024 might indicate that the ligand binds with lower affinity to the purified A₃AR construct JS104, which was expressed in *Sf9* cells, and thus diffuses out of the receptor faster than the tightly bound PSB-2115 during the chromatographic separation. The same experiment but employing an A₃AR protein expressed in CHO-S cells (JS116) revealed that TK-OT-024 was also co-eluted with the A₃AR construct. However, the extent of bound ligand remained relatively small, indicating no increase of affinity to the A₃AR construct expressed in CHO-S cells (JS116) compared to that expressed in *Sf9* cells (JS104).

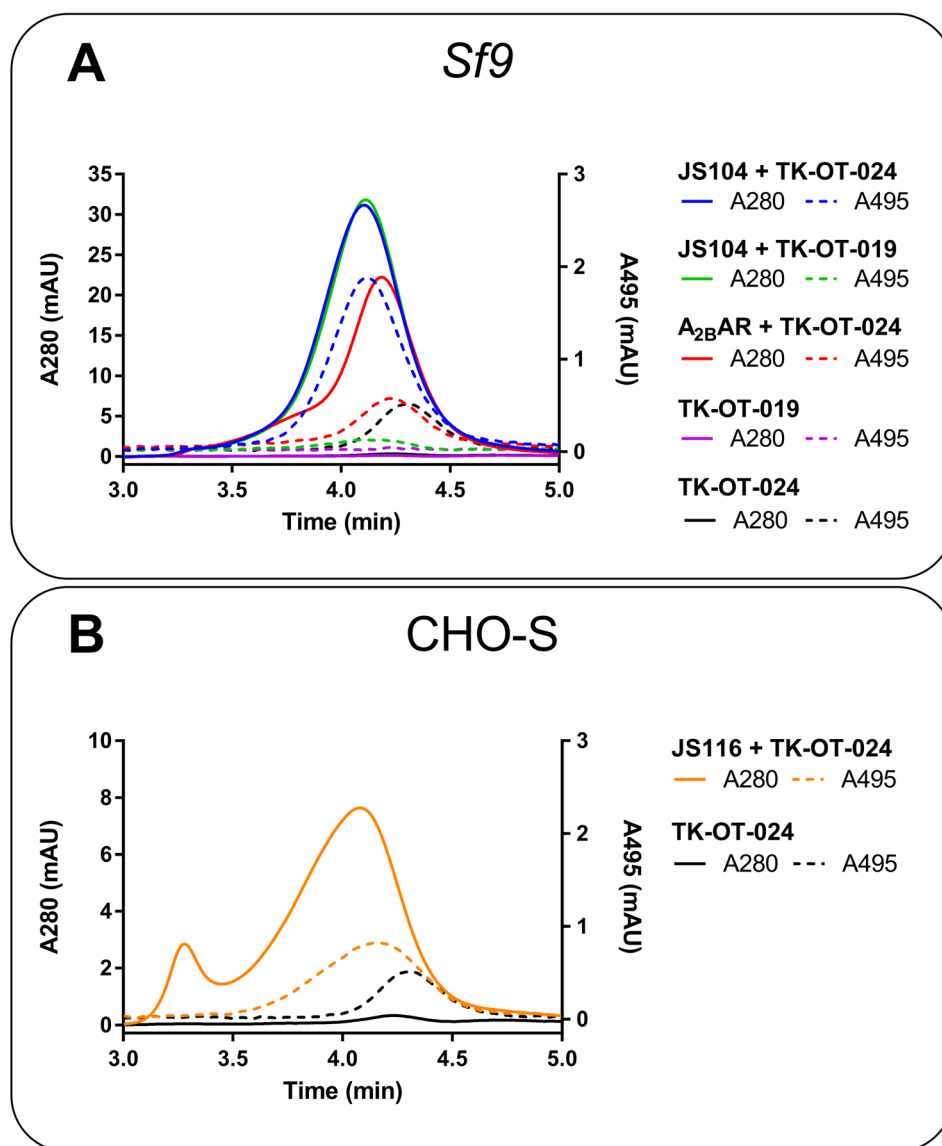


Figure 62. Incubation with the BODIPY-labeled ligand TK-OT-024.

A: SEC chromatogram (3–5 min) of JS104 (*Sf9*) + TK-OT-024, an A_{2B}AR construct (*Sf9*) + TK-OT-024 and JS104 (*Sf9*) + TK-OT-019, as well as both ligands without any protein at 280 nm and 495 nm. **B:** SEC chromatogram (3–5 min) of JS116 (CHO-S) + TK-OT-024 and TK-OT-024 alone. Incubation was carried out in the presence of 25 μ M TK-OT-024 and TK-OT-019 at room temperature for 30 min. Dashed lines are plotted against the right y-axis.

4. Summary & conclusions

Structural biology of membrane proteins such as GPCRs represents a challenging task. Hence, starting a project to prepare an elusive GPCR for crystallization is genuinely ambitious. The first obstacle to overcome is the inherent low stability of GPCRs outside their native membrane environment. This makes it exceedingly difficult to obtain sufficient amounts of pure and stable protein. The use of small and rigidified proteins replacing flexible receptor parts, the introduction of stabilizing point mutations, and receptor truncations display the main approaches which are employed to achieve receptor constructs suitable for structural biology (Figure 63).^{152; 153} Despite their similar architecture, each GPCR typically reveals individual difficulties that impede the success of these approaches. The subject of the present thesis was the A₃AR: A receptor that, on the one hand, has been part of medicinal chemistry research for almost 30 years and which belongs to a receptor family consisting of four subtypes, two of which have been elucidated by X-ray crystallography. However, on the other hand, elucidation of the A₃AR structure has not yet been achieved.

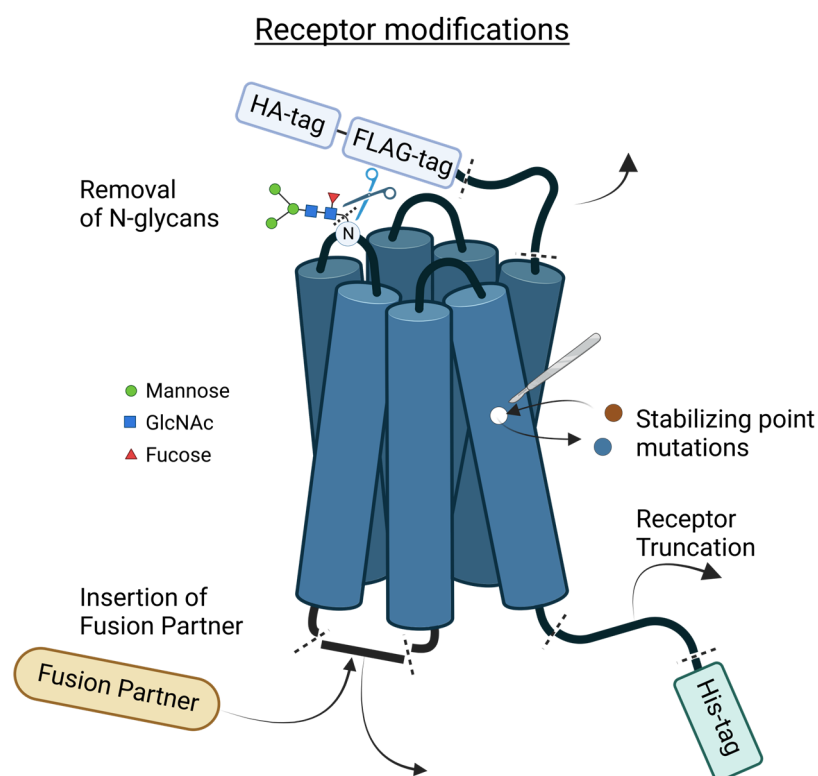


Figure 63. Schematic illustration of employed receptor modifications.
Created with BioRender.com

Initial A₃AR constructs with different fusion partners, which were inserted into the ICL3 of the A₃AR or fused to its N-terminus, featured extremely low stability and low overall protein yield. The first remarkable progress was achieved by introducing the A_{2A}/A₁ hybrid junction site resulting in first significant amounts of purified A₃AR protein (Figure 64). Further investigation of the junction site revealed that elongation of helix VI might be a key factor for the increased stability of the A_{2A}/A₁ hybrid junction site indicating the importance of adapting the junction site individually for each GPCR. Next, the mutation S97^{3.39}K, a recently employed mutation within the conserved sodium binding pocket of GPCRs that locks the receptor in its inactive state, was successfully transferred to the A₃AR, providing significantly improved stability. This mutation might indeed be an instrumental approach to achieving initial stability for a vast amount of class A GPCRs since it restrains a highly conserved domain within GPCRs.

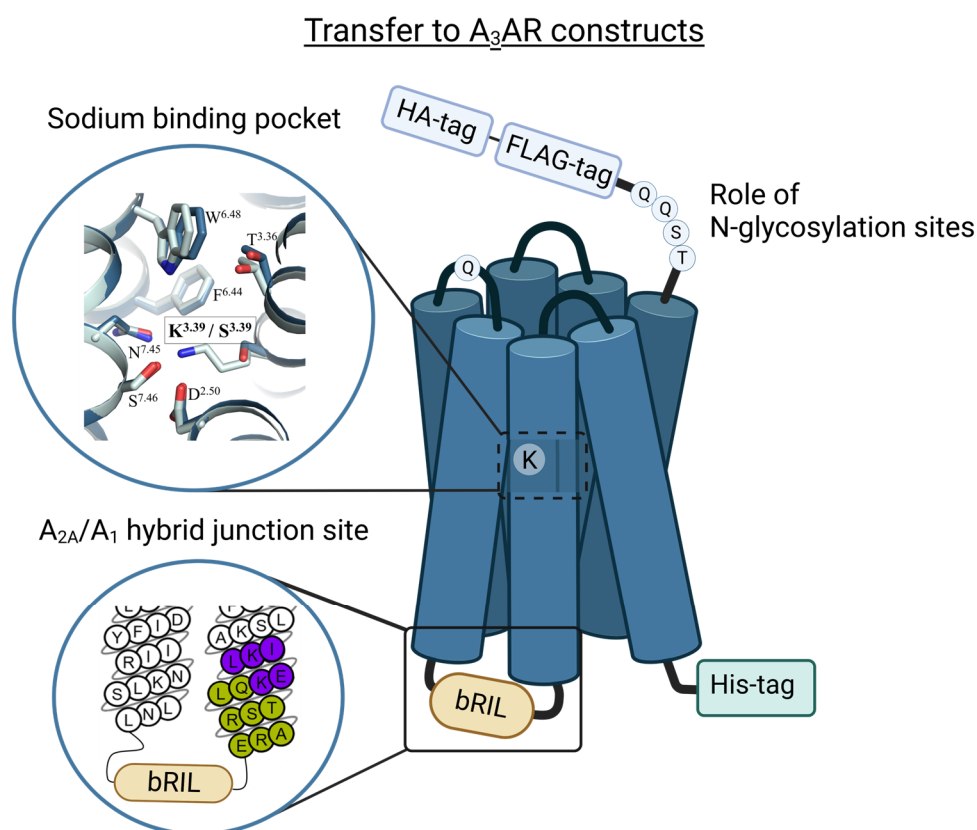


Figure 64. Model of the A₃AR crystallization construct.

The effect of the S^{3.39}K mutation was illustrated by comparing the architecture of the sodium binding pocket of the A_{2A}-PSB-1-bRIL structure (PDB 7PX4) with the inactive state model of the wt A₃AR taken from gpcrdb.org.^{257; 271} A_{2A}-PSB-1-bRIL, which carries the mutation S91^{3.39}K, is colored in gray and the wt A₃AR is colored in blue. All potential N-glycosylation sites (N3, N4, N12 (not shown), N160^{ECL2}) were mutated to glutamine. This figure was created with BioRender.com.

In the beginning, the M₄ mAChR N-terminus, which was already used to increase the expression of the A₁AR crystallization construct, was employed to enhance the inherent low expression levels and boost the protein yield of the A₃AR constructs. This beneficial effect was potentially provided by its three N-glycosylation sites.²¹⁴ Interestingly, the A₃AR is the only member of the AR family that natively possesses N-terminal N-glycosylation sites (N3, N4, N12). The effect of the M₄ mAChR N-terminus on the expression and protein yield could also be achieved by the native A₃AR N-terminus. However, the assumption that the presence of N-glycans is the reason for this effect was disproved since even A₃AR constructs bearing mutated N-glycosylation sites yielded similar expression levels and protein amounts. A thorough investigation of the N-terminal construct sequence led to the discovery of a short N-terminal linker that might display a universal approach to increasing the protein yield of GPCR crystallization constructs without introducing N-glycosylation sites. N-glycans are often undesirable since they might impede crystallogenes, especially when glycosylation occurs heterogeneously. Digestion steps before crystallization are commonly used to enzymatically cleave off N-glycans but bear the risk of losing precious protein.^{29; 152; 312}

The combination of the S97^{3.39}K mutation, the A_{2A}/A₁ hybrid junction site, the removal of N-glycosylation sites, as well as the C-terminal tail yielded excellent protein stability and protein yields. Novel A₃AR crystallization candidates developed in this thesis showed T_M values of 72–73°C, which could even be increased to 75°C by introducing the additional thermostabilizing mutation S271^{7.42}A. This achieved thermal stability is higher than that of most of the published GPCR crystallization constructs and even higher than that of the prototypical A_{2A}-StaR2-bRIL construct, which was utilized to obtain the largest number of A_{2A}AR crystal structures so far (Figure 65). Although the same method was employed, slightly varying concentrations of NaCl, glycerol, and detergents might influence the observed thermal stability. However, T_M values of the A_{2A}-PSB1-bRIL and A_{2A}-StaR2-bRIL were determined under the same conditions as that of the A₃AR constructs, and the developed A₃AR crystallization construct could become – similar to the A_{2A}-PSB1-bRIL construct – the gold standard for A₃AR crystallization experiments.²⁵⁷

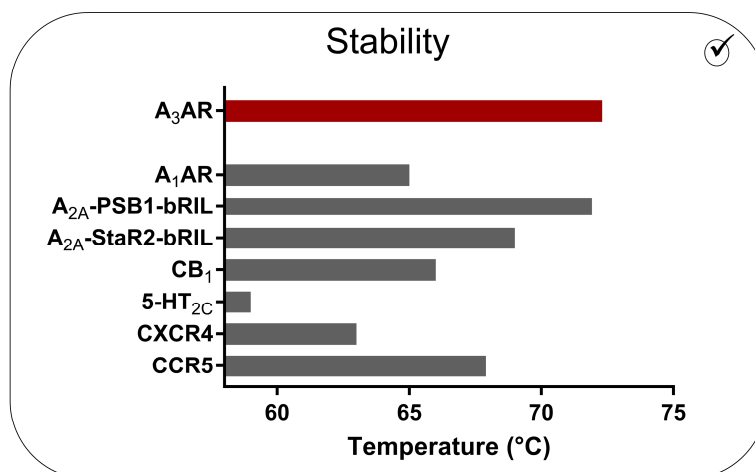


Figure 65. Conclusion — Thermal stability of crystallization constructs.

Thermal stability of GPCR crystallization constructs included for comparison were taken from references.^{201; 214; 257; 263; 313; 314}

The two highly conserved cysteine residues, C^{3.25} and C^{45.50}, are known to form a disulfide bond that connects the extracellular end of helix III with the ECL2 in most rhodopsin-like GPCRs; it is in most cases crucial for receptor structure, ligand binding, and activation.^{114; 315} The role of the extracellular disulfide bonds had been assessed for all other AR subtypes but not for the A₃AR.^{114; 116; 224} Investigation of the thermal stability of A₃AR constructs with a disrupted disulfide bond proved the major contribution of the conserved disulfide bond between C83^{3.25}–C166^{45.50} to the overall stability of the A₃AR, which might as well contribute to proper ligand binding. Interestingly, the corresponding receptor mutants that impede disulfide bond formation were well expressed and led to similar protein yields as constructs with a presumably intact disulfide bond. Therefore, it cannot always be assumed that GPCR proteins that are efficiently expressed display correctly assembled and folded receptor proteins. Detailed validation needs to ensure the structural integrity of the employed receptor constructs.

Thermostabilizing effects by ligands, especially antagonists, are usually observed, indicating that the expressed and solubilized GPCR is still correctly folded. The increased thermostability of GPCR-ligand complexes yielded ΔT_M values of $>10^\circ\text{C}$ in many cases.^{214; 313; 316; 317} However, in the present study, ligand binding experiments utilizing a thermal shift assay with various A₃AR protein constructs and different A₃AR agonists and antagonists did not show any ligand-mediated thermostabilizing effects.

Radioligand binding studies at A₃AR constructs expressed in *Sf9* insect cells revealed a reduced affinity of the A₃AR-selective antagonist PSB-11 (Figure 66). However, the employed modifications, such as the S97^{3.39}K mutation and the insertion of bRIL as a fusion partner, resulted in unaltered high-affinity binding when the constructs were expressed in mammalian CHO-S cells. Consequently, the altered

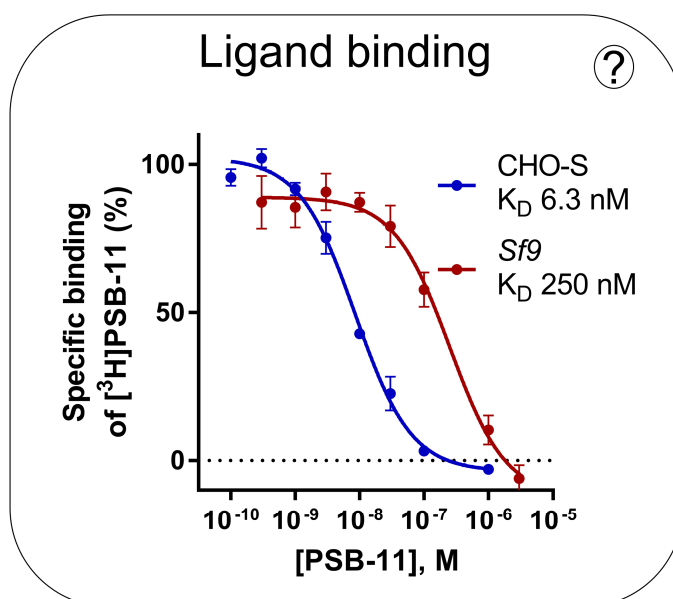


Figure 66. Conclusion ligand binding.

Homologous competition binding of PSB-11 vs. [³H]PSB-11 to the A₃AR construct JS68.

antagonist binding must be due to the receptor expression in insect cells. Evaluation of the binding of the non-selective AR agonist NECA at corresponding A₃AR constructs expressed in CHO-S cell membranes showed that bRIL replacing the ICL3 significantly decreased the affinity for the agonist NECA. In contrast to that, the insertion of a fusion partner into the ICL3 of the β₂AR and the closely related A₁- and A_{2A}ARs had resulted in increased agonist affinity.^{38; 150; 154; 214} Furthermore, even the wildtype A₃AR, when expressed in *Sf9* insect cells, failed to bind NECA with high affinity. Analogous experiments with the G_s-coupled β₂AR and A_{2A}AR had shown high-affinity agonist binding.^{150; 154} Only the co-expression with A₃AR's cognate G protein interaction partners, Gα_{i1}, Gβ₁, and Gγ₂, enabled the detection of NECA binding, however, only with moderate affinity. These data imply that the presence of G proteins might play a different role in ligand binding to the A₃AR compared to that of the A₁- and A_{2A}ARs, or the β₂AR. Investigation of ligand binding at solubilized A₃AR constructs showed that only the A₃AR-S97^{3.39}K construct solubilized by the non-ionic detergent DDM supplemented with the soluble cholesterol analog cholesteryl hemisuccinate (CHS) exhibited high affinity binding of PSB-11. Solubilization of A₃AR-S97^{3.39}K by the zwitterionic detergent CHAPS or solubilization of the A₃AR-bRIL construct by CHAPS or DDM/CHS showed decreased affinity of PSB-11 (Table 12). CHAPS and DDM are known to asymmetrically extract

membrane components, such as lipids and cholesterol upon solubilization, which might have caused the decreased affinity.^{308; 309}

Table 12. Effect of the expression system, the receptor modifications and receptor preparation on ligand affinity. High: $K_D < 20$ nM; Decreased: $K_D > 20$ nM; No binding: No detectable radioligand binding; n.d.: Not determined; CHAPS: zwitterionic detergent 3-[3-(cholamidopropyl)dimethylammonio]-1-propanesulfonate; DDM: non-ionic detergent *n*-dodecyl- β -D-maltoside; CHS: cholesterol derivative cholesteryl hemisuccinate. For further details see Section 3.18.

Expression system	Receptor modification	Receptor preparation	Ligand affinity (PSB-11/NECA)	
CHO-S	None	Membrane	High/high	
	S97 ^{3.39} K	Membrane	High/no binding	
	bRIL	Membrane	High/decreased	
	None	Solubilized	Insufficient	
	S97 ^{3.39} K	Solubilized (CHAPS)	Decreased/n.d.	
		Solubilized (DDM/CHS)	High/n.d.	
	bRIL	Solubilized (CHAPS)	Decreased/n.d.	
		Solubilized (DDM/CHS)	Decreased/n.d.	
	<i>Sf9</i>	None	Membrane	Decreased/decreased
		S97 ^{3.39} K	Membrane	Decreased/no binding
bRIL		Membrane	Decreased/decreased	
None/S97 ^{3.39} K/bRIL		Solubilized	Insufficient	

In a second approach, the membrane composition of insect cells was taken into focus, revealing that cholesterol is important for ligand binding at the A₃AR. Cholesterol depletion caused a significant decrease in specific [³H]PSB-11 binding but only a minor decrease in affinity. So far, cholesterol-A₃AR interaction has not been investigated or described in the literature. Thus, the data presented in this thesis might initiate new research projects focusing on the elucidation of the role of lipids for the A₃AR's structure and function. A₃AR constructs solubilized from mammalian CHO-S cell membranes, in which they still possessed high-affinity binding, failed to show efficient ligand binding. This implies that solubilization by detergents might not be suitable for preserving the A₃AR structure since it depletes membrane lipids and cholesterol. The use of nanodiscs or liposomes, leading to a more native-like environment upon solubilization, could be an

appropriate approach to overcome this problem.³¹⁸ Notably, the ligand binding profiles of almost all published GPCR crystallization constructs that were expressed in *Sf9* insect cells had been validated at membrane preparations of mammalian cell lines.^{38; 214; 220; 279; 314; 319} Only the first human GPCR crystallization constructs, those of the A_{2A}AR and the β₂AR, had been expressed in *Sf9* insect cells for ligand binding validation.^{150; 154} Their ligand binding profiles remained unaltered, but the present study shows that this cannot be generalized.

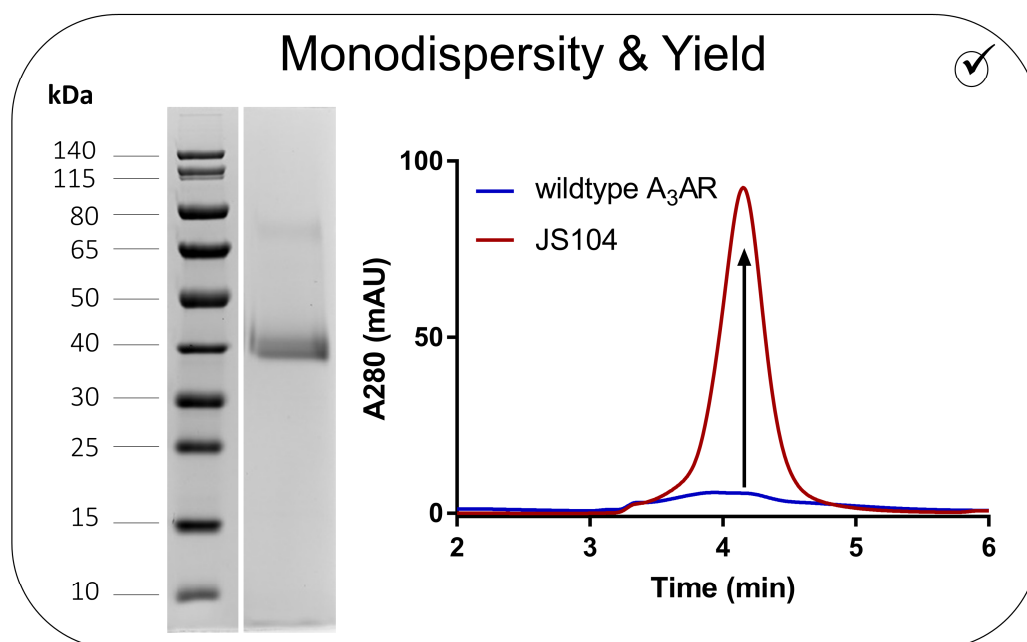


Figure 67. Conclusion — Monodispersity and yield.
SDS-PAGE and SEC chromatogram refer to Sections 3.2.1 and 3.16.5.

Altogether, the novel A₃AR constructs developed in this study show enhanced expression levels, excellent stability, and crystallization-grade monodispersity, homogeneity, and purity (Figure 67). The subsequent validation of ligand binding revealed discrepancies between A₃AR constructs expressed in insect or mammalian cells that need to be considered in future A₃AR research. Altered binding properties might result from the lipid environment or missing G proteins. Stabilized receptor constructs presented in this thesis are also essential, e.g., for the investigation of lipid interactions after reconstitution in High-Density-Lipoparticles or liposomes since the wildtype A₃AR might be too unstable to be extracted from membranes to a sufficient extent. Moreover, characterization by techniques focusing on protein-protein or protein-ligand interactions, employing, e.g.,

microscale thermophoresis, often requires sufficient amounts of solubilized proteins. Structural elucidation by cryo-EM might also be achieved by employing an A₃AR-S97^{3,39}K construct with an N-terminal fusion partner expressed in CHO-S cells and subsequently solubilized by the detergent DDM supplemented with the cholesterol derivative cholesteryl hemisuccinate since this approach possibly maintains high-affinity ligand binding (see Table 12)

Results of this thesis will assist in promoting research on the so far poorly studied A₃AR, eventually leading to its structure elucidation. Findings regarding ligand binding may help to further decrypt the pharmacological profile of the A₃AR and provide valuable information for GPCR pharmacology in general.

5. Methods

5.1 Molecular biology

5.1.1 Construct generation

Initially, DNA sequences encoding the hA₃AR and the mA₃AR were cloned into the pFastBac1 vector (Thermo Fisher), employing the restriction enzymes BamHI and HindIII. The receptor was flanked by N-terminal HA- and FLAG-tags and a C-terminal 10x His-tag. Restriction sites of the restriction enzymes AscI and EcoRI were inserted after the FLAG- and 10x His-tag, respectively. Constructs for the expression in CHO-S cells were cloned into the pcDNA3.1(+) vector using BamHI and EcoRI. All constructs expressed in CHO-S cells included a Kozak sequence to enhance their translation.

5.1.2 Cloning

If necessary, restriction sites were introduced by standard polymerase chain reactions (PCR). The purified PCR product or the plasmid bearing the desired insert and the acceptor plasmid were cut with the respective restriction enzymes in rCutSmart[®] buffer (New England Biolabs) for at least 15 min at 37°C. Subsequently, insert and vector were purified using the DNA Clean and Concentrator Kit (Zymo Research, CN D4013). Purified vector and insert were combined in a 1:5 molar ratio and ligated with T4 DNA Ligase in T4 DNA Ligase Buffer (New England Biolabs, M0202) at 16°C overnight. 5 µL of the ligation mixture were then subjected to transformation into competent DH5α cells (see Section 5.1.6).

5.1.3 Agarose gel electrophoresis

Agarose gel electrophoresis was carried out to purify digested plasmids or PCR products. Gels were made of 0.8 %–2 % (w/v) agarose (Biozym, CN 840001) in TAE buffer and stained with GelRed[®] (Biotium). Samples were mixed with 6x Gel Loading Dye, purple (New England Biolabs, CN B7024S) and transferred into the gel pockets. Two different DNA ladders were used to determine the sizes of DNA fragments: GeneRuler 1 kb DNA Ladder (Thermo Fisher scientific, CN SM0314), Lambda DNA/EcoRI plus HindIII marker (Thermo Fisher scientific, CN SM0192). The gel was run in TAE buffer at 90–130 V for 30–60 min. The required DNA band was cut out and DNA was recovered from the gel slice using the Zymoclean Gel DNA Recovery Kit (Zymo Research, CN D4001).

5.1.4 Site-directed mutagenesis

Point mutations resulting in the desired amino acid exchanges were introduced by site-directed mutagenesis. Primers for the mutagenesis PCR were designed using the web-based QuikChange® Primer Design tool provided by Agilent. The subsequent PCR was carried out according to Table 13. All ingredients were purchased from New England Biolabs except for the primer. Subsequently, the methylated template DNA was digested using DpnI (New England Biolabs, CN R0176). 0.5–1 μ L of DpnI were directly added to the PCR mixture and incubated for at least 30 min at 37°C. 5 μ L were subjected to transformation into DH5 α bacteria (see Section 5.1.6).

Table 13. Mutagenesis PCR

	Temperature [°C]	Duration [min]	Ingredient	Amount [μ L]
20x	98	3	5x GC buffer (NEB, CN B0519)	5
	98	0.5	dNTP mix, 10 mM (NEB, CN N0447)	0.6
	58	0.75	DMSO (NEB, CN B0515)	0.25
	72	5	Phusion polymerase (NEB, CN M0530)	0.3
	72	10	Water ¹	18.25
	12	store	Template DNA (90–150 ng)	
			Forward primer (5 μ M)	0.6
			Reverse primer (5 μ M)	0.6

¹diethylpyrocarbonat-treated water

5.1.5 Overlap extension PCR

Overlap extension PCR was employed to insert a fusion partner in the A₃AR constructs.³²⁰ This technique enables the insertion of a nucleotide sequence, such as that of

fusion partners, into a plasmid utilizing mega primers and two PCR reactions. Firstly, chimeric primers were designed whose 5' and 3' ends overlap (20–25 bp) with the fusion partners and the insertion sites of the A₃AR constructs, respectively. These chimeric primers were then used in a first PCR reaction (Table 14) to generate mega primers, which contain the fusion partners and whose 3' ends were complementary to the insertion sites of the constructs. Subsequently, mega primers were extracted and purified from the reaction mixture using agarose gel electrophoresis (see Section 5.1.3) and employed within a second PCR (Table 15). The result of the second PCR was a new construct in which the fusion partner was successfully introduced into the insertion sites of A₃AR constructs. DpnI digestion and transformation into DH5 α bacteria were carried out according to Sections 5.1.4 and 5.1.6.

Table 14. PCR to generate mega primers — insert preparation

	Temperature [°C]	Duration [min]	Ingredient	Amount [μ L]
30x	95	3	5x Q5 reaction buffer (NEB, CN B9027)	5
	95	0.5	dNTP mix, 2.5 mM (Takara, CN 4030)	1
	55	1	Q5 polymerase (NEB, CN M0491)	0.5
	68	1.5	Water ¹	34
	68	10	Template DNA (150–250 ng)	0.5
	12	store	Forward primer (5 μ M)	2
			Revers primer (5 μ M)	2

¹diethylpyrocarbonat-treated water

Table 15. Overlap extension PCR

	Temperature [°C]	Duration [min]	Ingredient	Amount [μL]
25x	98	3	5x GC buffer (NEB, CN B0519)	4
	98	0.5	dNTP mix, 10 mM (NEB, CN N0447)	0.6
	58	1	MgCl ₂ 50mM (NEB, CN B0510)	0.2
	72	5	Phusion polymerase (NEB, CN M0530)	0.4
	72	5	Water ¹	4.6
	12	store	Template DNA (60–100 ng)	0.2
			Mega primer solution	10

¹diethylpyrocarbonat-treated water

5.1.6 Transformation into competent DH5α *E. coli*

Plasmids were transformed and amplified in DH5α bacteria employing calcium chloride transformation. 10–50 ng plasmid DNA were added to 50 μL of competent DH5α bacteria and subsequently chilled on ice for 30 min. After 30 min incubation, the bacteria suspension was heat shocked for 45 s at 42°C and put back on ice for 2 min. Next, 100 μL of LB medium without any antibiotics were added, and the bacteria suspension was incubated for 1 h at 37°C at 350 rpm shaking in a thermocycler. Subsequently, the bacteria suspension was plated onto ampicillin-containing agar plates (100 μg/mL) and incubated overnight at 37°C. Afterward, single clones were picked with a sterile filter tip and transferred into a culture tube containing 5 mL LB medium supplemented with ampicillin (100 μg/mL). The inoculated bacteria culture was incubated overnight at 37°C in a bacteriological incubator while shaking at 220 rpm. The next day, the plasmid DNA was isolated and purified from the overnight culture using the ZR Plasmid Miniprep – Classic kit (Zymo Research, CN D4016). The purity and concentration were determined using a Colibri microvolume spectrophotometer (Titertek-Berthold, Berthold Technologies GmbH

&Co.KG). The absorbance ratios 260 nm/230 nm and 260 nm/280 nm were employed to assess the purity grade, and ratios of 1.8–2.0 (260/280) and 2.0–2.2 (260/280) were considered as pure DNA. Sequences of all plasmids were verified by sequencing performed by Eurofins Genomics.

5.2 Recombinant protein expression in insect cells

Modified protocols from the Invitrogen Bac-to-Bac Baculovirus Expression System were employed to generate high-titer recombinant baculoviruses and subsequently express generated A₃AR constructs in *Sf9* insect cells.^{321; 322} In contrast to approaches based on homologous recombination, this approach utilizes site-specific transposition into the *E. coli* host strain DH10Bac. The site-specific transposition between the mini-Tn7 element of the pFastBac1 vector and the mini-*att*Tn7 element of the bacmid plasmid (bMON14272) of the DH10Bac bacteria results in a recombinant bacmid bearing the gene of interest. The bacmid plasmid also confers a Kanamycin resistance and provides complementation of the *lacZ* deletion mutant *lacZΔM15* by expressing the necessary α -peptide. Transposition is assisted by a helper plasmid (pMON7124) encoding for a transposase and a tetracycline resistance. Successful insertion of the mini-Tn7 into the mini-*att*Tn7 prevents the expression of the LacZ α peptide, and subsequently, no functional β -galactosidase can be formed by α -complementation. Consequently, the growth on 3+2 agar plates containing the chromogenic substrate 5-Bromo-4-chloro-3-indolyl- β -D-galactopyranoside (X-gal) and the *lac* operon inducer isopropyl- β -D-thiogalactopyranoside (IPTG) yields white colonies. Cells bearing the unaltered bacmid and the intact *lacZ* gene retain functional β -galactosidase, which hydrolyzes X-gal into galactose and 5-Brom-4-chlor-3-indol. This indol then oxidizes and dimerizes spontaneously to a strong blue-colored indigo dye, resulting in blue colonies.

5.2.1 Transformation into DH10Bac *E. coli*

500 ng of the purified pFastBac1 plasmids were transformed into DH10Bac *E. coli* bacteria. The transformation was carried out according to Section 5.1.6 with minor modifications. The heat-shocked bacteria suspension was mixed with 800 μ L of antibiotic-free LB medium and incubated for 3 hours at 37°C at 350 rpm shaking. Subsequently, the bacteria suspension was diluted 1:10 in LB medium (Carl Roth, CN X968) and 100 μ L of

the diluted bacteria suspension were plated onto a 3+2 agar plate containing 10 µg/mL Tetracycline, 7 µg/mL Gentamicin, 50 µg/mL Kanamycin, 40 µg/mL IPTG, and 100 µg/mL X-gal. Inoculated agar plates were wrapped with tin foil and incubated for 48 hours at 37°C in a bacterial incubator. After incubation, separated white colonies were picked with a sterile filter tip and transferred into culture tubes filled with 5 mL of LB medium supplemented with 10 µg/mL tetracycline, 7 µg/mL gentamicin, and 50 µg/mL kanamycin. The inoculated bacteria culture was incubated for 16 h at 37°C and 220 rpm shaking.

5.2.2 Bacmid DNA preparation

The recombinant bacmid DNA was isolated and purified from the overnight cultures obtained in Section 5.2.1 by alcohol precipitation utilizing QIAGEN buffers. After centrifugation, the pellet was resuspended in 400 µL of P1 buffer (QIAGEN, CN 19051) and transferred into a sterile Eppendorf tube. Subsequently, cells were lysed by adding 400 µL of the alkaline P2 buffer (QIAGEN, CN 19052). 400 µL of P3 buffer (QIAGEN, CN 19053) were then used to neutralize the reaction mixture. Centrifugation at 14,000 g for 15 min yielded a supernatant containing the bacmid DNA, which was then added to 800 µL room-temperature isopropanol. After incubation for at least 30 min at -20°C, the bacmid DNA was precipitated by centrifugation at 20,627 g for 15 min at 4°C. The pellet was washed twice with pre-chilled 70 % ethanol (v/v) and dried under a sterile hood. The isolated bacmid DNA was dissolved in 30 µL of water (diethylpyrocarbonat-treated), and 5 µL of the bacmid DNA was subjected to the transfection procedure described in Section 5.2.5. The DNA concentration and purity was determined using a Colibri microvolume spectrophotometer (Titertek-Berthold, Berthold Technologies GmbH & Co.KG). All centrifugation steps were carried out at 4°C.

5.2.3 Verification of the recombinant bacmid DNA

PCR analysis was employed to verify that the gene of interest, the sequence of the A₃AR construct, was successfully transposed into the bacmid DNA (Table 16). The used pUC/M13 forward (5'-CCCAGTCACGACGTTGTAAAACG-3') and reverse (5'-AGCGGATAACAATTTACACAGG-3') primers are complementary to regions flanking the mini-*att*Tn7 cassette. Consequently, the PCR also amplifies the gene of interest if it is

present. The size of the PCR product was determined by agarose gel electrophoresis (see Section 5.1.3). A band at 300 bp indicated failure of the transposition, whereas a band at 2300 bp plus the insert size proved the presence of the construct DNA.

Table 16. Verification PCR

	Temperature [°C]	Duration [min]	Ingredient	Amount [μL]
25x	95	0.5	5x Standard Taq buffer (NEB, B9014)	2.5
			dNTP mix, 10 mM (NEB, CN N0447)	
	58	1	Taq polymerase (NEB, CN M0273)	0.15
	68	3	Water ¹	19.85
	72	5	Bacmid DNA	1
	12	store	M13 forward (5μM)	0.5
			M13 reverse (5μM)	0.5

¹diethylpyrocarbonat-treated water

5.2.4 Cell culture of *Sf9* insect cells

Suspension cultures of *Sf9* insect cells were grown in protein and serum free ESF 921 medium (Expression Systems) at 27°C and 160 rpm. Cells were counted in a hemocytometer and splitted to 1 mio cells/mL every Monday and Wednesday and to 0.8 mio cells/mL every Friday or to 0.8 mio cell/mL every Monday and Thursday. Cell viability was checked by adding 0.4 % Trypan Blue to the cell suspension dilution. When needed, tunicamycin (Cayman Chemical, CN 11445) was added at 1 μg/mL during expression to prevent N-glycosylation.

5.2.5 Transfection & infection

5 μL of the purified bacmid DNA (see Section 5.2.2) were mixed carefully with 100 μL of transfection medium (Expression Systems) and 3 μL of the X-tremeGENE HP

transfection reagent (Roche) and incubated at room temperature for 15 min. The transfection mix was added to 2.5 mL of *Sf9* insect cells (splitted to 1×10^6 cells/mL the same day) in a 24-deep well plate and incubated for 96 hours at 27°C and 400 rpm using a thermocycler. Before harvesting, a sample was taken to verify the success of transfection (Section 5.2.6). Subsequently, the 24-deep well plate was centrifuged at 2000 rpm for 15 min to pellet the cells and harvest the P0 virus. 400 μ L of the P0 virus were then used to infect 40 mL of *Sf9* insect cells at $2\text{--}3 \times 10^6$ cells/mL. After 48 hours incubation, a sample was drawn for evaluating the expression by flow cytometry and the cells were harvested by centrifugation at 2000 g for 15 min. The cell pellet was stored at -80°C until further use. The supernatant (P1 virus) was stored in the dark at 4°C until further use. 400 μ L or 6 mL of the P1 virus were used to infect 40 mL (small-scale) and 900 mL (large-scale) of *Sf9* insect cells. The harvesting of large-scale expression batches was achieved by spinning down the cells at 4000 g for at least 30 min. The pellets were resuspended in 30 mL of PBS and centrifuged for 20 min at 4000 g. After decanting the supernatant, the cell pellet was stored at -80°C until further use.

5.2.6 Transfection control

Transfection success was checked by flow cytometry with an Anti-Baculovirus Envelope glycoprotein 64 (gp64) protein antibody conjugated to phycoerythrin (Expression Systems, CN 97-201). The antibody (0.2 mg/mL) was diluted 1:100 in TBS buffer supplemented with 4 % bovine serum albumin (BSA). A cell sample containing approximately $1\text{--}1.5 \times 10^4$ cells was incubated with 0.01 μ g antibody for 20 min at 4°C in the dark. After the incubation, the mixture was filled up to 100 μ L with TBS buffer and analyzed using a Guava® easyCyte™ HP flow cytometer (blue laser $\lambda=488$ nm, detection channel yellow fluorescence). Baculovirus-infected cells express the envelope glycoprotein gp64 on their surfaces, which is recognized by the specific gp64 antibody and consequently results in a measurable fluorescence signal. Native *Sf9* insect cells lacking the gp64 protein were used as a negative control. Successful transfection was verified by ≥ 90 % infected cells.

5.2.7 Expression control

48 hours after the infection, total and surface expression levels were determined similarly to the gp64 assay but employing a fluorescein-conjugated anti-FLAG antibody (Genscript, CN A01632). The antibody stock solution (0.5 mg/mL) was diluted 1:100 in TBS buffer supplemented with 4 % BSA. 0.15 % Triton X-100 was added to permeabilize the cell membranes and detect intracellular FLAG-tags, determining the total expression. Cell viability was determined by employing the fluorescence intercalator 7-aminoactinomycin D (Thermo Fischer Scientific, eBioscience, CN 00-6993-50), which can only specifically stain the DNA when cell membranes are porous, e.g., like the membranes of dead cells. For each expression, two cell samples, each containing approximately $1-1.5 \times 10^4$ cells, were incubated with 0.025 μg antibody with and without Triton X-100 for 20 min at 4°C in the dark. Subsequently, the mixture was filled up to 100 μL with TBS buffer and analyzed using a Guava® easyCyte™ HP flow cytometer (blue laser $\lambda=488$ nm, detection channel green and red fluorescence). Native *Sf9* insect cells not expressing any FLAG-tagged proteins were used as a negative control to determine expressing and non-expressing cell populations.

5.2.8 Membrane preparation

Small scale (40 mL of infected *Sf9* insect cells)

Sf9 insect cells were disrupted by osmotic shock in a total of 25 mL low osmotic buffer (Table 19). Half a tablet of cOmplete™ EDTA-free protease inhibitor cocktail (Roche) was added to prevent protein degradation. Cells were homogenized in a 15 mL Dounce homogenizer and centrifuged for 30 min at 48,000 g. The pellet was washed by homogenization in high osmotic buffer (Table 19). After centrifugation, the pellet was resuspended thoroughly in 3 mL resuspension buffer (Table 19) using a 2 mL Dounce homogenizer and flash frozen in liquid nitrogen. All work steps were performed on ice, and membrane preparations were stored at -80°C until further use.

Large scale (900 mL of infected *Sf9* insect cells)

Sf9 insect cells were disrupted by homogenization in a 100 mL Dounce homogenizer in 80–90 mL low osmotic buffer (Table 19) supplemented with three tablets of cOmplete™ EDTA-free protease inhibitor cocktail (Roche). The suspension was centrifuged for 30–45 min at 48,000 g, and the resulting pellet was resuspended again in

80–90 mL low osmotic buffer supplemented with two tablets of protease inhibitor cocktail. After centrifugation, the pellet was washed three times with 80–90 mL high osmotic buffer (Table 19). The pellet was resuspended in 40 mL of resuspension buffer (Table 19) using a 40 mL Dounce homogenizer. The homogenizer was rinsed with buffer, and the resuspended membranes were filled up to 50 mL. Batches of 25 mL were flash frozen and stored at -80°C until further use.

5.3 Expression in CHO-S cells

CHO-S cells were grown in FreeStyle™ CHO-S medium (ThermoFisher, CN 12651022) supplemented with 8 mM L-Glutamine (Thermofisher, CN 25030081) in a humidified atmosphere of 8 % CO_2 in air at 37°C . The cell suspension was shaken on an orbital shaker at 120–140 rpm. Cells were splitted to at least 0.05 mio/mL as needed every 48–72 h when cell density reached 1–2 mio/mL.

The day before or approximately 24 h before transfection, cells were splitted to 0.5 mio/mL. At the day of transfection, cells were between 1.2–1.5 mio/mL and splitted to 1 mio/mL. For a small-scale expression (50 mL of cells), 62.5 μg of purified plasmid DNA and 187.5 μg of the 25 kDa linear polyethylenimine (1 mg/mL, DNA/PEI 1:3, Polysciences, CN 23966) were separately diluted in a total volume of each 1 mL of growth medium. Both dilutions were carefully mixed by inverting, incubated for 15 min, and then slowly added to the cell suspension while gently rotating the cell flask. The cells were harvested 24 h after transfection by centrifugation at 500 g for 15 min. The obtained cell pellets were directly subjected to the membrane preparation procedure. Amounts and volumes of PEI, DNA, and growth medium were increased in proportion to the used volume of cell suspension.

5.3.1 CHO-S cells — membrane preparation

CHO-S cell pellets were resuspended in 5/2 buffer (Table 19) and subsequently homogenized with an UltraTurrax at maximum speed for 2x 15 s. The homogenized cell suspension was then centrifuged for 10 min at 1000 g, resulting in the first pellet (P1) which contained cellular debris and nucleoli.¹⁵⁴ The obtained supernatant was centrifuged again for 60 min at 48,000 g. After high-speed centrifugation, the supernatant was discarded, and the pellet was washed by resuspension in 50 mM Tris, pH 7.4. The suspension was

centrifuged for at least 30 min at 48,000 g. All steps were performed on ice or at 4°C. Finally, the pellets were again resuspended in 50 mM Tris, pH 7.4, flash-frozen and stored until further use at -80°C.

5.3.2 PEI stock solution

The desired amount of 25 kDa PEI (Polysciences, CN 23966) were suspended in approximately 90 % of the volume required to obtain a final concentration of 1 mg/mL. The pH value was adjusted to < 2 with concentrated hydrochloric acid, and the mixture was shaken until PEI was completely dissolved. The pH was adjusted to ~7 with sodium hydroxide, and the volume was filled up to obtain a concentration of 1 mg/mL. Subsequently, the solution was sterile-filtered, aliquoted and stored at -80°C until use. Aliquots were thawed when needed but never re-frozen.

5.4 Preparation of the DDM/CHS stock solution

5 g of DDM (Anatrace, CN D310) were dissolved in 40 mL of freshly made 250 mM Tris, pH 8.0. Subsequently, 1 g of CHS (Sigma Aldrich, CN C6512) was added, and the suspension was sonicated using a Sonoplus HD 2070 sonicator equipped with the sonotrode MS73 microtip at 98 % power and 15:00x6 min until CHS was completely dissolved. Afterward, the volume was adjusted to 50 mL, rocked overnight at 4°C, and sterile-filtered the next day. The resulting 10 %/2 % (w/v) DDM/CHS stock solution was stored at 4°C. The LMNG/CHS 5 %/0.5 % (w/v) stock was made in the same way as the DDM/CHS stock.

5.5 Solubilization & Purification

Small scale (40 mL)

3 mL membrane preparations were incubated with 2 mg/mL iodoacetamide for 30 min and subsequently, when needed, incubated with any ligand (25–50 μM) for 30 min. Next, the solubilization was initiated by adding an equal volume (3 mL) of solubilization buffer (Table 19) followed by 3 h incubation at 4°C while slowly rocking. After solubilization, the mixture was centrifuged for 30 min at 10,000 g. The resulting supernatant was then incubated overnight with 12.5 μL (25 μL slurry in buffer) Co²⁺-based IMAC resin (TALON Superflow, Cytiva) in the presence of 20 mM imidazole while slowly rocking at 4°C. The next day, the resin beads were spun down at 100 g for 5 min and

transferred to an empty gravity flow column. The proteins were washed by 750 μL of wash buffer I and 500 μL of wash buffer II (Table 19). The columns were centrifuged for 1 s using a microcentrifuge to remove residual wash buffer after each washing step. Purified proteins were eluted by a 3-step elution using 25 μL of the elution buffer in the first and 50 μL of the elution buffer in the second and third elution step (Table 19). After adding the elution buffer, the columns were capped and incubated for 10 min. All steps were performed at 4°C or on ice and employing prechilled buffers. When needed, proteins were enzymatically deglycosylated with 500 units of PNGase F (New England Biolabs, CN P0704) in a total volume of 22.5 μL overnight at 16°C.

Large scale (900 mL)

25 mL membrane preparation were thawed and processed according to the solubilization and purification of small-scale expressions with minor adjustments. The standard detergent concentration used for solubilization was 0.5 %/0.1 % DDM/CHS. After solubilization, the mixture was centrifuged at 48,000 g for 30 min and the collected supernatant was incubated overnight with 375–500 μL (750–1000 μL slurry in buffer) in the presence of 20 mM imidazole. The next day, the resin beads were transferred to a large empty gravity flow column and let settled down. The protein was washed by 10–15 column volumes wash buffer I (Table 19), supplemented with 10 mM magnesium chloride and freshly added 8 mM adenosine triphosphate. Subsequently, 10 column volumes wash buffer II (Table 19) were added and let run through the column. The elution was carried using steps of 500 μL of elution buffer (Table 19) and 10 min of incubation time between the elution steps. The amount of elution steps was individually adapted but 4 steps of 500 μL were employed as a standard approach. The elution fractions were combined and concentrated to a volume of ~20 μL employing Vivaspin concentrators (100 kDa molecular weight cut-off, Satorius). Solubilization and purification was performed in the presence of 25 μM TK-OT-018.

5.6 Crystallization

Crystallization experiments were conducted using the LCP technique as previously described.^{323; 217; 257} The concentrated protein solution obtained in Section 5.5 was mixed with a molten lipid mixture consisting of 9 parts monoolein (Sigma, CN M7765) and 1 part CLR (Sigma, CN C8667) using two micro-syringes coupled by a narrow-bore coupler. 2

parts of protein were reconstituted in 3 parts of lipid mixture. 50 nL of the generated LCP was dispensed onto 96-well glass sandwich plates (Marienfeld) and overlaid with 800 nL precipitant solution using a Formulatrix NT8 crystallization robot. Plates were sealed with a coverslip and stored at 20°C in a Formulatrix RockImager 54. Stored plates were automatically imaged at increasing intervals for 2–3 weeks.

5.7 Protein analysis

5.7.1 SDS-PAGE and western blotting

Purified proteins were mixed with NuPAGE™ LDS sample buffer (Invitrogen, CN NP0007) containing 200 mM dithiothreitol in a total volume of 30 µL and incubated for 30 min at 37°C. Samples were then loaded into the lanes of 10 % Bis-tris SDS-PAGE gels. Gels consisted of a resolving gel (approximately 4.5 mL) composed of equal amounts of 3x gel buffer (Table 19), 30 % acrylamide/bis-acrylamide (37.5:1) solution and water, and a stacking gel composed of 3x gel buffer, 30 % acrylamide/bis-acrylamide (37.5:1) solution and water in a ratio of 1.5:1:3.5. Polymerization was initiated by adding freshly made 10 % ammonium persulfate solution and tetramethylethylenediamine solution in a ratio of 2.5:1 and 1.5:1 for the resolving gel and the stacking gel, respectively. 0.4 µL/mL and 0.3 µL/mL TEMED solution (Carl Roth, CN 2367) were employed for the resolving and the stacking gel, respectively. Electrophoresis was started at 50–60 V until samples reached the resolving gel and continued at 120–180 V until tracking dyes reached the end of the gel. The whole run was carried out in a 1x running buffer (Table 19). The gel was stained by soaking and heating in a Coomassie staining solution (Table 19).

If western blot analysis was required, the SDS-PAGE gels were blotted onto a nitrocellulose membrane using the Trans-Blot® Turbo™ Transfer System (Bio-Rad) and a transfer buffer (Table 19). The blotting conditions were 1.3 A (const.), 25 V, and 15 min. The membrane was blocked by incubation in the blocking buffer (Table 19) for 45–60 min. Subsequently, the western blot was incubated with the primary mouse anti-His antibody under gentle agitation at 4°C overnight and washed afterward with blocking buffer four times for 5 min. Then, the western blot was incubated with the secondary anti-mouse antibody conjugated to a horseradish peroxidase for 90 minutes and washed again four times for 5 min with PBS-T (Table 19). After a final washing step of 30 minutes in PBS-T,

approximately 800 μL of enhanced chemiluminescence substrate was applied to the membrane. The ChemiDoc MP system (Bio-Rad) was used to acquire the final image.

5.7.2 Size exclusion chromatography

SEC was carried out using an Agilent 1260 Infinity system equipped with a Sepax Nanofilm SEC-250 (4.6x250 mm, 5 μm particle size, 250 \AA) column coupled to a multi wavelength UV-detector. The standard detection wavelength was set to 280 nm. Purified protein samples were centrifuged for 10–15 min at 14,000 g at 4°C to remove residual particles and subsequently transferred into a water-cooled vials. A cooled autosampler was used to keep the samples at 4°C throughout the analysis and avoid any thermal stress. 30 μL of the protein samples were injected onto the column using the HPLC buffer as a mobile phase at a flowrate of 0.5 mL/min. Figures presenting normalized SEC chromatograms were generated by setting the highest mAU value within the time of 3–5 min to 100 %.

5.7.3 Thermostability assay

The thiol-specific fluorochrome CPM was employed to assess the thermostability of the purified proteins as previously described.^{257; 262} In short, the CPM stock solution (4 mg/mL in DMSO) was diluted freshly 1:40 in HPLC buffer before use. The assay was performed in a total volume of 50 μL in HPLC buffer. The purified proteins were incubated with CPM at a final concentration of 2 $\mu\text{g}/\text{mL}$ and, in case of evaluating ligand effects, with a ligand (in DMSO) at a final concentration of 20 μM for 15 min in the dark. After the incubation, samples were analyzed using a Rotor-Gene Q real-time PCR cycler (Qiagen) with $\lambda_{\text{excitation}}=365 \text{ nm}\pm 20 \text{ nm}$, $\lambda_{\text{detection}}=460\pm 20 \text{ nm}$ and a fluorescence gain of 1. The assay was performed over a temperature range of 30–100°C with a slope of 1°C/min. T_M values were determined by using non-linear regression employing the equation “Boltzmann sigmoidal” implemented in GraphPad Prism 7. The variables bottom, V50, and slope were not constrained, whereas the top was constrained to 100 since normalized values were fitted.

5.8 Radioligand displacement assays

Assays were performed according to Table 17 and harvested by rapid filtration through GF/B glass fiber filters (Whatman) using a 48-well Brandel harvester. 7.5–25 μg

protein of CHO-S membrane preparations and 150–200 μg of protein of *Sf9* membrane preparations per well were employed in these binding assays. Membrane preparations were incubated with 2 U of adenosine deaminase (Roche, CN 10102105001) per mL membrane preparation beforehand. Filters were rinsed three times with ice-cold washing buffer, cut, and transferred into scintillation vials. Subsequently, filters were incubated with 2.5 mL ProSafe FC plus scintillation cocktail for at least 6 h and radioactivity was determined using a liquid scintillation counter (Tricarb 2810TR, Perkin Elmer). Assays for the A₁-, A_{2A}-, and A_{2B}ARs were performed by Christin Vielmuth.

Table 17. Radioligand displacement assays.

Receptor	Radioligand (f.c.)	Assay buffer (volume)	Incubation Time [min]	Non-specific binding (f.c.)	Harvesting
hA ₁ AR	[³ H]CCPA (1 nM)	Tris pH 7.4 (400 µL)	90	2- chloradenosine (10 µM)	50 mM Tris pH 7.4, GF/B
hA _{2A} AR	[³ H]MSX-2 (1 nM)	Tris pH 7.4 (400 µL)	30	CGS15943 (10 µM)	50 mM Tris pH 7.4, GF/B filters soaked in 0.3 % (w/v) for 30 min
hA _{2B} AR	[³ H]PSB- 603 (0.3 nM)	Tris pH 7.4 (1000 µL)	75	8-cyclopentyl- 1,3- dipropylxanthine (10 µM)	50 mM Tris pH 7.4 + 0.1 % BSA (w/v), GF/B
hA ₃ AR antagonist	[³ H]PSB-11 (1 nM)	Tris pH 7.4 (400 µL)	45	(R)-N ⁶ - phenylisopropy- adenosine (100 µM) ^a	50 mM Tris pH 7.4, GF/B
hA ₃ AR agonist	[³ H]NECA (10 nM)	Tris pH 7.4, 1 mM EDTA, 10 mM MgCl ₂ (400 µL)	180	(R)-N ⁶ - phenylisopropy- adenosine (100 µM)	50 mM Tris pH 7.4, GF/B

^aCGS15943 was employed to determine the non-specific binding for A₃AR constructs expressed *Sf9* cells.

5.9 Wash-out experiments

Wash-out experiments were carried out as previously described.³²⁴ Membrane preparations were incubated with DMSO (control) or 10-fold of the K_i of the respective compounds for 2 h at room temperature. After incubation, membrane preparations were divided into two batches. One batch was centrifuged for 10 min at 20,627 g, and the other

was stored on ice until used in the radioligand displacement assay. The obtained pellets were resuspended in 50 mM Tris, pH 7.4 and centrifuged again for 10 min at 20,627 g. After four cycles of washing, pellets were resuspended in assay buffer and checked for their remaining binding of [³H]PSB-11. Counts were normalized to the DMSO control, which was used to determine total and non-specific binding.

5.10 CLR-M β CD inclusion complex

Inclusion complexes were generated according to Gimpl et al. 2002.³⁰¹ CLR (Carl Roth, CN 8866) was suspended in M β CD (Sigma Aldrich, CN C4555, 40 mg/mL in Tris 50 mM, pH 7.4) to obtain a final concentration of 3 mM CLR. The suspension was overlaid with argon gas and subsequently shaken at 37°C overnight. The next day, the clear solution was sterile-filtered (0.22 μ M) and used the same day.

5.11 Cholesterol depletion and restoration

Membrane preparations were incubated with solutions of M β CD or CLR-M β CD for 45 min at room temperature while rotating. After incubation, membranes were spun down, and the remaining pellet was washed three times according to the procedure described in Section 5.9. The washed pellet was resuspended in 50 mM Tris, pH 7.4 and used in the radioligand displacement assay.

5.12 Solubilization of A₃AR constructs for radioligand binding studies

In general, solubilization was carried out as previously described.³⁰⁴ Membrane preparations were incubated with 1 % CHAPS (Carl Roth, CN 1479.4) or 1 %/0.2 % DDM/CHS at a protein concentration of 5–15 mg/mL while slowly rocking at 4°C for 45 min. The solubilization mixture was centrifuged at 20,627 g at 4°C for 1 h. The resulting supernatant was diluted with 50 mM Tris, pH 7.4 (1:1) and subjected to the radioligand binding studies.

5.13 Analysis of data from radioligand binding experiments

All data obtained from radioligand assays were analyzed by non-linear regression using implemented equations of GraphPad Prism 7. Homologous binding data were fitted

to the equation “One site—Homologous” with no constraints to variables $\log K_D$, NS, and B_{\max} to determine the K_D value. Competition binding data were analyzed using the equation “One site—Fit K_i ” with no constraints to variables $\log K_i$, top, and bottom to obtain K_i of investigated compounds.

5.14 Protein determination

Protein concentration of membrane preparations was determined employing the Lowry method, which is based on the reaction of copper ions with peptide bonds and the subsequent reaction between Cu^+ and the Folin-Ciocalteu reagent.³²⁵ 200 μL of the diluted membrane preparation were mixed with 1000 μL of a solution consisting of 50 parts 0.1 M NaOH supplemented with 2 % (w/v) of Na_2CO_3 and 1 part of 0.5 % (w/v) $\text{Cu}_2\text{SO}_4 \cdot 5 \text{H}_2\text{O}$ and 1 % (w/v) sodium tartrate in water. After 20 min incubation, 100 μL of the Folin Ciocalteu reagent (5-fold dilution of Folin-Ciocalteu’s phenol reagent, Sigma Aldrich, CN 9252) were added and incubated for 30 min. The absorption at 500 nm and 750 nm were measured using a spectrophotometer, and the protein concentration was determined using a calibration curve employing BSA as a standard.

5.15 Synthesis of compounds

Compounds investigated in this thesis were synthesized by Dr. Ahmed Temirak (compounds ATXXX) and Dr. Tim Klapschinski (compounds TKXXX). Resynthesis of LUF7602 was done by Dr. Ahmed Temirak.

6. Supplementary

6.1 Constructs

Table 18. A₃AR constructs generated in this thesis.

Constructs possess an N-terminal HA- and FLAG-tag as well as a C-terminal 10x His-tag, if not stated otherwise.

Name	N-truncation	C-truncation	Fusion partner	Insertion site	Mutations/modifications
hA ₃ -JS1	-	-	-	-	-
hA ₃ -JS2	1–8	309–318	-	-	-
hA ₃ -JS3	1–8	309–318	b ₅₆₂ RIL	L208–G219	-
hA ₃ -JS4	-	-	b ₅₆₂ RIL	L208–G219	-
hA ₃ -JS5	1–8	309–318	T4L	L208–G219	-
hA ₃ -JS6	1–8	309–318	dsT4L	L208–G219	-
hA ₃ -JS7	1–8	309–318	Flavodoxin	L208–G219	-
hA ₃ -JS8	1–8	309–318	Rubredoxin	L208–G219	-
hA ₃ -JS9	1–8	309–318	Xylanase	L208–G219	-
hA ₃ -JS10	1–8	309–318	Lyso fragment	L208–G219	-
hA ₃ -JS11	1–8	309–318	PTD	L208–G219	-
hA ₃ -JS12	1–8	309–318	PGS	L208–G219	-
hA ₃ -JS1 ₃	1–8	309–318	b ₅₆₂ RIL	N-terminal	-
hA ₃ -JS14	1–8	309–318	T4L	N-terminal	-
hA ₃ -JS15	1–8	309–318	dsT4L	N-terminal	-
hA ₃ -JS16	1–8	309–318	Flavodoxin	N-terminal	-
hA ₃ -JS17	1–8	309–318	Rubredoxin	N-terminal	-
hA ₃ -JS18	1–8	309–318	Xylanase	N-terminal	-
hA ₃ -JS19	1–8	309–318	Lyso fragment	N-terminal	-
hA ₃ -JS20	1–8	309–318	PTD	N-terminal	-
hA ₃ -JS21	1–8	309–318	PGS	N-terminal	-
hA ₃ -JS22	1–8	309–318	b ₅₆₂ RIL	L208–G219	M ₄ receptor N-terminus inserted N-terminal ²¹⁴
hA ₃ -JS23	1–8	309–318	b ₅₆₂ RIL	L208–R224	E217 ^{6.22} to G223 ^{6.28} replaced by A _{2A} sequence ERARSTLQ
hA ₃ -JS24	1–8	309–318	b ₅₆₂ RIL	L208–A229	E217 ^{6.22} to G223 ^{6.28} replaced by A _{2A} sequence ERARSTLQ R224 ^{6.29} to T228 ^{6.33} replaced by A ₁ sequence KELKI
hA ₃ -JS25	1–8	309–318	b ₅₆₂ RIL	L208–A229	E217 ^{6.22} to T228 ^{6.33} replaced by A _{2A} sequence ERARSTLQKEVHA
hA ₃ -JS26	1–8	309–318	b ₅₆₂ RIL	L208–A220	

Name	N-truncation	C-truncation	Fusion partner	Insertion site	Mutations/modifications
hA ₃ -JS27	1–8	309–318	T4-Lysozyme	L208–A220	
hA ₃ -JS28	1–9	309–318	b ₅₆₂ RIL	L208–G219	
hA ₃ -JS29	1–10	309–318	b ₅₆₂ RIL	L208–G219	
hA ₃ -JS30	1–11	309–318	b ₅₆₂ RIL	L208–G219	
hA ₃ -JS31	1–12	309–318	b ₅₆₂ RIL	L208–G219	
hA ₃ -JS32	1–13	309–318	b ₅₆₂ RIL	L208–G219	
hA ₃ -JS33	1–14	309–318	b ₅₆₂ RIL	L208–G219	
hA ₃ -JS34	1–8	300–318	b ₅₆₂ RIL	L208–G219	
hA ₃ -JS35	1–8	306–318	b ₅₆₂ RIL	L208–G219	
mA ₃ -JS36	-	-	-	-	
mA ₃ -JS37	1–9	310–319	-	-	
mA ₃ -JS38	1–9	310–319	b ₅₆₂ RIL	L209–A221	
hA ₃ -JS39	1–8	309–318	b ₅₆₂ RIL	L208–R224	E217 ^{6.22} to G223 ^{6.28} replaced by A _{2A} sequence ERARSTLQ; M4 receptor N-terminus inserted N-terminal ²¹⁴
hA ₃ -JS40	1–8	309–318	b ₅₆₂ RIL	L208–A229	E217 ^{6.22} to G223 ^{6.28} replaced by A _{2A} sequence ERARSTLQ; R224 ^{6.29} to T228 ^{6.33} replaced by A ₁ sequence KELKI; M4 receptor N-terminus inserted N-terminal ²¹⁴ ; gp64 promoter
hA ₃ -JS41	1–8	309–318	b ₅₆₂ RIL	L208–A229	E217 ^{6.22} to T228 ^{6.33} replaced by A _{2A} sequence ERARSTLQKEVHA; M4 receptor N-terminus inserted N-terminal (see A1 crystal. Glukhova 2017)
hA ₃ -JS42	1–8	309–318	-	-	gp64 promoter
hA ₃ -JS43	1–8	309–318	b ₅₆₂ RIL	L208–G219	gp64 promoter
hA ₃ -JS44	1–8	309–318	b ₅₆₂ RIL	L208–G219	M4 receptor N-terminus inserted N-terminal ²¹⁴ ; gp64 promoter
mA ₃ -JS45	1–9	310–319			gp64 promoter

Name	N-truncation	C-truncation	Fusion partner	Insertion site	Mutations/modifications
hA ₃ -JS46	1–8	309–318	b ₅₆₂ RIL	L208–G219	S9 ^{1.29} to N40 ^{1.60} replaced by A _{2A} TM1 P2 ^{1.28} -N34 ^{1.60} ; gp64 promoter
hA ₃ -JS47	1–8	309–318	b ₅₆₂ RIL	L208–G219	-; No N-terminal tags, gp64 promoter
hA ₃ -JS48	1–8	309–318	b ₅₆₂ RIL	L208–G219	S9 ^{1.29} to N40 ^{1.60} replaced by A _{2A} TM1 P2 ^{1.28} -N34 ^{1.60} ; No N-terminal tags, gp64 promoter
hA ₃ -JS49	1–8	309–318	b ₅₆₂ RIL	L208–G219	S97 ^{3.39} K; gp64 promoter
hA ₃ -JS50	1–8	309–318	b ₅₆₂ RIL	L208–G219	S9 ^{1.29} to E19 ^{1.39} replaced by A _{2A} TM1 P2 ^{1.28} -E13 ^{1.39} ; gp64 promoter
hA ₃ -JS51	1–8	309–318	b ₅₆₂ RIL	L208–G219	S9 ^{1.29} to Y15 ^{1.35} replaced by A _{2A} TM1 P2 ^{1.28} -Y9 ^{1.35} ; gp64 promoter
hA ₃ -JS52	1–8	309–318	b ₅₆₂ RIL	L208–G219	N160Q; gp64 promoter
hA ₃ -JS53	1–8	309–318	b ₅₆₂ RIL	L208–A229	E217 ^{6.22} to G223 ^{6.28} replaced by A _{2A} sequence ERARSTLQ; R224 ^{6.29} to T228 ^{6.33} replaced by A ₁ sequence KELKI; M ₄ receptor N-terminus inserted N-terminal ²¹⁴ ; S97 ^{3.39} K; gp64 promoter
hA ₃ -JS54	1–8	309–318	b ₅₆₂ RIL	L208–A229	E217 ^{6.22} to G223 ^{6.28} replaced by A _{2A} sequence ERARSTLQ; R224 ^{6.29} to T228 ^{6.33} replaced by A ₁ sequence KELKI; S97 ^{3.39} K; gp64 promoter
hA ₃ -JS55	1–8	309–318	b ₅₆₂ RIL	L208–A229	E217 ^{6.22} to G223 ^{6.28} replaced by A _{2A} sequence ERARSTLQ; R224 ^{6.29} to T228 ^{6.33} replaced by A ₁ sequence KELKI; M ₄ receptor N-terminus inserted N-terminal ²¹⁴ ; gp64 promoter

Name	N-truncation	C-truncation	Fusion partner	Insertion site	Mutations/modifications
mA ₃ -JS56	1–9	310–319	b ₅₆₂ RIL	L209–A230	E218 ^{6.22} to G224 ^{6.28} replaced by A _{2A} sequence ERARSTLQ; R224 ^{6.29} to T228 ^{6.33}
mA ₃ -JS57	1–9	310–319	b ₅₆₂ RIL	-	S98 ^{3.39} K, gp64 promoter
hA ₃ -JS58	1–8	309–318	b ₅₆₂ RIL	L208–K216	gp64 promoter
hA ₃ -JS59	1–8	309–318	b ₅₆₂ RIL	L208–E217	T218 ^{6.23} replaced by A _{2A} sequence RA, gp64 promoter
hA ₃ -JS60	1–8	309–318	b ₅₆₂ RIL	L208–R224	E217 ^{6.22} to G223 ^{6.28} replaced by A _{2A} sequence ERARSTLQ; M4 receptor N-terminus inserted N-terminal ²¹⁴ , S97 ^{3.39} K
hA ₃ -JS61	1–8	309–318	b ₅₆₂ RIL	L208–R224	E217 ^{6.22} to G223 ^{6.28} replaced by A _{2A} sequence ERARSTLQ; M4 receptor N-terminus inserted N-terminal ²¹⁴ , gp64 promoter
mA ₃ -JS62	1–9	310–319	b ₅₆₂ RIL	L209–A230	E218 ^{6.22} to G224 ^{6.28} replaced by A _{2A} sequence ERARSTLQ; R225 ^{6.29} to T229 ^{6.33} replaced by A ₁ sequence KELKI; M ₄ receptor N-terminus inserted N-terminal ²¹⁴ ;
mA ₃ -JS63	1–9	310–319	b ₅₆₂ RIL	L209–A221	M ₄ receptor N-terminus inserted N-terminal ²¹⁴ ; S98 ^{3.39} K
mA ₃ -JS64	1–9	310–319	b ₅₆₂ RIL	L209–A221	S98 ^{3.39} K
hA ₃ -JS65	-	-	b ₅₆₂ RIL	L208–R224	E217 ^{6.22} to G223 ^{6.28} replaced by A _{2A} sequence ERARSTLQ
hA ₃ -JS66	1–8	309–318	b ₅₆₂ RIL	L208–G219	M ₄ receptor N-terminus inserted N-terminal ²¹⁴ ; N278 ^{7.49} R, gp64 promoter

Name	N-truncation	C-truncation	Fusion partner	Insertion site	Mutations/modifications
hA ₃ -JS67	1–8	309–318	b ₅₆₂ RIL	L208–R224	E217 ^{6.22} to G223 ^{6.28} replaced by A _{2A} sequence ERARSTLQ; M ₄ receptor N-terminus inserted N-terminal ²¹⁴ ; N278 ^{7.49} R, gp64 promoter
hA ₃ -JS68	-	-	b ₅₆₂ RIL	L208–A229	E217 ^{6.22} to G223 ^{6.28} replaced by A _{2A} sequence ERARSTLQ; R224 ^{6.29} to T228 ^{6.33} replaced by A ₁ sequence KELKI; S97 ^{3.39} K
hA ₃ -JS69	1–8	309–318	b ₅₆₂ RIL	L208–A229	E217 ^{6.22} to G223 ^{6.28} replaced by A _{2A} sequence ERARSTLQ; R224 ^{6.29} K, M ₄ receptor N-terminus inserted N-terminal ²¹⁴ ; S97 ^{3.39} K; gp64 promoter
hA ₃ -JS70	1–8	309–318	b ₅₆₂ RIL	L208–A229	E217 ^{6.22} to G223 ^{6.28} replaced by A _{2A} sequence ERARSTLQ; R224 ^{6.29} to T228 ^{6.33} replaced by KELHI; M ₄ receptor N-terminus inserted N-terminal ²¹⁴ ; S97 ^{3.39} K; gp64 promoter
hA ₃ -JS71	1–8	309–318	b ₅₆₂ RIL	L208–K216	R224 ^{6.29} to T228 ^{6.33} replaced by A ₁ sequence KELKI; M ₄ receptor N-terminus inserted N-terminal ²¹⁴ ; gp64 promoter
hA ₃ -JS72	1–8	309–318	b ₅₆₂ RIL	L208–E217	T218 ^{6.23} replaced by A _{2A} sequence RA; R224 ^{6.29} to T228 ^{6.33} replaced by A ₁ sequence KELKI; M ₄ receptor N-terminus inserted N-terminal ²¹⁴ ; gp64 promoter
hA ₃ -JS73	1–8	309–318	b ₅₆₂ RIL	L208–K216	M ₄ receptor N-terminus inserted N-terminal ²¹⁴ ; S97 ^{3.39} K; gp64 promoter

Name	N-truncation	C-truncation	Fusion partner	Insertion site	Mutations/modifications
hA ₃ -JS74	1–8	309–318	b ₅₆₂ RIL	L208–E217	T218 ^{6,23} replaced by A _{2A} sequence RA; M ₄ receptor N-terminus inserted N-terminal ²¹⁴ ; S97 ^{3,39} K; gp64 promoter
hA ₃ -JS75	1–8	309–318	b ₅₆₂ RIL	L208–K216	R224 ^{6,29} to T228 ^{6,33} replaced by A ₁ sequence KELKI; M ₄ receptor N-terminus inserted N-terminal ²¹⁴ ; S97 ^{3,39} K; gp64 promoter
hA ₃ -JS76	1–8	309–318	b ₅₆₂ RIL	L208–E217	T218 ^{6,23} replaced by A _{2A} sequence RA; R224 ^{6,29} to T228 ^{6,33} replaced by A ₁ sequence KELKI; M ₄ receptor N-terminus inserted N-terminal ²¹⁴ ; S97 ^{3,39} K; gp64 promoter
hA ₃ -JS77	-	-	-	-	S97 ^{3,39} K
hA ₃ -JS78	-	-	b ₅₆₂ RIL	L208–G219	S97 ^{3,39} K
hA ₃ -JS79	-	-	b ₅₆₂ RIL	L208–A229	E217 ^{6,22} to G223 ^{6,28} replaced by A _{2A} sequence ERARSTLQ; R224 ^{6,29} to T228 ^{6,33} replaced by A ₁ sequence KELKI;
hA ₃ -JS80	1–8	309–318	b ₅₆₂ RIL	L208–A229	E217 ^{6,22} to G223 ^{6,28} replaced by A _{2A} sequence ERARSTLQ; R224 ^{6,29} to T228 ^{6,33} replaced by A ₁ sequence KELKI; M ₄ receptor N-terminus inserted N-terminal ²¹⁴ ; S97 ^{3,39} K; K285 ^{7,56} to S308 ^{8,69} replaced by A _{2A} helix 8 (R291–A316); gp64 promoter

Name	N-truncation	C-truncation	Fusion partner	Insertion site	Mutations/modifications
hA ₃ -JS81	-	-	b ₅₆₂ RIL	L208–A229	E217 ^{6.22} to G223 ^{6.28} replaced by A _{2A} sequence ERARSTLQ; R224 ^{6.29} to T228 ^{6.33} replaced by A ₁ sequence KELKI; S97 ^{3.39} K; K285 ^{7.56} to S308 ^{8.69} replaced by A _{2A} helix 8 (R291–A316)
hA ₃ -JS82	-	-	b ₅₆₂ RIL	L208–A229	E217 ^{6.22} to G223 ^{6.28} replaced by A _{2A} sequence ERARSTLQ; R224 ^{6.29} to T228 ^{6.33} replaced by A ₁ sequence KELKI; S97 ^{3.39} K, no HA-tag
hA ₃ -JS83	-	-	-	-	K285 ^{7.56} to S308 ^{8.69} replaced by A _{2A} helix 8 (R291–A316)
hA ₃ -JS84	p10 promoter	-	-	-	-
hA ₃ -JS85	p10 promoter	-	b ₅₆₂ RIL	L208–A229	E217 ^{6.22} to G223 ^{6.28} replaced by A _{2A} sequence ERARSTLQ; R224 ^{6.29} to T228 ^{6.33} replaced by A ₁ sequence KELKI; S97 ^{3.39} K
hA ₃ -JS86	-	-	b ₅₆₂ RIL	L208–K216	S97 ^{3.39} K
hA ₃ -JS87	-	-	-	-	No HA-tag
hA ₃ -JS88	-	-	-	-	K285 ^{7.56} to S308 ^{8.69} replaced by A _{2A} helix 8 (R291–A316); No HA-tag
hA ₃ -JS89	-	-	b ₅₆₂ RIL	L208–A229	E217 ^{6.22} to G223 ^{6.28} replaced by A _{2A} sequence ERARSTLQ; R224 ^{6.29} to T228 ^{6.33} replaced by A ₁ sequence KELKI; S97 ^{3.39} K; C166S
hA ₃ -JS90	1–8; HA-NNST-FLAG	309–318	b ₅₆₂ RIL	L208–A229	E217 ^{6.22} to G223 ^{6.28} replaced by A _{2A} sequence ERARSTLQ; R224 ^{6.29} to T228 ^{6.33} replaced by A ₁ sequence KELKI; S97 ^{3.39} K; gp64 promoter
hA ₃ -JS91	1–12	309–318	b ₅₆₂ RIL	L208–K216	S97 ^{3.39} K
hA ₃ -JS92	-	-	-	-	No Tags

Name	N-truncation	C-truncation	Fusion partner	Insertion site	Mutations/modifications
hA ₃ -JS93	1–12; HA-NNST-FLAG	309–318	b ₅₆₂ RIL	L208–K216	S97 ^{3,39} K
hA ₃ -JS94	-	-	b ₅₆₂ RIL	L208–A229	N3Q; N4Q; N12Q; E217 ^{6,22} to G223 ^{6,28} replaced by A _{2A} sequence ERARSTLQ; R224 ^{6,29} to T228 ^{6,33} replaced by A ₁ sequence KELKI; S97 ^{3,39} K
hA ₃ -JS95	-	309–318	b ₅₆₂ RIL	L208–A229	N160Q; E217 ^{6,22} to G223 ^{6,28} replaced by A _{2A} sequence ERARSTLQ; R224 ^{6,29} to T228 ^{6,33} replaced by A ₁ sequence KELKI; S97 ^{3,39} K
hA ₃ -JS96	-; HA-NNST-FLAG	-	b ₅₆₂ RIL	L208–A229	N3Q; N4Q; N12Q; E217 ^{6,22} to G223 ^{6,28} replaced by A _{2A} sequence ERARSTLQ; R224 ^{6,29} to T228 ^{6,33} replaced by A ₁ sequence KELKI; S97 ^{3,39} K
hA ₃ -JS97	-	-	b ₅₆₂ RIL	L208–A229	N3Q; N4Q; N12Q; N16Q; E217 ^{6,22} to G223 ^{6,28} replaced by A _{2A} sequence ERARSTLQ; R224 ^{6,29} to T228 ^{6,33} replaced by A ₁ sequence KELKI; S97 ^{3,39} K
hA _{2A} -JS98	1	317–332	b ₅₆₂ RIL	L208–E219	S91 ^{3,39} K; N154A
hA ₃ -JS99	1–12	309–318	b ₅₆₂ RIL	L208–A229	E217 ^{6,22} to G223 ^{6,28} replaced by A _{2A} sequence ERARSTLQ; R224 ^{6,29} to T228 ^{6,33} replaced by A ₁ sequence KELKI; S97 ^{3,39} K
mA ₃ -JS100	1–9, HA-NNST-FLAG	310–319	b ₅₆₂ RIL	L209–A221	S98 ^{3,39} K

Name	N-truncation	C-truncation	Fusion partner	Insertion site	Mutations/modifications
hA ₃ - JS101	-, HA- QQST- FLAG	-	b ₅₆₂ RIL	L208–A229	N3Q; N4Q; N12Q; N16Q; E217 ^{6.22} to G223 ^{6.28} replaced by A _{2A} sequence ERARSTLQ; R224 ^{6.29} to T228 ^{6.33} replaced by A ₁ sequence KELKI; S97 ^{3.39} K
hA ₃ - JS102	-, HA- NNST- FLAG	-	b ₅₆₂ RIL	L208–A229	N3Q; N4Q; N12Q; N16Q; E217 ^{6.22} to G223 ^{6.28} replaced by A _{2A} sequence ERARSTLQ; R224 ^{6.29} to T228 ^{6.33} replaced by A ₁ sequence KELKI; S97 ^{3.39} K
hA ₃ - JS103	-, HA- GSGS- FLAG	-	b ₅₆₂ RIL	L208–A229	N3Q; N4Q; N12Q; N16Q; E217 ^{6.22} to G223 ^{6.28} replaced by A _{2A} sequence ERARSTLQ; R224 ^{6.29} to T228 ^{6.33} replaced by A ₁ sequence KELKI; S97 ^{3.39} K
hA ₃ - JS104	-	309–318; no protease cleavage site	b ₅₆₂ RIL	L208–A229	N3Q; N4Q; N12Q; N16Q; E217 ^{6.22} to G223 ^{6.28} replaced by A _{2A} sequence ERARSTLQ; R224 ^{6.29} to T228 ^{6.33} replaced by A ₁ sequence KELKI; S97 ^{3.39} K
hA ₃ - JS105	-	-	b ₅₆₂ RIL	L208–K216	A69 ^{2.61} S; S97 ^{3.39} K
hA ₃ - JS106	-	-	b ₅₆₂ RIL	L208–K216	F48 ^{2.40} N; S97 ^{3.39} K
hA ₃ - JS107	-	-	b ₅₆₂ RIL	L208–K216	S97 ^{3.39} K; F233 ^{6.38} A
hA ₃ - JS108	-	-	b ₅₆₂ RIL	L208–K216	S97 ^{3.39} K; M99 ^{3.41} W
hA ₃ - JS109	-	-	b ₅₆₂ RIL	L208–K216	S97 ^{3.39} K; S242 ^{6.47} C
hA ₃ - JS110	-	-	b ₅₆₂ RIL	L208–K216	S97 ^{3.39} K; L101 ^{3.43} A; I104 ^{3.46} A
hA ₃ - JS111	-	-	b ₅₆₂ RIL	L208–K216	S97 ^{3.39} K; S271 ^{7.42} A

Name	N-truncation	C-truncation	Fusion partner	Insertion site	Mutations/modifications
hA ₃ -JS112	-, N-terminal His-tag	309–318	b ₅₆₂ RIL	L208–A229	N3Q; N4Q; N12Q; N16Q; E217 ^{6.22} to G223 ^{6.28} replaced by A _{2A} sequence ERARSTLQ; R224 ^{6.29} to T228 ^{6.33} replaced by A ₁ sequence KELKI; S97 ^{3.39} K;
hA ₃ -JS113	-	309–318; no protease cleavage site	b ₅₆₂ RIL	L208–A229	N3Q; N4Q; N12Q; N16Q; E217 ^{6.22} to G223 ^{6.28} replaced by A _{2A} sequence ERARSTLQ; R224 ^{6.29} to T228 ^{6.33} replaced by A ₁ sequence KELKI; S97 ^{3.39} K; C83 ^{3.25} S
hA ₃ -JS114	-	309–318; no protease cleavage site	b ₅₆₂ RIL	L208–A229	N3Q; N4Q; N12Q; N16Q; E217 ^{6.22} to G223 ^{6.28} replaced by A _{2A} sequence ERARSTLQ; R224 ^{6.29} to T228 ^{6.33} replaced by A ₁ sequence KELKI; S97 ^{3.39} K; C88 ^{3.30} S
hA ₃ -JS115	-, No HA-tag	309–318; no protease cleavage site	b ₅₆₂ RIL	L208–A229	N3Q; N4Q; N12Q; N16Q; E217 ^{6.22} to G223 ^{6.28} replaced by A _{2A} sequence ERARSTLQ; R224 ^{6.29} to T228 ^{6.33} replaced by A ₁ sequence KELKI; S97 ^{3.39} K
hA ₃ -JS116 CHO-S	-	-	b ₅₆₂ RIL	L208–A229	E217 ^{6.22} to G223 ^{6.28} replaced by A _{2A} sequence ERARSTLQ; R224 ^{6.29} to T228 ^{6.33} replaced by A ₁ sequence KELKI; S97 ^{3.39} K
hA ₃ -JS117	-; HA-GSGS-FLAG	309–318; no protease cleavage site	b ₅₆₂ RIL	L208–A229	N3Q; N4Q; N12Q; N16Q; E217 ^{6.22} to G223 ^{6.28} replaced by A _{2A} sequence ERARSTLQ; R224 ^{6.29} to T228 ^{6.33} replaced by A ₁ sequence KELKI; S97 ^{3.39} K

Name	N-truncation	C-truncation	Fusion partner	Insertion site	Mutations/modifications
hA ₃ - JS118	-	309–318; no protease cleavage site	b ₅₆₂ RIL	L208–A229	N3Q; N4Q; N12Q; N16Q; E217 ^{6.22} to G223 ^{6.28} replaced by A _{2A} sequence ERARSTLQ; R224 ^{6.29} to T228 ^{6.33} replaced by A ₁ sequence KELKI; S97 ^{3.39} K, S271 ^{7.42} A
hA ₃ - JS119	-	309–318; no protease cleavage site	b ₅₆₂ RIL	L208–A229	N3Q; N4Q; N12Q; N16Q; E217 ^{6.22} to G223 ^{6.28} replaced by A _{2A} sequence ERARSTLQ; R224 ^{6.29} to T228 ^{6.33} replaced by A ₁ sequence KELKI; S97 ^{3.39} K, F233 ^{6.38} A
hA ₃ - JS120	-	309–318; no protease cleavage site	b ₅₆₂ RIL	L208–A229	N3Q; N4Q; N12Q; N16Q; E217 ^{6.22} to G223 ^{6.28} replaced by A _{2A} sequence ERARSTLQ; R224 ^{6.29} to T228 ^{6.33} replaced by A ₁ sequence KELKI; S97 ^{3.39} K, F233 ^{6.38} A, S271 ^{7.42} A
hA ₃ - JS121 CHO-S	-	-; no His- tag			S97 ^{3.39} K
hA ₃ - JS122 CHO-S	-	-; no His- tag			E217 ^{6.22} to G223 ^{6.28} replaced by A _{2A} sequence ERARSTLQ; R224 ^{6.29} to T228 ^{6.33} replaced by A ₁ sequence KELKI

6.2 Amino acid sequences

6.2.1 Human A₃AR

MPNNSTALSLANVTYITMEIFIGLCAIVGNVLVICVVKLNPSLQTTTFYFIVSLALADIAVG
 VLVMPLAIVVSLGITIHFYSCLFMTCLLLIFTHASIMSLLAIAVDYRLRVKLTVRYKRVTTTH
 RRIWLALGLCWLVSFLVGLTPMFGWNMKL TSEYHRNVTF LSCQFVSVMRMDYMVYFSF
 LTWIFIPLVVMCAIYLDIFYIIRNKLSLNLNSKETGAFYGREFKTAKSLFLVFLFALS WLP
 LSIINCIIFYNGEV PQLVLYMGILLSHANSMMNP IVYAYKIKKFKETYLLILKACVVCHPSD
 SLDTSIEKNSE

6.2.2 Mouse A₃AR

MEADNTTETDWLNITYITMEAAIGLCAVVG NMLVIWVVKLNPTLR TTTV
YFIVSLALADIAVGV LVIPLAIAVSLQVKMHFYACLFMSCVLLIFTHASIMSL LAIA
VHRYLRVKLTVRYRTVTTQRRIWLFGLGCWLV SFLVGLTPMFGWNRKATLASS
QNSSTLLCHFRSVVSLDYMVFFSFITWILVPLVVMCH IYLDIFYIIRNKLSQNL TGFR
ETRAFYGREFKTA KSLFLVLFLFALCWLP LSIINFVSYFDVKIPDVAMCLGILLSHA
NSMMNP IVYACKIKKFKETYFLILRAVRLCQTSDSLDSNMEQTTE

6.2.3 Tags

M₄-N-terminus

(M)ANFTPVNGSSGNQSVRLVTSSS

HA-tag

MKTIIALS YIFCLVFA

FLAG-tag

DYKDDDDA/D/K

6.2.4 Fusion partner

6.2.4.1 b₅₆₂RIL

ADLEDNWETLNDNLKVIEKADNAAQVKDALTKMRAAALDAQKATPPKL
EDKSPDSEMKDFRHGFDILVGQIDDALKLANEGKVKEAQAAAEQLKTTRNAYI
QKYL

6.2.4.2 T4L

NIFEMLRIDEGLRLKIYKDTEGYTIGIGHLLTKSPSLNAAKSELDKAIGRN
TNGVITKDEAEKLFNQDVDAAVRGILRNAKLKPVYDSLDAVRRALINMVFQM
GETGVAGFTNSLRMLQQKRWDEAAVNLA KSRWYNQTPNRAKRVITTFRTGTW
DAY

6.2.4.3 dsT4L

NCFEMLRIDEGLRLKIYKDCEGYTIGIGHLLTKSPSLNAAKSELDKAIGR
NTNGVITKDEAEKLFNQDVDAAVRGILRNAKLKPVYDSLDAVRRALINMVFQM
MGETGVAGFTNSLRMLQQKRWDEAAVNLA KSRWYNQCPNRAKRVITTFRTGT
WDAY

6.2.4.4 Flavodoxin

AKALIVYGSTTGNT EYTAETIARELADAGYEVD SRDAASVEAGGLFEGFD
LVLLGCSTWGD DSIELQDDFIPLFDSLEETGAQGRKVACFGCGDSSWEYFCGAV
DAIEEKLK NLGAEIVQDGLRIDGDPRAARDDIVGWAHDVIRGAI

6.2.4.5 Rubredoxin

MKKYTCTVCGYIYNPEDGDPDNGVNP GTDFKDIPDDWVCPLCGVGKDQF
EEVEE

6.2.4.6 Xylanase

ASTDYWQNWTFGGGIVNAVNGSGGNYSVNWSNTGNFVVGKGWTTGSPF
RTINYNAGVWAPNGNGYLTLYGWTRSPLIEYYVVD SWGTYRPTGTYKGTVKSD
GGTYDIYTTTRYNAPSIDGDDTTFTQYWSVRQSKRPTGSNATITFTNHVNAWKS
HGMNLGSNWAYQVMATEGYQSSGSSNVTVW

6.2.4.7 Lyso Fragment

KDEAEKLFNQDVDAAVRGILRNAKLKPVYDSLDAVRRRAALINMVFQMG
ETGVAGFTNSLRMLQQKRWDEAAVNLA KSRWYNQTPNRAKR VITTFRTGTWD
AYKNLSGGGGAMDIFEMLRIDEG

6.2.4.8 PTD

GSHMEYLGVFVDETKEYLQNLNDTLLELEKNPEDMELINEAFRALHTLKG
MAGTMGFSSMAKLCHTLENILDKARNSEIKITSDLLDKIFAGVDMITRMVDKIVS

6.2.4.9 PGS

GIDCSFWNESYLTGSRDERKKSLLSKFGMDEGVTFMFIGRFDRGQKGV DV
LLKAIEILSSKKEFQEMRFIIIGKGDPELEGWARSLEEKHG NVKVITEMLSREFVRE
LYGSVDFVIIPSYFEPFGLVALEAMCLGAIPASAVGGLRDIITNETGILVKAGDPG
ELANAILKALELSRSDL SKFRENCKKRAMSFS

6.3 Buffers

Table 19. Composition of used buffers.

Name	Composition
Blocking buffer	5 % (w/v) milk powder in PBS-T
Coomassie staining solution	1.25 g Coomassie Brilliant Blue R-250, 670 mL ddH ₂ O, 250 mL glacial acetic acid, 80 mL ethanol absolute
Elution buffer	25 mM HEPES pH 7.5, 800 mM sodium chloride, 0.025 % DDM (w/v), 0.05 % CHS (w/v), 10 % glycerol, 200 mM imidazole
3x Gel buffer	1 M bis-Tris pH 6.5-6.7
High osmotic buffer	10 mM HEPES pH 7.5, 10 mM MgCl ₂ , 20 mM KCl, 1 M NaCl
HPLC buffer	25 mM HEPES pH 7.5, 500 mM NaCl, 2 % glycerol, 0.05 % DDM (w/v), 0.01 % CHS (w/v)
Low osmotic buffer	10 mM HEPES pH 7.5, 10 mM MgCl ₂ , 20 mM KCl
PBS-T	0.1 % Tween [®] -20 in 1x phosphate-buffered saline (PBS)
Resuspension buffer	10 mM HEPES pH 7.5, 10 mM MgCl ₂ , 20 mM KCl, 30 % glycerol (v/v)
20x Running buffer	1 M 3-morpholinopropane-1-sulfonic acid (MOPS), 1 Tris, 20 mM EDTA, 2 % SDS,
Solubilization buffer (2x)	100 mM HEPES pH 7.5, 1.6 M sodium chloride, 2 % DDM (w/v), 0.2% CHS (w/v)

Name	Composition
TAE	2 M Tris-HCl, 1 M acetic acid, 50 mM EDTA
TBS	150 mM sodium chloride, 50 mM Tris-HCl pH 7.6
Transfer buffer	48 mM Tris, 39 mM glycine, 10 % ethanol, 0.1 % sodium dodecyl sulfate (SDS)
Wash buffer I	50 mM HEPES pH 7.5, 800 mM sodium chloride, 0.1 % DDM, 0.02 % CHS, 10 % glycerol (v/v), 25 mM imidazole
Wash buffer II	50 mM HEPES pH 7.5, 800 mM sodium chloride, 0.05 % DDM (w/v), 0.01 % CHS (w/v), 10 % glycerol (v/v), 50 mM imidazole
5/2	5 mM Tris, 2 mM EDTA, pH 7.4

7. Danksagung

Zunächst möchte ich mich ganz herzlich bei Prof. Dr. Christa Müller für die Möglichkeit und das Vertrauen ein solch spannendes Projekt zu bearbeiten bedanken. Danke für dein offenes Ohr, deine Betreuung und deine Unterstützung während der letzten fast 4,5 Jahre. Ein Dank geht auch an die weiteren Mitglieder der Promotionskommission: Prof. Dr. Gerd Bendas als Zweitgutachter, Prof. Dr. Finn Kristian Hansen als Vorsitz der Kommission und Prof. Dr. Rainer Manthey als weiteres Mitglied.

Ein ganz besonderer Dank geht an Tobias Claff und Victoria Vaaßen. Danke für die tolle Zeit und eure unglaubliche Unterstützung. Ohne euch wäre meine Promotion so nicht möglich gewesen. Danke an Dr. Lukas Wendt und Dr. Georg Rolshoven, die mich damals in ihr Labor, ihre Mensafahrten und die Feierabendaktivitäten aufgenommen und willkommen geheißen haben. Danke auch an Jan Voß, der mich vor allem durch meine Anfangszeit begleitet hat. An die weiteren Mitglieder des Büros 4.107, Andhika Mahardhika, der stets für mein leibliches Wohl gesorgt hat, und Haneen Al-Hroub geht natürlich auch ein Dank.

Ich bedanke mich zudem bei Dr. Ahmed Temirak und Dr. Tim Klapschinski für die Synthese chemischer Verbindungen, die ich während meiner Arbeit verwendet habe, sowie Dr. Markus Kuschak für seine Einarbeitung. Danke an Christiane Bous, Marion Schneider, Katharina Sylvester und Christin Vielmuth für eure Expertise, Organisation und Geduld bei allen Anliegen. Für die Zeit als betreuender Assistent bedanke ich mich bei allen Beteiligten des 7. Semesters. Es war mir stets eine große Freude mit euch den Nachwuchs auszubilden. An alle weiteren Mitglieder des AK Müllers geht ebenso ein großer Dank für die tolle Arbeitsatmosphäre. Trotz aller Mühen bedanke ich mich bei allen Menschen, die mich unterstützt haben und die ich aus noch unerklärlichen Gründen vergessen habe explizit zu erwähnen.

Natürlich bedanke ich mich auch für die Unterstützung durch meine Familie, Freunde und meine Freundin, die abseits der Uni und Forschung für Spaß und Ablenkung gesorgt haben.

8. References

- (1) Duc, N. M.; Kim, H. R.; Chung, K. Y. Structural mechanism of G protein activation by G protein-coupled receptor. *Eur. J. Pharmacol.* **2015**, *763*, 214–222.
- (2) Fredriksson, R.; Lagerström, M. C.; Lundin, L.-G.; Schiöth, H. B. The G-protein-coupled receptors in the human genome form five main families. Phylogenetic analysis, paralogon groups, and fingerprints. *Mol. Pharmacol.* **2003**, *63*, 1256–1272.
- (3) Venkatakrisnan, A. J.; Deupi, X.; Lebon, G.; Tate, C. G.; Schertler, G. F.; Babu, M. M. Molecular signatures of G-protein-coupled receptors. *Nature* **2013**, *494*.
- (4) Hauser, A. S.; Attwood, M. M.; Rask-Andersen, M.; Schiöth, H. B.; Gloriam, D. E. Trends in GPCR drug discovery: new agents, targets and indications. *Nat. Rev. Drug Discov.* **2017**, *16*, 829–842.
- (5) Attwood, T. K.; Findlay, J. B. Fingerprinting G-protein-coupled receptors. *Protein Eng.* **1994**, *7*, 195–203.
- (6) Kolakowski, L. F. GCRDb: a G-protein-coupled receptor database. *Recept. Channels* **1994**, *2*, 1–7.
- (7) Schiöth, H. B.; Fredriksson, R. The GRAFS classification system of G protein coupled receptors in comparative perspective. *Gen. Comp. Endocrinol.* **2005**, *142*, 94–101.
- (8) Hu, G.-M.; Mai, T.-L.; Chen, C.-M. Visualizing the GPCR network: classification and evolution. *Sci. Rep.* **2017**, *7*, 15495.
- (9) Oldham, W. M.; Hamm, H. E. Heterotrimeric G protein activation by G protein-coupled receptors. *Nat. Rev. Mol. Cell Biol.* **2008**, *9*, 60–71.
- (10) Milligan, G.; Kostenis, E. Heterotrimeric G-proteins: a short history. *Br. J. Pharmacol.* **2006**, *147 Suppl 1*, S46-55.
- (11) Wingler, L. M.; Lefkowitz, R. J. Conformational basis of G Protein-coupled receptor signaling versatility. *Trends in Cell Biol.* **2020**, *30*.
- (12) Hilger, D.; Masureel, M.; Kobilka, B. K. Structure and dynamics of GPCR signaling complexes. *Nat. Struct. Mol. Biol.* **2018**, *25*, 4–12.
- (13) Inoue, A.; Raimondi, F.; Kadji, F. M. N.; Singh, G.; Kishi, T.; Uwamizu, A.; Ono, Y.; Shinjo, Y.; Ishida, S.; Arang, N.; Kawakami, K.; Gutkind, J. S.; Aoki, J.; Russell, R. B. Illuminating G-protein-coupling selectivity of GPCRs. *Cell* **2019**, *177*, 1933-1947.e25.
- (14) Downes, G. B.; Gautam, N. The G protein subunit gene families. *Genomics* **1999**, *62*, 544–552.
- (15) Kamato, D.; Mitra, P.; Davis, F.; Osman, N.; Chaplin, R.; Cabot, P. J.; Afroz, R.; Thomas, W.; Zheng, W.; Kaur, H.; Brimble, M.; Little, P. J. $G\alpha_q$ proteins: molecular pharmacology and therapeutic potential. *Cell Mol. Life Sci.* **2017**, *74*, 1379–1390.
- (16) Neves, S. R.; Ram, P. T.; Iyengar, R. G protein pathways. *Science* **2002**, *296*, 1636–1639.
- (17) Kozasa, T.; Jiang, X.; Hart, M. J.; Sternweis, P. M.; Singer, W. D.; Gilman, A. G.; Bollag, G.; Sternweis, P. C. p115 RhoGEF, a GTPase activating protein for $G\alpha_{12}$ and $G\alpha_{13}$. *Science* **1998**, *280*, 2109–2111.
- (18) Khan, S. M.; Sleno, R.; Gora, S.; Zylbergold, P.; Laverdure, J.-P.; Labbé, J.-C.; Miller, G. J.; Hébert, T. E. The expanding roles of $G\beta\gamma$ subunits in G protein-coupled receptor signaling and drug action. *Pharmacol. Rev.* **2013**, *65*, 545–577.
- (19) Smrcka, A. V. G protein $\beta\gamma$ subunits: central mediators of G protein-coupled receptor signaling. *Cell Mol. Life Sci.* **2008**, *65*, 2191–2214.
- (20) Gurevich, V. V.; Gurevich, E. V. GPCR signaling regulation: the role of GRKs and arrestins. *Front. Pharmacol.* **2019**, *10*, 125.
- (21) Komolov, K. E.; Benovic, J. L. G protein-coupled receptor kinases: past, present and future. *Cell. Signal.* **2018**, *41*, 17–24.

- (22) Reiter, E.; Lefkowitz, R. J. GRKs and β -arrestins: roles in receptor silencing, trafficking and signaling. *Trends Endocrinol. Metab.* **2006**, *17*, 159–165.
- (23) Hilger, D. The role of structural dynamics in GPCR-mediated signaling. *FEBS J.* **2021**, *288*, 2461–2489.
- (24) Ross, E. M.; Wilkie, T. M. GTPase-activating proteins for heterotrimeric G proteins: regulators of G protein signaling (RGS) and RGS-like proteins. *Annu. Rev. Biochem.* **2000**, *69*, 795–827.
- (25) Manglik, A.; Kruse, A. C. Structural basis for G protein-coupled receptor activation. *Biochemistry* **2017**, *56*, 5628–5634.
- (26) Venkatakrishnan, A. J.; Deupi, X.; Lebon, G.; Heydenreich, F. M.; Flock, T.; Miljus, T.; Balaji, S.; Bouvier, M.; Veprintsev, D. B.; Tate, C. G.; Schertler, G. F. X.; Babu, M. M. Diverse activation pathways in class A GPCRs converge near the G-protein-coupling region. *Nature* **2016**, *536*, 484–487.
- (27) Zhou, Q.; Yang, D.; Wu, M.; Guo, Y.; Guo, W.; Zhong, L.; Cai, X.; Dai, A.; Jang, W.; Shakhnovich, E. I.; Liu, Z.-J.; Stevens, R. C.; Lambert, N. A.; Babu, M. M.; Wang, M.-W.; Zhao, S. Common activation mechanism of class A GPCRs. *eLife* **2019**, *8*.
- (28) Mahoney, J. P.; Sunahara, R. K. Mechanistic insights into GPCR-G protein interactions. *Curr. Opin. Struct. Biol.* **2016**, *41*, 247–254.
- (29) Rasmussen, S. G. F.; DeVree, B. T.; Zou, Y.; Kruse, A. C.; Chung, K. Y.; Kobilka, T. S.; Thian, F. S.; Chae, P. S.; Pardon, E.; Calinski, D.; Mathiesen, J. M.; Shah, S. T. A.; Lyons, J. A.; Caffrey, M.; Gellman, S. H.; Steyaert, J.; Skiniotis, G.; Weis, W. I.; Sunahara, R. K.; Kobilka, B. K. Crystal structure of the β_2 -adrenergic receptor-G_s protein complex. *Nature* **2011**, *477*, 549–555.
- (30) Carpenter, B.; Nehmé, R.; Warne, T.; Leslie, A. G. W.; Tate, C. G. Structure of the adenosine A_{2A} receptor bound to an engineered G protein. *Nature* **2016**, *536*, 104–107.
- (31) Chung, K. Y.; Rasmussen, S. G. F.; Liu, T.; Li, S.; DeVree, B. T.; Chae, P. S.; Calinski, D.; Kobilka, B. K.; Woods, V. L.; Sunahara, R. K. Conformational changes in the G protein G_s induced by the β_2 adrenergic receptor. *Nature* **2011**, *477*, 611–615.
- (32) Dror, R. O.; Mildorf, T. J.; Hilger, D.; Manglik, A.; Borhani, D. W.; Arlow, D. H.; Philippsen, A.; Villanueva, N.; Yang, Z.; Lerch, M. T.; Hubbell, W. L.; Kobilka, B. K.; Sunahara, R. K.; Shaw, D. E. Structural basis for nucleotide exchange in heterotrimeric G proteins. *Science* **2015**, *348*, 1361–1365.
- (33) Taghon, G. J.; Rowe, J. B.; Kapolka, N. J.; Isom, D. G. Predictable cholesterol binding sites in GPCRs lack consensus motifs. *Structure* **2021**, *29*, 499-506.e3.
- (34) Jakubík, J.; El-Fakahany, E. E. Allosteric modulation of GPCRs of class A by cholesterol. *Int. J. Mol. Sci.* **2021**, *22*.
- (35) Yang, S.-T.; Kreutzberger, A. J. B.; Lee, J.; Kiessling, V.; Tamm, L. K. The role of cholesterol in membrane fusion. *Chem. Phys. Lipids* **2016**, *199*, 136–143.
- (36) Hanson, M. A.; Cherezov, V.; Griffith, M. T.; Roth, C. B.; Jaakola, V.-P.; Chien, E. Y. T.; Velasquez, J.; Kuhn, P.; Stevens, R. C. A specific cholesterol binding site is established by the 2.8 Å structure of the human β_2 -adrenergic receptor. *Structure* **2008**, *16*, 897–905.
- (37) Wacker, D.; Wang, S.; McCorvy, J. D.; Betz, R. M.; Venkatakrishnan, A. J.; Levit, A.; Lansu, K.; Schools, Z. L.; Che, T.; Nichols, D. E.; Shoichet, B. K.; Dror, R. O.; Roth, B. L. Crystal structure of an LSD-bound human serotonin receptor. *Cell* **2017**, *168*, 377-389.e12.
- (38) Liu, W.; Chun, E.; Thompson, A. A.; Chubukov, P.; Xu, F.; Katritch, V.; Han, G. W.; Roth, C. B.; Heitman, L. H.; IJzerman, A. P.; Cherezov, V.; Stevens, R. C. Structural basis for allosteric regulation of GPCRs by sodium ions. *Science* **2012**, *337*, 232–236.
- (39) Fantini, J.; Di Scala, C.; Baier, C. J.; Barrantes, F. J. Molecular mechanisms of protein-cholesterol interactions in plasma membranes: Functional distinction between topological (tilted) and consensus (CARC/CRAC) domains. *Chem. Phys. Lipids* **2016**, *199*, 52–60.
- (40) Sarkar, P.; Chattopadhyay, A. Cholesterol interaction motifs in G protein-coupled receptors: slippery hot spots? *Wiley Interdiscip. Rev. Syst. Biol. Med.* **2020**, *12*, e1481.

- (41) Dawaliby, R.; Trubbia, C.; Delporte, C.; Masureel, M.; van Antwerpen, P.; Kobilka, B. K.; Govaerts, C. Allosteric regulation of G protein-coupled receptor activity by phospholipids. *Nat. Chem. Biol.* **2016**, *12*, 35–39.
- (42) Duncan, A. L.; Song, W.; Sansom, M. S. P. Lipid-dependent regulation of ion channels and G Protein-coupled receptors: insights from structures and simulations. *Annu. Rev. Pharmacol. Toxicol.* **2020**, *60*, 31–50.
- (43) Gimpl, G.; Klein, U.; Reiländer, H.; Fahrenholz, F. Expression of the human oxytocin receptor in baculovirus-infected insect cells: high-affinity binding is induced by a cholesterol-cyclodextrin complex. *Biochemistry* **1995**, *34*, 13794–13801.
- (44) Milić, D.; Veprintsev, D. B. Large-scale production and protein engineering of G protein-coupled receptors for structural studies. *Front. Pharmacol.* **2015**, *6*, 66.
- (45) Waltenspühl, Y.; Schöppe, J.; Ehrenmann, J.; Kummer, L.; Plückthun, A. Crystal structure of the human oxytocin receptor. *Sci. Adv.* **2020**, *6*, eabb5419.
- (46) Chattopadhyay, A.; Jafurulla, M.; Kalipatnapu, S.; Pucadyil, T. J.; Harikumar, K. G. Role of cholesterol in ligand binding and G-protein coupling of serotonin_{1A} receptors solubilized from bovine hippocampus. *Biochem. Biophys. Res. Commun.* **2005**, *327*, 1036–1041.
- (47) McGraw, C.; Yang, L.; Levental, I.; Lyman, E.; Robinson, A. S. Membrane cholesterol depletion reduces downstream signaling activity of the adenosine A_{2A} receptor. *Biochim. Biophys. Acta Biomembr.* **2019**, *1861*, 760–767.
- (48) Michal, P.; El-Fakahany, E. E.; Doležal, V. Changes in membrane cholesterol differentially influence preferential and non-preferential signaling of the M₁ and M₃ muscarinic acetylcholine Receptors. *Neurochem. Res.* **2015**, *40*, 2068–2077.
- (49) Pontier, S. M.; Percherancier, Y.; Galandrin, S.; Breit, A.; Galés, C.; Bouvier, M. Cholesterol-dependent separation of the β₂-adrenergic receptor from its partners determines signaling efficacy: insight into nanoscale organization of signal transduction. *J. Biol. Chem.* **2008**, *283*, 24659–24672.
- (50) Levitt, E. S.; Clark, M. J.; Jenkins, P. M.; Martens, J. R.; Traynor, J. R. Differential effect of membrane cholesterol removal on μ- and δ-opioid receptors: a parallel comparison of acute and chronic signaling to adenylyl cyclase. *J. Biol. Chem.* **2009**, *284*, 22108–22122.
- (51) Baccouch, R.; Rascol, E.; Stoklosa, K.; Alves, I. D. The role of the lipid environment in the activity of G protein coupled receptors. *Biophys. Chem.* **2022**, *285*, 106794.
- (52) Kiriakidi, S.; Kolocouris, A.; Liapakis, G.; Ikram, S.; Durdagi, S.; Mavromoustakos, T. Effects of cholesterol on GPCR function: insights from computational and experimental studies. *Adv. Exp. Med. Biol.* **2019**, *1135*, 89–103.
- (53) Ali, H.; Cunha-Melo, J. R.; Saul, W. F.; Beaven, M. A. Activation of phospholipase C via adenosine receptors provides synergistic signals for secretion in antigen-stimulated RBL-2H3 cells. Evidence for a novel adenosine receptor. *J. Biol. Chem.* **1990**, *265*, 745–753.
- (54) Meyerhof, W.; Müller-Brechlin, R.; Richter, D. Molecular cloning of a novel putative G-protein coupled receptor expressed during rat spermiogenesis. *FEBS Lett.* **1991**, *284*, 155–160.
- (55) Zhou, Q. Y.; Li, C.; Olah, M. E.; Johnson, R. A.; Stiles, G. L.; Civelli, O. Molecular cloning and characterization of an adenosine receptor: the A₃ adenosine receptor. *Proc. Natl. Acad. Sci. U. S. A.* **1992**, *89*, 7432–7436.
- (56) Atkinson, M. R.; Townsend-Nicholson, A.; Nicholl, J. K.; Sutherland, G. R.; Schofield, P. R. Cloning, characterisation and chromosomal assignment of the human adenosine A₃ receptor (*ADORA3*) gene¹. *Neurosci. Res.* **1997**, *29*, 73–79.
- (57) Borea, P. A.; Gessi, S.; Merighi, S.; Vincenzi, F.; Varani, K. Pharmacology of adenosine receptors: the state of the art. *Physiol. Rev.* **2018**, *98*, 1591–1625.
- (58) Borea, P. A.; Varani, K.; Gessi, S.; Merighi, S.; Vincenzi, F., Eds. *The adenosine receptors*; Humana Press, Cham, Switzerland, 2018.
- (59) Borea, P. A.; Varani, K.; Vincenzi, F.; Baraldi, P. G.; Tabrizi, M. A.; Merighi, S.; Gessi, S. The A₃ adenosine receptor: history and perspectives. *Pharmacol. Rev.* **2015**, *67*, 74–102.

- (60) Salvatore, C. A.; Jacobson, M. A.; Taylor, H. E.; Linden, J.; Johnson, R. G. Molecular cloning and characterization of the human A₃ adenosine receptor. *Proc. Natl. Acad. Sci. U. S. A.* **1993**, *90*, 10365–10369.
- (61) Linden, J.; Taylor, H. E.; Robeva, A. S.; Tucker, A. L.; Stehle, J. H.; Rivkees, S. A.; Fink, J. S.; Reppert, S. M. Molecular cloning and functional expression of a sheep A₃ adenosine receptor with widespread tissue distribution. *Mol. Pharmacol.* **1993**, *44*, 524–532.
- (62) Müller, C. E. Medicinal chemistry of adenosine A₃ receptor ligands. *Curr. Top. Med. Chem.* **2003**, *3*, 445–462.
- (63) Yaar, R.; Jones, M. R.; Chen, J.-F.; Ravid, K. Animal models for the study of adenosine receptor function. *J. Cell. Physiol.* **2005**, *202*, 9–20.
- (64) Varani, K.; Merighi, S.; Gessi, S.; Klotz, K. N.; Leung, E.; Baraldi, P. G.; Cacciari, B.; Romagnoli, R.; Spalluto, G.; Borea, P. A. [³H]MRE 3008F20: a novel antagonist radioligand for the pharmacological and biochemical characterization of human A₃ adenosine receptors. *Mol. Pharmacol.* **2000**, *57*, 968–975.
- (65) Gao, Z.-G.; Teng, B.; Wu, H.; Joshi, B. V.; Griffiths, G. L.; Jacobson, K. A. Synthesis and pharmacological characterization of [¹²⁵I]MRS1898, a high-affinity, selective radioligand for the rat A₃ adenosine receptor. *Purinergic Signal.* **2009**, *5*, 31–37.
- (66) Li, A. H.; Moro, S.; Melman, N.; Ji, X. D.; Jacobson, K. A. Structure-activity relationships and molecular modeling of 3, 5-diacyl-2,4-dialkylpyridine derivatives as selective A₃ adenosine receptor antagonists. *J. Med. Chem.* **1998**, *41*, 3186–3201.
- (67) Jacobson, K. A.; Merighi, S.; Varani, K.; Borea, P. A.; Baraldi, S.; Aghazadeh Tabrizi, M.; Romagnoli, R.; Baraldi, P. G.; Cianchetta, A.; Tosh, D. K.; Gao, Z.-G.; Gessi, S. A₃ adenosine receptors as modulators of inflammation: from medicinal chemistry to therapy. *Med. Res. Rev.* **2018**, *38*, 1031–1072.
- (68) Tchilibon, S.; Joshi, B. V.; Kim, S.-K.; Duong, H. T.; Gao, Z.-G.; Jacobson, K. A. (N)-methanocarba 2,N⁶-disubstituted adenine nucleosides as highly potent and selective A₃ adenosine receptor agonists. *J. Med. Chem.* **2005**, *48*, 1745–1758.
- (69) Kim, H. O.; Ji, X. D.; Siddiqi, S. M.; Olah, M. E.; Stiles, G. L.; Jacobson, K. A. 2-Substitution of N⁶-benzyladenosine-5'-uronamides enhances selectivity for A₃ adenosine receptors. *J. Med. Chem.* **1994**, *37*, 3614–3621.
- (70) Mazziotta, C.; Rotondo, J. C.; Lanzillotti, C.; Campione, G.; Martini, F.; Tognon, M. Cancer biology and molecular genetics of A₃ adenosine receptor. *Oncogene* **2021**.
- (71) Gessi, S.; Cattabriga, E.; Avitabile, A.; Gafa', R.; Lanza, G.; Cavazzini, L.; Bianchi, N.; Gambari, R.; Feo, C.; Liboni, A.; Gullini, S.; Leung, E.; Mac-Lennan, S.; Borea, P. A. Elevated expression of A₃ adenosine receptors in human colorectal cancer is reflected in peripheral blood cells. *Clin. Cancer Res.* **2004**, *10*, 5895–5901.
- (72) Bar-Yehuda, S.; Stemmer, S. M.; Madi, L.; Castel, D.; Ochaion, A.; Cohen, S.; Barer, F.; Zabutti, A.; Perez-Liz, G.; Del Valle, L.; Fishman, P. The A₃ adenosine receptor agonist CF102 induces apoptosis of hepatocellular carcinoma via de-regulation of the Wnt and NF-κB signal transduction pathways. *Int. J. Oncol.* **2008**, *33*, 287–295.
- (73) Hajizadeh, F.; Masjedi, A.; Heydarzadeh Asl, S.; Karoon Kiani, F.; Peydaveisi, M.; Ghalamfarsa, G.; Jadidi-Niaragh, F.; Sevbitov, A. Adenosine and adenosine receptors in colorectal cancer. *Int. Immunopharmacol.* **2020**, *87*, 106853.
- (74) Kazemi, M. H.; Raoofi Mohseni, S.; Hojjat-Farsangi, M.; Anvari, E.; Ghalamfarsa, G.; Mohammadi, H.; Jadidi-Niaragh, F. Adenosine and adenosine receptors in the immunopathogenesis and treatment of cancer. *J. Cell. Physiol.* **2018**, *233*, 2032–2057.
- (75) Stemmer, S. M.; Benjaminov, O.; Medalia, G.; Ciuraru, N. B.; Silverman, M. H.; Bar-Yehuda, S.; Fishman, S.; Harpaz, Z.; Farbstein, M.; Cohen, S.; Patoka, R.; Singer, B.; Kerns, W. D.; Fishman, P. CF102 for the treatment of hepatocellular carcinoma: a phase I/II, open-label, dose-escalation study. *Oncologist* **2013**, *18*, 25–26.

- (76) Koszałka, P.; Gołuńska, M.; Urban, A.; Stasiłój, G.; Stanisławowski, M.; Majewski, M.; Składanowski, A. C.; Bigda, J. Specific activation of A₃, A_{2A} and A₁ adenosine receptors in CD73-knockout mice affects B16F10 melanoma growth, neovascularization, angiogenesis and macrophage infiltration. *PloS one* **2016**, *11*.
- (77) Merighi, S.; Benini, A.; Mirandola, P.; Gessi, S.; Varani, K.; Simioni, C.; Leung, E.; MacLennan, S.; Baraldi, P. G.; Borea, P. A. Caffeine inhibits adenosine-induced accumulation of hypoxia-inducible factor-1 α , vascular endothelial growth factor, and interleukin-8 expression in hypoxic human colon cancer cells. *Mol. Pharmacol.* **2007**, *72*, 395–406.
- (78) Gessi, S.; Sacchetto, V.; Fogli, E.; Merighi, S.; Varani, K.; Baraldi, P. G.; Tabrizi, M. A.; Leung, E.; MacLennan, S.; Borea, P. A. Modulation of metalloproteinase-9 in U87MG glioblastoma cells by A₃ adenosine receptors. *Biochem. Pharmacol.* **2010**, *79*, 1483–1495.
- (79) Haskó, G.; Cronstein, B. Regulation of inflammation by adenosine. *Front. Immunol.* **2013**, *4*, 85.
- (80) Hinze, A. V.; Mayer, P.; Harst, A.; Kügelgen, I. von. Adenosine A₃ receptor-induced proliferation of primary human coronary smooth muscle cells involving the induction of early growth response genes. *J. Mol. Cell. Cardiol.* **2012**, *53*, 639–645.
- (81) Grandoch, M.; Hoffmann, J.; Röck, K.; Wenzel, F.; Oberhuber, A.; Schelzig, H.; Fischer, J. W. Novel effects of adenosine receptors on pericellular hyaluronan matrix: implications for human smooth muscle cell phenotype and interactions with monocytes during atherosclerosis. *Basic Res. Cardiol.* **2013**, *108*, 340.
- (82) Peart, J. N.; Headrick, J. P. Adenosinergic cardioprotection: multiple receptors, multiple pathways. *Pharmacol. Ther.* **2007**, *114*, 208–221.
- (83) Jacobson, K. A.; Tosh, D. K.; Jain, S.; Gao, Z.-G. Historical and current adenosine receptor agonists in preclinical and clinical development. *Front. Cell. Neurosci.* **2019**, *13*, 124.
- (84) Wan, T. C.; Tampo, A.; Kwok, W.-M.; Auchampach, J. A. Ability of CP-532,903 to protect mouse hearts from ischemia/reperfusion injury is dependent on expression of A₃ adenosine receptors in cardiomyocytes. *Biochem. Pharmacol.* **2019**, *163*, 21–31.
- (85) DeNinno, M. P.; Masamune, H.; Chenard, L. K.; DiRico, K. J.; Eller, C.; Etienne, J. B.; Tickner, J. E.; Kennedy, S. P.; Knight, D. R.; Kong, J.; Oleynek, J. J.; Tracey, W. R.; Hill, R. J. 3'-Aminoadenosine-5'-uronamides: discovery of the first highly selective agonist at the human adenosine A₃ receptor. *J. Med. Chem.* **2003**, *46*, 353–355.
- (86) Lasley, R. D. Adenosine receptor-mediated cardioprotection-current limitations and future directions. *Front. Pharmacol.* **2018**, *9*, 310.
- (87) Coppi, E.; Cherchi, F.; Lucarini, E.; Ghelardini, C.; Pedata, F.; Jacobson, K. A.; Di Cesare Mannelli, L.; Pugliese, A. M.; Salvemini, D. Uncovering the mechanisms of adenosine receptor-mediated pain control: focus on the A₃ receptor subtype. *Int. J. Mol. Sci.* **2021**, *22*.
- (88) Janes, K.; Symons-Liguori, A. M.; Jacobson, K. A.; Salvemini, D. Identification of A₃ adenosine receptor agonists as novel non-narcotic analgesics. *Br. J. Pharmacol.* **2016**, *173*, 1253–1267.
- (89) Vincenzi, F.; Pasquini, S.; Borea, P. A.; Varani, K. Targeting adenosine receptors: a potential pharmacological avenue for acute and chronic pain. *Int. J. Mol. Sci.* **2020**, *21*.
- (90) Chen, Z.; Janes, K.; Chen, C.; Doyle, T.; Bryant, L.; Tosh, D. K.; Jacobson, K. A.; Salvemini, D. Controlling murine and rat chronic pain through A₃ adenosine receptor activation. *FASEB J.* **2012**, *26*, 1855–1865.
- (91) Little, J. W.; Ford, A.; Symons-Liguori, A. M.; Chen, Z.; Janes, K.; Doyle, T.; Xie, J.; Luongo, L.; Tosh, D. K.; Maione, S.; Bannister, K.; Dickenson, A. H.; Vanderah, T. W.; Porreca, F.; Jacobson, K. A.; Salvemini, D. Endogenous adenosine A₃ receptor activation selectively alleviates persistent pain states. *Brain* **2015**, *138*, 28–35.
- (92) Petrelli, R.; Scortichini, M.; Kachler, S.; Boccella, S.; Cerchia, C.; Torquati, I.; Del Bello, F.; Salvemini, D.; Novellino, E.; Luongo, L.; Maione, S.; Jacobson, K. A.; Lavecchia, A.; Klotz, K.-N.; Cappellacci, L. Exploring the role of N⁶-substituents in potent dual acting 5'-C-

ethyltetrazolyladenosine derivatives: synthesis, binding, functional assays, and antinociceptive effects in mice^v. *J. Med. Chem.* **2017**, *60*, 4327–4341.

(93) Varani, K.; Vincenzi, F.; Targa, M.; Paradiso, B.; Parrilli, A.; Fini, M.; Lanza, G.; Borea, P. A. The stimulation of A₃ adenosine receptors reduces bone-residing breast cancer in a rat preclinical model. *Eur. J. Cancer* **2013**, *49*, 482–491.

(94) Yan, H.; Zhang, E.; Feng, C.; Zhao, X. Role of A₃ adenosine receptor in diabetic neuropathy. *J. Neurosci. Res.* **2016**, *94*, 936–946.

(95) Jacobson, K. A.; Giancotti, L. A.; Lauro, F.; Mufti, F.; Salvemini, D. Treatment of chronic neuropathic pain: purine receptor modulation. *Pain* **2020**, *161*, 1425–1441.

(96) Wahlman, C.; Doyle, T. M.; Little, J. W.; Luongo, L.; Janes, K.; Chen, Z.; Esposito, E.; Tosh, D. K.; Cuzzocrea, S.; Jacobson, K. A.; Salvemini, D. Chemotherapy-induced pain is promoted by enhanced spinal adenosine kinase levels through astrocyte-dependent mechanisms. *Pain* **2018**, *159*, 1025–1034.

(97) Janes, K.; Wahlman, C.; Little, J. W.; Doyle, T.; Tosh, D. K.; Jacobson, K. A.; Salvemini, D. Spinal neuroimmune activation is independent of T-cell infiltration and attenuated by A₃ adenosine receptor agonists in a model of oxaliplatin-induced peripheral neuropathy. *Brain Behav. Immun.* **2015**, *44*, 91–99.

(98) Janes, K.; Esposito, E.; Doyle, T.; Cuzzocrea, S.; Tosh, D. K.; Jacobson, K. A.; Salvemini, D. A₃ adenosine receptor agonist prevents the development of paclitaxel-induced neuropathic pain by modulating spinal glial-restricted redox-dependent signaling pathways. *Pain* **2014**, *155*, 2560–2567.

(99) Kim, Y.; Kwon, S. Y.; Jung, H. S.; Park, Y. J.; Kim, Y. S.; In, J. H.; Choi, J. W.; Kim, J. A.; Joo, J. D. Amitriptyline inhibits the MAPK/ERK and CREB pathways and proinflammatory cytokines through A₃AR activation in rat neuropathic pain models. *Korean J. Anesthesiol.* **2019**, *72*, 60–67.

(100) Fishman, P.; Bar-Yehuda, S.; Madi, L.; Cohn, I. A₃ adenosine receptor as a target for cancer therapy. *Anticancer Drugs* **2002**, *13*, 437–443.

(101) Palmer, T. M.; Gettys, T. W.; Stiles, G. L. Differential interaction with and regulation of multiple G-proteins by the rat A₃ adenosine receptor. *J. Biol. Chem.* **1995**, *270*, 16895–16902.

(102) Lee, J. E.; Bokoch, G.; Liang, B. T. A novel cardioprotective role of RhoA: new signaling mechanism for adenosine. *FASEB J.* **2001**, *15*, 1886–1894.

(103) Abbracchio, M. P.; Brambilla, R.; Ceruti, S.; Kim, H. O.; Lubitz, D. K. von; Jacobson, K. A.; Cattabeni, F. G protein-dependent activation of phospholipase C by adenosine A₃ receptors in rat brain. *Mol. Pharmacol.* **1995**, *48*, 1038–1045.

(104) Zheng, J.; Wang, R.; Zambraski, E.; Wu, D.; Jacobson, K. A.; Liang, B. T. Protective roles of adenosine A₁, A_{2A}, and A₃ receptors in skeletal muscle ischemia and reperfusion injury. *Am. J. Physiol. Heart Circ. Physiol.* **2007**, *293*, H3685–91.

(105) Trincavelli, M. L.; Tuscano, D.; Marroni, M.; Falleni, A.; Gremigni, V.; Ceruti, S.; Abbracchio, M. P.; Jacobson, K. A.; Cattabeni, F.; Martini, C. A₃ adenosine receptors in human astrocytoma cells: agonist-mediated desensitization, internalization, and down-regulation. *Mol. Pharmacol.* **2002**, *62*, 1373–1384.

(106) Jacobson, K. A.; Klutz, A. M.; Tosh, D. K.; Ivanov, A. A.; Preti, D.; Baraldi, P. G. Medicinal chemistry of the A₃ adenosine receptor: agonists, antagonists, and receptor engineering. *Handb. Exp. Pharmacol.* **2009**, 123–159.

(107) Klotz, K. N.; Hessling, J.; Hegler, J.; Owman, C.; Kull, B.; Fredholm, B. B.; Lohse, M. J. Comparative pharmacology of human adenosine receptor subtypes - characterization of stably transfected receptors in CHO cells. *Naunyn Schmiedeberg's Arch. Pharmacol.* **1998**, *357*, 1–9.

(108) Zwart, M. de; Link, R.; Frijtag Drabbe Künzel, J. K. von; Cristalli, G.; Jacobson, K. A.; Townsend-Nicholson, A.; IJzerman, A. P. A functional screening of adenosine analogues at the adenosine A_{2B} receptor: a search for potent agonists. *Nucleosides & nucleotides* **1998**, *17*, 969–985.

- (109) Borrmann, T.; Hinz, S.; Bertarelli, D. C. G.; Li, W.; Florin, N. C.; Scheiff, A. B.; Müller, C. E. 1-alkyl-8-(piperazine-1-sulfonyl)phenylxanthines: development and characterization of adenosine A_{2B} receptor antagonists and a new radioligand with subnanomolar affinity and subtype specificity. *J. Med. Chem.* **2009**, *52*, 3994–4006.
- (110) Jeong, L. S.; Lee, H. W.; Jacobson, K. A.; Kim, H. O.; Shin, D. H.; Lee, J. A.; Gao, Z.-G.; Lu, C.; Duong, H. T.; Gunaga, P.; Lee, S. K.; Jin, D. Z.; Chun, M. W.; Moon, H. R. Structure-activity relationships of 2-chloro-*N*⁶-substituted-4'-thioadenosine-5'-uronamides as highly potent and selective agonists at the human A₃ adenosine receptor. *J. Med. Chem.* **2006**, *49*, 273–281.
- (111) Volpini, R.; Buccioni, M.; Dal Ben, D.; Lambertucci, C.; Lammi, C.; Marucci, G.; Ramadori, A. T.; Klotz, K.-N.; Cristalli, G. Synthesis and biological evaluation of 2-alkynyl-*N*⁶-methyl-5'-*N*-methylcarboxamidoadenosine derivatives as potent and highly selective agonists for the human adenosine A₃ receptor. *J. Med. Chem.* **2009**, *52*, 7897–7900.
- (112) Volpini, R.; Costanzi, S.; Lambertucci, C.; Taffi, S.; Vittori, S.; Klotz, K.-N.; Cristalli, G. *N*⁶-alkyl-2-alkynyl derivatives of adenosine as potent and selective agonists at the human adenosine A₃ receptor and a starting point for searching A_{2B} ligands. *J. Med. Chem.* **2002**, *45*, 3271–3279.
- (113) IJzerman, A. P.; Jacobson, K. A.; Müller, C. E.; Cronstein, B. N.; Cunha, R. A. International Union of Basic and Clinical Pharmacology. CXII: Adenosine receptors: a further update. *Pharmacol. Rev.* **2022**, *74*, 340–372.
- (114) Filippo, E. de; Namasivayam, V.; Zappe, L.; El-Tayeb, A.; Schiedel, A. C.; Müller, C. E. Role of extracellular cysteine residues in the adenosine A_{2A} receptor. *Purinergic Signal.* **2016**, *12*, 313–329.
- (115) Thimm, D.; Schiedel, A. C.; Sherbiny, F. F.; Hinz, S.; Hochheiser, K.; Bertarelli, D. C. G.; Maass, A.; Müller, C. E. Ligand-specific binding and activation of the human adenosine A_{2B} receptor. *Biochemistry* **2013**, *52*, 726–740.
- (116) Schiedel, A. C.; Hinz, S.; Thimm, D.; Sherbiny, F.; Borrmann, T.; Maass, A.; Müller, C. E. The four cysteine residues in the second extracellular loop of the human adenosine A_{2B} receptor: role in ligand binding and receptor function. *Biochem. Pharmacol.* **2011**, *82*, 389–399.
- (117) Klotz, K. N.; Camaioni, E.; Volpini, R.; Kachler, S.; Vittori, S.; Cristalli, G. 2-Substituted *N*-ethylcarboxamidoadenosine derivatives as high-affinity agonists at human A₃ adenosine receptors. *Naunyn Schmiedeberg's Arch. Pharmacol.* **1999**, *360*, 103–108.
- (118) Müller, C. E.; Jacobson, K. A. Xanthines as adenosine receptor antagonists. *Handb. Exp. Pharmacol.* **2011**, 151–199.
- (119) Klotz, K. N. Adenosine receptors and their ligands. *Naunyn Schmiedeberg's Arch. Pharmacol.* **2000**, *362*, 382–391.
- (120) Kim, Y. C.; Ji, X. D.; Jacobson, K. A. Derivatives of the triazoloquinazoline adenosine antagonist (CGS15943) are selective for the human A₃ receptor subtype. *J. Med. Chem.* **1996**, *39*, 4142–4148.
- (121) van Muijlwijk-Koezen, J. E.; Timmerman, H.; van der Goot, H.; Menge, W. M.; Frijtag Von Drabbe Künzel, J.; Grootte, M. de; IJzerman, A. P. Isoquinoline and quinazoline urea analogues as antagonists for the human adenosine A₃ receptor. *J. Med. Chem.* **2000**, *43*, 2227–2238.
- (122) Baraldi, P. G.; Saponaro, G.; Romagnoli, R.; Aghazadeh Tabrizi, M.; Baraldi, S.; Moorman, A. R.; Cosconati, S.; Di Maro, S.; Marinelli, L.; Gessi, S.; Merighi, S.; Varani, K.; Borea, P. A.; Preti, D. Water-soluble pyrazolo[4,3-*e*]1,2,4-triazolo[1,5-*c*]pyrimidines as human A₃ adenosine receptor antagonists. *J. Med. Chem.* **2012**, *55*, 5380–5390.
- (123) Baraldi, P. G.; Cacciari, B.; Moro, S.; Romagnoli, R.; Ji, X.; Jacobson, K. A.; Gessi, S.; Borea, P. A.; Spalluto, G. Fluorosulfonyl- and bis-(β -chloroethyl)amino-phenylamino functionalized pyrazolo[4,3-*e*]1,2,4-triazolo[1,5-*c*]pyrimidine derivatives: irreversible antagonists at the human A₃ adenosine receptor and molecular modeling studies. *J. Med. Chem.* **2001**, *44*, 2735–2742.
- (124) Baraldi, P. G.; Cacciari, B.; Romagnoli, R.; Spalluto, G.; Moro, S.; Klotz, K. N.; Leung, E.; Varani, K.; Gessi, S.; Merighi, S.; Borea, P. A. Pyrazolo[4,3-*e*]1,2,4-triazolo[1,5-*c*]pyrimidine

- derivatives as highly potent and selective human A₃ adenosine receptor antagonists: influence of the chain at the N⁸ pyrazole nitrogen. *J. Med. Chem.* **2000**, *43*, 4768–4780.
- (125) Klapschinski, T. A. Rationales Design und Aufbau DNA- und Fluorophor-markierter chemischer Sonden für G-Protein-gekoppelte Rezeptoren. Ph. D. Thesis, Rheinische Friedrich-Wihlms-Universität Bonn, Bonn, Germany, 2020.
- (126) Müller, C. E.; Diekmann, M.; Thorand, M.; Ozola, V. [³H]8-Ethyl-4-methyl-2-phenyl-(8*R*)-4,5,7,8-tetrahydro-1*H*-imidazo[2,1-*i*]purin-5-one ([³H]PSB-11), a novel high-affinity antagonist radioligand for human A₃ adenosine receptors. *Bioorg. Med. Chem. Lett.* **2002**, *12*, 501–503.
- (127) Ozola, V. 2-Phenylimidazo[2,1-*i*]purin-5-ones structure–activity relationships and characterization of potent and selective inverse agonists at human A₃ adenosine receptors. *Bioorg. Med. Chem.* **2003**, *11*, 347–356.
- (128) Taliani, S.; La Motta, C.; Mugnaini, L.; Simorini, F.; Salerno, S.; Marini, A. M.; Da Settimo, F.; Cosconati, S.; Cosimelli, B.; Greco, G.; Limongelli, V.; Marinelli, L.; Novellino, E.; Ciampi, O.; Daniele, S.; Trincavelli, M. L.; Martini, C. Novel *N*²-substituted pyrazolo[3,4-*d*]pyrimidine adenosine A₃ receptor antagonists: inhibition of A₃-mediated human glioblastoma cell proliferation. *J. Med. Chem.* **2010**, *53*, 3954–3963.
- (129) Priego, E.-M.; Frijtag Drabbe Kuenzel, J. von; IJzerman, A. P.; Camarasa, M.-J.; Pérez-Pérez, M.-J. Pyrido[2,1-*f*]purine-2,4-dione derivatives as a novel class of highly potent human A₃ adenosine receptor antagonists. *J. Med. Chem.* **2002**, *45*, 3337–3344.
- (130) Baraldi, P. G.; Preti, D.; Tabrizi, M. A.; Fruttarolo, F.; Romagnoli, R.; Zaid, N. A.; Moorman, A. R.; Merighi, S.; Varani, K.; Borea, P. A. New pyrrolo[2,1-*f*]purine-2,4-dione and imidazo[2,1-*f*]purine-2,4-dione derivatives as potent and selective human A₃ adenosine receptor antagonists. *J. Med. Chem.* **2005**, *48*, 4697–4701.
- (131) Yang, X.; van Veldhoven, J. P. D.; Offringa, J.; Kuiper, B. J.; Lenselink, E. B.; Heitman, L. H.; van der Es, D.; IJzerman, A. P. Development of covalent ligands for G Protein-coupled receptors: a case for the human adenosine A₃ receptor. *J. Med. Chem.* **2019**, *62*, 3539–3552.
- (132) Jeong, L. S.; Choe, S. A.; Gunaga, P.; Kim, H. O.; Lee, H. W.; Lee, S. K.; Tosh, D. K.; Patel, A.; Palaniappan, K. K.; Gao, Z.-G.; Jacobson, K. A.; Moon, H. R. Discovery of a new nucleoside template for human A₃ adenosine receptor ligands: D-4'-thioadenosine derivatives without 4'-hydroxymethyl group as highly potent and selective antagonists. *J. Med. Chem.* **2007**, *50*, 3159–3162.
- (133) Jeong, L. S.; Pal, S.; Choe, S. A.; Choi, W. J.; Jacobson, K. A.; Gao, Z.-G.; Klutz, A. M.; Hou, X.; Kim, H. O.; Lee, H. W.; Lee, S. K.; Tosh, D. K.; Moon, H. R. Structure-activity relationships of truncated D- and 1-4'-thioadenosine derivatives as species-independent A₃ adenosine receptor antagonists. *J. Med. Chem.* **2008**, *51*, 6609–6613.
- (134) Nayak, A.; Chandra, G.; Hwang, I.; Kim, K.; Hou, X.; Kim, H. O.; Sahu, P. K.; Roy, K. K.; Yoo, J.; Lee, Y.; Cui, M.; Choi, S.; Moss, S. M.; Phan, K.; Gao, Z.-G.; Ha, H.; Jacobson, K. A.; Jeong, L. S. Synthesis and anti-renal fibrosis activity of conformationally locked truncated 2-hexynyl-*N*⁶-substituted-(*N*)-methanocarba-nucleosides as A₃ adenosine receptor antagonists and partial agonists. *J. Med. Chem.* **2014**, *57*, 1344–1354.
- (135) Liang, B. T.; Urso, M.; Zambraski, E.; Jacobson, K. A. Adenosine A₃ receptors in muscle protection. In *A3 adenosine receptors from cell biology to pharmacology and therapeutics*. Borea, P. A., Ed.; Springer: Dordrecht; pp. 257–280.
- (136) Xu, D.; Meisburger, S. P.; Ando, N. Correlated motions in structural biology. *Biochemistry* **2021**, *60*, 2331–2340.
- (137) Moore, P. B. Structural biology: Past, present, and future. *N. Biotechnol.* **2017**, *38*, 29–35.
- (138) Kendrew, J. C.; Bodo, G.; Dintzis, H. M.; Parrish, R. G.; Wyckoff, H.; Phillips, D. C. A three-dimensional model of the myoglobin molecule obtained by X-ray analysis. *Nature* **1958**, *181*, 662–666.

- (139) Perutz, M. F.; Rossmann, M. G.; Cullis, A. F.; Muirhead, H.; WILL, G.; North, A. C. Structure of haemoglobin: a three-dimensional Fourier synthesis at 5.5-Å resolution, obtained by X-ray analysis. *Nature* **1960**, *185*, 416–422.
- (140) Johnson, L. N.; Phillips, D. C. Structure of some crystalline lysozyme-inhibitor complexes determined by X-ray analysis at 6 Å resolution. *Nature* **1965**, *206*, 761–763.
- (141) Berman, H. M.; Lawson, C. L.; Vallat, B.; Gabanyi, M. J. Anticipating innovations in structural biology. *Q. Rev. Biophys.* **2018**, *51*, e8.
- (142) Berman, H. M.; Westbrook, J.; Feng, Z.; Gilliland, G.; Bhat, T. N.; Weissig, H.; Shindyalov, I. N.; Bourne, P. E. The Protein Data Bank. *Nucleic Acids Res.* **2000**, *28*, 235–242.
- (143) García-Nafria, J.; Tate, C. G. Structure determination of GPCRs: cryo-EM compared with X-ray crystallography. *Biochem. Soc. Trans.* **2021**, *49*, 2345–2355.
- (144) Schertler, G. F.; Villa, C.; Henderson, R. Projection structure of rhodopsin. *Nature* **1993**, *362*, 770–772.
- (145) Landau, E. M.; Rosenbusch, J. P. Lipidic cubic phases: a novel concept for the crystallization of membrane proteins. *Proc. Natl. Acad. Sci. U. S. A.* **1996**, *93*, 14532–14535.
- (146) Palczewski, K.; Kumasaka, T.; Hori, T.; Behnke, C. A.; Motoshima, H.; Fox, B. A.; Le Trong, I.; Teller, D. C.; Okada, T.; Stenkamp, R. E.; Yamamoto, M.; Miyano, M. Crystal structure of rhodopsin: a G protein-coupled receptor. *Science* **2000**, *289*, 739–745.
- (147) Okada, T.; Le Trong, I.; Fox, B. A.; Behnke, C. A.; Stenkamp, R. E.; Palczewski, K. X-Ray diffraction analysis of three-dimensional crystals of bovine rhodopsin obtained from mixed micelles. *J. Struct. Biol.* **2000**, *130*, 73–80.
- (148) Cherezov, V.; Rosenbaum, D. M.; Hanson, M. A.; Rasmussen, S. G. F.; Thian, F. S.; Kobilka, T. S.; Choi, H.-J.; Kuhn, P.; Weis, W. I.; Kobilka, B. K.; Stevens, R. C. High-resolution crystal structure of an engineered human β_2 -adrenergic G protein-coupled receptor. *Science* **2007**, *318*, 1258–1265.
- (149) Rasmussen, S. G. F.; Choi, H.-J.; Rosenbaum, D. M.; Kobilka, T. S.; Thian, F. S.; Edwards, P. C.; Burghammer, M.; Ratnala, V. R. P.; Sanishvili, R.; Fischetti, R. F.; Schertler, G. F. X.; Weis, W. I.; Kobilka, B. K. Crystal structure of the human β_2 adrenergic G protein-coupled receptor. *Nature* **2007**, *450*, 383–387.
- (150) Rosenbaum, D. M.; Cherezov, V.; Hanson, M. A.; Rasmussen, S. G. F.; Thian, F. S.; Kobilka, T. S.; Choi, H.-J.; Yao, X.-J.; Weis, W. I.; Stevens, R. C.; Kobilka, B. K. GPCR engineering yields high-resolution structural insights into β_2 -adrenergic receptor function. *Science* **2007**, *318*, 1266–1273.
- (151) Gacasan, S. B.; Baker, D. L.; Parrill, A. L. G protein-coupled receptors: the evolution of structural insight. *AIMS Biophys.* **2017**, *4*, 491–527.
- (152) Xiang, J.; Chun, E.; Liu, C.; Jing, L.; Al-Sahouri, Z.; Zhu, L.; Liu, W. Successful strategies to determine high-resolution structures of GPCRs. *Trends Pharmacol. Sci.* **2016**, *37*, 1055–1069.
- (153) Chun, E.; Thompson, A. A.; Liu, W.; Roth, C. B.; Griffith, M. T.; Katritch, V.; Kunken, J.; Xu, F.; Cherezov, V.; Hanson, M. A.; Stevens, R. C. Fusion partner toolchest for the stabilization and crystallization of G protein-coupled receptors. *Structure* **2012**, *20*, 967–976.
- (154) Jaakola, V.-P.; Griffith, M. T.; Hanson, M. A.; Cherezov, V.; Chien, E. Y. T.; Lane, J. R.; IJzerman, A. P.; Stevens, R. C. The 2.6 Å crystal structure of a human A_{2A} adenosine receptor bound to an antagonist. *Science* **2008**, *322*, 1211–1217.
- (155) Serrano-Vega, M. J.; Magnani, F.; Shibata, Y.; Tate, C. G. Conformational thermostabilization of the β_1 -adrenergic receptor in a detergent-resistant form. *Proc. Natl. Acad. Sci. U. S. A.* **2008**, *105*, 877–882.
- (156) Miller, J. L.; Tate, C. G. Engineering an ultra-thermostable β_1 -adrenoceptor. *J. Mol. Biol.* **2011**, *413*, 628–638.
- (157) Ballesteros, J. A.; Weinstein, H. Integrated methods for the construction of three-dimensional models and computational probing of structure-function relations in G protein-coupled

- receptors. In *Receptor molecular biology*. Sealfon, S. C., Ed.; Academic Press: San Diego; pp. 366–428.
- (158) Lebon, G.; Warne, T.; Edwards, P. C.; Bennett, K.; Langmead, C. J.; Leslie, A. G. W.; Tate, C. G. Agonist-bound adenosine A_{2A} receptor structures reveal common features of GPCR activation. *Nature* **2011**, *474*, 521–525.
- (159) Sun, B.; Feng, D.; Chu, M. L.-H.; Fish, I.; Lovera, S.; Sands, Z. A.; Kelm, S.; Valade, A.; Wood, M.; Ceska, T.; Kobilka, T. S.; Lebon, F.; Kobilka, B. K. Crystal structure of dopamine D1 receptor in complex with G protein and a non-catechol agonist. *Nat. Commun.* **2021**, *12*, 3305.
- (160) Rasmussen, S. G. F.; Choi, H.-J.; Fung, J. J.; Pardon, E.; Casarosa, P.; Chae, P. S.; DeVree, B. T.; Rosenbaum, D. M.; Thian, F. S.; Kobilka, T. S.; Schnapp, A.; Konetzki, I.; Sunahara, R. K.; Gellman, S. H.; Pautsch, A.; Steyaert, J.; Weis, W. I.; Kobilka, B. K. Structure of a nanobody-stabilized active state of the β_2 adrenoceptor. *Nature* **2011**, *469*, 175–180.
- (161) Li, Q.; Kang, C. Mechanisms of action for small molecules revealed by structural biology in drug discovery. *Int. J. Mol. Sci.* **2020**, *21*.
- (162) Anderson, A. C. The process of structure-based drug design. *Chem. Biol.* **2003**, *10*, 787–797.
- (163) Hol, W. G. J. Protein crystallography and computer Graphics—toward rational drug design. *Angew. Chem. Int. Ed. Engl.* **1986**, *25*, 767–778.
- (164) Hughes, J. P.; Rees, S.; Kalindjian, S. B.; Philpott, K. L. Principles of early drug discovery. *Br. J. Pharmacol.* **2011**, *162*, 1239–1249.
- (165) Congreve, M.; Graaf, C. de; Swain, N. A.; Tate, C. G. Impact of GPCR structures on drug discovery. *Cell* **2020**, *181*, 81–91.
- (166) Wang, X.; Song, K.; Li, L.; Chen, L. Structure-based drug design strategies and challenges. *Curr. Top. Med. Chem.* **2018**, *18*, 998–1006.
- (167) Congreve, M.; Andrews, S. P.; Doré, A. S.; Hollenstein, K.; Hurrell, E.; Langmead, C. J.; Mason, J. S.; Ng, I. W.; Tehan, B.; Zhukov, A.; Weir, M.; Marshall, F. H. Discovery of 1,2,4-triazine derivatives as adenosine A_{2A} antagonists using structure based drug design. *J. Med. Chem.* **2012**, *55*, 1898–1903.
- (168) Borodovsky, A.; Barbon, C. M.; Wang, Y.; Ye, M.; Prickett, L.; Chandra, D.; Shaw, J.; Deng, N.; Sachsenmeier, K.; Clarke, J. D.; Linghu, B.; Brown, G. A.; Brown, J.; Congreve, M.; Cheng, R. K.; Dore, A. S.; Hurrell, E.; Shao, W.; Woessner, R.; Reimer, C.; Drew, L.; Fawell, S.; Schuller, A. G.; Mele, D. A. Small molecule AZD4635 inhibitor of A_{2A}R signaling rescues immune cell function including CD103⁺ dendritic cells enhancing anti-tumor immunity. *J. Immunother. Cancer* **2020**, *8*.
- (169) Bai, X.; McMullan, G.; Scheres, S. H. W. How cryo-EM is revolutionizing structural biology. *Trends Biochem. Sci.* **2015**, *40*, 49–57.
- (170) Nogales, E.; Scheres, S. H. W. Cryo-EM: a unique tool for the visualization of macromolecular complexity. *Mol. Cell* **2015**, *58*, 677–689.
- (171) Dubochet, J.; Lepault, J.; Freeman, R.; Berriman, J. A.; Homo, J.-C. Electron microscopy of frozen water and aqueous solutions. *J. Microsc.* **1982**, *128*, 219–237.
- (172) Dubochet, J.; McDowell, A. W. Vitrication of pure water for electron microscopy. *J. Microsc.* **1981**, *124*, 3–4.
- (173) Renaud, J.-P.; Chari, A.; Ciferri, C.; Liu, W.-T.; Rémigy, H.-W.; Stark, H.; Wiesmann, C. Cryo-EM in drug discovery: achievements, limitations and prospects. *Nat. Rev. Drug Discov.* **2018**, *17*, 471–492.
- (174) Sigworth, F. J. Principles of cryo-EM single-particle image processing. *Microscopy* **2015**, *65*, 57–67.
- (175) Rupp, B. *Biomolecular crystallography*; Garland Science, New York, 2010.
- (176) Baslé, A.; Lewis, R. J. Principles and practice in macromolecular X-ray crystallography. In *Biomolecular and bioanalytical techniques*. Ramesh, V., Ed.; John Wiley & Sons, Inc: Hoboken, NJ; pp. 385–419.

- (177) Maveyraud, L.; Mourey, L. Protein X-ray crystallography and drug discovery. *Molecules* **2020**, *25*.
- (178) Hickman, A. B.; Davies, D. R. Principles of macromolecular X-ray crystallography. *Curr. Protoc. Protein Sci.* **2001**, Chapter 17, Unit 17.3.
- (179) Aroyo, M. I.; Hahn, T., Eds. *International Tables for Crystallography, 6th Edition, Volume A: Space-Group*; John Wiley & Sons, Chichester, West Sussex, 2016.
- (180) Taylor, G. L. Introduction to phasing. *Acta Crystallogr. D Biol. Crystallogr.* **2010**, *66*, 325–338.
- (181) Bragg, W. L. The diffraction of short electromagnetic waves by a crystal. *Proceedings of the Cambridge Philosophical Society* **1913**, *17*, 43–57.
- (182) Wiseman, D. N.; Otchere, A.; Patel, J. H.; Uddin, R.; Pollock, N. L.; Routledge, S. J.; Rothnie, A. J.; Slack, C.; Poyner, D. R.; Bill, R. M.; Goddard, A. D. Expression and purification of recombinant G protein-coupled receptors: A review. *Protein Expr. Purif.* **2020**, *167*, 105524.
- (183) Abiko, L. A.; Rogowski, M.; Gautier, A.; Schertler, G.; Grzesiek, S. Efficient production of a functional G protein-coupled receptor in *E. coli* for structural studies. *J. Biomol. NMR* **2021**, *75*, 25–38.
- (184) Mallipeddi, S.; Zvonok, N.; Makriyannis, A. Expression, purification and characterization of the human cannabinoid 1 receptor. *Sci. Rep.* **2018**, *8*, 2935.
- (185) Link, A. J.; Skretas, G.; Strauch, E.-M.; Chari, N. S.; Georgiou, G. Efficient production of membrane-integrated and detergent-soluble G protein-coupled receptors in *Escherichia coli*. *Protein Sci.* **2008**, *17*, 1857–1863.
- (186) Petrovskaya, L. E.; Shulga, A. A.; Bocharova, O. V.; Ermolyuk, Y. S.; Kryukova, E. A.; Chupin, V. V.; Blommers, M. J. J.; Arseniev, A. S.; Kirpichnikov, M. P. Expression of G-protein coupled receptors in *Escherichia coli* for structural studies. *Biochemistry. Biokhimiia* **2010**, *75*, 881–891.
- (187) Weiss, H. M.; Grisshammer, R. Purification and characterization of the human adenosine A_{2A} receptor functionally expressed in *Escherichia coli*. *Eur. J. Biochem.* **2002**, *269*, 82–92.
- (188) Furukawa, H.; Haga, T. Expression of functional M₂ muscarinic acetylcholine receptor in *Escherichia coli*. *J. Biochem.* **2000**, *127*, 151–161.
- (189) Saarenpää, T.; Jaakola, V.-P.; Goldman, A. Baculovirus-mediated expression of GPCRs in insect cells. *Methods Enzymol.* **2015**, *556*, 185–218.
- (190) McKenzie, E. A.; Abbott, W. M. Expression of recombinant proteins in insect and mammalian cells. *Methods* **2018**, *147*, 40–49.
- (191) Marheineke, K.; Grünewald, S.; Christie, W.; Reiländer, H. Lipid composition of *Spodoptera frugiperda* (*Sf9*) and *Trichoplusia ni* (*Tn*) insect cells used for baculovirus infection. *FEBS Lett.* **1998**, *441*, 49–52.
- (192) Warne, T.; Chirnside, J.; Schertler, G. F. Expression and purification of truncated, non-glycosylated turkey beta-adrenergic receptors for crystallization. *Biochim. Biophys. Acta* **2003**, *1610*, 133–140.
- (193) Chien, E. Y. T.; Liu, W.; Zhao, Q.; Katritch, V.; Han, G. W.; Hanson, M. A.; Shi, L.; Newman, A. H.; Javitch, J. A.; Cherezov, V.; Stevens, R. C. Structure of the human dopamine D₃ receptor in complex with a D₂/D₃ selective antagonist. *Science* **2010**, *330*, 1091–1095.
- (194) Singh, S.; Gras, A.; Fiez-Vandal, C.; Ruprecht, J.; Rana, R.; Martinez, M.; Strange, P. G.; Wagner, R.; Byrne, B. Large-scale functional expression of WT and truncated human adenosine A_{2A} receptor in *Pichia pastoris* bioreactor cultures. *Microb. Cell Fact.* **2008**, *7*, 28.
- (195) Weiss, H. M.; Haase, W.; Michel, H.; Reiländer, H. Comparative biochemical and pharmacological characterization of the mouse 5-HT_{5A} 5-hydroxytryptamine receptor and the human β₂-adrenergic receptor produced in the methylotrophic yeast *Pichia pastoris*. *Biochem. J.* **1998**, *330* (Pt 3), 1137–1147.
- (196) Asada, H.; Uemura, T.; Yurugi-Kobayashi, T.; Shiroishi, M.; Shimamura, T.; Tsujimoto, H.; Ito, K.; Sugawara, T.; Nakane, T.; Nomura, N.; Murata, T.; Haga, T.; Iwata, S.; Kobayashi, T.

- Evaluation of the *Pichia pastoris* expression system for the production of GPCRs for structural analysis. *Microb. Cell Fact.* **2011**, *10*, 24.
- (197) Shimamura, T.; Shiroishi, M.; Weyand, S.; Tsujimoto, H.; Winter, G.; Katritch, V.; Abagyan, R.; Cherezov, V.; Liu, W.; Han, G. W.; Kobayashi, T.; Stevens, R. C.; Iwata, S. Structure of the human histamine H₁ receptor complex with doxepin. *Nature* **2011**, *475*, 65–70.
- (198) Hino, T.; Arakawa, T.; Iwanari, H.; Yurugi-Kobayashi, T.; Ikeda-Suno, C.; Nakada-Nakura, Y.; Kusano-Arai, O.; Weyand, S.; Shimamura, T.; Nomura, N.; Cameron, A. D.; Kobayashi, T.; Hamakubo, T.; Iwata, S.; Murata, T. G-protein-coupled receptor inactivation by an allosteric inverse-agonist antibody. *Nature* **2012**, *482*, 237–240.
- (199) Vieira Gomes, A. M.; Souza Carmo, T.; Silva Carvalho, L.; Mendonça Bahia, F.; Parachin, N. S. Comparison of yeasts as hosts for recombinant protein production. *Microorganisms* **2018**, *6*.
- (200) Hirz, M.; Richter, G.; Leitner, E.; Wriessnegger, T.; Pichler, H. A novel cholesterol-producing *Pichia pastoris* strain is an ideal host for functional expression of human Na,K-ATPase $\alpha 3\beta 1$ isoform. *Appl. Microbiol. Biotechnol.* **2013**, *97*, 9465–9478.
- (201) Hua, T.; Vemuri, K.; Pu, M.; Qu, L.; Han, G. W.; Wu, Y.; Zhao, S.; Shui, W.; Li, S.; Korde, A.; Laprairie, R. B.; Stahl, E. L.; Ho, J.-H.; Zvonok, N.; Zhou, H.; Kufareva, I.; Wu, B.; Zhao, Q.; Hanson, M. A.; Bohn, L. M.; Makriyannis, A.; Stevens, R. C.; Liu, Z.-J. Crystal structure of the human cannabinoid receptor CB₁. *Cell* **2016**, *167*, 750-762.e14.
- (202) Wingler, L. M.; McMahon, C.; Staus, D. P.; Lefkowitz, R. J.; Kruse, A. C. Distinctive activation mechanism for angiotensin receptor revealed by a synthetic nanobody. *Cell* **2019**, *176*, 479-490.e12.
- (203) Jamshad, M.; Charlton, J.; Lin, Y.-P.; Routledge, S. J.; Bawa, Z.; Knowles, T. J.; Overduin, M.; Dekker, N.; Dafforn, T. R.; Bill, R. M.; Poyner, D. R.; Wheatley, M. G-protein coupled receptor solubilization and purification for biophysical analysis and functional studies, in the total absence of detergent. *Biosci. Rep.* **2015**, *35*.
- (204) Lyons, J. A.; Shahsavar, A.; Paulsen, P. A.; Pedersen, B. P.; Nissen, P. Expression strategies for structural studies of eukaryotic membrane proteins. *Curr. Opin. Struct. Biol.* **2016**, *38*, 137–144.
- (205) Chae, P. S.; Rasmussen, S. G. F.; Rana, R. R.; Gotfryd, K.; Chandra, R.; Goren, M. A.; Kruse, A. C.; Nurva, S.; Loland, C. J.; Pierre, Y.; Drew, D.; Popot, J.-L.; Picot, D.; Fox, B. G.; Guan, L.; Gether, U.; Byrne, B.; Kobilka, B.; Gellman, S. H. Maltose-neopentyl glycol (MNG) amphiphiles for solubilization, stabilization and crystallization of membrane proteins. *Nat. Methods* **2010**, *7*, 1003–1008.
- (206) Breyton, C.; Javed, W.; Vermot, A.; Arnaud, C.-A.; Hajjar, C.; Dupuy, J.; Petit-Hartlein, I.; Le Roy, A.; Martel, A.; Thépaut, M.; Orelle, C.; Jault, J.-M.; Fieschi, F.; Porcar, L.; Ebel, C. Assemblies of lauryl maltose neopentyl glycol (LMNG) and LMNG-solubilized membrane proteins. *Biochim. Biophys. Acta Biomembr.* **2019**, *1861*, 939–957.
- (207) Lee, S.; Ghosh, S.; Jana, S.; Robertson, N.; Tate, C. G.; Vaidehi, N. How do branched detergents stabilize GPCRs in micelles? *Biochemistry* **2020**, *59*, 2125–2134.
- (208) Bornhorst, J. A.; Falke, J. J. Purification of proteins using polyhistidine affinity tags. *Methods Enzymol.* **2000**, *326*, 245–254.
- (209) Kobilka, B. K. Amino and carboxyl terminal modifications to facilitate the production and purification of a G protein-coupled receptor. *Anal. Biochem.* **1995**, *231*, 269–271.
- (210) Zou, Y.; Weis, W. I.; Kobilka, B. K. N-terminal T4 lysozyme fusion facilitates crystallization of a G protein coupled receptor. *PLoS one* **2012**, *7*, e46039.
- (211) Rosenbaum, D. M.; Zhang, C.; Lyons, J. A.; Holl, R.; Aragao, D.; Arlow, D. H.; Rasmussen, S. G. F.; Choi, H.-J.; DeVree, B. T.; Sunahara, R. K.; Chae, P. S.; Gellman, S. H.; Dror, R. O.; Shaw, D. E.; Weis, W. I.; Caffrey, M.; Gmeiner, P.; Kobilka, B. K. Structure and function of an irreversible agonist- β_2 adrenoceptor complex. *Nature* **2011**, *469*, 236–240.

- (212) Warne, T.; Serrano-Vega, M. J.; Baker, J. G.; Moukhametzianov, R.; Edwards, P. C.; Henderson, R.; Leslie, A. G. W.; Tate, C. G.; Schertler, G. F. X. Structure of a β_1 -adrenergic G-protein-coupled receptor. *Nature* **2008**, *454*, 486–491.
- (213) Yin, J.; Mobarec, J. C.; Kolb, P.; Rosenbaum, D. M. Crystal structure of the human OX2 orexin receptor bound to the insomnia drug suvorexant. *Nature* **2015**, *519*, 247–250.
- (214) Glukhova, A.; Thal, D. M.; Nguyen, A. T.; Vecchio, E. A.; Jörg, M.; Scammells, P. J.; May, L. T.; Sexton, P. M.; Christopoulos, A. Structure of the adenosine A₁ receptor reveals the basis for subtype selectivity. *Cell* **2017**, *168*, 867–877.e13.
- (215) Landau, E. M.; Rosenbusch, J. P. Lipidic cubic phases: a novel concept for the crystallization of membrane proteins. *Proc. Natl. Acad. Sci. U. S. A.* **1996**, *93*, 14532–14535.
- (216) Caffrey, M. On the mechanism of membrane protein crystallization in lipidic mesophases. *Cryst. Growth Des.* **2008**, *8*, 4244–4254.
- (217) Caffrey, M. A comprehensive review of the lipid cubic phase or *in meso* method for crystallizing membrane and soluble proteins and complexes. *Acta Crystallogr. F Struct. Biol. Commun.* **2015**, *71*, 3–18.
- (218) Cheng, A.; Hummel, B.; Qiu, H.; Caffrey, M. A simple mechanical mixer for small viscous lipid-containing samples. *Chem. Phys. Lipids* **1998**, *95*, 11–21.
- (219) Caffrey, M.; Li, D.; Dukkupati, A. Membrane protein structure determination using crystallography and lipidic mesophases: recent advances and successes. *Biochemistry* **2012**, *51*, 6266–6288.
- (220) Cheng, R. K. Y.; Segala, E.; Robertson, N.; Deflorian, F.; Doré, A. S.; Errey, J. C.; Fiez-Vandal, C.; Marshall, F. H.; Cooke, R. M. Structures of human A₁ and A_{2A} adenosine receptors with xanthines reveal determinants of selectivity. *Structure* **2017**, *25*, 1275–1285.e4.
- (221) Draper-Joyce, C. J.; Bhola, R.; Wang, J.; Bhattarai, A.; Nguyen, A. T. N.; Cowie-Kent, I.; O'Sullivan, K.; Chia, L. Y.; Venugopal, H.; Valant, C.; Thal, D. M.; Wootten, D.; Panel, N.; Carlsson, J.; Christie, M. J.; White, P. J.; Scammells, P.; May, L. T.; Sexton, P. M.; Danev, R.; Miao, Y.; Glukhova, A.; Imlach, W. L.; Christopoulos, A. Positive allosteric mechanisms of adenosine A₁ receptor-mediated analgesia. *Nature* **2021**, *597*, 571–576.
- (222) Draper-Joyce, C. J.; Khoshouei, M.; Thal, D. M.; Liang, Y.-L.; Nguyen, A. T. N.; Furness, S. G. B.; Venugopal, H.; Baltos, J.-A.; Plitzko, J. M.; Danev, R.; Baumeister, W.; May, L. T.; Wootten, D.; Sexton, P. M.; Glukhova, A.; Christopoulos, A. Structure of the adenosine-bound human adenosine A₁ receptor-G_i complex. *Nature* **2018**, *558*, 559–563.
- (223) Jespers, W.; Schiedel, A. C.; Heitman, L. H.; Cooke, R. M.; Kleene, L.; van Westen, G. J. P.; Gloriam, D. E.; Müller, C. E.; Sotelo, E.; Gutiérrez-de-Terán, H. Structural mapping of adenosine receptor mutations: ligand binding and signaling mechanisms. *Trends Pharmacol. Sci.* **2018**, *39*, 75–89.
- (224) Scholl, D.; Wells, J. N. Serine and alanine mutagenesis of the nine native cysteine residues of the human A₁ adenosine receptor. *Biochem. Pharmacol.* **2000**, *60*, 1647–1654.
- (225) Naranjo, A. N.; Chevalier, A.; Cousins, G. D.; Ayettey, E.; McCusker, E. C.; Wenk, C.; Robinson, A. S. Conserved disulfide bond is not essential for the adenosine A_{2A} receptor: extracellular cysteines influence receptor distribution within the cell and ligand-binding recognition. *Biochim. biophys. acta* **2015**, *1848*, 603–614.
- (226) Bause, E.; Hettkamp, H. Primary structural requirements for N-glycosylation of peptides in rat liver. *FEBS Lett.* **1979**, *108*, 341–344.
- (227) Patwardhan, A.; Cheng, N.; Trejo, J. Post-translational modifications of G Protein-coupled receptors control cellular signaling dynamics in space and time. *Pharmacol. Rev.* **2021**, *73*, 120–151.
- (228) Stamatis, D.; Lagarias, P.; Barkan, K.; Vrontaki, E.; Ladds, G.; Kolocouris, A. Structural characterization of agonist binding to an A₃ adenosine receptor through biomolecular simulations and mutagenesis experiments. *J. Med. Chem.* **2019**, *62*, 8831–8846.

- (229) Gao, Z.-G.; Chen, A.; Barak, D.; Kim, S.-K.; Müller, C. E.; Jacobson, K. A. Identification by site-directed mutagenesis of residues involved in ligand recognition and activation of the human A₃ adenosine receptor. *J. Biol. Chem.* **2002**, *277*, 19056–19063.
- (230) May, L. T.; Bridge, L. J.; Stoddart, L. A.; Briddon, S. J.; Hill, S. J. Allosteric interactions across native adenosine-A₃ receptor homodimers: quantification using single-cell ligand-binding kinetics. *FASEB journal : official publication of the Federation of American Societies for Experimental Biology* **2011**, *25*, 3465–3476.
- (231) Lagarias, P.; Barkan, K.; Tzortzini, E.; Stampelou, M.; Vrontaki, E.; Ladds, G.; Kolocouris, A. Insights to the binding of a selective adenosine A₃ receptor antagonist using molecular dynamic simulations, MM-PBSA and MM-GBSA free energy calculations, and mutagenesis. *J. Chem. Inf. Model.* **2019**, *59*, 5183–5197.
- (232) Duong, H. T.; Gao, Z.-G.; Jacobson, K. A. Nucleoside modification and concerted mutagenesis of the human A₃ adenosine receptor to probe interactions between the 2-position of adenosine analogs and Gln167 in the second extracellular loop. *Nucleosides, nucleotides & nucleic acids* **2005**, *24*, 1507–1517.
- (233) Gao, Z.-G.; Kim, S.-K.; Gross, A. S.; Chen, A.; Blaustein, J. B.; Jacobson, K. A. Identification of essential residues involved in the allosteric modulation of the human A₃ adenosine receptor. *Mol. Pharmacol.* **2003**, *63*, 1021–1031.
- (234) Jacobson, K. A.; Gao, Z.-G.; Chen, A.; Barak, D.; Kim, S.-A.; Lee, K.; Link, A.; van Rompaey, P.; van Calenbergh, S.; Liang, B. T. Neoreceptor concept based on molecular complementarity in GPCRs: a mutant adenosine A₃ receptor with selectively enhanced affinity for amine-modified nucleosides. *J. Med. Chem.* **2001**, *44*, 4125–4136.
- (235) Kim, J.; Wess, J.; van Rhee, A. M.; Schöneberg, T.; Jacobson, K. A. Site-directed mutagenesis identifies residues involved in ligand recognition in the human A_{2A} adenosine receptor. *J. Biol. Chem.* **1995**, *270*, 13987–13997.
- (236) Chen, A.; Gao, Z. G.; Barak, D.; Liang, B. T.; Jacobson, K. A. Constitutive activation of A₃ adenosine receptors by site-directed mutagenesis. *Biochem. Biophys. Res. Commun.* **2001**, *284*, 596–601.
- (237) Ciancetta, A.; Rubio, P.; Lieberman, D. I.; Jacobson, K. A. A₃ adenosine receptor activation mechanisms: molecular dynamics analysis of inactive, active, and fully active states. *J. Comput. Aided Mol. Des.* **2019**, *33*, 983–996.
- (238) Stoddart, L. A.; Kellam, B.; Briddon, S. J.; Hill, S. J. Effect of a toggle switch mutation in TM6 of the human adenosine A₃ receptor on G_i protein-dependent signalling and G_i-independent receptor internalization. *Br. J. Pharmacol.* **2014**, *171*, 3827–3844.
- (239) Pope, A. L.; Sanchez-Reyes, O. B.; South, K.; Zaitseva, E.; Ziliox, M.; Vogel, R.; Reeves, P. J.; Smith, S. O. A conserved proline hinge mediates helix dynamics and activation of rhodopsin. *Structure* **2020**, *28*, 1004-1013.e4.
- (240) Gao, Z.-G.; Kim, S.-K.; Biadatti, T.; Chen, W.; Lee, K.; Barak, D.; Kim, S. G.; Johnson, C. R.; Jacobson, K. A. Structural determinants of A₃ adenosine receptor activation: nucleoside ligands at the agonist/antagonist boundary. *J. Med. Chem.* **2002**, *45*, 4471–4484.
- (241) Barkan, K.; Lagarias, P.; Stampelou, M.; Stamatis, D.; Hoare, S.; Safitri, D.; Klotz, K.-N.; Vrontaki, E.; Kolocouris, A.; Ladds, G. Pharmacological characterisation of novel adenosine A₃ receptor antagonists. *Sci. Rep.* **2020**, *10*, 20781.
- (242) Xu, F.; Wu, H.; Katritch, V.; Han, G. W.; Jacobson, K. A.; Gao, Z.-G.; Cherezov, V.; Stevens, R. C. Structure of an agonist-bound human A_{2A} adenosine receptor. *Science* **2011**, *332*, 322–327.
- (243) Ragnarsson, L.; Andersson, Å.; Thomas, W. G.; Lewis, R. J. Mutations in the NPXXY motif stabilize pharmacologically distinct conformational states of the α_{1B}- and β₂-adrenoceptors. *Sci. Signal.* **2019**, *12*.
- (244) Filipek, S. Molecular switches in GPCRs. *Curr. Opin. Struct. Biol.* **2019**, *55*, 114–120.

- (245) Sansuk, K.; Deupi, X.; Torrecillas, I. R.; Jongejan, A.; Nijmeijer, S.; Bakker, R. A.; Pardo, L.; Leurs, R. A structural insight into the reorientation of transmembrane domains 3 and 5 during family A G protein-coupled receptor activation. *Mol. Pharmacol.* **2011**, *79*, 262–269.
- (246) Valentin-Hansen, L.; Holst, B.; Frimurer, T. M.; Schwartz, T. W. PheVI:09 (Phe6.44) as a sliding microswitch in seven-transmembrane (7TM) G protein-coupled receptor activation. *J. Biol. Chem.* **2012**, *287*, 43516–43526.
- (247) Olivella, M.; Caltabiano, G.; Cordoní, A. The role of cysteine 6.47 in class A GPCRs. *BMC Struct. Biol.* **2013**, *13*, 3.
- (248) Katritch, V.; Cherezov, V.; Stevens, R. C. Structure-function of the G-protein-coupled receptor superfamily. *Annu. Rev. Pharmacol. Toxicol.* **2012**, *53*, 531–556.
- (249) Pert, C. B.; Pasternak, G.; Snyder, S. H. Opiate agonists and antagonists discriminated by receptor binding in brain. *Science* **1973**, *182*.
- (250) C. B. Pert; S. H. Snyder. Opiate receptor binding of agonists and antagonists affected differentially by sodium. *Mol. Pharmacol.* **1974**, *10*, 868–879.
- (251) Gao, Z.-G.; Kim, S.-K.; IJzerman, A. P.; Jacobson, K. A. Allosteric modulation of the adenosine family of receptors. *Mini Rev. Med. Chem.* **2005**, *5*, 545–553.
- (252) Zarzycka, B.; Zaidi, S. A.; Roth, B. L.; Katritch, V. Harnessing ion-binding sites for GPCR pharmacology. *Pharmacol. Rev.* **2019**, *71*, 571–595.
- (253) Katritch, V.; Fenalti, G.; Abola, E. E.; Roth, B. L.; Cherezov, V.; Stevens, R. C. Allosteric sodium in class A GPCR signaling. *Trends Biochem. Sci.* **2014**, *39*, 233–244.
- (254) White, K. L.; Eddy, M. T.; Gao, Z.-G.; Han, G. W.; Lian, T.; Deary, A.; Patel, N.; Jacobson, K. A.; Katritch, V.; Stevens, R. C. Structural connection between activation microswitch and allosteric sodium site in GPCR signaling. *Structure* **2018**, *26*, 259–269.e5.
- (255) Jin Zhang; Kaihua Zhang; Zhan-Guo Gao; Silvia Paoletta; Dandan Zhang; Gye Won Han; Tingting Li; Limin Ma; Wenru Zhang; Christa E. Müller; Huaiyu Yang; Hualiang Jiang; Vadim Cherezov; Vsevolod Katritch; Kenneth A. Jacobson; Raymond C. Stevens; Beili Wu; Qiang Zhao. Agonist-bound structure of the human P2Y₁₂ receptor. *Nature* **2014**, *509*, 119–122.
- (256) Zhang, D.; Gao, Z. G.; Zhang, K.; Kiselev, E.; Crane, S.; Wang, J.; Paoletta, S.; Yi, C.; Ma, L.; Zhang, W.; Han, G. W.; Liu, H.; Cherezov, V.; Katritch, V.; Jiang, H.; Stevens, R. C.; Jacobson, K. A.; Zhao, Q.; Wu, B. Two disparate ligand-binding sites in the human P2Y₁ receptor. *Nature* **2015**, *520*.
- (257) Claff, T.; Klapschinski, T. A.; Subhramanyam, U. K. T.; Vaaßen, V. J.; Schlegel, J. G.; Vielmuth, C.; Voß, J. H.; Labahn, J.; Müller, C. E. Single stabilizing point mutation enables high-resolution co-crystal structures of the adenosine A_{2A} receptor with Preladenant conjugates. *Angew. Chem. Int. Ed. Engl.* **2022**.
- (258) Doré, A. S.; Robertson, N.; Errey, J. C.; Ng, I.; Hollenstein, K.; Tehan, B.; Hurrell, E.; Bennett, K.; Congreve, M.; Magnani, F.; Tate, C. G.; Weir, M.; Marshall, F. H. Structure of the adenosine A(2A) receptor in complex with ZM241385 and the xanthines XAC and caffeine. *Structure* **2011**, *19*, 1283–1293.
- (259) Fishman, P. Drugs targeting the A₃ adenosine receptor: human clinical study data. *Molecules* **2022**, *27*.
- (260) Gessi, S.; Merighi, S.; Varani, K.; Leung, E.; Mac Lennan, S.; Borea, P. A. The A₃ adenosine receptor: an enigmatic player in cell biology. *Pharmacol. Ther.* **2008**, *117*, 123–140.
- (261) Guan, X. M.; Kobilka, T. S.; Kobilka, B. K. Enhancement of membrane insertion and function in a type IIIb membrane protein following introduction of a cleavable signal peptide. *J. Biol. Chem.* **1992**, *267*, 21995–21998.
- (262) Alexandrov, A. I.; Mileni, M.; Chien, E. Y. T.; Hanson, M. A.; Stevens, R. C. Microscale fluorescent thermal stability assay for membrane proteins. *Structure* **2008**, *16*, 351–359.
- (263) Qin, L.; Kufareva, I.; Holden, L. G.; Wang, C.; Zheng, Y.; Zhao, C.; Fenalti, G.; Wu, H.; Han, G. W.; Cherezov, V.; Abagyan, R.; Stevens, R. C.; Handel, T. M. Crystal structure of the chemokine receptor CXCR4 in complex with a viral chemokine. *Science* **2015**, *347*, 1117–1122.

- (264) Chu, R.; Takei, J.; Knowlton, J.; Andrykovitch, M.; Pei, W.; Kajava, A. V.; Steinbach, P. J.; Ji, X.; Bai, Y. Redesign of a Four-helix Bundle Protein by Phage Display Coupled with Proteolysis and Structural Characterization by NMR and X-ray Crystallography. *J. Mol. Biol.* **2002**, *323*, 253–262.
- (265) Cellitti, J.; Llinas, M.; Echols, N.; Shank, E. A.; Gillespie, B.; Kwon, E.; Crowder, S. M.; Dahlquist, F. W.; Alber, T.; Marqusee, S. Exploring subdomain cooperativity in T4 lysozyme I: structural and energetic studies of a circular permutant and protein fragment. *Protein Sci.* **2007**, *16*, 842–851.
- (266) Quezada, C. M.; Gradinaru, C.; Simon, M. I.; Bilwes, A. M.; Crane, B. R. *CheA phosphotransferase domain from Thermotoga maritima*, 2004.
- (267) Horcajada, C.; Guinovart, J. J.; Fita, I.; Ferrer, J. C. *Structure of the C domain of glycogen synthase from Pyrococcus abyssi*, 2005.
- (268) Martínez-Solís, M.; Gómez-Sebastián, S.; Escribano, J. M.; Jakubowska, A. K.; Herrero, S. A novel baculovirus-derived promoter with high activity in the baculovirus expression system. *PeerJ* **2016**, *4*, e2183.
- (269) Garrity, D. B.; Chang, M. J.; Blissard, G. W. Late promoter selection in the baculovirus gp64 envelope fusion protein gene. *Virology* **1997**, *231*, 167–181.
- (270) Rucktooa, P.; Cheng, R. K. Y.; Segala, E.; Geng, T.; Errey, J. C.; Brown, G. A.; Cooke, R. M.; Marshall, F. H.; Doré, A. S. Towards high throughput GPCR crystallography: In Meso soaking of Adenosine A_{2A} Receptor crystals. *Sci. Rep.* **2018**, *8*, 41.
- (271) Kooistra, A. J.; Mordalski, S.; Pándy-Szekeres, G.; Esguerra, M.; Mamyrbekov, A.; Munk, C.; Keserü, G. M.; Gloriam, D. E. GPCRdb in 2021: integrating GPCR sequence, structure and function. *Nucleic Acids Res.* **2021**, *49*, D335-D343.
- (272) Wang, G.; Jong, R. N. de; van den Bremer, E. T. J.; Parren, Paul W. H. I.; Heck, A. J. R. Enhancing accuracy in molecular weight determination of highly heterogeneously glycosylated proteins by native tandem mass spectrometry. *Anal. Chem.* **2017**, *89*, 4793–4797.
- (273) Harrison, R. L.; Jarvis, D. L. Protein N-glycosylation in the Baculovirus–Insect cell expression system and engineering of insect cells to produce “mammalianized” recombinant glycoproteins. In *Insect Viruses: Biotechnological Applications*; Elsevier; pp. 159–191.
- (274) Goth, C. K.; Petäjä-Repo, U. E.; Rosenkilde, M. M. G protein-coupled receptors in the sweet spot: glycosylation and other post-translational modifications. *ACS Pharmacol. Transl. Sci.* **2020**, *3*, 237–245.
- (275) Yamamoto, K.; Ichikawa, S. Tunicamycin: chemical synthesis and biosynthesis. *J. Antibiot. (Tokyo)* **2019**, *72*, 924–933.
- (276) Maley, F.; Trimble, R. B.; Tarentino, A. L.; Plummer, T. H. Characterization of glycoproteins and their associated oligosaccharides through the use of endoglycosidases. *Anal. Biochem.* **1989**, *180*, 195–204.
- (277) Abdullahi, A.; Stanojic, M.; Parousis, A.; Patsouris, D.; Jeschke, M. G. Modeling acute ER stress in vivo and in vitro. *Shock (Augusta, Ga.)* **2017**, *47*, 506–513.
- (278) Jain, A. R.; Robinson, A. S. Functional expression of adenosine A₃ receptor in yeast utilizing a chimera with the A_{2A}R C-Terminus. *Int. J. Mol. Sci.* **2020**, *21*.
- (279) Robertson, N.; Jazayeri, A.; Errey, J.; Baig, A.; Hurrell, E.; Zhukov, A.; Langmead, C. J.; Weir, M.; Marshall, F. H. The properties of thermostabilised G protein-coupled receptors (StaRs) and their use in drug discovery. *Neuropharmacology* **2011**, *60*, 36–44.
- (280) Pándy-Szekeres, G.; Esguerra, M.; Hauser, A. S.; Caroli, J.; Munk, C.; Pilger, S.; Keserü, G. M.; Kooistra, A. J.; Gloriam, D. E. The G protein database, GproteinDb. *Nucleic Acids Res.* **2022**, *50*, D518-D525.
- (281) Doherty, E.; Pakarinen, P.; Tiitinen, A.; Kiilavuori, A.; Huhtaniemi, I.; Forrest, S.; Aittomäki, K. A Novel mutation in the FSH receptor inhibiting signal transduction and causing primary ovarian failure. *J. Clin. Endocrinol. Metab.* **2002**, *87*, 1151–1155.

- (282) Huang, R. R.; Yu, H.; Strader, C. D.; Fong, T. M. Interaction of substance P with the second and seventh transmembrane domains of the neurokinin-1 receptor. *Biochemistry* **1994**, *33*, 3007–3013.
- (283) Salchow, K.; Bond, M. E.; Evans, S. C.; Press, N. J.; Charlton, S. J.; Hunt, P. A.; Bradley, M. E. A common intracellular allosteric binding site for antagonists of the CXCR2 receptor. *Br. J. Pharmacol.* **2010**, *159*, 1429–1439.
- (284) Lebon, G.; Bennett, K.; Jazayeri, A.; Tate, C. G. Thermostabilisation of an agonist-bound conformation of the human adenosine A(2A) receptor. *J. Mol. Biol.* **2011**, *409*, 298–310.
- (285) Roth, C. B.; Hanson, M. A.; Stevens, R. C. Stabilization of the human β_2 -adrenergic receptor TM4-TM3-TM5 helix interface by mutagenesis of Glu122^{3,41}, a critical residue in GPCR structure. *J. Mol. Biol.* **2008**, *376*, 1305–1319.
- (286) Angelova, K.; Fanelli, F.; Puett, D. Contributions of intracellular loops 2 and 3 of the lutropin receptor in Gs coupling. *Mol. Endocrinol.* **2008**, *22*, 126–138.
- (287) Graaf, C. de; Foata, N.; Engkvist, O.; Rognan, D. Molecular modeling of the second extracellular loop of G-protein coupled receptors and its implication on structure-based virtual screening. *Proteins* **2008**, *71*, 599–620.
- (288) Cook, J. V.; Eidne, K. A. An intramolecular disulfide bond between conserved extracellular cysteines in the gonadotropin-releasing hormone receptor is essential for binding and activation. *Endocrinology* **1997**, *138*, 2800–2806.
- (289) Iglesias, A.; Cimadevila, M.; La Fuente, R. A. de; Martí-Solano, M.; Cadavid, M. I.; Castro, M.; Selent, J.; Loza, M. I.; Brea, J. Serotonin 2A receptor disulfide bridge integrity is crucial for ligand binding to different signalling states but not for its homodimerization. *Eur. J. Pharmacol.* **2017**, *815*, 138–146.
- (290) Reader, T. A.; Molina-Holgado, E.; Lima, L.; Boulianne, S.; Dewar, K. M. Specific [³H]raclopride binding to neostriatal dopamine D₂ receptors: role of disulfide and sulfhydryl groups. *Neurochem. Res.* **1992**, *17*, 749–759.
- (291) Harikumar, K. G.; John, P. T.; Chattopadhyay, A. Role of disulfides and sulfhydryl groups in agonist and antagonist binding in serotonin1A receptors from bovine hippocampus. *Cell. Mol. Neurobiol.* **2000**, *20*, 665–681.
- (292) Malawski, G. A.; Hillig, R. C.; Monteclaro, F.; Eberspaecher, U.; Schmitz, A. A. P.; Crusius, K.; Huber, M.; Egner, U.; Donner, P.; Müller-Tiemann, B. Identifying protein construct variants with increased crystallization propensity--a case study. *Protein Sci.* **2006**, *15*, 2718–2728.
- (293) Weichert, D.; Gmeiner, P. Covalent molecular probes for class A G protein-coupled receptors: advances and applications. *ACS Chem. Biol.* **2015**, *10*, 1376–1386.
- (294) Martin, J. S.; MacKenzie, C. J.; Fletcher, D.; Gilbert, I. H. Characterising covalent warhead reactivity. *Bioorg. Med. Chem.* **2019**, *27*, 2066–2074.
- (295) Xia, L.; Burger, W. A. C.; van Veldhoven, J. P. D.; Kuiper, B. J.; van Duijl, T. T.; Lenselink, E. B.; Paasman, E.; Heitman, L. H.; IJzerman, A. P. Structure-affinity relationships and structure-kinetics relationships of Pyrido[2,1-*f*]purine-2,4-dione derivatives as human adenosine A₃ receptor antagonists. *J. Med. Chem.* **2017**, *60*, 7555–7568.
- (296) Avet, C.; Mancini, A.; Breton, B.; Le Gouill, C.; Hauser, A. S.; Normand, C.; Kobayashi, H.; Gross, F.; Hogue, M.; Lukasheva, V.; St-Onge, S.; Carrier, M.; Héroux, M.; Morissette, S.; Fauman, E.; Fortin, J.-P.; Schann, S.; Leroy, X.; Gloriam, D. E.; Bouvier, M. *Effector membrane translocation biosensors reveal G protein and β arrestin coupling profiles of 100 therapeutically relevant GPCRs*, 2020.
- (297) Galés, C.; van Durm, J. J. J.; Schaak, S.; Pontier, S.; Percherancier, Y.; Audet, M.; Paris, H.; Bouvier, M. Probing the activation-promoted structural rearrangements in preassembled receptor-G protein complexes. *Nat. Struct. Mol. Biol.* **2006**, *13*, 778–786.
- (298) Srivastava, D.; Gakhar, L.; Artemyev, N. O. Structural underpinnings of Ric8A function as a G-protein α -subunit chaperone and guanine-nucleotide exchange factor. *Nat. Commun.* **2019**, *10*, 3084.

- (299) Mahammad, S.; Parmryd, I. Cholesterol depletion using methyl- β -cyclodextrin. *Methods Mol. Bio.* **2015**, *1232*, 91–102.
- (300) Behrenswerth, A. Adenosin-rezeptoren und neurodegenerative Erkrankungen: Untersuchung des Einflusses von Cholesterol und Evaluierung neuer funktionalisierter Liganden als pharmakologische Werkzeuge. Ph. D. Thesis, Rheinische Friedrich-Wihlms-Universität Bonn, Bonn, Germany, 2008.
- (301) Gimpl, G.; Fahrenholz, F. Cholesterol as stabilizer of the oxytocin receptor. *Biochim. Biophys. Acta* **2002**, *1564*, 384–392.
- (302) Monteiro, F.; Bernal, V.; Chaillet, M.; Berger, I.; Alves, P. M. Targeted supplementation design for improved production and quality of enveloped viral particles in insect cell-baculovirus expression system. *J. Biotechnol.* **2016**, *233*, 34–41.
- (303) Mao, C.; Shen, C.; Li, C.; Shen, D.-D.; Xu, C.; Zhang, S.; Zhou, R.; Shen, Q.; Chen, L.-N.; Jiang, Z.; Liu, J.; Zhang, Y. Cryo-EM structures of inactive and active GABA_B receptor. *Cell Res.* **2020**, *30*, 564–573.
- (304) Klotz, K. N.; Lohse, M. J.; Schwabe, U. Characterization of the solubilized A₁ adenosine receptor from rat brain membranes. *J. Neurochem.* **1986**, *46*, 1528–1534.
- (305) Ji, X. D.; Jacobson, K. A. Solubilized rabbit striatal A_{2A}-adenosine receptors: stability and antagonist binding. *Arch. Biochem. Biophys.* **1993**, *305*, 611–617.
- (306) Harvey, V.; Jones, J.; Misra, A.; Knight, A. R.; Quirk, K. Solubilisation and immunoprecipitation of rat striatal adenosine A_{2A} receptors. *Eur. J. Pharmacol.* **2001**, *431*, 171–177.
- (307) Miljus, T.; Sykes, D. A.; Harwood, C. R.; Vuckovic, Z.; Veprintsev, D. B. GPCR solubilization and quality control. *Methods Mol. Bio.* **2020**, *2127*, 105–127.
- (308) Banerjee, P.; Buse, J. T.; Dawson, G. Asymmetric extraction of membrane lipids by CHAPS. *Biochim. Biophys. Acta* **1990**, *1044*, 305–314.
- (309) Banerjee, P.; Joo, J. B.; Buse, J. T.; Dawson, G. Differential solubilization of lipids along with membrane proteins by different classes of detergents. *Chem. Phys. Lipids* **1995**, *77*, 65–78.
- (310) Soave, M.; Briddon, S. J.; Hill, S. J.; Stoddart, L. A. Fluorescent ligands: Bringing light to emerging GPCR paradigms. *Br. J. Pharmacol.* **2020**, *177*, 978–991.
- (311) Kozma, E.; Jayasekara, P. S.; Squarcialupi, L.; Paoletta, S.; Moro, S.; Federico, S.; Spalluto, G.; Jacobson, K. A. Fluorescent ligands for adenosine receptors. *Bioorg. Med. Chem. Lett.* **2013**, *23*, 26–36.
- (312) Grueninger-Leitch, F.; D'Arcy, A.; D'Arcy, B.; Chène, C. Deglycosylation of proteins for crystallization using recombinant fusion protein glycosidases. *Protein Sci.* **1996**, *5*, 2617–2622.
- (313) Zheng, Y.; Han, G. W.; Abagyan, R.; Wu, B.; Stevens, R. C.; Cherezov, V.; Kufareva, I.; Handel, T. M. Structure of CC chemokine receptor 5 with a potent chemokine antagonist reveals mechanisms of chemokine recognition and molecular mimicry by HIV. *Immunity* **2017**, *46*, 1005–1017.e5.
- (314) Peng, Y.; McCorvy, J. D.; Harpsøe, K.; Lansu, K.; Yuan, S.; Popov, P.; Qu, L.; Pu, M.; Che, T.; Nikolajsen, L. F.; Huang, X.-P.; Wu, Y.; Shen, L.; Bjørn-Yoshimoto, W. E.; Ding, K.; Wacker, D.; Han, G. W.; Cheng, J.; Katritch, V.; Jensen, A. A.; Hanson, M. A.; Zhao, S.; Gloriam, D. E.; Roth, B. L.; Stevens, R. C.; Liu, Z.-J. 5-HT_{2C} receptor structures reveal the structural basis of GPCR polypharmacology. *Cell* **2018**, *172*, 719–730.e14.
- (315) Rader, A. J.; Anderson, G.; Isin, B.; Khorana, H. G.; Bahar, I.; Klein-Seetharaman, J. Identification of core amino acids stabilizing rhodopsin. *Proc. Natl. Acad. Sci. U. S. A.* **2004**, *101*, 7246–7251.
- (316) Gutiérrez-de-Terán, H.; Massink, A.; Rodríguez, D.; Liu, W.; Han, G. W.; Joseph, J. S.; Katritch, I.; Heitman, L. H.; Xia, L.; IJzerman, A. P.; Cherezov, V.; Katritch, V.; Stevens, R. C. The role of a sodium ion binding site in the allosteric modulation of the A_{2A} adenosine G protein-coupled receptor. *Structure* **2013**, *21*, 2175–2185.

- (317) Zheng, Y.; Qin, L.; Zacarías, N. V. O.; Vries, H. de; Han, G. W.; Gustavsson, M.; Dabros, M.; Zhao, C.; Cherney, R. J.; Carter, P.; Stamos, D.; Abagyan, R.; Cherezov, V.; Stevens, R. C.; IJzerman, A. P.; Heitman, L. H.; Tebben, A.; Kufareva, I.; Handel, T. M. Structure of CC chemokine receptor 2 with orthosteric and allosteric antagonists. *Nature* **2016**, *540*, 458–461.
- (318) Lavington, S.; Watts, A. Lipid nanoparticle technologies for the study of G protein-coupled receptors in lipid environments. *Biophys. Rev.* **2020**.
- (319) Li, X.; Hua, T.; Vemuri, K.; Ho, J.-H.; Wu, Y.; Wu, L.; Popov, P.; Benchama, O.; Zvonok, N.; Locke, K.; Qu, L.; Han, G. W.; Iyer, M. R.; Cinar, R.; Coffey, N. J.; Wang, J.; Wu, M.; Katritch, V.; Zhao, S.; Kunos, G.; Bohn, L. M.; Makriyannis, A.; Stevens, R. C.; Liu, Z.-J. Crystal structure of the human cannabinoid receptor CB₂. *Cell* **2019**, *176*, 459–467.e13.
- (320) Bryksin, A. V.; Matsumura, I. Overlap extension PCR cloning: a simple and reliable way to create recombinant plasmids. *BioTechniques* **2010**, *48*, 463–465.
- (321) Ciccarone, V. C.; Polayes, D. A.; Luckow, V. A. Generation of recombinant baculovirus DNA in *E.coli* using a baculovirus shuttle vector. *Methods Mol. Med.* **1998**, *13*, 213–235.
- (322) Luckow, V. A.; Lee, S. C.; Barry, G. F.; Olins, P. O. Efficient generation of infectious recombinant baculoviruses by site-specific transposon-mediated insertion of foreign genes into a baculovirus genome propagated in *Escherichia coli*. *J. Virol.* **1993**, *67*, 4566–4579.
- (323) Caffrey, M.; Cherezov, V. Crystallizing membrane proteins using lipidic mesophases. *Nat. Protoc.* **2009**, *4*, 706–731.
- (324) Temirak, A.; Schlegel, J. G.; Voss, J. H.; Vaaßen, V. J.; Vielmuth, C.; Claff, T.; Müller, C. E. Irreversible antagonists for the adenosine A_{2B} receptor. *Molecules* **2022**, *27*.
- (325) Lowry, O. H.; Rosebrough, N. J.; Farr, A. L.; Randall, R. J. Protein measurement with the Folin phenol reagent. *J. Biol. Chem.* **1951**, *193*, 265–275.